

Lisa Wronski, BSc

Extraction of the rock structure directly out of a 3D point cloud – a case study of the Ricobayo dam site

MASTER THESIS

presented to achieve the degree of

Master of Science

in the Master's programme Earth Sciences

Graz University of Technology

Supervisor:

Ao.Univ.-Prof. Dr. Qian Liu

Institute of Applied Geosciences

Graz, June 2019

EIDESSTATTLICHE ERKLÄRUNG

Ich erkläre an Eides statt, dass ich diese Arbeit selbstständig und ohne fremde Hilfe verfasst, keine anderen Quellen als die angegebenen benützt und die den benützten Quellen wörtlich und inhaltlich entnommenen Stellen gekennzeichnet habe.

Diese Arbeit wurde bisher weder im In- noch im Ausland als Prüfungsarbeit vorgelegt.

Das in TUGRAZonline hochgeladene Textdokument ist mit der vorliegenden Masterarbeit identisch.

Graz, im Juni 2019

Lisa Wronski

ACKNOWLEDGEMENTS

I would like to thank my supervisor Prof. Qian Liu for his support, advice, forward-looking guidance, and inspiring discussions which helped to enhance my motivation for the preparation of this thesis.

Further, I would like to thank my family and my boyfriend Alex for their support during my studies.

Abstract

This thesis proposes a method for feature extraction directly out of a 3D point cloud while trying to enhance the use of open-source software for this purpose. The procedure is rather objective without losing the connection to the user's knowledge, can handle huge datasets, and includes several steps to improve the orientation accuracy as well as to evaluate its performance. In addition, it considers dip and dip direction at the same time for set extraction with the Facets Plugin (Dewez et al., 2016), a CloudCompare (2019) plugin initially made for structural geology. The main steps are the Hough normals calculation (Boulch and Marlet, 2016) and visualization as dip and dip direction scalar fields, a spherical k-means clustering (Hornik et al., 2017) with a silhouette plot (Rousseeuw, 1987) and user-based evaluation of the clusters, the orientation statistics of the identified sets including variability angle and confidence angle, the set extraction with the Facets Plugin (Dewez et al., 2016), the statistical outlier removal, the surface segmentation, and the plane fitting. Afterwards, the planes are investigated in terms of their orientation, size, and spatial relations, i.e. termination which is evaluated by means of a 3D-version of the termination index approach by ISRM (1978). The procedure has been developed and tested on geometric forms (Riquelme et al., 2014) before its application on the TLS point cloud from the Ricobayo dam site. Although the surface roundness and sometimes the TLS point cloud itself posed challenges to the plane fitting, the fracture pattern has been extracted successfully. Improvements of the method could mainly address the clustering and the orientation statistics.

Sheeting joints have been identified to control the slope direction. They are pre-dated by two conjugated sets which can be assigned to the NE-SW striking subvertical faults reported by González Clavijo and Martínez Catalán (2002). Another set, which post-dates the sheeting joints, has been identified in some segments of the TLS data sets. However, its small plane size might have caused that it has been overlooked, concealed by noise, or not mapped due to the small planes which are irrelevant to the engineering geological behavior of the rock mass. The waviness, high persistence, and weathering state of the sheeting joints are particularly critical for this behavior as well as for slope stability. The slope around the Ricobayo dam's plunge pool seems to be controlled by sheeting joints, including slope failures at the massive scour events which occurred in the first years of the dam.

Table of contents

1.	Introduction and intention	1
2.	Laser Scanning & Digital Feature Extraction	2
2.1	Laser Scanning	2
2.2	Feature Extraction.....	4
2.3	Data acquisition at Ricobayo	7
3.	Geology of Ricobayo, Western Spain	8
3.1	The Ricobayo dam site.....	8
3.2	Geological Units	10
3.2.1	Stratigraphy	10
3.2.2	Structural Geology.....	13
3.3	Regional Geological Evolution.....	16
3.3.1	Variscan Orogeny.....	16
3.3.2	Detailed evolution	17
4.	Methodology.....	20
4.1	Normals computation	20
4.2	Dip / Dip Direction	21
4.3	Set identification.....	22
4.4	Orientation statistics.....	24
4.5	Filtering & plane fitting.....	26
4.6	Set characteristics.....	28
4.7	Workflow summary	31
5	Results	33
5.1	Observations from tests with geometrical forms	33
5.2	Observations from the Ricobayo data	37
5.2.1	Remarks to the method	37
5.2.2	Sets in segment 1 (BK).....	38
5.2.3	Sets in segment 2 (BI-part 2).....	60
5.2.3	Sets in segment 3 (BI-part 1).....	78
5.2.4	Sets in segment 4 (WG)	95
6	Interpretation	122
6.1	Joint sets.....	122
6.2	Plane fitting problems.....	132
7	Discussion.....	134
7.1	Method.....	134
7.2	Results	138

8 Conclusion	144
Literature	147
Appendix	154

1. Introduction and intention

This Master's Thesis' aim is to identify the in situ discontinuity pattern of the Ricobayo dam site, Western Spain, out of point cloud data acquired by TLS. The joints are identified in the point cloud, organized in sets, and described by planes. The workflow is developed using the open-source software CloudCompare (2019) and R (R Core Team, 2018), and the commercial software FracMan (Golder Associates Inc., 2018).

In general, the extraction of discontinuities and their properties out of photogrammetry or LiDAR data has been investigated intensively in the last decade. Based on many different extraction methods developed during extensive research, a new method is developed and applied in this thesis. It tries to use the power of CloudCompare (2019) as far as possible, to maintain a certain objectivity while profiting from the user's knowledge, and provide a tool to effectively extract the discontinuity pattern out of a point cloud. In a first step, the workflow is applied to geometric forms in order to examine the performance. Afterwards, the method is applied to the TLS data of the Ricobayo dam site to investigate the in situ discontinuity pattern as well as the joints' spatial relations and their engineering geological behavior. This information is critical for rock mass behavior, further kinematic analyses, and mass wasting, for example.

2. Laser Scanning & Digital Feature Extraction

2.1 Laser Scanning

Laser Scanning, also called LiDAR (light detection and ranging), is a fast data acquisition technique to conduct 3D measurements of a rock face with high resolution (up to 10000 points/m², Riquelme et al., 2017) and accuracy (standard deviation <1 cm at 100 m, Riquelme et al., 2017). It uses wavelengths of 500 nm to 1700 nm (Jaboyedoff et al., 2012, review paper – citation always includes references therein). Among its many applications are discontinuity orientation assessment (e.g. Riquelme et al., 2017) and slope displacement detection (Oppikofer et al., 2012), as well as slope deformation modelling and rock slopes monitoring (Abellán et al., 2014, review paper – citation always includes references therein).

According to Jaboyedoff et al. (2012) the scanner can be ground-based (terrestrial, TLS) or air-based (airborne, ALS), both providing efficient data from remote areas. The range can be up to 2000 m, depending on the used wavelengths (longer wavelength – higher range). The working principle (Figure 1) is based on laser pulses which are sent out by the instrument sensor and back-scattered by any object in the line of sight (LOS). The sensor records the returning signal. There are phase- and pulse- based sensors, the latter being more widely used as greater ranges are possible (Jaboyedoff et al., 2012; Abellán et al., 2014). Therefore, this pulse-based methodology is described here. By using the laser pulse's time of flight Δt , the distance d can be computed as given in equation (1), where c is the speed of light. In case of objects in the LOS, like vegetation, several return pulses reach the sensor for one emitted pulse (Figure 1). This can be used to filter these objects out. Vegetation, for example, is undesirable in the point cloud (Jaboyedoff et al., 2012).

$$2 * d = c * \Delta t \quad (1)$$

With the laser scanner's known position and attitude as well as the laser pulse's direction (LOS), the coordinates (Δx , Δy , Δz) of the measured reflective surface relative to the scanner can be determined (Jaboyedoff et al., 2012). Natural rock slopes have a reflectivity of about 20% (Abellán et al., 2014). By aligning the point cloud by ground control points (GCP), absolute coordinates (x , y , z) of the measured surfaces can be calculated (Jaboyedoff et al., 2012).

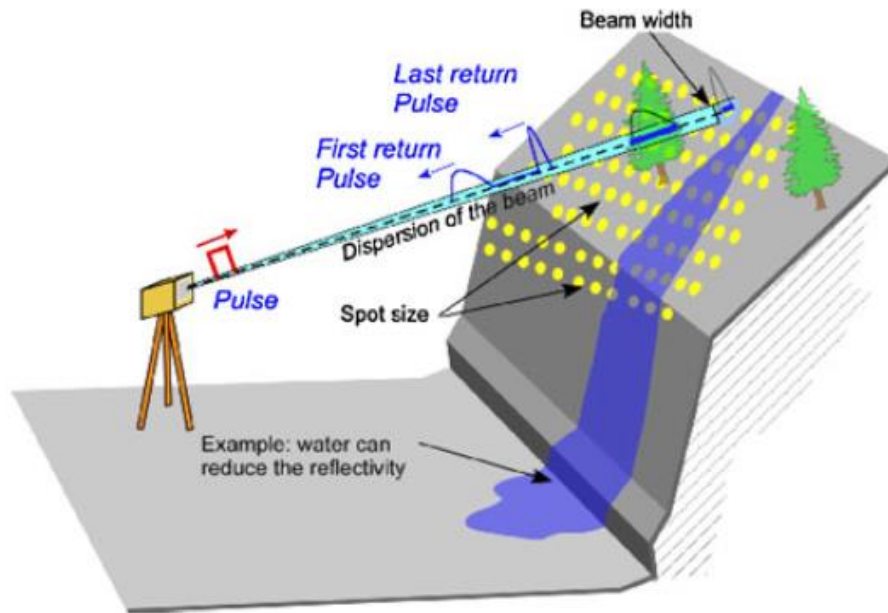


Figure 1: Principle of TLS (modified after Jaboyedoff et al., 2012)

As the laser beam diverges with distance, its footprint increases at greater ranges which decreases the resolution. The beam width and the sampling interval together define the angular resolution, which is the ability to distinguish two neighboring spots from each other (two LOS). In LOS direction, the range resolution is the governing parameter (Jaboyedoff et al., 2012). The resolution is for example decreased by very rough or low reflective surfaces (see Figure 1), surfaces parallel to the LOS, rain, hot wind, or fog, a too great range as already mentioned, shadows or very bright ambience (Jaboyedoff et al., 2012). According to Abellán et al. (2014), these parameters also decrease the accuracy. Shadows, i.e. occlusions (Figure 2), occur when the concerned surface is parallel to the scanner's LOS which equals a highly oblique incidence angle of the laser beam and a big footprint (Jaboyedoff et al., 2012; Abellán et al., 2014). Noise, which depends on the target material's reflectivity (Assali et al., 2014) also decreases the data quality. Vegetation, weathered surfaces, and residual soils also increase the noise (Chen et al., 2016).

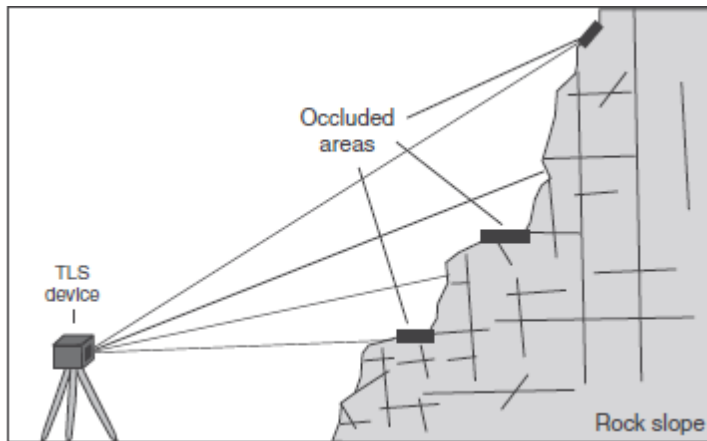


Figure 2: Occlusion problem during TLS (modified after Abellán et al., 2014)

Remote sensing techniques hold numerous advantages compared to field work which is time-consuming, sometimes dangerous, biased and error prone (Chen et al., 2016 and references therein). Its disadvantages are also caused by the remoteness, of course, i.e. sampling is impossible, and the resolution and quality of the scanned data determine the amount of information which can be acquired by its investigation and analysis. Another remote sensing technique is photogrammetry, also called structure from motion (SfM). It is cheaper than laser scanning, but its precision depends on the applied camera's resolution (Riquelme et al., 2017). In addition, the laser scanning results are more reliable and accurate concerning the data geometry, in particular at edges and on oblique or sub-horizontal surfaces (Riquelme et al., 2017). However, it must be mentioned that Riquelme et al. (2017) only used photographs from a standing position. In general, SfM is more flexible, more effective and more economic to use than laser scanning (Tung et al., 2018). Photogrammetry-based point clouds show more noise than point clouds from laser scanning (Assali et al., 2014).

2.2 Feature Extraction

During the last about 15 years, several methods have been developed and tested to extract discontinuities as well as their characteristics out of point clouds. Possibly the widest known among these methods are the Matlab-based discontinuity set extractor (DSE) by Riquelme et al. (2014) and the commercial Coltop3D software by Jaboyedoff et al. (2007). References concerning the mentioned software used in the various methodologies are given in the corresponding papers.

Some methods need a mesh and facets to evaluate the orientation, while others work directly with the points in the cloud. 2.5D meshing sometimes creates data artefacts (Abellán et al., 2014, review paper – citation always includes references therein). Coltop3D (Jaboyedoff et al., 2007), for example, uses an eigenvalue analysis of the neighborhood's covariance matrix to determine dip and dip direction of a normal on a plane triangulated between neighboring

points. The results are visualized by a HSI wheel based color code. The software needs a DEM to analyze. Another commercial application is the GAIA-GeoRoc software by Assali et al. (2014), based on R and C++. It uses the HSV wheel (Jaboyedoff et al., 2007) for point-cloud visualization and CloudCompare for the pre-processing. With a spherical k-means algorithm implemented in R and the silhouette concept (Rousseeuw, 1987), the data is classified into subsets according to the orientation of the normals of each point in the cloud. Outliers are eliminated through their silhouette widths. Therefore, this concept does not need a meshed surface. The orientation matrix and its eigenvectors provide the mean cluster orientations (Assali et al., 2014). A virtual scanline can be applied afterwards to determine set parameters like spacing and persistence (Assali et al., 2014). Abellán et al. (2014) also mention the very simple technique of manually extracting a specific area followed by a least-square plane fitting. This is a very subjective procedure, but it can be useful for artificially fractured rock faces after blasting, for example (Abellán et al., 2014). The DSE by Riquelme et al. (2014) extracts the discontinuities directly out of a 3D point cloud. At first, the method searches for coplanar points. Afterwards, it proceeds to project normal vectors of the detected planes to a stereonet. Therefore, the number of sets is identified. This summary of the DSE has been given by Chen et al. (2016). In detail, the DSE (Riquelme et al., 2014) calculates the normal vector of each point in the cloud based on coplanar neighboring points. Afterwards, it determines the orientation of the best-fit plane of each identified subset, plots the plane normal vectors into a stereonet, and identifies the local density maxima. After a filtering process, the sets are identified and all normal vectors are classified to the set whose normal vector differs by the minimum angle of the concerned normal vector. A final clustering algorithm classifies all points to their corresponding sets which are represented by a best-fit plane. Chen et al. (2016) use a k-means clustering and the silhouette index (Rousseeuw, 1987) to automatically group discontinuities, segment and optimize these and redistribute misclassified features. The method finishes with a RANSAC plane fitting. Chen et al. (2016) tested their methodology on two geometric forms (Riquelme et al., 2014). The point cloud's noise is reduced and a DSM is calculated, i.e. this method needs a mesh and the corresponding facets' normal vectors. Chen et al. (2016) improved the k-means clustering algorithm in terms of its capability to identify clusters in noisy data also. The number of clusters, whose possible values are user-defined at first, is automatically determined by the maximum of the average silhouette index (Rousseeuw, 1987). Afterwards, neighboring facets are classified to one discontinuity plane. In case the number of facets in a plane is too low, the concerned facets are reassigned. This corrects curvy or undulating surfaces in the DSM. The orientation of the discontinuity surface is calculated by means of its best-fit plane's dip and dip direction (Chen et al., 2016). In the proposed methodology of Guo et al. (2017), planes are fitted to point subsets at first and the plane normals are calculated afterwards. In

detail, the point cloud is segmented into cubes, a coplanarity test inside a cube identifies the points belonging to a fitting plane, and the plane's orientation is calculated via its normal vector. Afterwards, the optimal number of clusters is identified by the firefly algorithm and the plane normal vectors are clustered by a fuzzy-c-means algorithm. By cluster analysis, clusters of the same discontinuity set are identified and merged. A cluster validity function is applied to evaluate the clustering, giving the result in terms of the Xie-Beni index (Xie and Beni, 1991), for example. Guo et al. (2017) work with the point cloud directly. Their method does not need any triangulation. The data pre-processing to remove outliers is partly done in CloudCompare. In comparison to the DSE by Riquelme et al. (2014), Guo et al. (2017) provide quite good results, although the method needs improvements concerning the details. Buyer and Schubert (2016) calculate the point normals in Matlab and plot their dip and dip direction in a stereogram. The clustering method is based on the density and a Gaussian kernel, as in Riquelme et al. (2014), for example. The extraction is done with the software Dips. The results show a good performance for clearly defined planes, while rarely occurring or small planes pose problems. In addition, no information about linear features can be provided as the method investigates planes only (Buyer and Schubert, 2016).

Tung et al. (2018) use CloudCompare and the Facets Plugin by Dewez et al. (2016) to extract discontinuities out of a SfM point cloud as proposed by Dewez et al. (2016), so with the use of a mesh. Tung et al. (2018) conclude that the orientation values from the plugin are accurate as the variation between the plugin's results and hand measurements are 2° maximum. Additionally, they outline that the input point cloud quality is critical for the result's quality.

All methods are concerned by scale and orientation biases (Jaboyedoff et al., 2012, review paper – citation always includes references therein). Scale bias means that if a discontinuity set is smaller than the spatial resolution, it will not be sampled. Orientation bias occurs due to the laser beam's incidence angle, so its footprint. At greater footprints, the spatial resolution decreases and fewer points are sampled on the concerned surfaces. In automatic procedures, this bias can pose problems due to the lower number of points on such surfaces (Jaboyedoff et al., 2012).

2.3 Data acquisition at Ricobayo

The Ricobayo data which is analyzed in this thesis has been acquired by TLS from 24 different scan positions over an area of 1000m*800m*150m, under the direction of professor Scott Kieffer, Head of the Institute of Applied Geosciences at the Technical University of Graz, in February 2011. Liu (2013) has already analyzed a part of this data with a different methodology. The whole model of the dam site consists of $213 \cdot 10^6$ points in an UTM coordinate system ($x=E$, $y=N$, $z=Up$). The Riegl LMS-Z620 laser scanner, which may scan 360° around its vertical axis with a highest angle resolution of $0.004^\circ \cdot 0.004^\circ$, was used. The maximum possible scan distance of this laser scanner is 2000 m, and it can acquire 11000 points per second. RTK-GPS and a Nikon D300 camera are mounted on the laser scanner. The data is highly accurate.

Three datasets have been merged and processed (Figure 3): BK (11279261 points), BI (20282339 points) and WG (13708836 points). Due to the high amount of points in BI, this dataset is divided into two parts. Part one has 13879121 points, part 2 has 6403218 points. Vegetation, concrete, and shotcrete conceal the rock structure in some areas. In the segments shown in Figure 3, the rock structure can be seen very clearly. The analysis below is therefore focused on these segments.

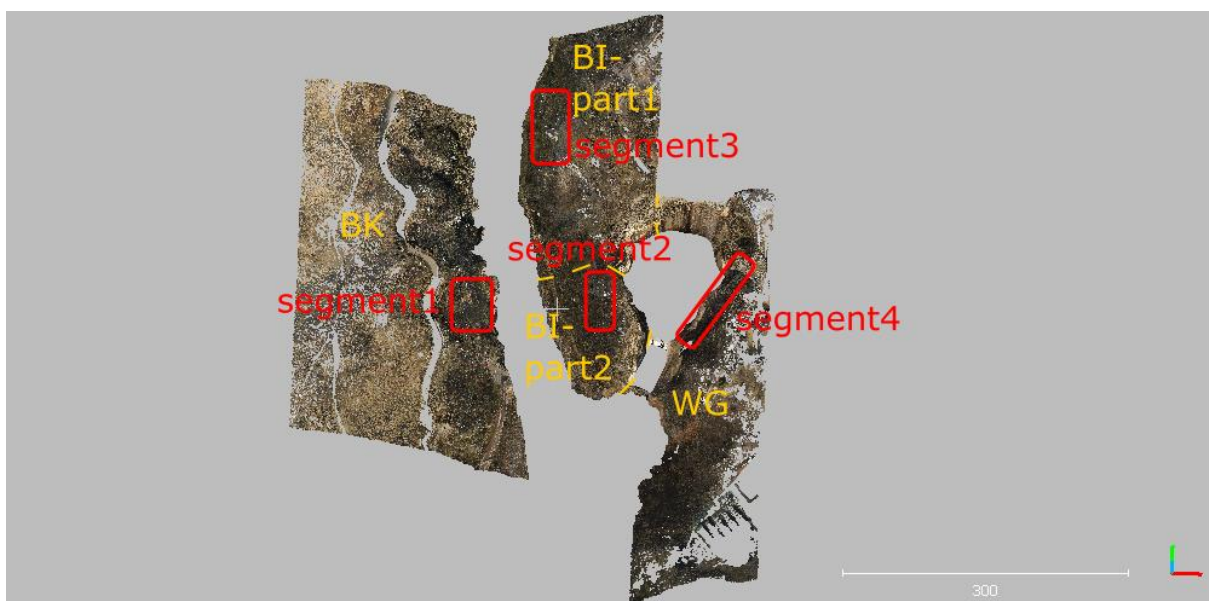


Figure 3: Overview over the datasets and parts (yellow) as well as the best rocky segments (red). Point cloud shown with CloudCompare (2019).

3. Geology of Ricobayo, Western Spain

3.1 The Ricobayo dam site

The TLS data has been collected in the surroundings of the Ricobayo dam in Western Spain (Figure 4). Figure 5 shows the area around the plunge pool and downstream of the dam, which is nearly the same area as represented by the point cloud (Figure 3).

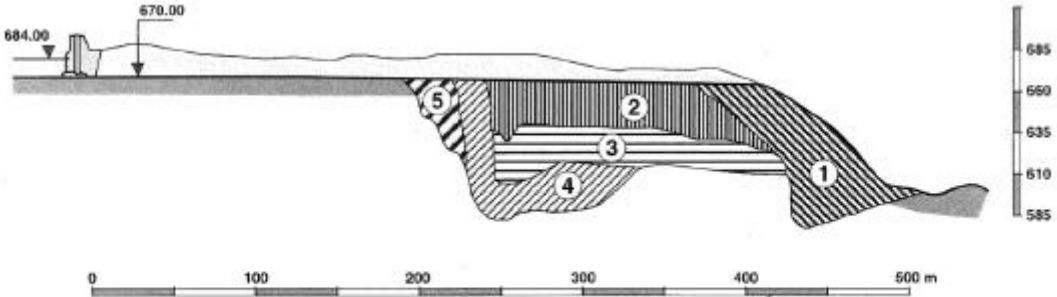


Figure 4: Location of the Ricobayo dam. Madrid and countries shown for orientation. Base map provided by Google Earth (2018).



Figure 5: The Ricobayo dam site. The figure shows more or less the same area which is represented by the point cloud in figure 3. Photo by Coelho Rocha (2012).

The Ricobayo dam is held by Iberdrola S.A., a Spanish electricity supplier company (SEPREM, 2018). It belongs to the “Saltos del Duero” hydropower system, which is comprised of several dams in northern Spain and Portugal. The dam’s name is derived from the nearby town of Ricobayo de Alba, which belongs to the town of Muelas del Pan (Iberdrola, 2009). It was built as a gravity dam (SEPREM, 2018) between 1929 and 1934 to use the Río Esla to provide electricity to northern Spain as well as to regulate the river’s discharge (Iberdrola, 2009). Measured from the foundation, the dam is 99.4 m high (SEPREM, 2018). Over the stream channel, its height is 92.5 m. The water holding capacity is $398 \times 10^3 \text{ m}^3$. The dam’s crest is 270 m long (SEPREM, 2018). In January, 1935, the dam was brought into service with a power output of 100 MW. In 1947, the power was raised to 133 MW. Ricobayo II (158 MW) was brought into service in 1999 (Iberdrola, 2009). The Río Esla is a tributary of the Río Duero (Bueno Hernández and Saldana Arce, year unknown), which has cut canyons of up to 400 m in depth in the peneplane (Iberdrola, 2009). The difference in level and the high discharge are favorable for hydropower use (Bueno Hernández and Saldana Arce, year unknown). The Ricobayo dam is especially known for the scour of its spillway which occurred between 1933 and 1939 in several stages (Figure 6): January, 1934; March, 1934; March, 1935; March, 1936 (Rubio, 1940); and one later event in January, 1939 (Kaspar, 2012, and references therein; Coelho Rocha, 2012, and references therein). $1.1 \times 10^6 \text{ m}^3$ of rock were eroded (Kaspar, 2012, and references therein). The extremely varying flow conditions, the dam and spillway construction and the rock mass behavior, including a much lower resistance to erosion as expected, initially contributed to the massive rock scour (Coelho Rocha, 2012). The resulting hole was protected from further scour by several structures and concrete linings (Coelho Rocha, 2012, and references therein). However, in 1962, a scour event damaged parts of the plunge pool, but minor modifications of the spillway outlet solved the problem. Coelho Rocha (2012) states that no signs of erosion have occurred since 1962 and the spillway works properly even at high discharge.



1 - January 1934, 2 - March 1934, 3 - March 1935, 4 - March 1936, 5 - January 1939

Figure 6: Stages of scour. Source: Coelho Rocha (2012, and references therein)

3.2 Geological Units

North-western Spain is widely made up of rocks of Variscan origin (Martínez Catalán, 2011). These include autochthonous, e.g. the Iberian Massif, and allochthonous terranes, which occur as nappe stacks. In general, there are two major zones (González Clavijo and Martínez Catalán, 2002): The Central Iberian Zone (CIZ) and the Galicia-Trás-Os-Montes Zone (GTMZ). Additionally, several Variscan granitoid intrusions are present in the area.

The area has been affected by three metamorphic and three deformation events. These include the evolution of schistosity and lineations, as well as folds, thrusts, and shear zones (González Clavijo and Martínez Catalán, 2002).

3.2.1 Stratigraphy

The Central Iberian Zone consists of several formations ranging from late Vendian to Devonian (González Clavijo and Martínez Catalán, 2002, and references therein). The lower part, called Río Duero Unit, represents the autochthon (Vendian to Silurian), while the Bajo Río Esla Unit and the Río Aliste Unit represent Silurian to Devonian allochthones which are thrust over the autochthon. The units are shown in a sketch in Figure 7.

In the Río Duero Unit, the lowermost part is formed by the Villalcampo Schists with a thickness of more than 2000 m and an age of late Vendian, possibly back to Cambrian (González Clavijo and Martínez Catalán, 2002, and references therein). They are of clastic origin and mainly include schists and greywackes. Therefore, they also belong to the so-called Schist-Greywacke Complex in the CIZ. The Villalcampo Schists are overlain by the Villadepera Gneisses of the early Ordovician, which are 250 m thick porphyritic gneisses of volcanic to volcanoclastic origin. A strong foliation and lineation is present. An unconformity separates the gneisses from the Ordovician Santa Eufemia Formation, about 1000 m thick and consisting of schists and quartzites. The Peña Gorda Formation conformably lies above the Santa Eufemia Formation. It is about 400 m thick and includes mainly quartzites as well as slates. Its age is Ordovician. The overlying formation is called Villaflor Formation, dating back to the middle Ordovician. It is 300-600 m thick and consists of slates and subordinate quartzites. Conformably above it lies the Campillo Formation, 150-450 m thick and consisting of mainly greenish schists, and sandstones. Glaciogenic pebbles and olistoliths can be found, too. The formation is middle to upper Ordovician. The uppermost part of the Río Duero Unit is the Silurian Manzanal del Barco Formation, which conformably overlies the Campillo Formation. It is about 500 m thick and includes mostly slates, but also cherts, sandstones, conglomerates, limestones, and igneous rocks. The rocks show strong and penetrative deformation (González Clavijo and Martínez Catalán, 2002, and references therein).

The allochthonous Bajo Río Esla Unit and Río Aliste Unit consist of rocks from the Silurian and the Devonian (González Clavijo and Martínez Catalán, 2002, and references therein). The Silurian is represented by the Manzanal del Barco Formation, which is repeated in the stratigraphy due to thrusting. In the Bajo Río Esla Unit, the Devonian is represented by the 200 m thick Almendra Formation, which conformably overlies the Manzanal del Barco Formation. It shows rhythmic alterations of limestones and slates. Metamorphic pebbles are present, too, as in the Manzanal del Barco Formation. The Almendra Formation dates back to latest Silurian/early Devonian. The Devonian formation in the Río Aliste Unit is the San Vitero Formation. With a thickness of about 1000 m, it represents flysch including terrigenous turbidites, and metamorphic pebbles. A disconformity in terms of an erosive surface separates this formation from the underlying Manzanal del Barco Formation (González Clavijo and Martínez Catalán, 2002, and references therein).

The uppermost unit, called Río Manzanas Unit (Figure 7), belongs to the GTMZ and is thrust over the CIZ units (González Clavijo and Martínez Catalán, 2002, and references therein). It consists of only one formation: the Rábano Formation. This formation of about 4000 m thickness includes rocks from the Silurian and the Devonian, being slates with limestones, sandstones, greywackes, olistostromes, rhyolites, quartzites, carbonaceous cherts, and metamorphic pebbles. However, any tectonic repetitions could be hidden by the monotony of the formation. The Rábano Formation corresponds to the Manzanal del Barco and the Almendra Formation of the CIZ, but it is younger and located in the uppermost thrust sheet (González Clavijo and Martínez Catalán, 2002, and references therein).

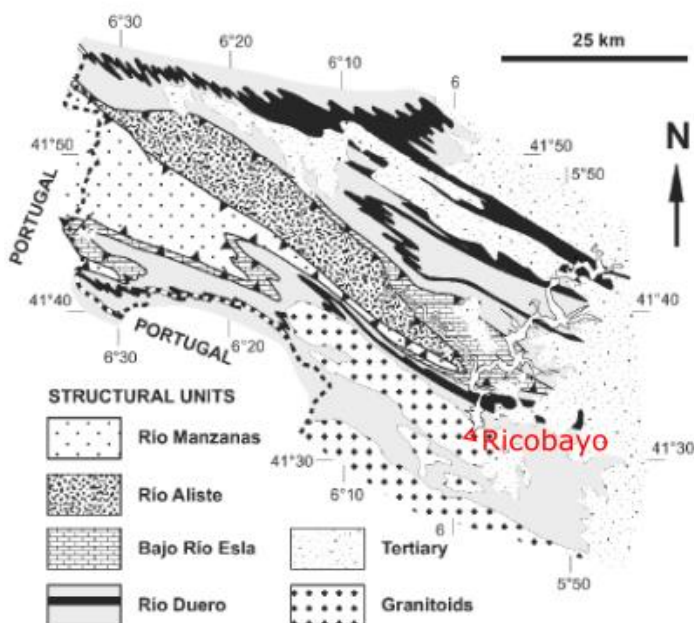


Figure 7: Structural units (modified after González Clavijo and Martínez Catalán, 2002)

One important granitoid intrusion is the Ricobayo batholith, which is located near the northern boundary of the CIZ (Fernández-Turiel et al., 1990). It has a size of 45 km * 8 km and shows a rather rectangular shape on the map. WNW-ESE striking Variscan structures like the Villadepera Antiform and a shear zone determined its emplacement as well as its shape and morphology. The Ricobayo batholith intruded Pre-Ordovician and Ordovician rocks. It is shown in Figure 8. Concerning lithologies, the peraluminous batholith consists of different syntectonic granites, namely two mica granite, muscovite granite and biotite-cordierite granite (Fernández-Turiel et al., 1991). The most common alterations in this tin-bearing batholith are microclinization and muscovitization (Fernández-Turiel et al., 1990). However, chloritization, albitization, tourmalinization and garnetization are also present (Fernández-Turiel et al., 1991). The tin, which is associated with the alteration, is present as cassiterite in quartz veins and aplite dykes (Fernández-Turiel et al., 1991). Its concentration seems to be associated with surface variations of CaO (Fernández-Turiel et al., 1990). The granites have been dated by Gutierrez-Alonso et al. (2013) to around 307 Ma.

Tertiary sediments cover parts of the surface (Figure 7, Figure 8).

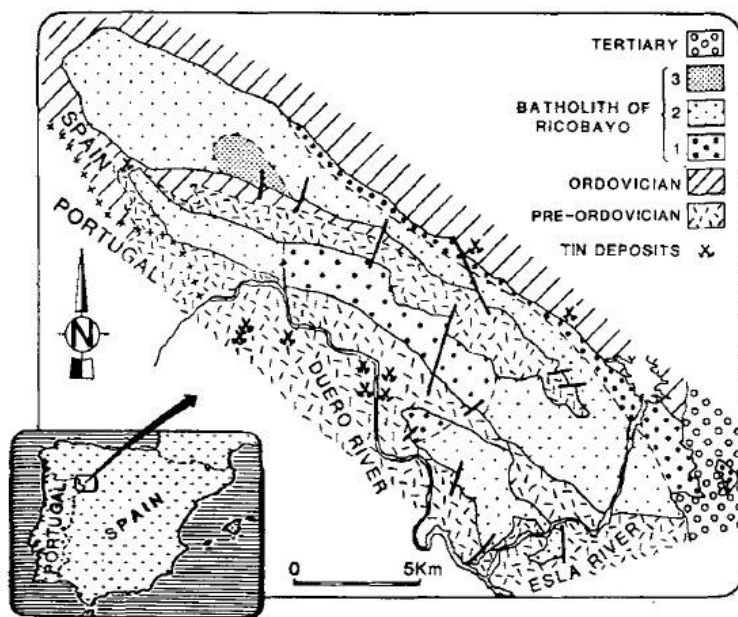


Figure 8: The Ricobayo batholith in a geological map of the area. 1= muscovite granite, 2=two mica granite, 3=biotite-cordierite granite. Source: Fernández-Turiel et al. (1991)

3.2.2 Structural Geology

As already mentioned above, three metamorphic and three deformation events can be distinguished in this area (González Clavijo and Martínez Catalán, 2002). The deformation events D1 and D2, with corresponding foliations or schistosity S1 and S2 as well as lineations L1 and L2, can be assigned to the Variscan Fold and Thrust Tectonics. D3 with S3 and L3 is characterized by the evolution of upright folds and transcurrent shear zones. The first metamorphic event M1 occurred between D1 and D2. M2 and M3 occurred contemporaneously to the corresponding deformation events (González Clavijo and Martínez Catalán, 2002). Table 1 gives an overview of the structures.

Pre-Variscan structures are merely present, just in terms of an unconformity at the base of the Ordovician sediments which can be explained by a half-graben model or block tilting in an extensional regime (González Clavijo and Martínez Catalán, 2002, and references therein).

Deformation event D1 is characterized by NE-vergent (attitude: 120° SE) recumbent folds with a subhorizontal axis. S1 represents the folds' axial planar cleavage, which is mainly developed in the slates. S1 intersects the bedding to form intersection lineation L1, which has an attitude of NW-SE and therefore parallel to the D1 fold axes. The shortening in the folds is 20% to 60% (González Clavijo and Martínez Catalán, 2002, and references therein).

D2 is characterized by thin skinned thrust tectonics, displacing and imbricating Silurian and Devonian rocks as allochthones in form of three sheets and many imbricates (González Clavijo and Martínez Catalán, 2002, and references therein). Some imbricates in the Río Aliste and Bajo Río Esla Units appear as duplexes which dip to the hinterland. The thrusts crosscut D1 folds and S1, and merge downward into a decollement in the slates at the bottom of the Manzanal del Barco and Rábano Formations. The thrust surfaces are characterized by fault gouge, while their surroundings show bands indicating ductile deformation. In the hanging wall of the thrusts, especially of the decollement, phyllonites of several to 100 m thickness show the tectonic foliation S2. S2 has been dated to 342.6 ± 0.3 Ma, which represents the allochthones' final emplacement. The phyllonites also show a subhorizontal stretching lineation L2, striking NW-SE. However, sheath folds occurring in shear zones near to the thrusts show a top-to-the-NE movement. Therefore, two movements might have taken place at the basal decollement: At first, one SE-directed, i.e. parallel to D1 and D3 fold axes with ductile deformation (S2, L2). Afterwards, a NE-directed one, i.e. orthogonal to the fold axes, which coincides with the geometry of imbricates with brittle deformation. Additionally, extensional detachments with a stretching lineation parallel to the orogenic trend (top-to-the-SE) are found in the area. These are common in the CIZ and thought to be caused by gravitational collapse in a compressional regime when the rock

shows a lateral flow due to the thickened crust (González Clavijo and Martínez Catalán, 2002, and references therein).

During deformation event D3, folds and transcurrent shear zones developed (González Clavijo and Martínez Catalán, 2002, and references therein). The open, upright folds trend NW-SE, their axial plane dips to NE. These folds rotated D1 folds and folded D2 thrusts. Therefore, S1 and S2 got folded, while L1 and L2 are parallel to the D3 fold axes. During this event, an axial planar cleavage S3 developed. However, S3 is not visible in all lithologies, e.g. cherts do not show S3. In addition, D3 is characterized by shear zones, namely by the Villalcampo Shear System, which is related with the folds and developed during late D3 deformation. The shear system shows ductile shear bands with a trend of 130° SE and a steep dip. On the surface, the system occurs as only one band in the NW, while it is splayed open to the SE where it enters the syn-D3 Ricobayo granites. The deformation is visible in the plutonic rocks, but also in gneisses and schists, in form of mylonites with a subhorizontal stretching lineation, for example. The Villalcampo Shear System shows dextral kinematics with a relative displacement of 3 to 4 km. Conjugated shear bands trending 70°-110° (ENE-ESE) show a sinistral strike-slip movement and are interpreted to have developed as a fan in an extensional regime. Such strike-slip structures are common in the northwest of the Iberian Peninsula, especially in synkinematic Variscan intrusives. Other late D3-structures are subvertical faults, being either parallel or normal to NW-SE features. The NE-SW ones are very well developed near Río Esla and the Ricobayo Reservoir, where they control the present fluvial system (González Clavijo and Martínez Catalán, 2002, and references therein).

Table 1: Structure Overview. Citation after González Clavijo and Martínez Catalán, 2002, and references therein.
 1 = Gutierrez-Alonso et al., 2013.

Structure	Orientation / Age	Deformation event
Recumbent folds	NE-vergent, attitude 120° SE, subhorizontal axis. +S1 axial planar cleavage +L1 intersection lineation, attitude NW-SE (D1 fold axes)	D1
Thrusts (decollement)	Crosscut D1 folds and S1 +S2: tectonic foliation, 342.6±0.3 Ma +L2: stretching lineation, subhorizontal, trend NW-SE	D2
Sheath folds	Top to NE	D2
Extensional detachments	Stretching lineation orogenic trend (top to SE)	D2
Upright, open folds	Trend NW-SE, axial plane dips to NE +S3 axial planar cleavage	D3
Granite intrusion	307 Ma ¹	D3
Shear Zone (strike-slip) – Villalcampo Shear System	Trend 130°SE, steep dip Subhorizontal stretching lineation Dextral, 3-4 km displacement Conjugated shear bands: trend 70°-110° ENE-ESE, sinistral	D3
Subvertical faults	NW-SE; or NE-SW (in Ricobayo granites)	D3

Regarding metamorphism, the first event M1 is characterized by intermediate pressure and temperature of about 350°C (González Clavijo and Martínez Catalán, 2002, and references therein). The peak of this low to medium grade regional metamorphism occurred after D1, but before D2. A Barrovian-type zoning has been observed (González Clavijo and Martínez Catalán, 2002, and references therein).

M2 was a low pressure-high temperature metamorphic event driven by gravitational collapse of the crust and partial melting due to decompression, which was caused by an extensional detachment and the rising of an anatectic dome (González Clavijo and Martínez Catalán, 2002, and references therein). A thermal aureole developed at the bottom of the allochthonous Manzanal del Barco formation. Parts of the aureole have been carried above the autochthon by the D2 floor thrust (decollement) which truncated the aureole. S2

developed contemporaneously to M2 (González Clavijo and Martínez Catalán, 2002, and references therein).

M3 is a syn-D3, contact metamorphic event characterized by granite intrusions as the one of the Ricobayo granite, for example (González Clavijo and Martínez Catalán, 2002, and references therein). This intrusive body is elongated along D3 folds and overprints them. It continues at depth and a thermal aureole developed in its surroundings. The intrusion consisted of several pulses during the evolution of the D3 folds. However, the Villalcampo Shear System deformation affected the granites and caused a retrograde metamorphism (González Clavijo and Martínez Catalán, 2002, and references therein). According to Fernández-Turiel et al. (1991), the petrogenesis of the Ricobayo batholith took place in two major steps: At first, pressure and temperature fell from more than 7 Kb to 2 Kb and more than 700°C to 650°C. This resulted in magma rise and granite emplacement. Afterwards, pressure and temperature fell again to about 1 to 1.5 Kb and below 600°C, which allowed the alterations to take place as interaction of rock and fluid (Fernández-Turiel et al., 1991). The alterations and their connection to tin deposits have already been mentioned above.

According to the history of deformation and metamorphosis described above, only the strike-slip shear zone of D3 and the subvertical D3 faults could be expected in the Ricobayo batholith. The expected orientations linked to the shear zone are the steeply dipping, 130°SE trending strike-slip shear zone itself, and 70°-110° ENE-ESE trending conjugated shear bands. Concerning the subvertical faults, the NE-SW oriented structural features are expected to be more dominant than the NW-SE oriented ones (González Clavijo and Martínez Catalán, 2002).

3.3 Regional Geological Evolution

3.3.1 Variscan Orogeny

The region of today's north-west part of the Iberian Peninsula can be used to reconstruct the passive northern margin of Gondwana's evolution at the onset of the Variscan Orogeny (González Clavijo and Martínez Catalán, 2002, and references therein). During this orogenic process, the collision of the two continents Gondwana and Laurentia led to the formation of Pangaea (Pfiffner, 2010). There were two major collision phases (Pfiffner, 2010): One at about 345 Ma (Devonian/Carboniferous) and one at about 320-300Ma (younger Carboniferous).

Generally spoken, Gondwana's former passive margin was transformed to synorogenic throughs (Pfiffner, 2010). The sedimentary cover was peeled off, imbricated and thrust over its basement (González Clavijo and Martínez Catalán, 2002), i.e. the basement was

also affected by the orogeny (Pfiffner, 2010). This is commonly known as thick-skinned tectonics. The allochthonous terranes and ophiolites of the Rheic Ocean were stacked above (González Clavijo and Martínez Catalán, 2002). The nappes were transported to the SE at Gondwana's continental margin, and to the NW at Baltica's continental margin (Pfiffner, 2010). The Variscan Orogeny not only included compression, but also extension (González Clavijo and Martínez Catalán, 2002). A steeply dipping major discontinuity, probably a strike-slip zone, can be followed through the orogen from Portugal to the Czech Republic (Pfiffner, 2010).

The autochthonous zones of the Bohemian Massif, which also crops out in Austria, as well as the ones in Massif Central in France, for example, can be compared with the Iberian Massif in terms of their shared peri-Gondwanan origin (Martínez Catalán, 2011). The Ordovician to Devonian parts of the "Grazer Paläozoikum" near Graz, Styria, can also be assigned to Gondwana's passive continental margin (Pfiffner, 2010). As already mentioned above, there are two major geological parts in north-western Spain (González Clavijo and Martínez Catalán, 2002): the Central Iberian Zone (CIZ) and the Galicia-Trás-Os-Montes Zone (GTMZ). The CIZ includes the autochthonous units, whereas the GTMZ consists of allochthonous terranes and ophiolites which mark the suture. Not all Variscan granitoids are synkinematic as the Ricobayo batholith; some are also postkinematic (González Clavijo and Martínez Catalán, 2002). In Central Europe, mainly post-Variscan granitoids occur. However, there are some exceptions, as in the Schwarzwald, for example (Pfiffner, 2010). These are bounded to Carboniferous Graben-structures, which can be interpreted as a change from compressional to extensional tectonics (Pfiffner, 2010).

3.3.2 Detailed evolution

The autochthonous Villalcampo Schists represent the filling of troughs of a Pan-African orogenic belt including the presence of a magmatic arc (González Clavijo and Martínez Catalán, 2002, and references therein). The Villadepera Gneisses' origin is a postcollisional magmatism in Gondwana's continental crust due to crustal thickening or stress relaxation when the Rheic Ocean started to open and Gondwana's passive margin evolved. Crustal extension and thermal subsidence in combination with transgression caused the appearance of today's Santa Eufemia Formation. The Peña Gorda Formation records the maximum transgression, including several sedimentary facies. The Villaflor Formation's origin are offshore shales formed during ongoing transgression. Due to the increased tectonic instability, a fragmentary basin evolved, which is today represented by the varying facies and thicknesses in the Campillo Formation (González Clavijo and Martínez Catalán, 2002, and references therein).

Normal faulting caused thinning of the passive margin. Mass movements occurred, causing talus deposits as in the Almendra Formation, which was deposited in the lower part of a slope. The Rábano Formation (GTMZ) forms the so-called “lower allochthon”, which underlies far-traveled terranes, i.e. the lower allochthon had a distal position at the passive margin. Slumps, debris flows and mud flows can also be discerned from the Rábano Formation. An extensional regime is imaginable, i.e. the Almendra and the Rábano Formations may have formed in the same environment, but at different locations (González Clavijo and Martínez Catalán, 2002, and references therein). The unstable basin was affected by tectonism, extension, and rifting of the passive margin. This evolution is represented in the Manzanal del Barco Formation.

The metamorphic pebbles, which are present in several formations especially in the upper parts of the Almendra and Rábano Formations, mark the onset of the Variscan orogeny in Lower Devonian and the transition of the sedimentary basin to a synorogenic through (González Clavijo and Martínez Catalán, 2002, and references therein). In Late Silurian to Early Devonian, convergence of Gondwana and Laurentia started. The collision started with the arrival of Laurentia’s accretionary wedge, which incorporated allochthonous terranes, oceanic lithosphere of the Rheic Ocean and in the end also parts of the subducted margin of Gondwana. This arrival is recorded through the metamorphic pebbles mentioned above.

Due to the subduction and the consequent lithospheric flexure, a forebulge developed. This might have caused the reactivation of faults, mass flows, slumps, and volcanic activity. The results can be seen in the Almendra and Rábano Formations. The San Vitero Formation represents a Variscan synorogenic Flysch. Its turbidites fill the depression which was created later during convergence at the bulge’s previous place (González Clavijo and Martínez Catalán, 2002).

The orogenic front moved from West to East. In a first step at the Devonian/Carboniferous boundary, the cover was folded (D1, S1) and shortened. Therefore, Cadomian and lower Paleozoic orthogneisses of the basement were folded and piled up, i.e. the deformation affected both basement and cover which is called thick-skinned tectonics (González Clavijo and Martínez Catalán, 2002, and references therein). Before this shortening, thin-skinned tectonics had dominated the evolution. During collision, the sedimentary pile acted as a soft cushion, while the allochthonous terranes behaved as rigid bodies. A horizontal ductile shear zone developed between these terranes and the basement. Due to crustal thickening, which resulted from the margin’s deformation and the emplacement of the allochthones, M1 occurred (González Clavijo and Martínez Catalán, 2002).

In Early Carboniferous, thrusting of the metasediments (D2, S2) took place as concentrated expression of compressional deformation. Parallel to the orogen, extensional conditions caused gravitational collapse of the crust. This can be seen in L2 and shear criteria developed in shear zones. The weakened and heated mid-crust made the subsequent evolution of a tectonic discontinuity possible. This resulted in the development of the ductile detachment (decollement), including granite intrusions and a thermal aureole (M2). Thin-skinned tectonics were established by this decollement. During D2, movement occurred to the SE as extension, and to the NE along thrust faults. However, these two directions could also relate to different phases of the decollement's movement. Different parts of the passive margin were stacked and imbricated in various thrust sheets. In Tournaisian-Viséan (Carboniferous), the allochthonous stack was finally emplaced (González Clavijo and Martínez Catalán, 2002, and references therein).

In the following (D3), further shortening (S3) as well as granite intrusion and their deformation in a ductile shear zone due to later shortening characterized the region's evolution before cratonization (González Clavijo and Martínez Catalán, 2002, and references therein).

4. Methodology

This methodology aims to extract discontinuities directly out of a 3D point cloud, in a semi-automatic and user-guided, but nevertheless objective and reproducible way. The method proposes to calculate normal vectors at each point, to cluster the data by a spherical k-means method, and to use a silhouette plot to filter the data as well as to evaluate the discontinuity set number. With the help of calculated orientation statistical parameters, a sub-dataset for each discontinuity set is created. Afterwards, planes are fitted to the sets' surfaces.

A big part of the method uses CloudCompare (2019), an open source program available to download on www.cloudcompare.org. Each point in a previously imported point cloud has its $[x, y, z]$ coordinates. The method is developed on a point cloud shaped in the form of an icosahedron and of a dodecahedron, which have already been used by Riquelme et al. (2014) to develop the “discontinuity set extractor” and are available online. R (R Core Team, 2018) is used for the clustering. R is dedicated to statistical computing and can be downloaded via r-project.org. For the orientation statistics, FracMan, a commercial application sold by Golder Associates Inc. (2018), has been used. It provides fracture system modelling and stereogram plotting also for very large datasets, which is the reason why it has been chosen here. The possibility to create a workflow using open software only is discussed below (see chapter “discussion”).

4.1 Normals computation

Normals (n_x, n_y, n_z) are a powerful mathematical instrument to describe planes. In point clouds, the normals on each point indicate to which plane the point belongs. However, the computation of a normal on a point does not make sense as the normal's direction could go to anywhere in space. Therefore, the neighboring points must be taken into account during the normals computation in order to fit a plane to which the normal can refer. This plane is not visible in the point cloud at any time, as it just serves as a reference for the normal computation. Such a reference plane is fitted for each point and its neighborhood in the cloud. This results in a normal in each point of the point cloud.

In general, CloudCompare (2019) features two possibilities for normal computation. On one hand, the common normals computation which is just straight forward, on the other hand, there is the Hough Normals Computation Plugin (Boulch and Marlet, 2016). Both possibilities will be investigated in the following to reveal which provides the best computation result.

The first possibility is the straight-forward normal computation, which is accessible via the edit-menu in CloudCompare (2019). There are three groups of parameter settings: Firstly, the local surface model can be chosen to be planar, quadric or 2D triangulated. Secondly,

there is the neighborhood setting. By default, an octree structure is used to search for neighboring points, and the searching radius can be changed. The third parameter is the orientation of the normals. This can also be ticked off to use the “raw” computation. The option “use preferred orientation” states the direction, to which the normals should be as parallel as possible (CloudCompareWiki, 2018a). The second possibility is to use the Hough Normals Computation Plugin by Boulch and Marlet (2016). The dialogue provided by the plugin (Boulch and Marlet, 2016) asks for several parameters. These are the neighborhood size for computing the normals, the number of random planes to be picked to estimate the distribution (number of planes), the discretization of the sphere accumulator (accumulator steps), the number of random accumulator rotations (number of rotations), the maximum angle used for the cluster normal selection and the final decision about the normals (tolerance angle), and the neighborhood size for density estimation (Boulch, 2017). The density of triplets estimation may be used, too. Boulch and Marlet (2016, slides) suggest using the plugin for normals computation at sharp edges, in case of varying data density as well as for noisy and outlier-bearing data. However, they suggest not using the plugin in case of smooth surfaces and a homogeneous data density (Boulch and Marlet, 2016, slides).

After several tests on the geometrical forms, it seems that the Hough Normals Computation Plugin by Boulch and Marlet (2016) performs exceptionally well at the forms’ sharp edges. For the computation, all parameters are left as by default, except the neighborhood size (knn) which is set to 20. This is an empirical value. On the planes, the results of both calculation approaches, i.e. of the straight-forward computation and of the Hough Normals Computation Plugin (Boulch and Marlet, 2016), are of similar quality. As the plugin is better adjusted to the characteristics of geological data, which are high noise, inhomogeneous data density, and sharp edges, it is chosen for the normal computation in this methodology.

After the normals have been computed, it might be necessary to invert them. The normals are displayed in relation to light and might appear backlit, so black, before inversion (CloudCompareWiki, 2018b). The inversion causes the normals to point to the right direction which is to the outside of the geometric form. In case the normals do not appear black, no inversion is necessary.

4.2 Dip / Dip Direction

As a simple scalar field does not have any meaning in engineering geology, the normals are converted to dip and dip direction scalar fields. Therefore, the data has three scalar fields now: the original one, the dip one, and the dip direction one. Each may have its own legend. The dip scalar field has a proper legend by default. However, concerning the dip direction scalar field’s legend, the default legend of CloudCompare (2019) is not exact enough for engineering geological purposes as the legend includes all colors in just 0° to 180° and

repeats the color coding from 180° to 360° . Therefore, a plane dipping to 80° has the same color coding as a plane dipping to 260° . To avoid this, the legend has to be stretched and adapted in the color scale editor so that all dip directions from 0° to 360° have their own color equivalent. A histogram of the colors gives a first, but very subjective, idea about the planes' orientations in space and about the number of discontinuity sets in the dataset. The subhorizontal plane at the top of the geometrical form might appear very colorful. This is due to the laser beam's wide footprint at surfaces (sub-) parallel to the LOS (see above). The colorful plane does not show up as a separate peak in the dip direction's histogram, of course. However, when using the dip scalar field, the plane can be seen very clearly.

4.3 Set identification

To examine the planes, the stereogram provided by the Facets Plugin (Dewez et al., 2016) is a very useful and intuitive tool. It shows the whole point cloud with dip and dip direction at the same time, which is a big advantage. However, with real, huge datasets, the plotting and clustering might reveal problems concerning the stereogram's resolution and the identifiable number of sets. It is impossible to identify the sets in the stereogram for large point clouds because the whole plot is covered with data.

Therefore, a skmeans clustering algorithm and a silhouette plot are implemented using R (R Core Team, 2018). The R code is given in the appendix. Skmeans clustering stands for "spherical k-means clustering", where k is the number of classes, i.e. clusters (Hornik et al., 2017). With this clustering method, all values get assigned to their nearest cluster. The mean of each cluster is calculated (Hornik et al., 2012; stackexchange.com, 2018). The silhouette plot can reveal the "natural" number of clusters in the data and is appropriate for data with rational distances (e.g. euclidean), which shall be classified into (sub-) spherical clusters (Rousseeuw, 1987). Each cluster is represented by a silhouette of a certain width, and all silhouettes are displayed in one plot. The silhouette index evaluates the quality of classification for each value in a cluster. The mean of the silhouette indices in one cluster is the silhouette width. The higher the silhouette width, i.e. the larger the silhouette indices, the more pronounced is the cluster. The average silhouette width is the mean of all silhouette widths of all clusters and ranges from -1 to +1. It allows evaluating the result's validity: The higher the average silhouette width, the better the clustering. This is also valid for each cluster's silhouette width, of course. Generally, the silhouettes do not depend on the clustering algorithm, but only on the data structure. Therefore, it is a tool for evaluating the "natural" number of clusters and prevents creating artificial clusters in the data. However, outliers may influence the clustering structure negatively, i.e. they may make the other data look like one cluster. The silhouette widths as well as the average silhouette width should be evaluated with this possible problem kept in mind. If outliers distort the classification, they

should be removed and the clustering should be done again (Rousseeuw, 1987). Chen et al. (2016) also use a k-means clustering method combined with the silhouette index, but with a higher degree of automatization. Their algorithm always uses the number of clusters which corresponds to the highest average silhouette index. In a case study, the number of sets did not match the pre-existing study of the same rock slope. However, Chen et al. (2016) justify their result by the similar orientation of two sets and by weathering and exfoliation effects which caused another set. In the method used in this thesis, the decision about the true number of clusters needed to get the best clustering is made by the user to ensure good results even in noisy data.

Afterwards, the ASCII file generated by the clustering procedure is reimported in CloudCompare (2019) and the last scalar field in the list is activated. This is the scalar field which contains the silhouette widths. A negative silhouette width implies that the data has been classified to the wrong cluster (R documentation, 2019; Rousseeuw, 1987). By filtering using the histogram, the data with negative silhouette widths can be removed. Afterwards, the scalar field which contains the cluster number is activated. To separate the sets, the histogram is a very useful tool, as each class (i.e. cluster) is shown as a peak in the histogram. On the dodecahedron's histogram, for example, there are six peaks according to the six sets present in the dodecahedron. The scalar field has to be filtered by value, which generates a sub-dataset for each class, i.e. cluster. Ideally, the sets can be extracted from these sub-datasets. If the sets are not clearly differentiated in the clusters yet, clustering a cluster again with R (R Core Team, 2018) can help. The number of clusters for the re-clustering has to be estimated from the data structure in the concerned cluster. According to Rousseeuw's (1987) suggestion, the data should be cleaned before re-clustering. In CloudCompare (2019), this can be done by the SOR filter tool (CloudCompareWiki, 2019b). SOR stands for statistical outlier removal. The "number of points to use for mean distance estimation" in SOR is set to 10, i.e. the 10 nearest neighboring points are considered for the calculation of their average distance to the concerned point. The second parameter is the "standard deviation multiplier threshold (nSigma)", which is set to 1. This is a factor used for the rejection of points which are too far away from the concerned point after the relation given in (2) (CloudCompareWiki, 2019b). The rejected points exceed the maximum distance and are removed as outliers. The values 10 and 1 are empirical and provide the best outlier removal results in the datasets used in this thesis.

$$\textit{Maximum distance} = \textit{average distance} + n\textit{Sigma} * \textit{standard deviation} \quad (2)$$

Clusters can also be merged if one set is artificially split apart by the clustering, which might occur in steeply dipping sets. To evaluate each set's orientation statistics on its own, the sub-datasets have to be exported as ASCII to prepare the data for FracMan (Golder Associates

Inc., 2018). In addition, the extracted sets should be projected and checked on the RGB point cloud in CloudCompare (2019).

The decision which planes belong to one set is primarily based on dip, dip direction, and persistence in the outcrop, i.e. segment. Some degrees of variation in dip and dip direction are acceptable. In the segments, the discrimination of the sets is much easier than in the whole datasets, as no noise or vegetation conceals the rock structures. It is assumed that all existing sets are present in the segments. This assumption is an analogue to classical field mapping, where all discontinuities in the rock mass are assumed to be mapped in the outcrop. However, the orientation bias and the size bias are lower in this digital mapping procedure thanks to the clustering. The orientation bias occurs due to the relative orientation of the discontinuity and the outcrop, while the size bias concerns the fracture size in terms of smaller fractures are less likely to be sampled (in a traditional field survey).

4.4 Orientation statistics

As a next step, the data is loaded into FracMan (Golder Associates Inc., 2018) as Well Log Data. This allows importing ASCII files, including x, y, z as well as dip angle and dip direction. Afterwards, a stereogram is plotted and its display should be changed to contours instead of distinct values in order to be able to identify the data's centroid. FracMan's "Fracture Set Identification" is used to calculate each set's mean orientation and Fisher's concentration parameter k. As a set consists of more or less parallel planes, the normals belonging to one set are assumed to scatter in a cluster around their mean orientation, i.e. to be Fisher distributed. FracMan (Golder Associates Inc., 2018) needs a "marker" created on the stereogram as a starting point for the classification. Another stereogram will be plotted automatically with the calculated mean orientation. Both stereonets are 2D equal angle projections of the lower hemisphere. The nets are polar as these are better suited for plotting poles and other linear features than equatorial nets which are better suited for planes (Diederichs, 1990).

So far, the mean orientation and Fisher's k per set are calculated by FracMan (Golder Associates Inc., 2018). However, the variability is needed in degrees for the next step. Therefore, the variability angle α_{var} is calculated with formula (3) which is also used in Dips (Rocscience Inc., 2019). P is the probability. Any normal of the set lies with this probability within the cone spanned by the variability angle around the mean orientation.

$$\cos(\alpha_{var}) = 1 + \frac{\ln(1-P)}{k} \quad (3)$$

The confidence limit angle α_{con} is also calculated with an equation (4) used in Dips (Rocscience Inc., 2019). Here, the true mean value lies with the probability P in the cone

spanned by α_{con} around the calculated mean value. The confidence limit angle is always smaller than the variability limit angle (Wallbrecher, 1986). R is the length of the resultant vector (Rocscience Inc., 2019), so a scalar value. It is calculated by rewriting equation (5), a formula to calculate Fisher's concentration parameter k , to equation (6). There, n equals the number of values as long as the normals are all unit vectors, which is the case here as the calculation is done for a unit sphere. In any other case, n is the total length of normals in the set (Rocscience Inc., 2019). R is always smaller or equal n (Rocscience Inc., 2019).

$$\cos(\alpha_{con}) = 1 + \frac{\ln(1-P)}{R*k} \quad (4)$$

$$k = \frac{n-1}{n-R} \quad (5)$$

$$R = n - \frac{n-1}{k} \quad (6)$$

According to Figure 9, the curves for the variability angle and the confidence angle start nearly linear, but become exponential at higher probability values. This change can also be seen in the curves' tangents, which clearly change direction at higher probabilities. Due to the exponential behavior, both angles grow rapidly above a probability of 0.954 (red in Figure 9). However, this growth is not represented by an appropriate increase in probability as it is at lower probability values. Therefore, this probability of 0.954 is used for the calculations of these angles with equations (3) and (4). The curve shown in figure 9 has been calculated for set 1 of segment 1. The number of values (n in the equations above) is 298255, the Fisher k is 18.9877. The curve behavior has been checked on two other sets, namely set A and set 4. While set A has a higher number of values (451121), its Fisher k is lower (17.4851). Set 4 contains a far lower amount of points (27698) than both, sets 1 and A, while its Fisher k is the highest among them (21.4098). For the further usage in the Facets Plugin (Dewez et al., 2016) in CloudCompare (2019), these angles are valid for both, dip and dip direction (see also Figure 20 below), and form a small circle around the mean orientation in a Schmidt's net stereogram (Genske, 2014).

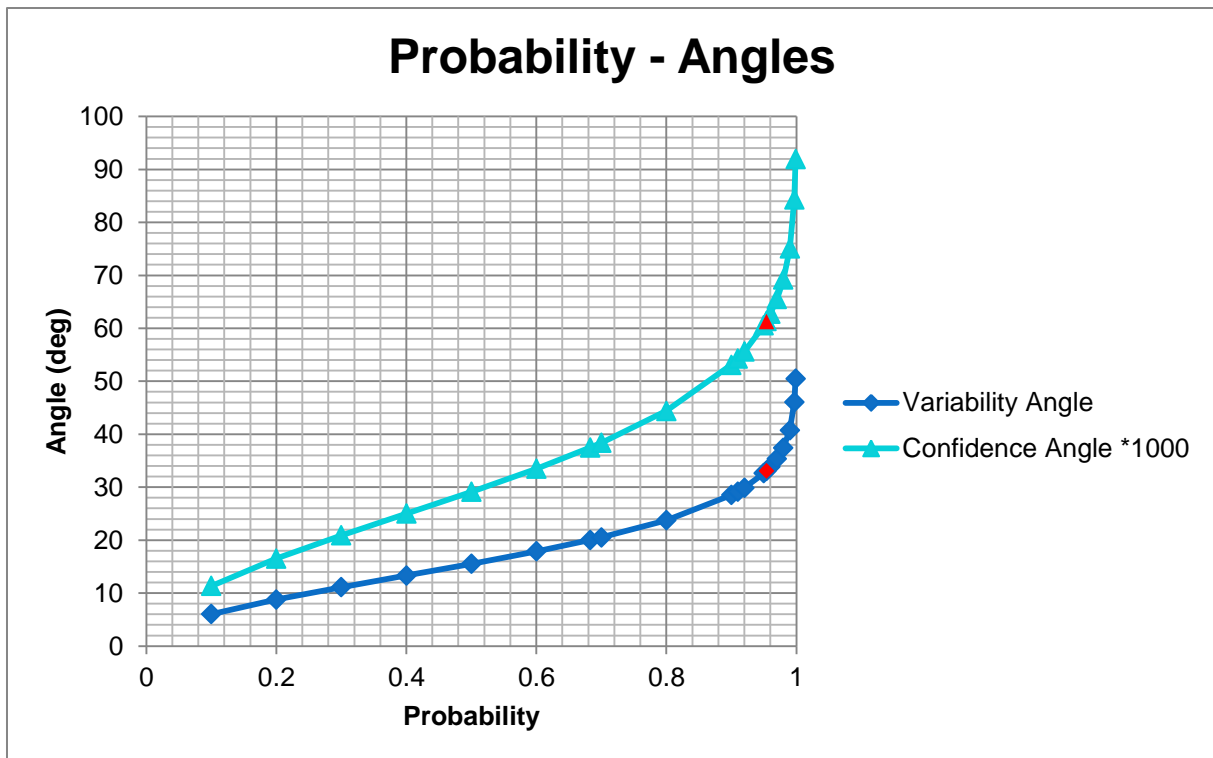


Figure 9: Plot Variability Angle and Confidence Angle. The probability does not vary much over 0.954 (marked red). Calculated for segment 1-set 1 (see below).

4.5 Filtering & plane fitting

For further visualization, the dip-dip direction point cloud is opened in CloudCompare (2019) again. Now, the stereogram provided by the Facets Plugin (Dewez et al., 2016) is used to filter the set-specific points by dip and dip direction simultaneously. With the orientation statistics, the location-based visualization of the sets with the Facets Plugin (Dewez et al., 2016) is an objective and user-controlled filtering procedure. In the stereogram, the normals are shown in density clusters. The empirically best plotting settings are 20° or 30° for the main sector step and a resolution of 0.5°. One has to keep in mind that a steeply dipping set with very flatly dipping normals might cause the cluster to be split apart in dip direction by 180°. The sets can be filtered out of the stereogram and exported from it directly. Therefore, each set is represented in one sub-dataset after filtering in the stereogram.

To remove outliers, CloudCompare’s SOR (parameters as above) is used on each set. The SOR can also filter out “ghost points”, which are due to the laser scanning procedure and actually do not belong to the set.

Most of the time, there are several point clusters in one set, which means several planes-to-be. This makes segmentation necessary in order to prevent wrong statistical plane fitting. An important decision during segmentation is the fracture surface size. Generally, the segmented surfaces should be as big as possible and no natural surfaces should be separated artificially. Concerning the minimum surface size which is taken into account,

mechanics as well as the possible failure modes should be considered. According to Ni et al. (2017), rock mass usually fails because of discontinuities instead of failure in intact rock. However, the relevant fracture size influencing the rock mass' behavior seems to be challenging to identify. Farahmand et al. (2018) worked with a LiDAR-scanning dataset of granite to investigate the scale-dependency of the rock mass' geometrical and mechanical properties. The latter depend on the behavior of discontinuities as well as on the one of rock bridges. Scale is another factor which needs to be considered. Farahmand et al. (2018) identified three Fisher-distributed discontinuity sets with fracture intensities $P_{21} > 1 \text{ m/m}^2$. P_{21} describes the fracture intensity in terms of the length of fracture traces per unit area. In the fracture network model of Farahmand et al. (2018), the trace lengths are $>0.2 \text{ m}$ for one set. For the geometrical representative elementary volume (REV) of 7 m for the area, the mean P_{21} is 2.5 m/m^2 (Farahmand et al., 2018). The REV features all characteristic properties of the whole rock mass, while being as small as possible. Its size depends on the rock mass' properties variability. Wu and Kulatilake (2012) conducted a scanline survey in limestone where they mapped fractures with calculated mean diameters of $>2.69 \text{ m}$. The 1D-intensity along the mean vector direction ranges from 0.507 and 0.905 to 1.953, 2.924, and 3.284 joints/m (Wu and Kulatilake, 2012). Ni et al. (2017) give an example of a previously investigated rock mass (other authors) with four joint sets, with mean trace lengths $>3.82 \text{ m}$. In another example (again other authors), Ni et al. (2017) give the disc radius of four fracture sets. The trace length is the secant on a disc of this disc radius, described by the relationship given below (7). The mean disc radii are 1.03 m, 1.04 m, 0.85 m, and 3.63 m. The standard deviation of the disc radius $<1 \text{ m}$ is 0.46.

$$\text{disc radius} = 2 * \text{trace length} / \pi \quad (7)$$

Zhang et al. (2012) ignored fractures with trace lengths $<0.5 \text{ m}$ in their window sampling survey of basalt. The mean trace lengths of the three identified sets are 1.3 m, 1.4 m, and 3.1 m, the corresponding mean fracture diameters 1.4 m, 1.9 m, and 4.5 m. P_{21} of the sets is 0.077 m/m^2 , 0.113 m/m^2 , and 0.106 m/m^2 (Zhang et al., 2012). After this literature study, the minimum relevant surface area was set to be $>1 \text{ m}^2$. For sets crosscutting the slope surface, the minimum side length was set to 1 m. Discontinuities with smaller surface areas or side lengths are assumed to conclude a high percentage of rock bridges, and therefore a low persistence, which enhance strength. CloudCompare (2019) provides the scissors-tool to segment the cloud. This generates a sub-dataset for each surface. These sub-datasets are treated separately in the following.

Afterwards, a plane is fitted to the surface, accessible via edit-plane-fit. Its size is deduced automatically and its RMS is shown in the plane properties (CloudCompareWiki, 2019a). The plane's color can be set by edit-colors-colorize. The plane information can be saved as .csv

for all planes by using the plane information batch export tool. The generated file contains dip and dip direction, plane width and length, as well as the coordinates of the plane's center and its normal vector.

The plane data quality is evaluated by the use of stereogram plots. As the planes of one set are fitted to surfaces of similar orientation, the poles of the planes should plot in the same area in the stereogram as the point normals of the concerned set. To ensure the orientation statistics' validity and to prevent the distortion of the statistical parameters by the relatively low amount of planes, the orientation statistics have been done on the high amount of point cloud normals per set. The stereogram plots of the planes' poles mainly serve as controlling mechanism.

4.6 Set characteristics

In this thesis, the location-specific analysis and visualization of the discontinuity sets are made for parts of the investigated site only because the rock mass structure is assumed to be similar in neighboring areas. In addition, discontinuities are assumed to originate from regional stress events and stress states, which is why the local discontinuity pattern should not vary much over the area. The spatial orientation and relations of the sets, their plane sizes and their prominence in the structure can be examined in the segments. In the case of the dam site here, there is no necessity to assess every meter of the rock face. However, this is always a matter of danger, vulnerability, and risk. In highly vulnerable areas, it might be inevitable to evaluate the rock mass structure at every spatial point. In case the spatial variation of the sets in different segments increases, the gaps between the evaluated segments should also be smaller.

In general, discontinuities are described by several small- and large-scale parameters, which are orientation, spacing, persistence, roughness, wall strength, aperture, filling, seepage, the number of sets, and the block size (ISRM, 1978). As TLS is a remote sensing method, sampling is not possible to investigate the intact rock's strength. This can just be estimated, or the TLS is combined with a sampling procedure on site. The discontinuity roughness, wall strength, aperture, filling, and seepage can barely be measured in a point cloud of the resolution of the Ricobayo one. Seepage may appear as lower reflective surface parts of the TLS point cloud (see also Figure 1; Jaboyedoff et al., 2012; Feng and Röshoff, 2015). Waviness, as a form of large scale roughness, might be assessable in a point cloud. Spacing helps to describe the rock mass quality and its degree of fracturing. It is the mean or modal of the individual spacing in the set between each two adjacent joints (ISRM, 1978). The spatial variation within one set must be very low, i.e. the parallelism of the discontinuities must be very high, to get a good result for the overall set spacing. As spacing varies locally, the application, e.g. mining or tunneling, and risk define whether a mean spacing provides

enough preciseness. Riquelme et al. (2015), for example, proposed a methodology to calculate spacing after a digital feature extraction and set classification. However, smoothed discontinuity surfaces, or even debris-covered ones, posed problems. The persistence of the set also influences the spacing and the spacing influences the block size. Orientation measurements are improved due to the advantages of remote sensing (see above in chapter 0). The orientation statistical parameters calculated for the point normals of one set describe its mean orientation and variation in space. The number of sets is also available directly from the point cloud. The persistence, and moreover, the termination and spatial relation of the discontinuities, can be evaluated at least qualitatively from a point cloud. The persistence is defined as the trace length observed in an outcrop (ISRM, 1978). It should help to identify the plane size of the discontinuity (ISRM, 1978). However, with the TLS data and the methodology described above, the area of the planes itself can be assessed. Therefore, the persistence as a tool to estimate the plane size seems to be not necessary any more. The relative areas of the set planes might be visible immediately after the plane fitting process. The quantitative approach is very straight forward. Based on the plane fitting procedure, it is assumed that all planes are $>1 \text{ m}^2$. Their true extent can be estimated by simple $\text{area}=\text{length}*\text{width}$ calculations from the plane information extracted from CloudCompare (2019).

To determine the spatial relations of the sets, the fitted planes as well as the RGB point cloud are investigated. In general, discontinuities may terminate against intact rock (N_R ...number of terminations against intact rock, see relation (8)), against other discontinuities (N_D), or beyond exposure (N_X). After ISRM (1978), the termination index T_R is calculated as given in (8). The denominator is the total number of terminations and equals twice the total number of discontinuities, as each discontinuity has two ends.

$$T_R = \frac{N_R*100}{N_R+N_D+N_X} \% \quad (8)$$

However, since most of the sets are present as surfaces instead of traces, the termination might be difficult to define and the persistence might be replaced by the plane size. In addition, CloudCompare (2019) seems to tend towards an overestimation of the plane size as it always fits a rectangular plane over the selected points. On the other hand, the plane sizes might be underestimated as the orientation statistics based Facets (Dewez et al., 2016) extraction does not necessarily include the rounded margins of the planes. This roundness of the surface margins can be due to weathering, for example. Therefore, the termination of the planes might be concealed as the plane is limited in its extent by the procedure itself. The surface roundness can be assessed for each plane by a visual investigation of the plane's surroundings in 3D, using the RGB point cloud, the dip and dip direction scalar fields, as well

as all fitted planes. An example is shown in Figure 10, where the red and the blue plane should actually intersect each other from a geological point of view. However, they do not intersect because of the roundness of the edge between the planes.

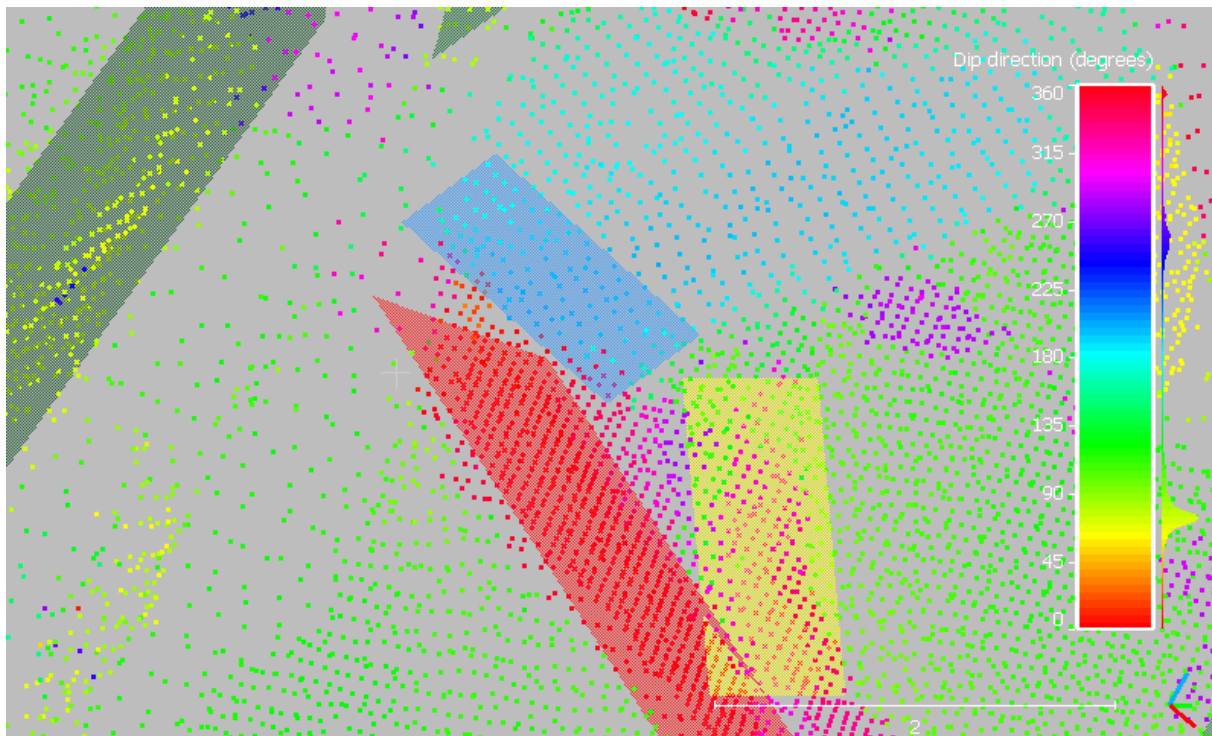


Figure 10: Roundness, shown on an example of two planes (red, blue) of segment 1.

Concerning the termination index, a plane does not only have two ends as a trace does, but it has four edges. The termination index is nearly impossible to apply on planes which have four edges to get in contact with their surroundings and which are moreover restricted by rounded borders, i.e. they are affected by the already mentioned roundness. Therefore, the termination might have better investigated by a somehow 3D version of the termination index. In addition, it might be important to relate the terminations to the sets, i.e. to relate the sets to each other instead of producing one single value to describe one set's spatial relation to all sets. A termination into a discontinuity of a very high plane size might be more important for the rock mass behavior than a termination into a set of very small plane size. In order not to lose any spatial information, the termination of each plane to its neighbors is investigated and added to the plane data table. This table already holds the information for each plane extracted from CloudCompare (2019), the calculated plane size, and now also the termination. In addition, in case the plane size seems to be underestimated due to roundness or TLS data holes, the plane's terminations are estimated for its true size with the help of the RGB, dip and dip direction point clouds. The estimated terminations are called "termination including the neighborhood". If a plane does not terminate in any plane, so it is isolated in space, the termination is marked as "0". Various problems posing difficulties to the plane fitting process cause the difference in termination of the planes and their estimated

true termination, which takes the problems into account. These problems are the already mentioned roundness and underestimation of planes, noise or vegetation, holes in the TLS point cloud, point cloud areas with few points, i.e. a lower local point cloud density, planes exceeding the segment, or not mapped planes due to too high roundness (outside the set's statistical orientation) or a too small plane size.

4.7 Workflow summary

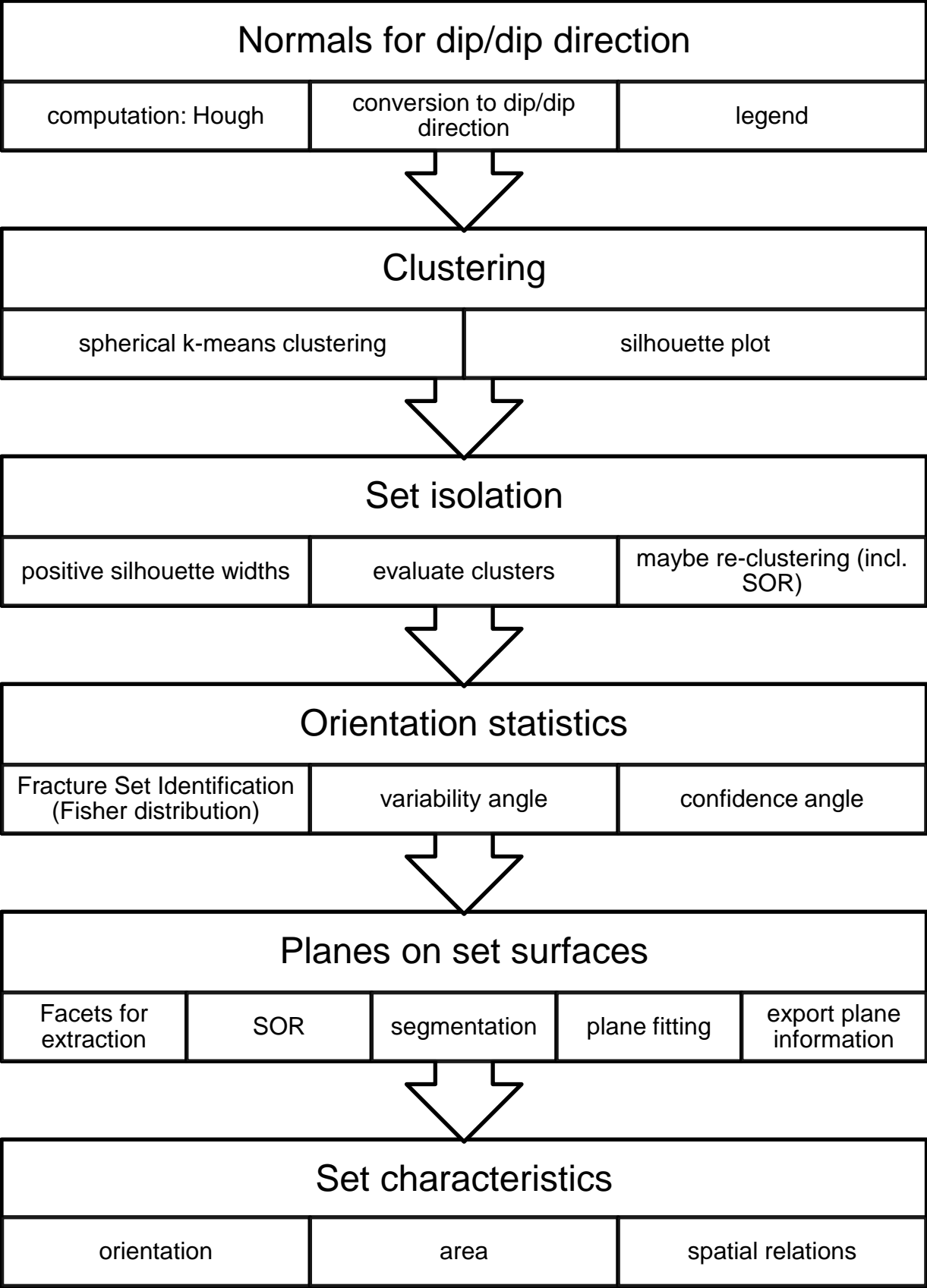
The procedure described in this methodology chapter is summarized by the flow chart given below (Table 2). To maintain the overview of the workflow and as all citations are already given in the detailed methodology description above, no software or plugins are cited again in the flow chart.

The first step in the workflow is the normals calculation for each point of the 3D point cloud in CloudCompare (2019) using the Hough Normals Computation Plugin by Boulch and Marlet (2016). Afterwards, these normals are converted to two scalar fields, a dip scalar field and a dip direction scalar field. The correct legend has to be assigned to each scalar field. Afterwards, the point cloud normals are clustered by the skmeans algorithm (Hornik et al., 2017) implemented in R (R Core Team, 2018). The silhouette plot (Rousseeuw, 1987) helps to identify the best number of clusters for the data's inherent structure. A visual investigation of the clustered normals in CloudCompare (2019) might also reveal which number of clusters provides the best classification result. In CloudCompare (2019), all negative silhouette widths are filtered out, as these normals are probably wrongly classified. Therefore, only the positive silhouette widths are used for the set identification. Now, each cluster is evaluated on its own concerning the classification quality and the discrimination of sets in different clusters. In case several sets are classified into one cluster, this cluster has to be re-clustered by the same clustering in R (R Core Team, 2018) as before. However, before the re-clustering, a statistical outlier removal (SOR) is conducted in CloudCompare (2019). As soon as each set is classified into its own cluster, the orientation statistics is calculated in FracMan (Golder Associates Inc., 2018) using the "Fracture Set Identification" with a Fisher distribution. The output includes the mean orientation of each cluster, i.e. set, and the Fisher constant k . By using k , the variability angle and the confidence angle for each set are calculated. For the next steps, CloudCompare (2019) is needed again. The Facets Plugin (Dewez et al., 2016) is used for the extraction of the sets directly out of the original, unclustered 3D point cloud. It needs the mean set orientation as well as the variability angle as inputs. Then, the SOR tool is applied on each set. The set is segmented into its planar surfaces, to which the planes are fitted. Finally, the plane information is extracted from CloudCompare (2019).

The set orientation has already been calculated. The plane data extracted from CloudCompare (2019) includes the orientations of all fitted set planes and their length and

width. This allows the calculation of the plane area. By visual inspection in CloudCompare (2019), the spatial relations of the planes can be evaluated.

Table 2: Workflow overview



5 Results

5.1 Observations from tests with geometrical forms

The point cloud shows a very homogeneous point density. The Hough Normals Computation Plugin (Boulch and Marlet, 2016) reveals good normal computation results on the planes and at the edges of the dodecahedron and of the icosahedron. The silhouette plot is given in Figure 11 for the dodecahedron. The average silhouette width of 0.95 states that the number of clusters which has been set before corresponds to the number of clusters naturally included in the data. As the dodecahedron has six different planes, this plot confirms the previously assumed number of sets, i.e. clusters. There are no negative silhouette widths.

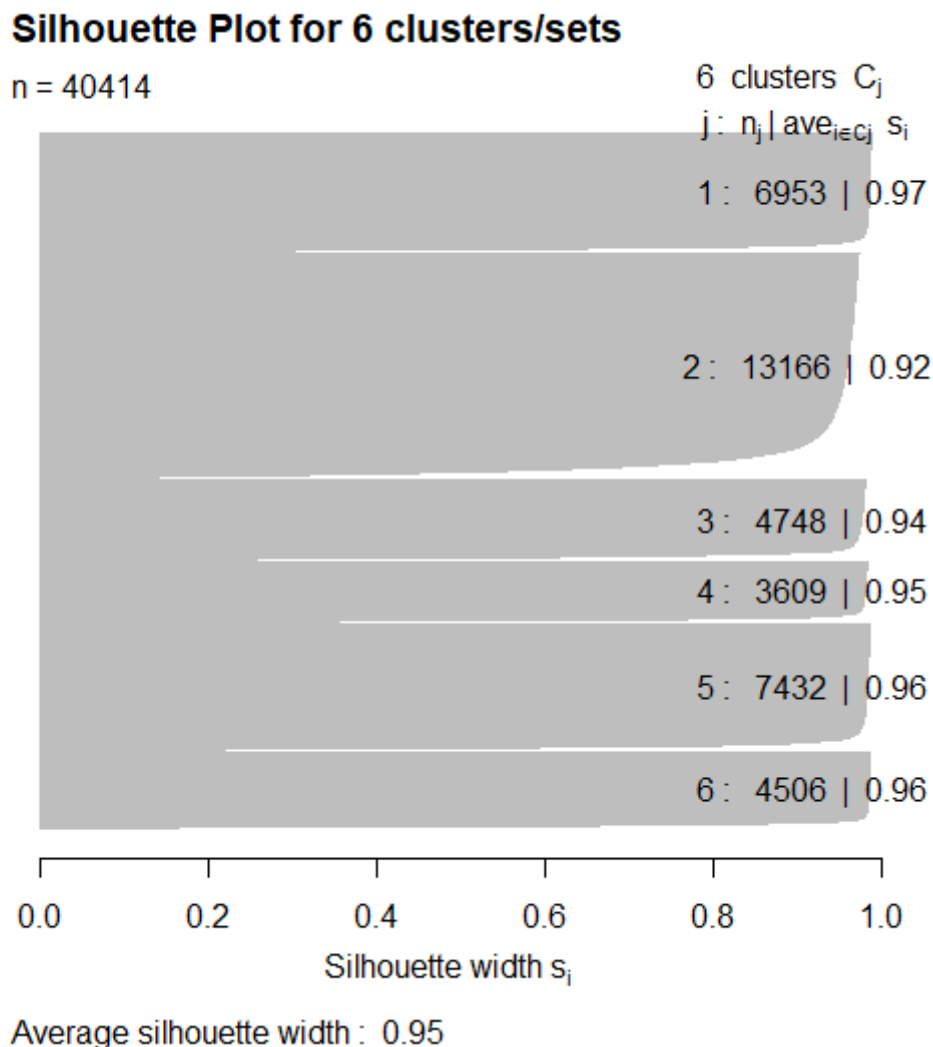


Figure 11: Silhouette Plot for the dodecahedron

In CloudCompare (2019), the “scalar field #3” is activated, which corresponds to the column “class” in the ASCII file. The histogram to extract the six sets is shown in Figure 12, in addition to the dodecahedron colored according to “scalar field #3”.

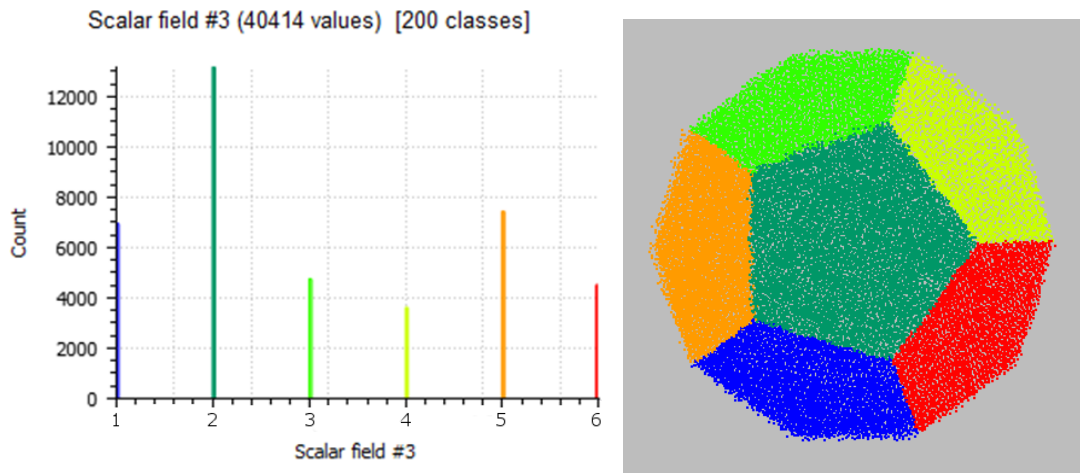


Figure 12: Histogram of the dodecahedron's classes and the dodecahedron in CloudCompare (2019)

The point normals have been plotted in a stereogram in FracMan (Golder Associates Inc., 2018) as shown in Figure 13. The whole dodecahedron point cloud, including all sets, has been imported in FracMan (Golder Associates Inc., 2018) first. Afterwards, each set has been imported on its own. The mean orientations are given in Table 3. It is obviously possible to calculate the mean orientations of the whole dataset at the same time. However, for real data, this might not be possible due to not so clearly distinguishable sets and far more points in the point cloud which increases computing time. Nevertheless is it advisable to try the mean orientation calculation for the whole point cloud, so for all sets in one ASCII file, in case of small datasets with very clear sets. However, for the Ricobayo data, it will be necessary to discriminate the sets before the orientation statistics calculation.

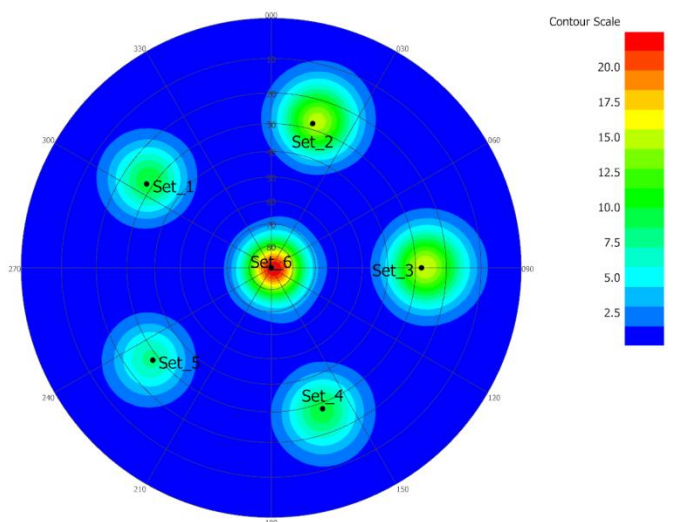


Figure 13: Stereogram with contours in FracMan (Golder Associates Inc., 2018), showing the six sets

Table 3: Mean orientations of the dodecahedron

Calculation of all sets	Calculation of each set alone
233/30	233/29
306/30	306/29
18/28	18/28
90/28	90/28
160/30	160/28
105/88	113/83

The parameters for the dodecahedron, calculated from the orientation statistics for the whole point cloud, are shown in Table 4. The probability for the variability limit angle and for the confidence limit angle is 95.4%, the same as for the Ricobayo data.

Table 4: Orientation statistics and fitted planes for the dodecahedron

Mean orientation	Fisher's k	variability angle (P=95.4%)	confidence angle (P=95.4%)	CloudCompare plane	Set color in Figure 16
52.85/59.61	22.3590	15.6144	0.1395	52/62	green
126.34/60.23	31.8377	18.5698	0.2166	125/62	dark blue
197.86/61.64	51.1891	27.1032	0.3889	197/63	orange
269.72/61.92	59.1413	30.4256	0.4961	269/64	light blue
339.54/60.31	28.0398	25.4064	0.3764	340/63	magenta
286.71/1.74	83.4336	19.9739	0.2403	290/1	yellow

The next step is to filter the sets out of the original dip - dip direction point cloud. This is shown for set 1 in Figure 14. Figure 15 shows the filtering of the horizontal set. The dip direction scalar field shows many different colors due to the laser scanning procedure itself. The clustering approach can classify this as one set and the orientation statistics also works. For the extraction with Facets (Dewez et al., 2016), the variability limit angle is only valid for the dip, as the dip direction variability limit angle must be 360° for vertical normals of a horizontal set (Figure 15).

For the geometric form, the sets' identification could have also happened in the Facets-Stereogram (Dewez et al., 2016) as each cluster can be identified by the user's eye easily directly in the plot (Figure 14, Figure 15). However, with the real geological data, the orientation statistics is an important part of the workflow to ensure the results' quality (see below).

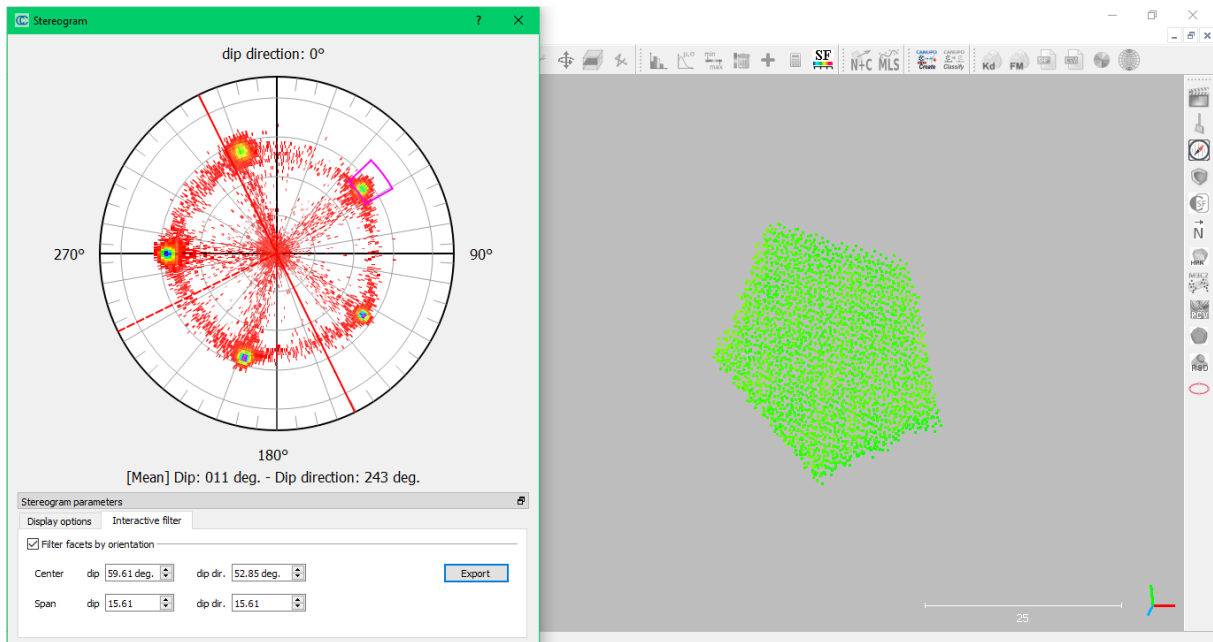


Figure 14: Facets Plugin (Dewez et al., 2016) filtering set 1 out of the dodecahedron

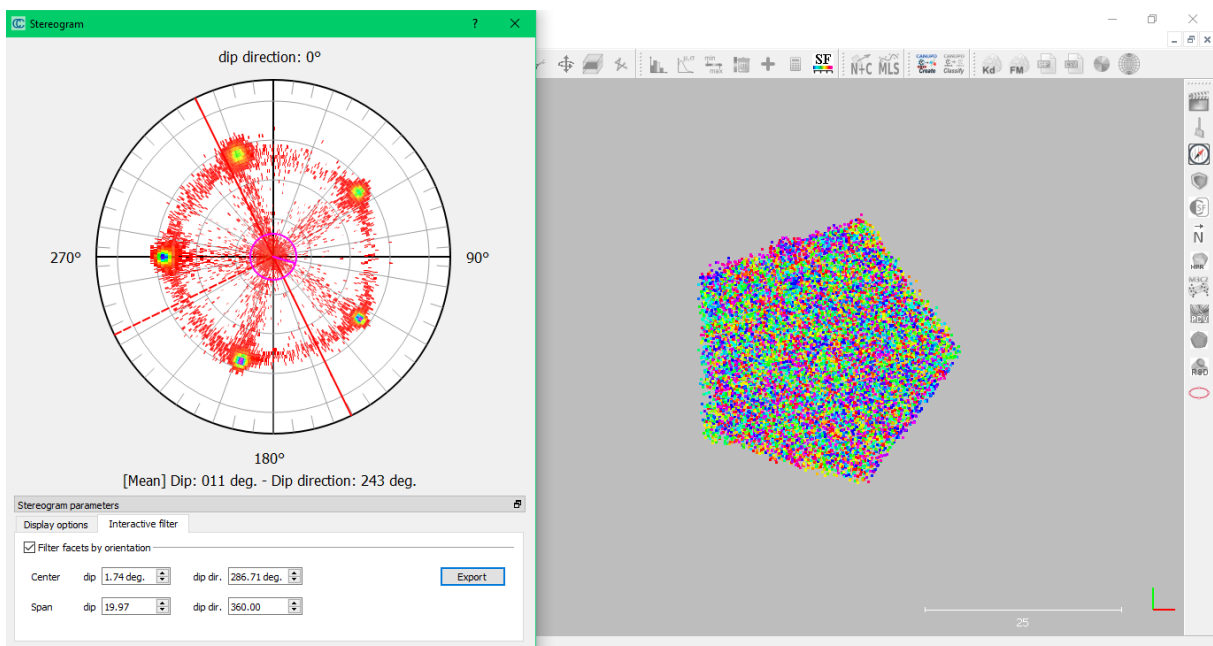


Figure 15: Extracting a horizontal plane with Facets (Dewez et al., 2016)

It is obvious that each set consists of just one plane in the dodecahedron. Therefore, segmentation is not necessary. However, outlier reduction is always done. The plane fitting finally gives the result shown in Figure 16. The plane orientations calculated by CloudCompare (2019) and the set colors according to Figure 16 are also shown in Table 4 above.

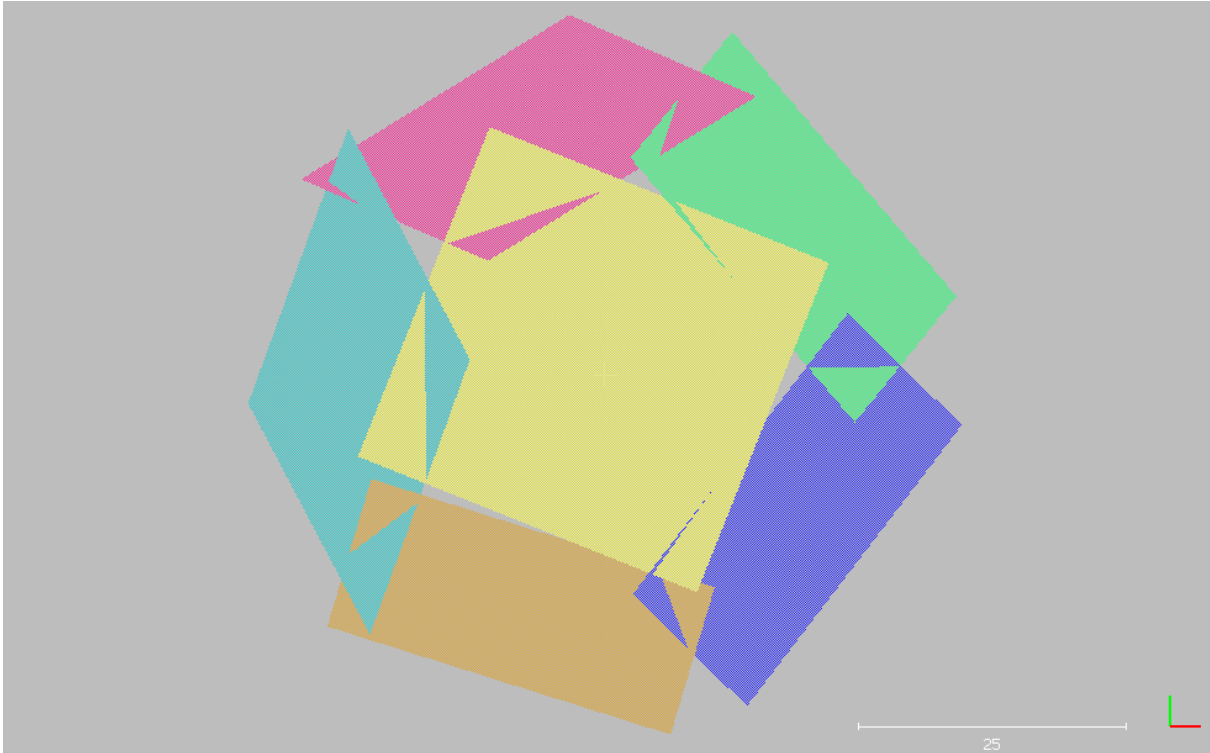


Figure 16: Planes of the dodecahedron

Regarding the computation time, the dodecahedron (40414 points) and the icosahedron (37226 points) are quite quickly computed, i.e. the workflow does not have to be paused due to computation time as the user just has to wait seconds to a few minutes. The procedure works well for the dodecahedron. As this geometrical form was just used to test the methodology, the planes will not be further interpreted.

5.2 Observations from the Ricobayo data

5.2.1 Remarks to the method

For real geological data, the first arising problem is the estimation of the number of sets. This is not as easy as for geometrical forms and requires some geological understanding and knowledge, as well as some experience with the clustering. The real amount of sets does not necessarily fit the appropriate number of clusters as noise may need one extra cluster and (sub-) vertical rock faces may need two clusters. The average silhouette width should not be the ultimate value of deciding about the number of clusters. When comparing different numbers of clusters, the highest average silhouette value does not necessarily correspond to the best clustering result. Instead, each cluster's silhouette width should be evaluated. Very low silhouette widths (about <0.3) often do not hold any valuable information. However, such very low values seldom occur.

Due to the higher amount of points in the cloud, all computation procedures take longer. For the normal computation of several million points like in the datasets BK, BI or WG, the computation time is about one hour. The clustering takes about one to two hours, depending on the point cloud size. In case re-clustering is necessary, this process is much quicker, of course. For the segments, the computation time is lower (about 15 minutes). Concerning the degree of automatization, the procedure can be classified as semi-automatic. The most time-consuming part of the workflow is the plane fitting, as each surface has to be segmented and the plane fitted.

The point clouds include several man-made structures, e.g. roads and concrete or shotcrete linings in the spillway. During data acquisition, areas with clearly visible rock faces and without much vegetation have been scanned more precisely resulting in a locally higher point density. The segments are mostly congruent with these areas. The point clouds seem to lack points in shadowed areas, which obviously depend on the scanning position, and on horizontal surfaces.

5.2.2 Sets in segment 1 (BK)

For segment 1 (Figure 17), the best clustering results are produced for six clusters. The corresponding silhouette plot is shown in Figure 18. The minimum individual silhouette width for this clustering procedure is -0.3489, the first quartile 0.4046, the median 0.6333, the mean 0.5502, the third quartile 0.7513, and the maximum individual silhouette width is 0.8551. Some negative silhouette widths are to be expected. The average silhouette width for data clustering into four clusters is 0.58, into five clusters 0.54, and into seven clusters 0.55. Although the silhouette width for four clusters is higher, visual inspection reveals a better performance in set differentiation when the data is classified into six clusters, i.e. the data classification is clearer for six clusters in accordance to the geological sets. The silhouette plot for four clusters is shown in Figure 19. The individual silhouette width statistics are: minimum -0.1978, first quartile 0.4667, median 0.6566, mean 0.5793, third quartile 0.7505, maximum 0.8244. Therefore, the minimum, first quartile, median, and mean are lower for the six-classes-clustering, but the third quartile and the maximum are higher.

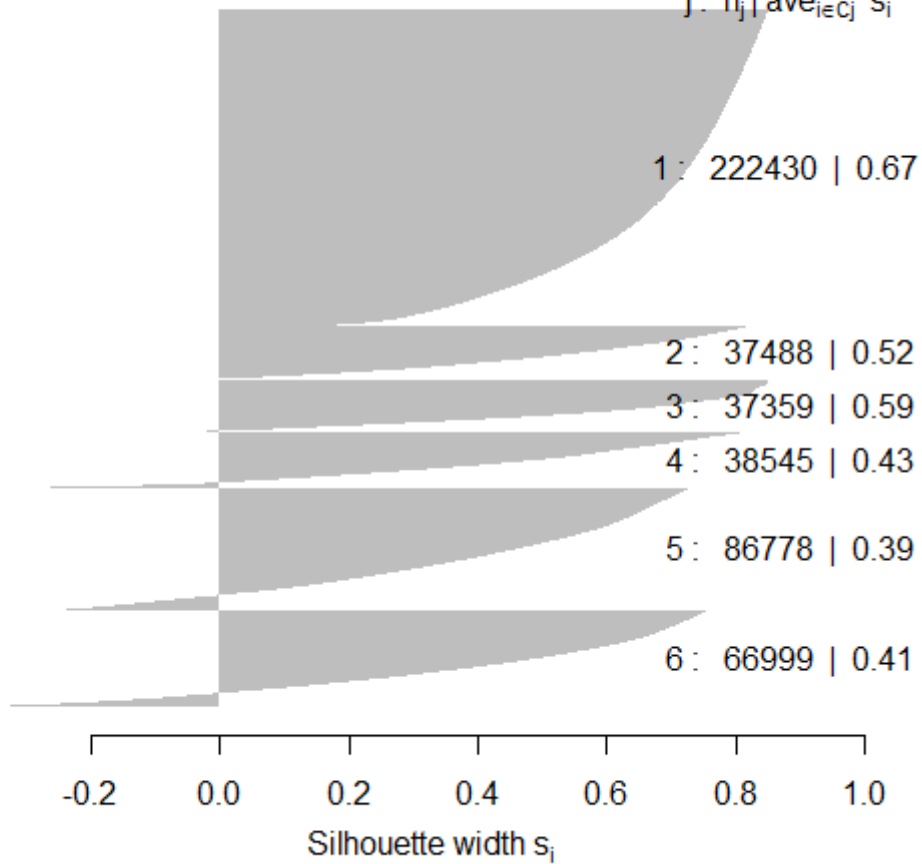


Figure 17: Segment 1, RGB colors (shown in CloudCompare, 2019)

Silhouette Plot for 6 clusters/sets

$n = 489599$

6 clusters C_j
 $j: n_j | \text{ave}_{i \in C_j} s_i$



Average silhouette width : 0.55

Figure 18: Silhouette plot for segment 1, six clusters

Silhouette Plot for 4 clusters/sets

$n = 489599$

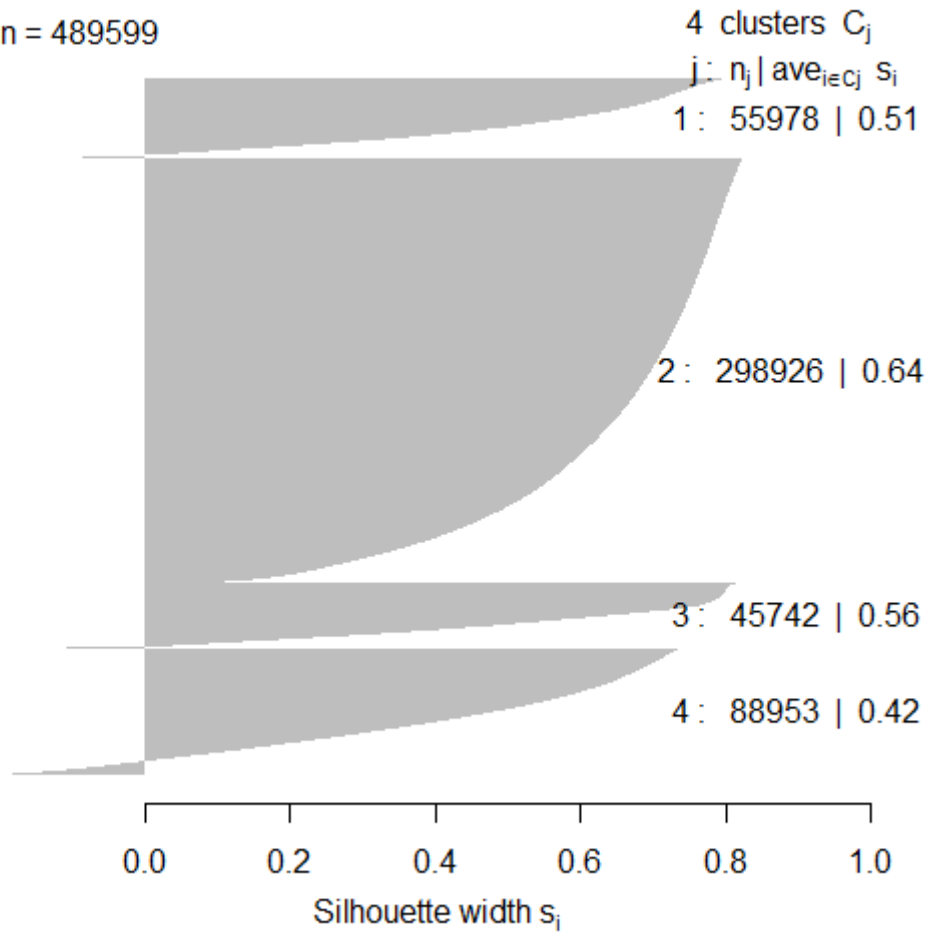


Figure 19: Silhouette plot for segment 1, four clusters

The data is clustered into six classes. Cluster 1 has the highest silhouette width and holds the most points. It contains the most prominent set, very steeply dipping and about parallel to this page in Figure 17. In clusters 2 and 3, two sets are mixed, which causes the need for reclustering these clusters. Cluster 4 contains a blue oblique set. Cluster 5 consists of parts of the most prominent set, and some traces of another set. These cannot be filtered out properly as they are too similar to the rest of this cluster. The traces belong to a set which is also represented in cluster 6, but this cluster also includes a lot of noise. The reclustering of clusters 2 and 3 in three clusters each clearly separates the sets.

Therefore, five sets can be identified. Their orientation statistical parameters are shown in Table 5. The largest set, i.e. with the most points, is set 1, which is the most prominent set as described above. Set 2 contains the fewest points. This might be caused by the TLS procedure as well as by the visually low surface area in the outcrop, as this set is mostly represented by traces instead of surfaces. Some features of this set are missed. In order not

to lose further points, no SOR is conducted. The variability angles are similar for sets 1, 2, 4, and 5. However, set 3 has a very high variability angle, which is also represented in its low Fisher concentration parameter k. The very low confidence angles are due to the high number of values, which increase the confidence as the sample grows.

As an example for the importance of the orientation statistics for such big datasets, Figure 20 shows the extraction of set 4 with the Facets Plugin by Dewez et al. (2016) in CloudCompare (2019). Without the orientation statistics, this set might have been overlooked in the Facets stereogram, which is dominated by a high density cluster representing set 1, marked by the orange circles in Figure 20. The steep dip angle of this set causes the cluster to be split apart and the dip direction to vary around two mean values, which are 180° apart. The other sets, namely sets 2, 3, and 5, can also just be vaguely discerned in the stereogram.

Table 5: Orientation statistics for segment 1. The angles are given in degrees.

set	number of values	mean dip direction ("major axis")	mean dip ("major axis")	Fisher k	variability angle (P=95.4%)	confidence angle (P=95.4%)
set 1	298255	74.4690	86.6400	18.9877	33.0877	0.0614
set 2	4415	287.1220	28.3890	17.8258	34.1810	0.5217
set 3	46672	182.2950	71.8200	7.7415	52.9682	0.2535
set 4	27698	359.9710	38.8400	21.4098	31.1094	0.1891
set 5	22680	323.6080	77.3450	14.0617	38.6452	0.2612

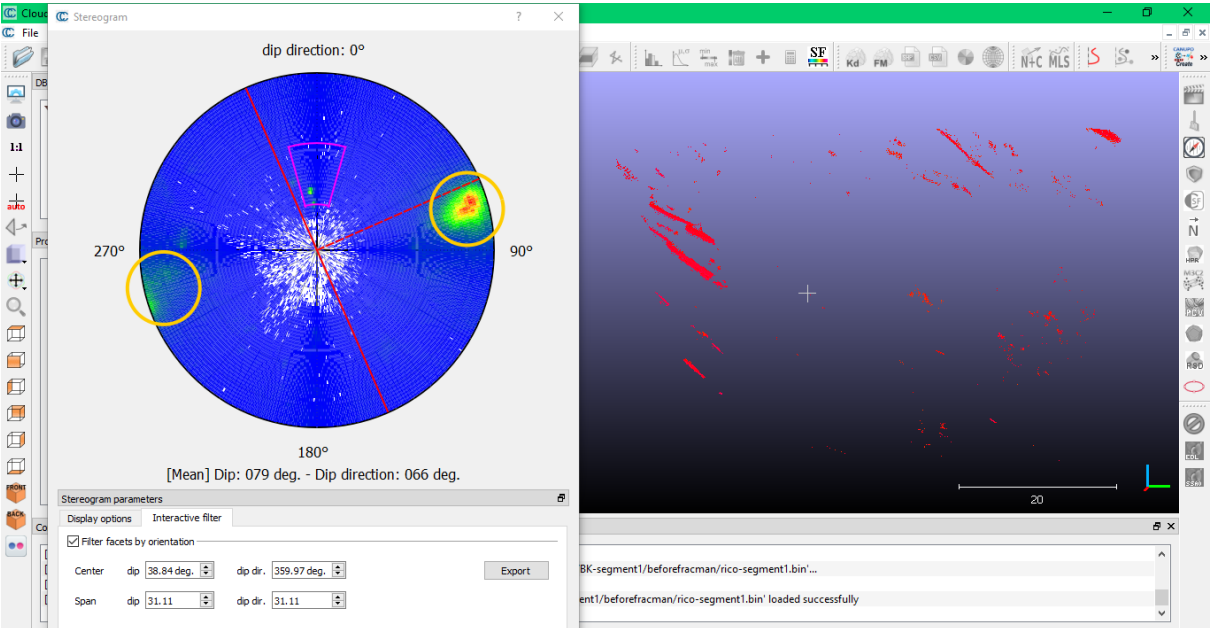


Figure 20: Extraction of set 4 with the Facets Plugin (Dewez et al., 2016) in CloudCompare (2019)

The points belonging to sets 1 to 5 after the extraction with the Facets Plugin (Dewez et al., 2016) and the SOR are shown in Figure 21 to Figure 25. A certain amount of noise cannot be eliminated and is still included in the sets' point clouds. As already mentioned, no SOR has been conducted for set 2 (Figure 22). Figure 26 to Figure 33 show the visualization of the fracture pattern with the fitted planes.

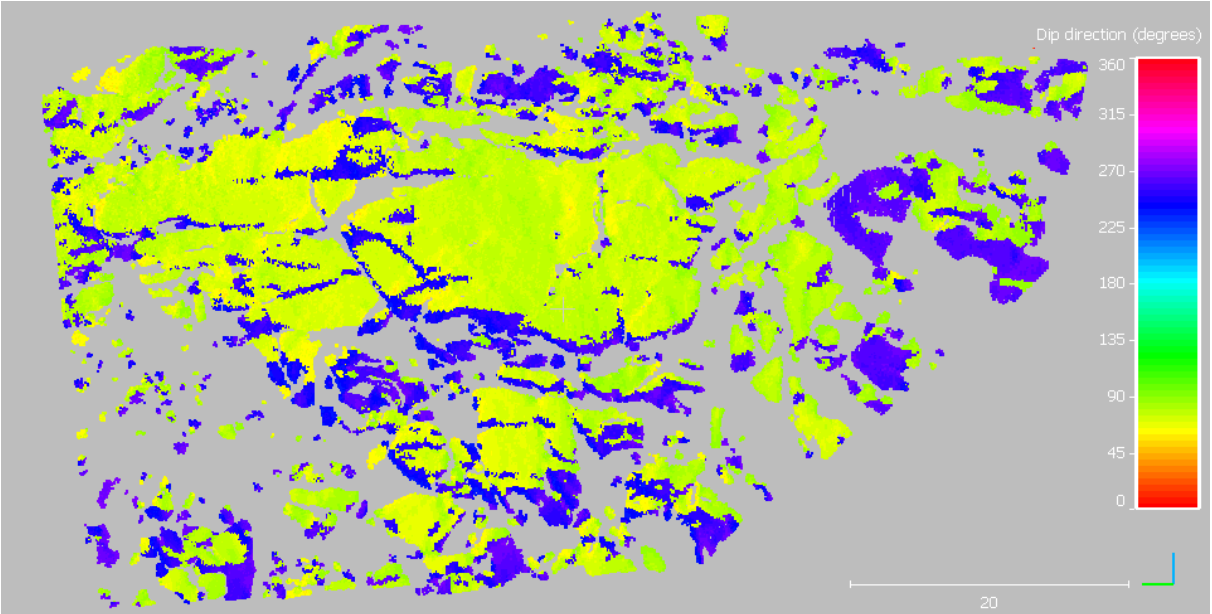


Figure 21: Points of set 1. Software used: CloudCompare (2019).

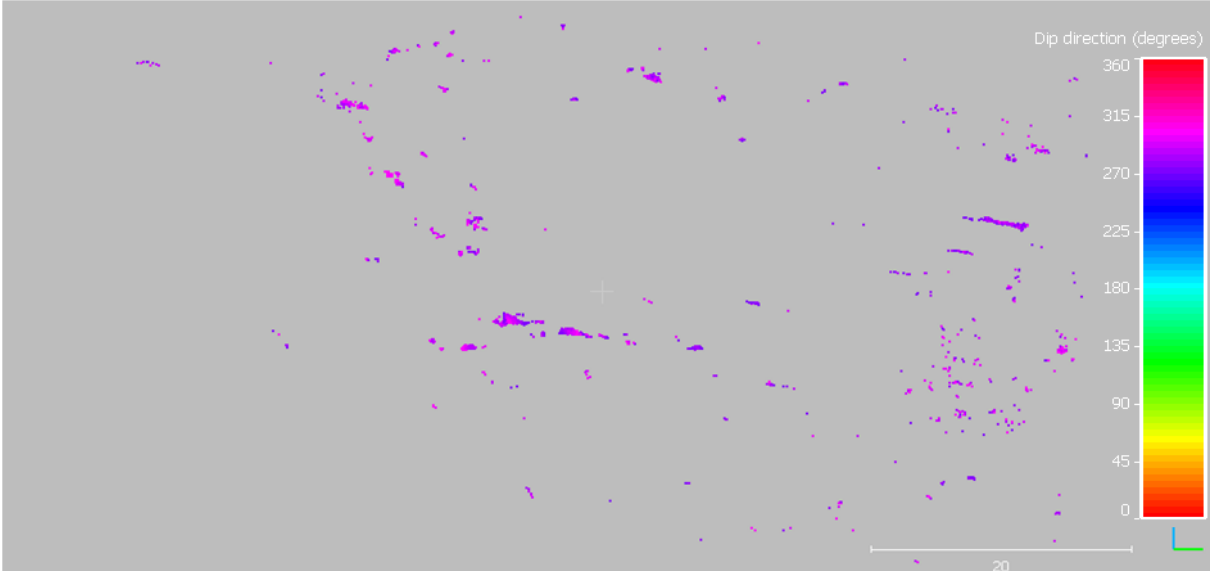


Figure 22: Points of set 2. Software used: CloudCompare (2019).

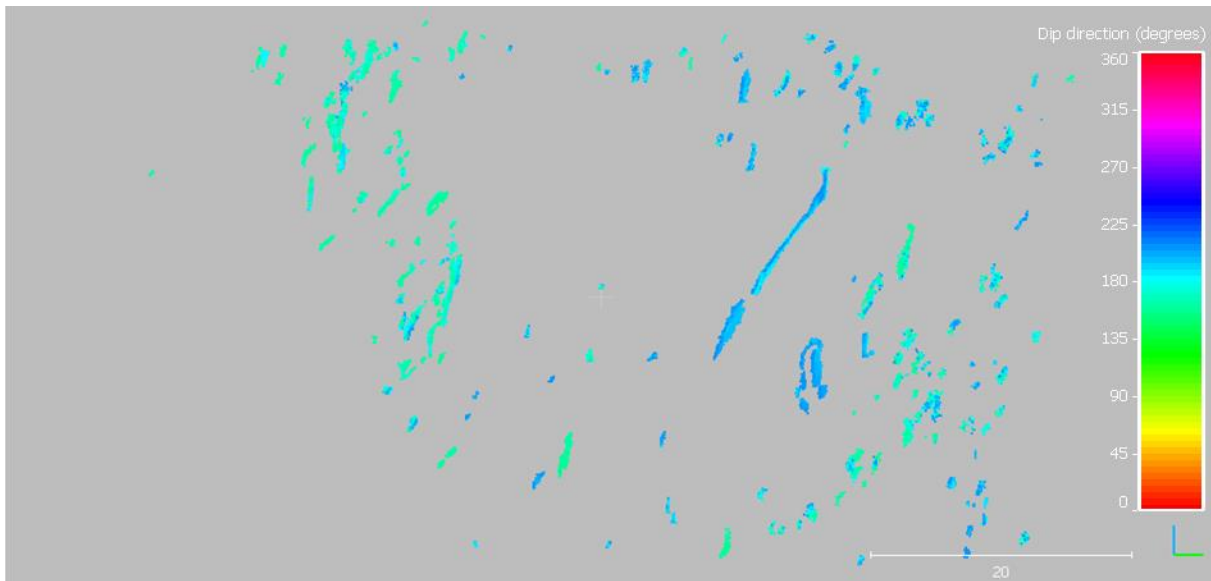


Figure 23: Points of set 3. Software used: CloudCompare (2019).

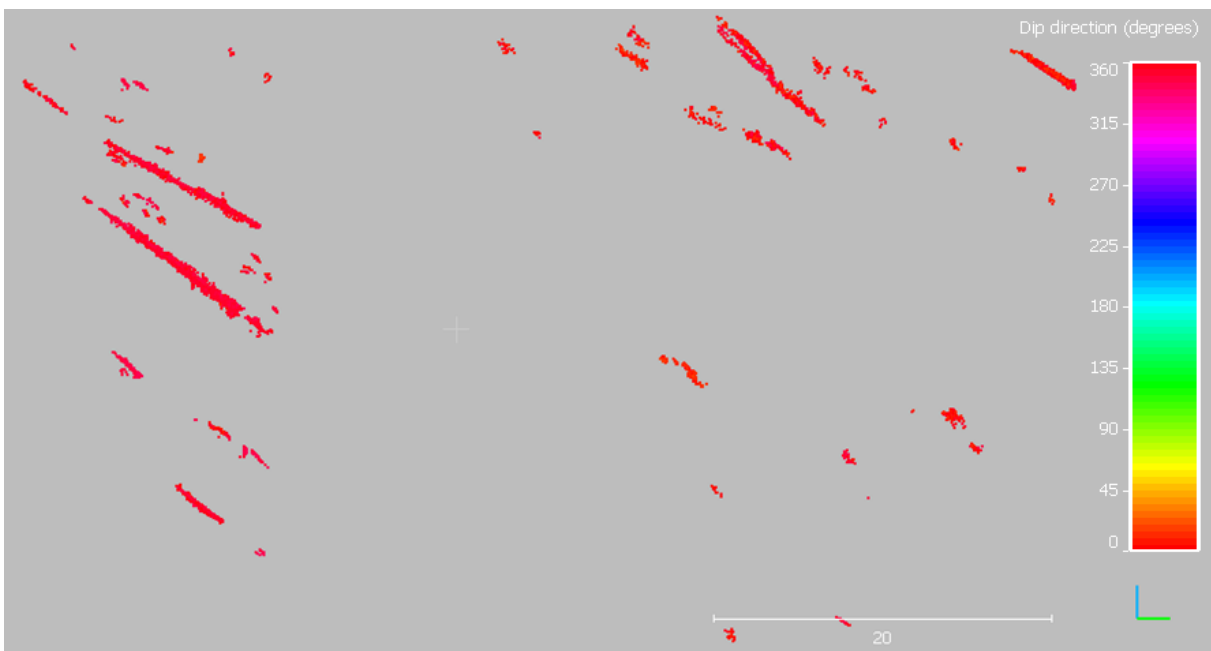


Figure 24: Points of set 4. Software used: CloudCompare (2019).

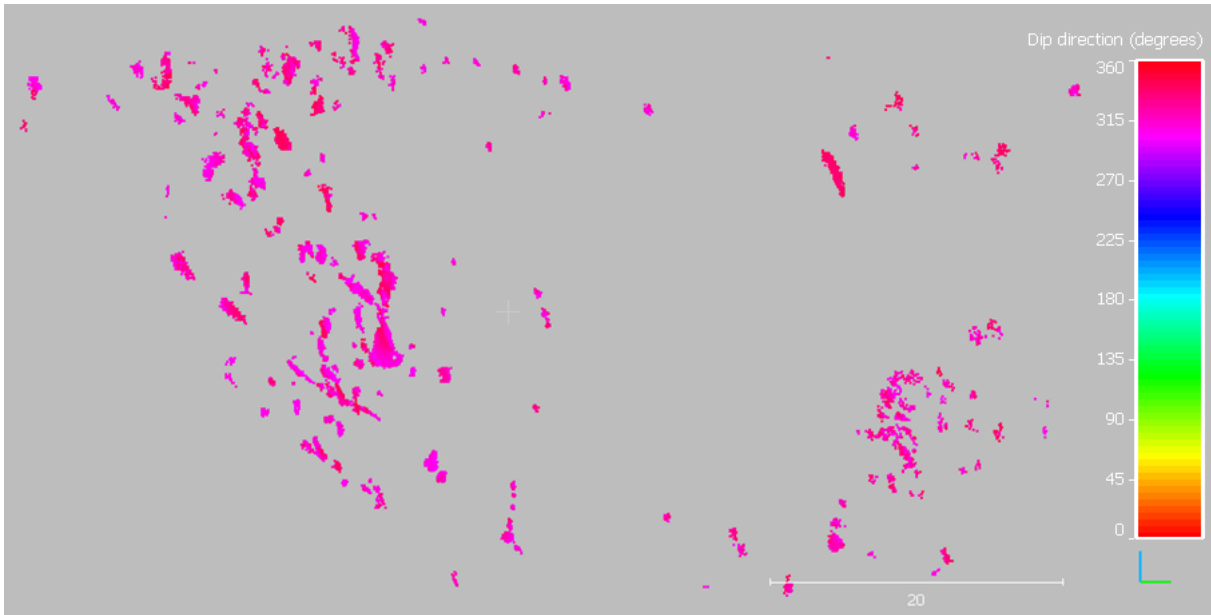


Figure 25: Points of set 5. Software used: CloudCompare (2019).

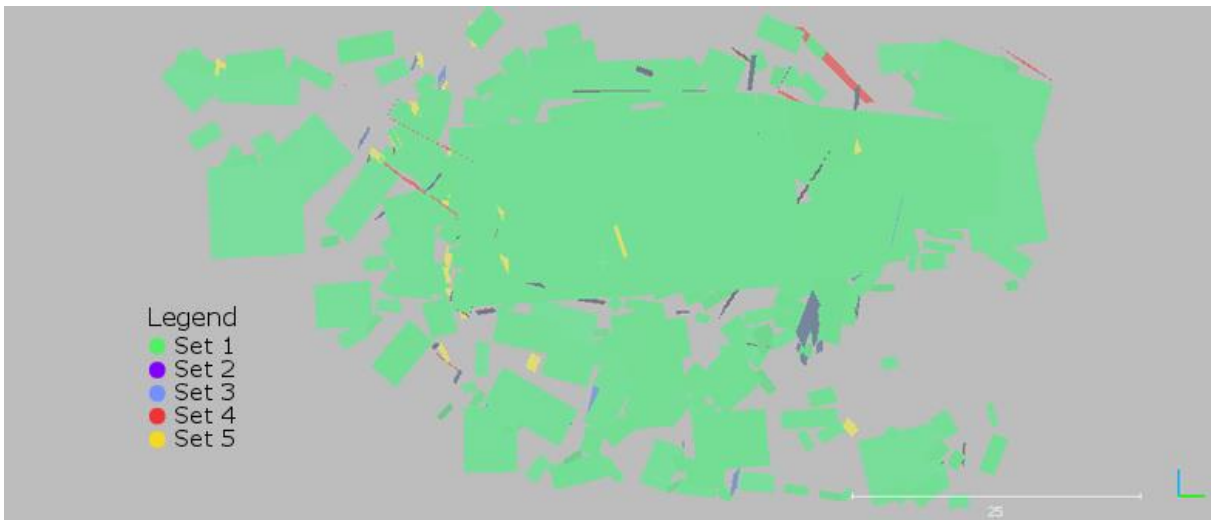


Figure 26: Fracture pattern in frontal view. Software used: CloudCompare (2019).



Figure 27: Fracture pattern in side view (left side from viewer's point). Software used: CloudCompare (2019).



Figure 28: Fracture pattern in side view (right side from viewer's point). Software used: CloudCompare (2019).

When the planes are laid above the RGB point cloud of the segment, their fit can be evaluated. As can be seen in Figure 29, 30, 32, and 33, the result is acceptable. The planes have a certain transparency, which improves the visibility of the fitting quality. The plane elongation does not imply any set specific characteristic, as CloudCompare (2019) just fits a plane over all selected points of the surface. Due to this fitting process, some points of a plane are located below it, and some are above.

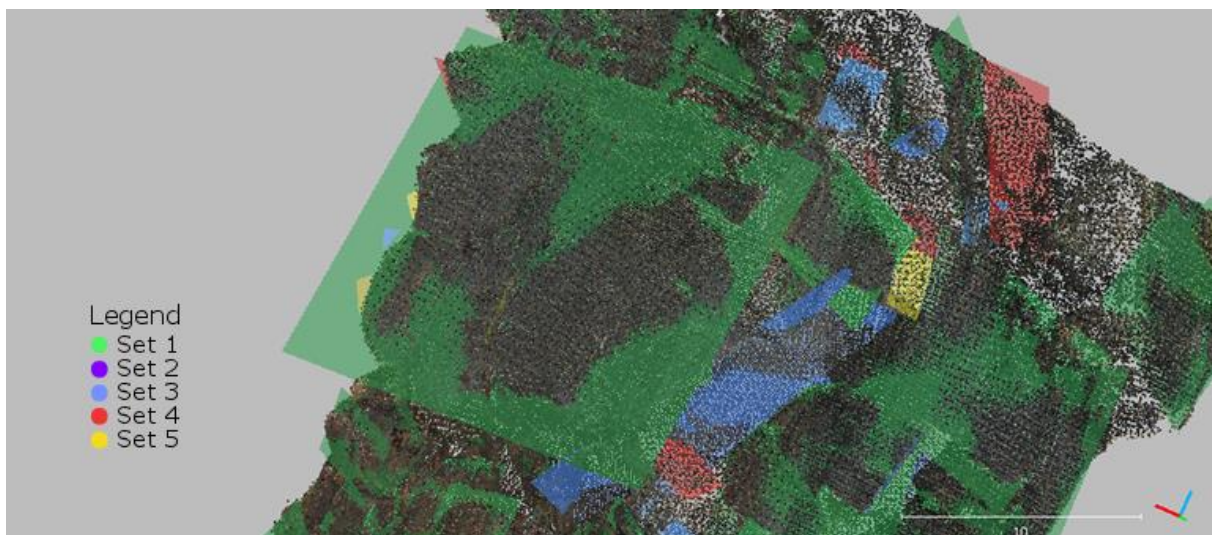


Figure 29: Fracture pattern of the right side over the RGB point cloud. Software used: CloudCompare (2019).

In order to provide a better view of the “smaller” sets, i.e. all sets except set 1, Figure 31 to Figure 33 show the fracture pattern without set 1. Unfortunately, there are not many planes in set 2, and they are difficult to see in the figures. In addition, as can be seen from the comparison with the RGB point cloud (e.g. Figure 31 and Figure 32), set 2 lacks some planes. However, this effect is caused by the laser scanning itself and not due to the method used in this thesis.

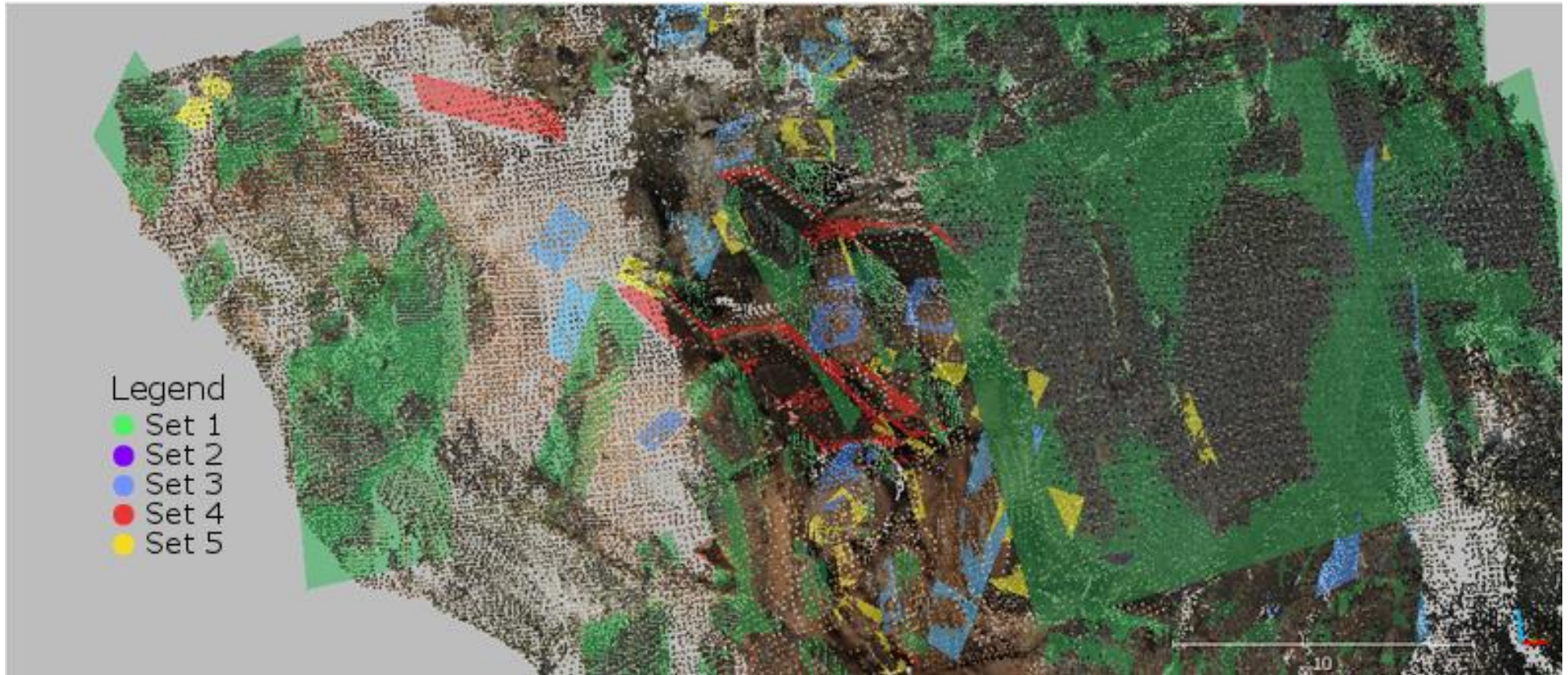


Figure 30: Fracture pattern of the left side in detail over the RGB point cloud. Software used: CloudCompare (2019).

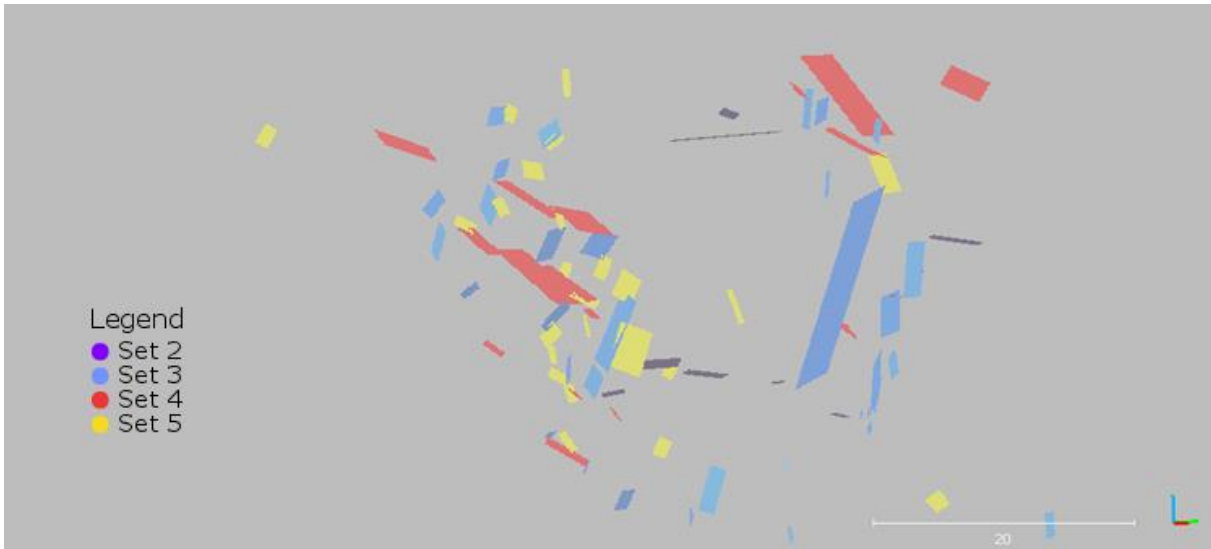


Figure 31: Fracture pattern in side view from the left (from viewer's point of view), without set 1. Software used: CloudCompare (2019).



Figure 32: Fracture pattern in detail over the RGB point cloud from the left (from viewer's point of view), without set 1. Software used: CloudCompare (2019).



Figure 33: Fracture pattern in detail over the RGB point cloud from the right (from viewer's point of view), without set 1. Software used: CloudCompare (2019).

The planes' poles are calculated and plotted with the software Dips (Rocscience Inc., 2018). To evaluate the plane fitting performance, the orientation statistics plot of the point normals and of the calculated Fisher distributions from FracMan (Golder Associates Inc., 2018) are compared with the planes' poles (Figure 34). The fact that the planes' poles mostly plot in the area of the stereogram where the normals did shows that the planes correspond well to the sets' surfaces. The mean plane orientation, which is calculated by Dips (Rocscience Inc., 2018), could be further used for a kinematic analysis. Due to the orientation statistics with a probability for the variability angle of 95.4% and the following extraction with Facets (Dewez et al., 2016), the planes' orientations are more strongly centered on the mean orientation. A higher probability value might have caused a higher variability of the plane orientations.

As can be seen in Figure 34, the plane poles distribution follows the original point cloud normals distribution rather than the calculated Fisher distribution. This effect has been expected because of the extraction of the points per set directly out of the point cloud, while the Fisher distribution calculation is just a model. The plots for set 5 are a good example, as the normals stereogram (on the left in Figure 34) shows two local maxima, while the calculation smooths these local peaks to one wide peak. The plane poles, however, show two peaks again, because they have been extracted from the point cloud directly. The stereograms for set 3 are of similar appearance.

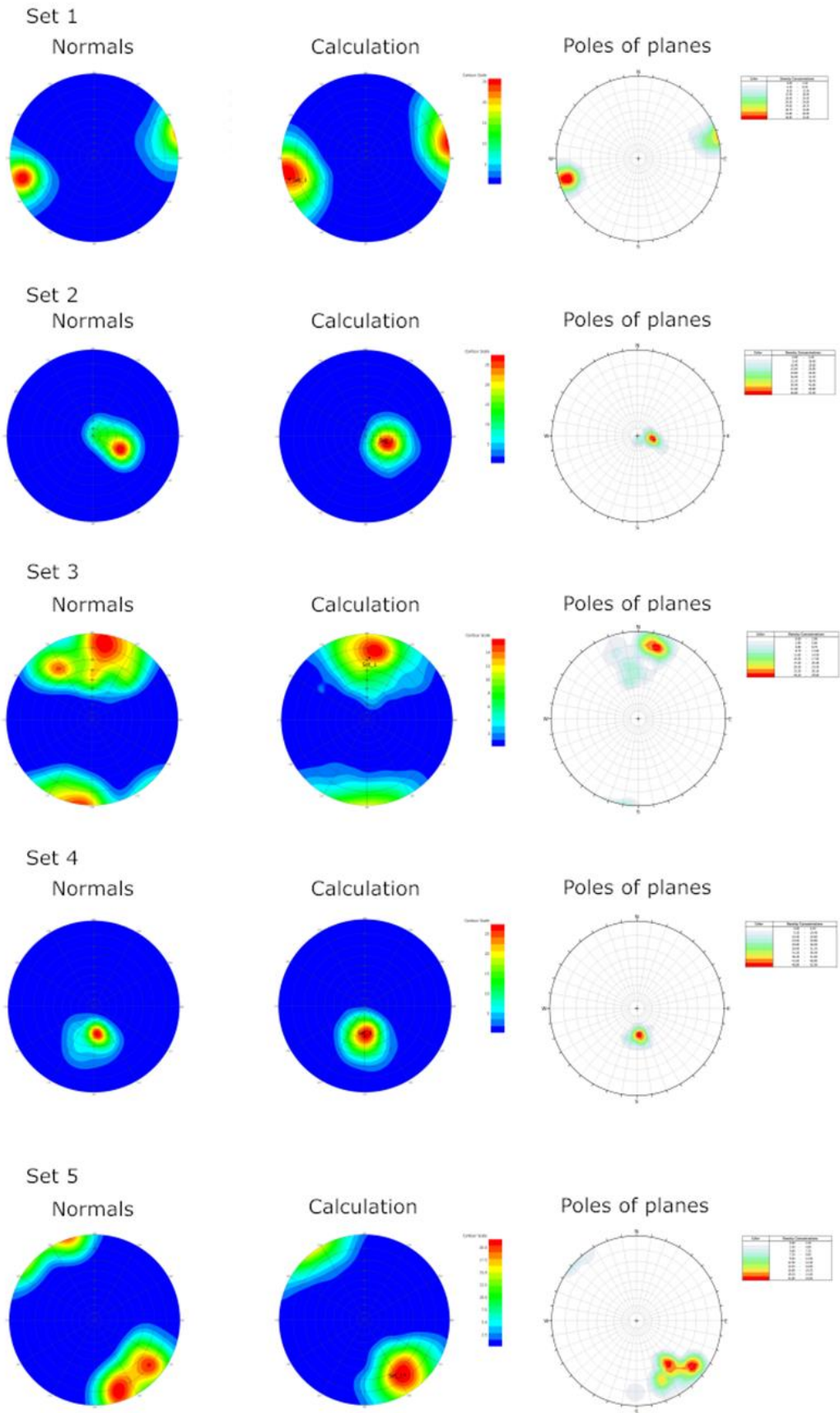


Figure 34: Stereograms for segment 1's sets of the point cloud (left, middle; FracMan (Golder Associates Inc., 2018)) and the plane data (right; Dips (Rocscience Inc., 2018))

By visual inspection, set 1 has the biggest planes while set 5 shows the smallest planes. Table 6 gives an overview of the mean, median, maximum and minimum plane sizes of the sets in segment 1. As the plane fitting is based on a visual estimation of the plane size, some planes' areas are $<1 \text{ m}^2$. This is also given in Table 6. Set 1 has the highest mean plane size, which is clearly influenced by the extremely high maximum plane size. However, the highest median plane size has set 4, which also includes the least planes $<1 \text{ m}^2$. The planes $<1 \text{ m}^2$ do not influence the mean and the median much, but for set 2, which has 40% of fitted planes $<1 \text{ m}^2$, the median increases a lot. However, set 2 is difficult to assess since it consists mainly of traces instead of surfaces. Its plane size is therefore just an indication and has to be interpreted with caution. In addition, the low amount of planes in some sets, as in set 2 for example, might distort the plane statistics.

Table 6: Plane sizes in segment 1

	Set 1	Set 2	Set 3	Set 4	Set 5
Mean	12.8074	2.6553	6.1732	9.8101	2.2535
Mean (>1 m²)	13.6214	3.9828	6.6922	10.3901	2.5270
Median	4.2512	1.3992	3.2705	7.0198	1.5238
Median (>1 m²)	4.5918	4.0200	3.3434	7.1739	1.6716
Maximum	477.6739	6.7551	74.6938	31.3099	10.4315
Minimum	0.6707	0.3496	0.5648	0.5315	0.7639
Number of planes	172	10	35	17	24
Number of planes <1m², total	11	4	3	1	4
Number of planes <1m², %	6.3953%	40%	8.5714%	5.8824%	16.6667%

A comparison of the mean and the median in Table 6 shows the same as a plane size histogram (Figure 35 to Figure 39): There are more small planes than big planes in a set. This does not depend on the absolute plane size, obviously, since this trend is true for all sets in this segment. Due to the high plane sizes, the histograms of sets 1 and 3 plot them as logarithmic to the base 10. A red density line is added to the histograms to show the trend to smaller plane sizes even more clearly. As already mentioned, set 2 might be biased. The histograms include all plane sizes, even $<1 \text{ m}^2$, since this does not influence the result and the planes have been fitted anyway before knowing the exact plane size. The plane size might be difficult to estimate during the plane fitting procedure, which is why surfaces of uncertain size have been included in the plane fitting in order not to overlook any relevant planes.

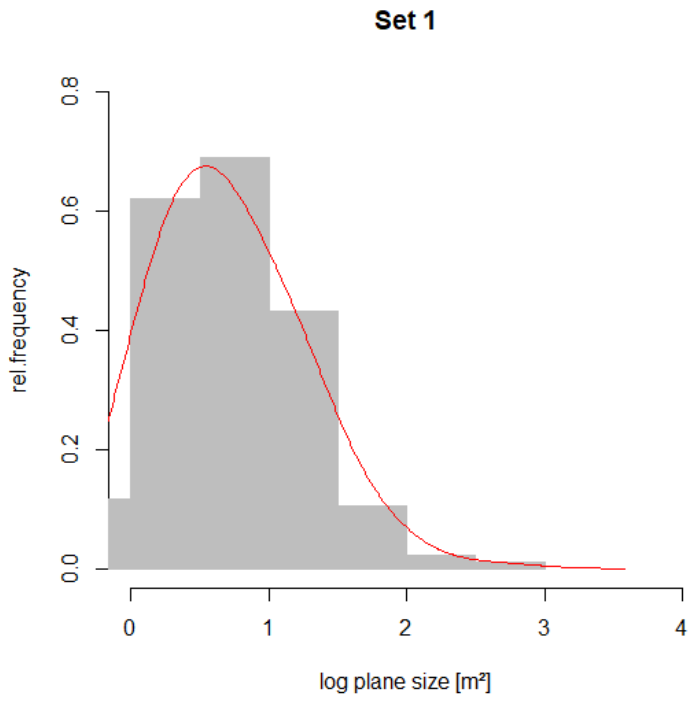


Figure 35: Plane sizes of set 1, density line shown in red

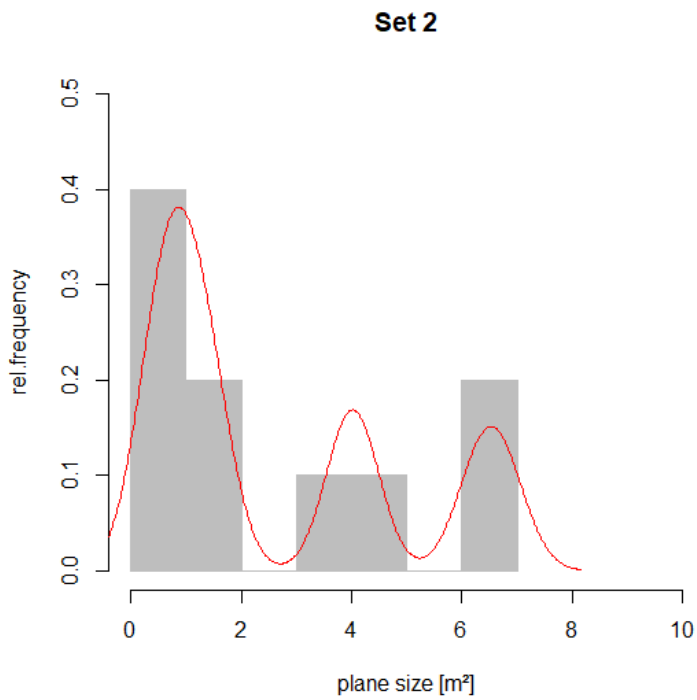


Figure 36: Plane sizes of set 2, density line shown in red

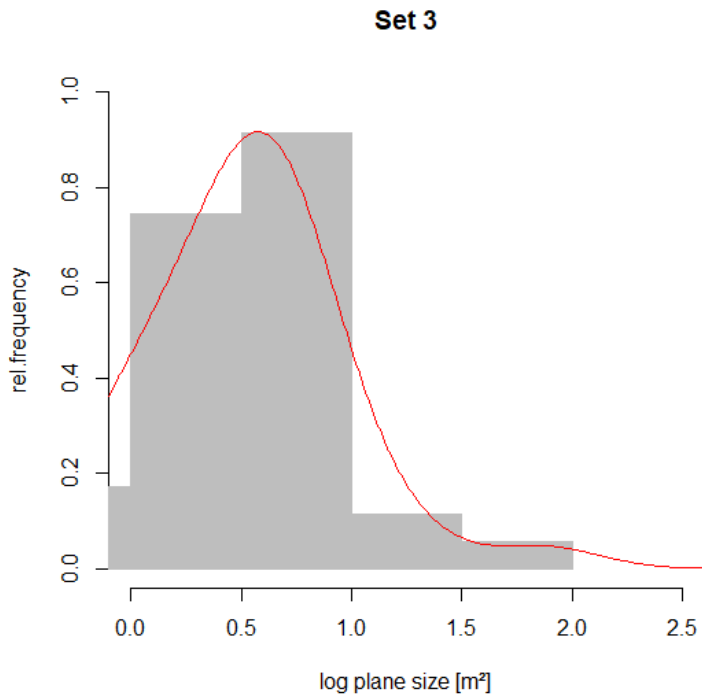


Figure 37: Plane sizes of set 3, density line shown in red

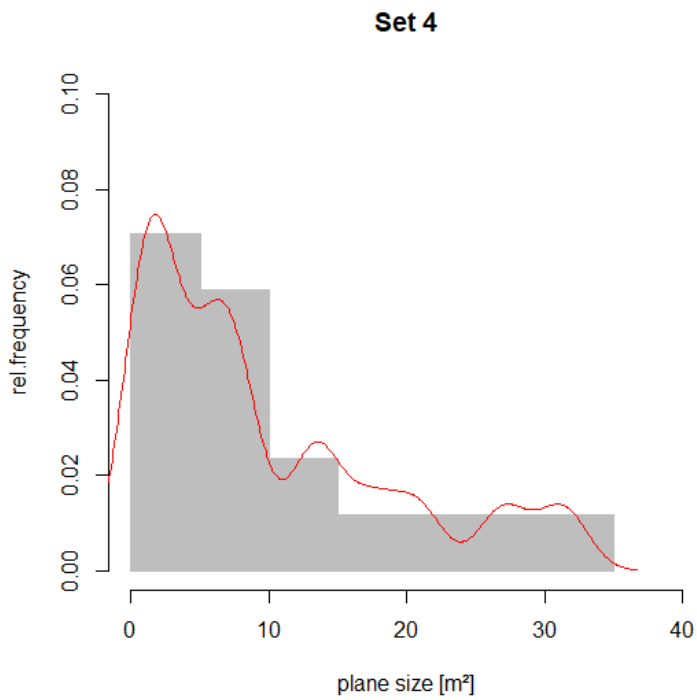


Figure 38: Plane sizes of set 4, density line shown in red

Set 5

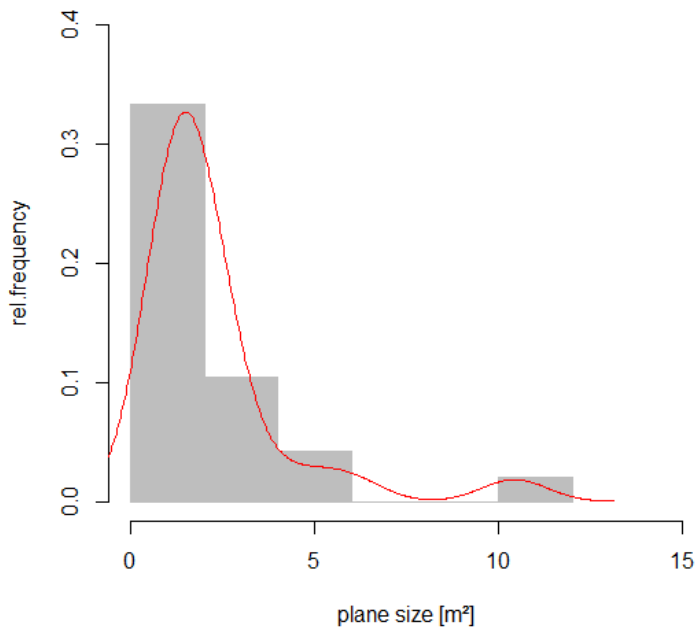


Figure 39: Plane sizes of set 5, density line shown in red

The spatial relation between the sets is described by the termination. These relations are plotted for all sets in the following. One plot reveals to which sets the concerned set connects (“Termination in which set?”), while another plot (“Termination in how many sets?”) shows the number of connected sets, ranging from zero (isolated plane) to all sets including the concerned set itself. The “problems” plot reveals the main obstacles for the plane fitting, which makes the “neighborhood” investigation necessary, i.e. the plot shows the reason why two planes which should actually crosscut each other according to visual geological evaluation are nevertheless separated by a small gap. The details on which the plots are based on are given in the appendix. Due to its persistence, plane size, orientation, and waviness, combined with a visual investigation of the rock face, set 1 is classified as a sheeting joint set. Set 2 is also a sheeting joint set. This will be further explained and interpreted in chapters 6.1 interpretation – joint sets, and 7.2 discussion – results.

Figure 40 shows the termination of set 1, which obviously tends to terminate in itself, i.e. most of the planes of set 1 connect to each other. This is due to the roundness, which is also the biggest problem during the plane fitting (Figure 41), and means that the planes are narrowly stepped or nearly merging. If the plane’s waviness is taken into account, many planes would possibly merge into a bigger plane. However, this can just be estimated, which causes the difference between termination and termination including the neighborhood. In relation to the roundness problem, other factors seem to be of minor importance during plane fitting (Figure 41). Concerning the termination in other sets given in Figure 40, many set 1

planes terminate in set 3. In general, set 1 planes terminate in all sets. Concerning the number of sets in which set 1 planes terminate (Figure 42), most of them are isolated or connect with just one set at first sight. However, when including the neighborhood, no plane is isolated, and most of the planes terminate in one or two sets.

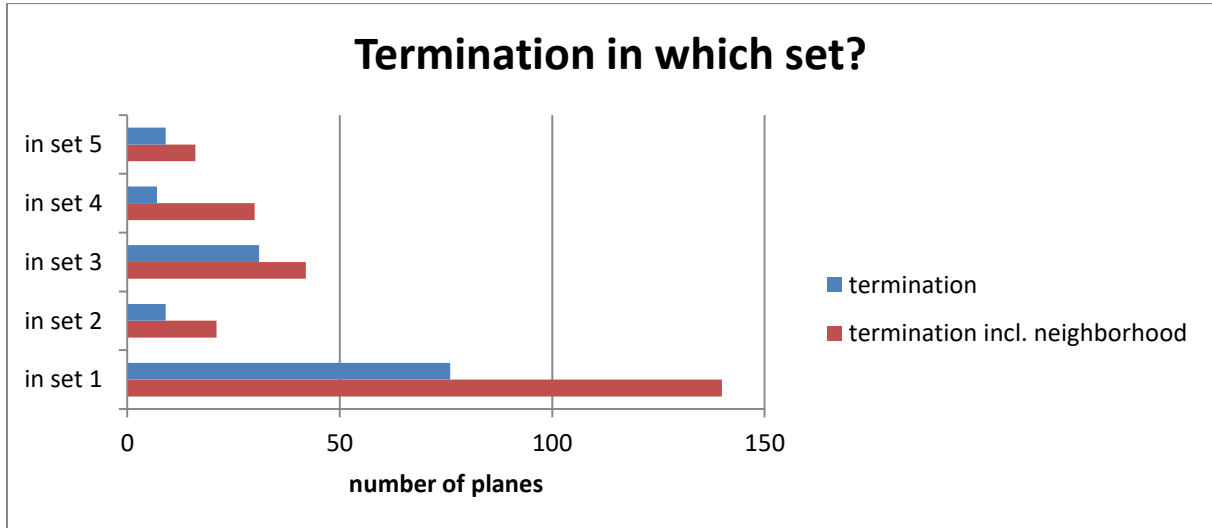


Figure 40: Termination of set 1

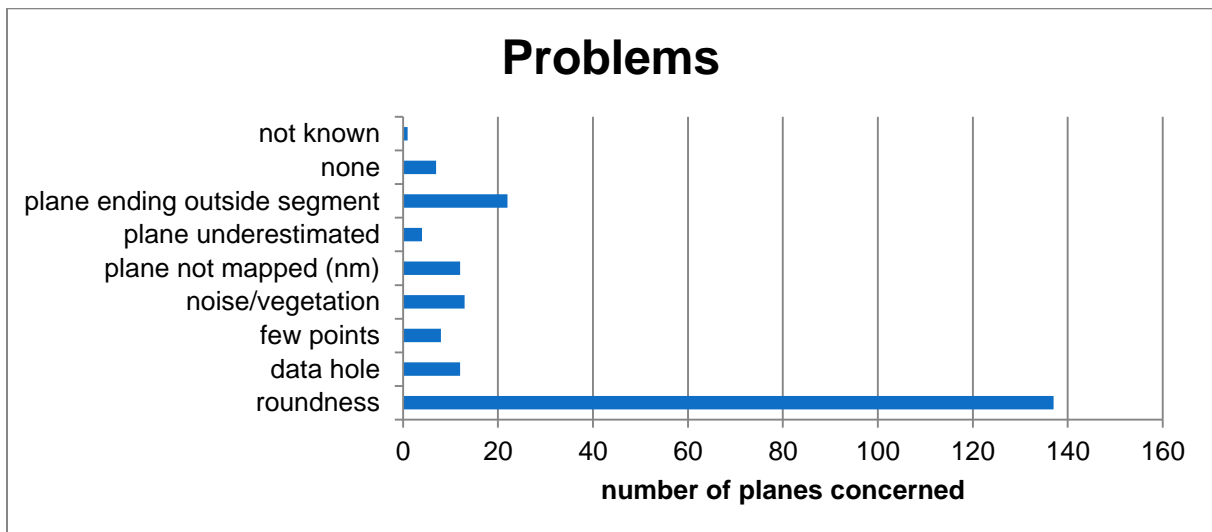


Figure 41: Problems for plane fitting in set 1

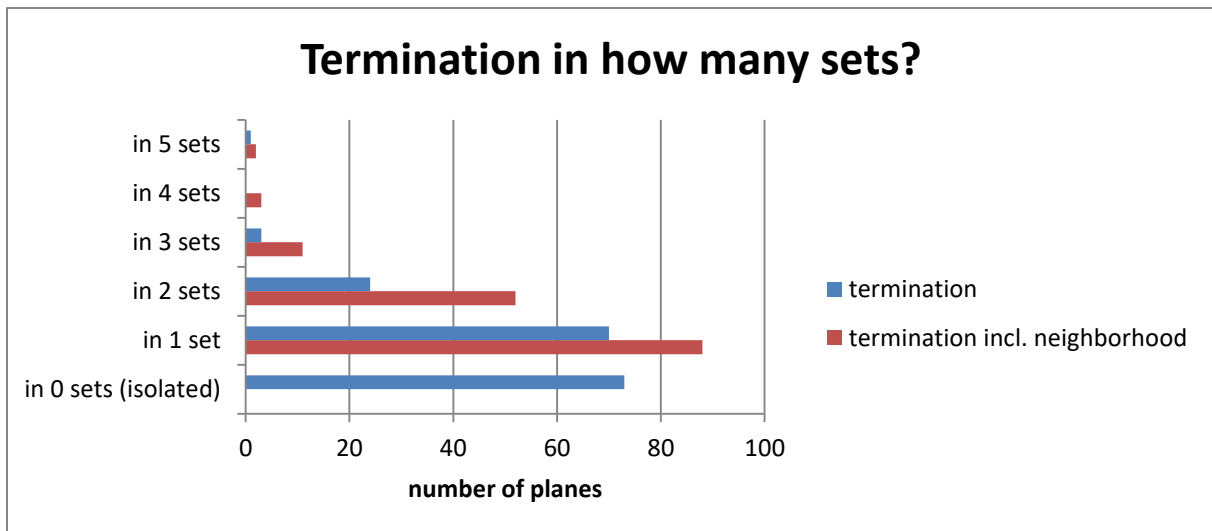


Figure 42: Termination of set 1

Set 2 mainly terminates in set 1 (Figure 43). It never terminates in itself. Concerning the number of sets in which set 2 terminates (Figure 44), three planes seem to be isolated regarding the termination. Including the neighborhood changes this to six planes terminating in one set, and four planes terminating in two sets. The main problems faced in this set are the low number of points, roundness, and data holes adjacent to the planes. This confuses the issue of the true termination estimation as there is just no information in parts of the plane's direct neighborhood.

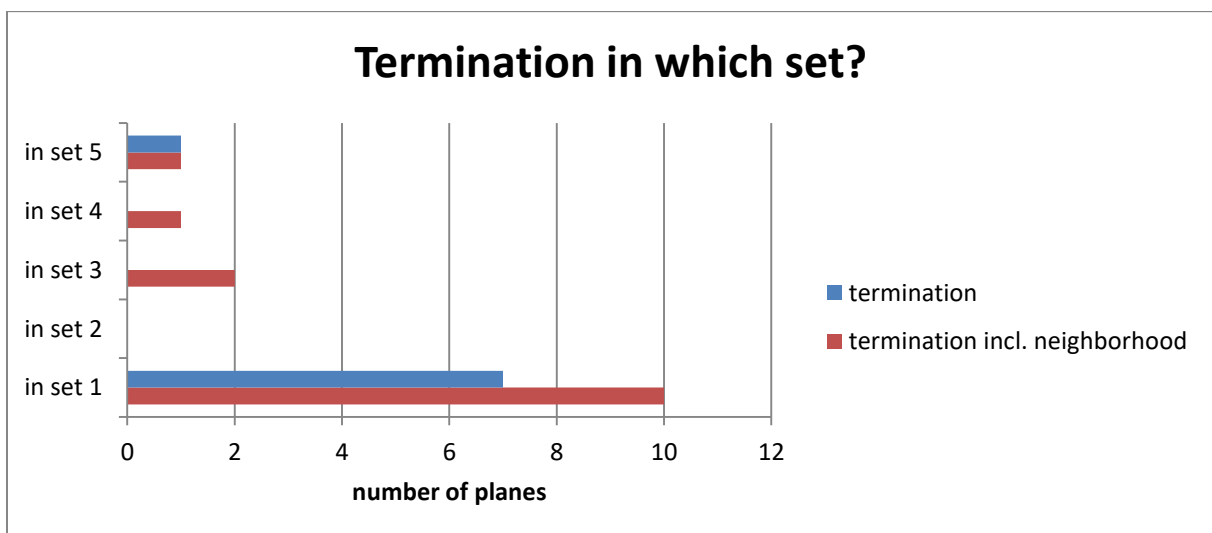


Figure 43: Termination of set 2

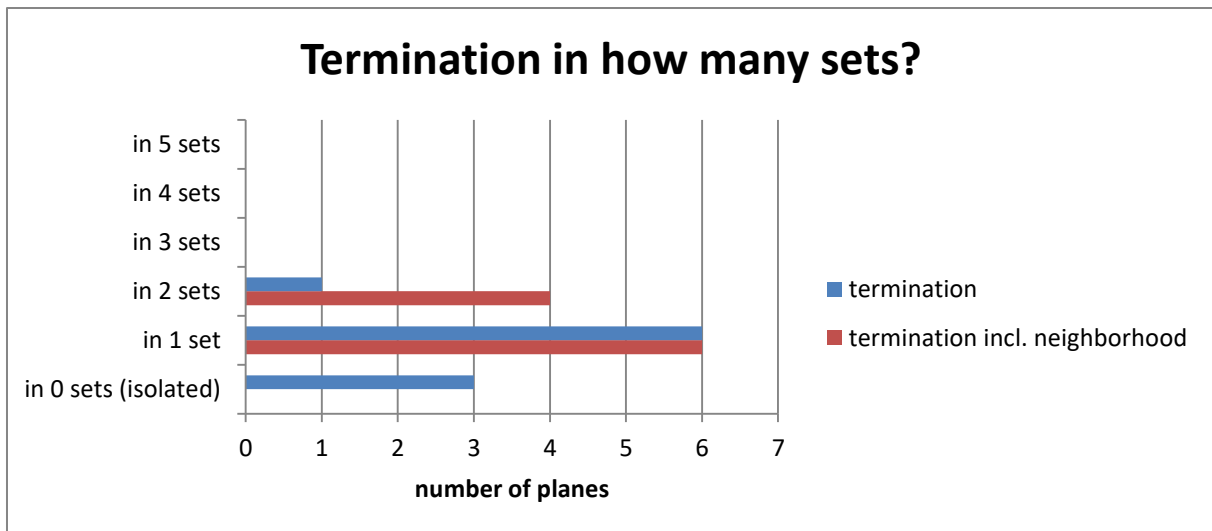


Figure 44: Termination of set 2

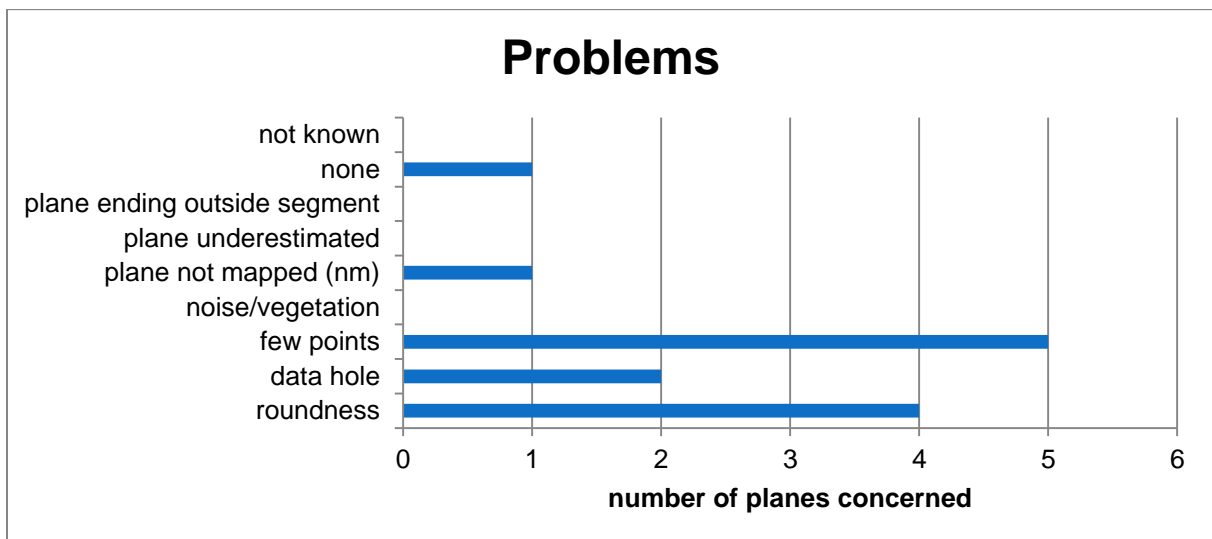


Figure 45: Problems for plane fitting in set 2

Set 3 tends to terminate in set 1, but also in sets 4 and 5 (Figure 46). It is connected with one, two or three other sets (Figure 47). The isolated planes cannot be affirmed when taking the neighborhood into account. As for set 1, the biggest plane fitting problem is the roundness. Several other problems, as noise or vegetation as well as data holes and a low local point density also preclude better plane fitting and therefore better termination at first sight, so without further estimation.

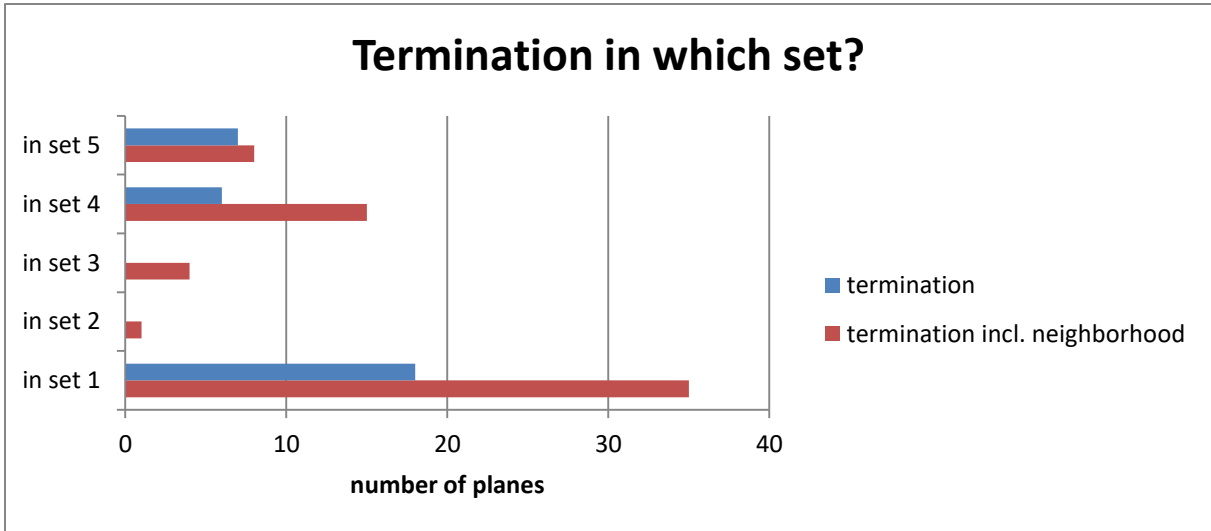


Figure 46: Termination of set 3

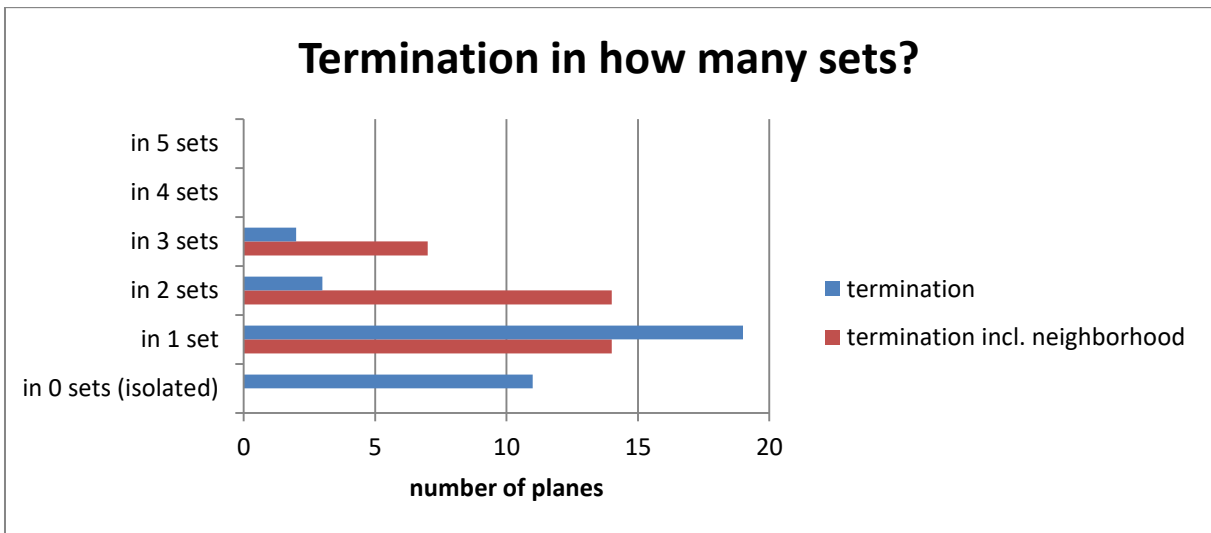


Figure 47: Termination of set 3

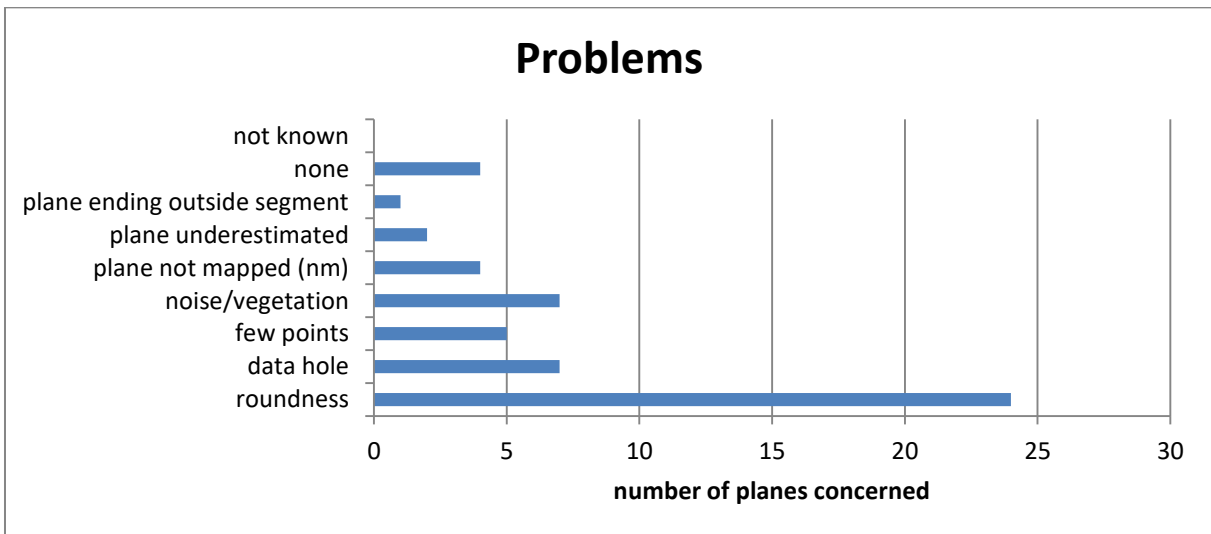


Figure 48: Problems for plane fitting in set 3

The termination of set 4 is shown in Figure 49 and Figure 50. Set 4 mostly terminates in set 1, 3, and 5. Their relative percentages depend on the inclusion of the neighborhood. Set 4 never terminates in set 2. It is connected to up to four sets. As for the other sets, the isolated planes are no longer isolated when the neighborhood is taken into account. The biggest problem for plane fitting in set 4 is the roundness (Figure 51). This is the same for set 1 and set 3.

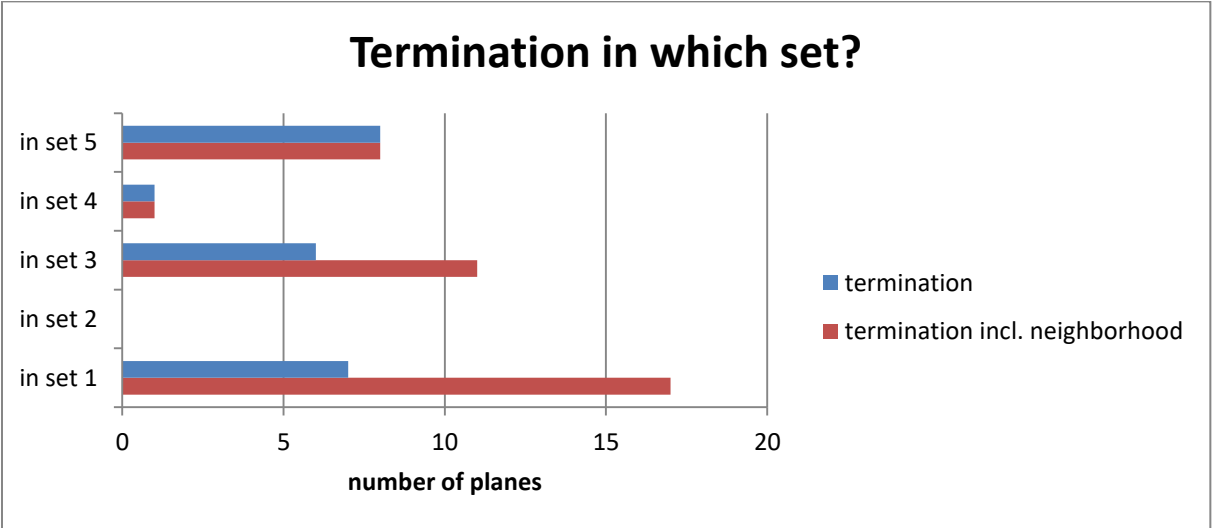


Figure 49: Termination of set 4

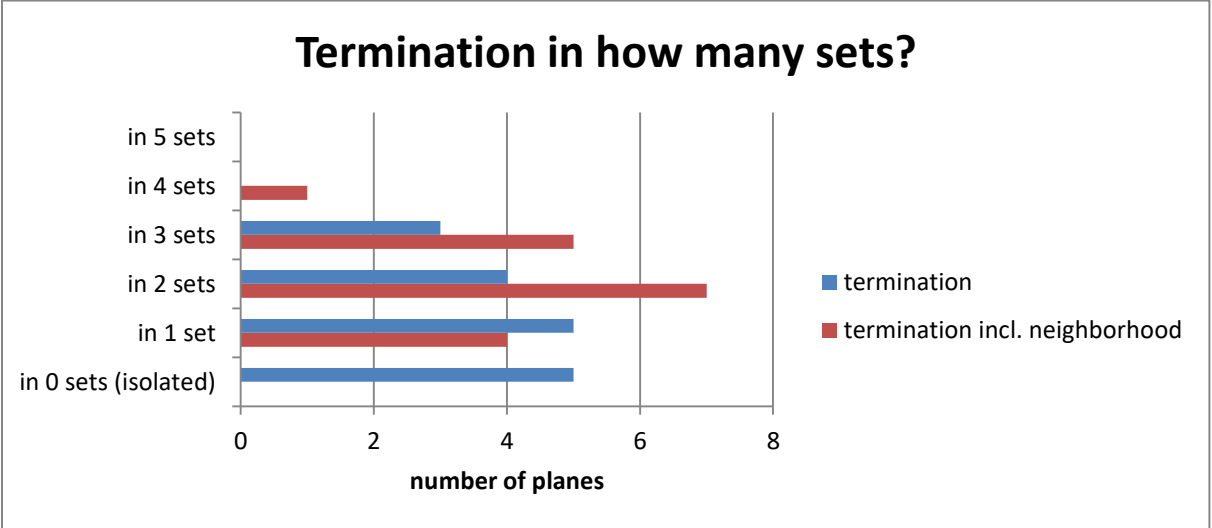


Figure 50: Termination of set 4

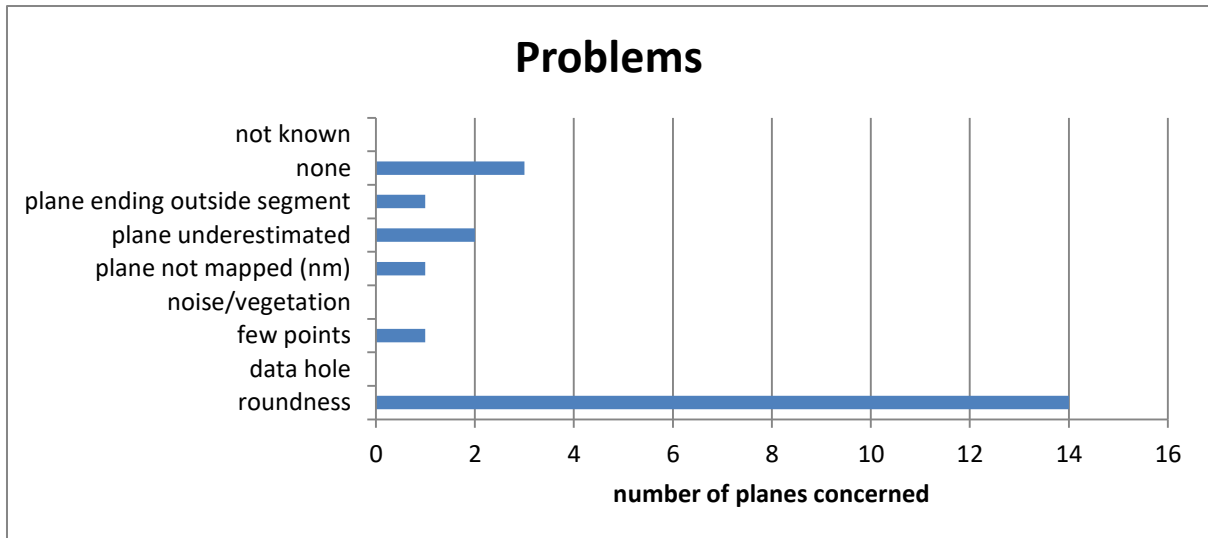


Figure 51: Problems for plane fitting in set 4

Set 5 mostly terminates in set 1, but also in sets 3 and 4, and sometimes in set 2 (Figure 52). It never terminates in itself, so all set planes are clearly defined. As for all other sets, there are some isolated planes which are actually connected with other sets (Figure 53). Most of the set 5 planes are connected with one or two, some with three other sets. The roundness is again the biggest plane fitting problem (Figure 54).

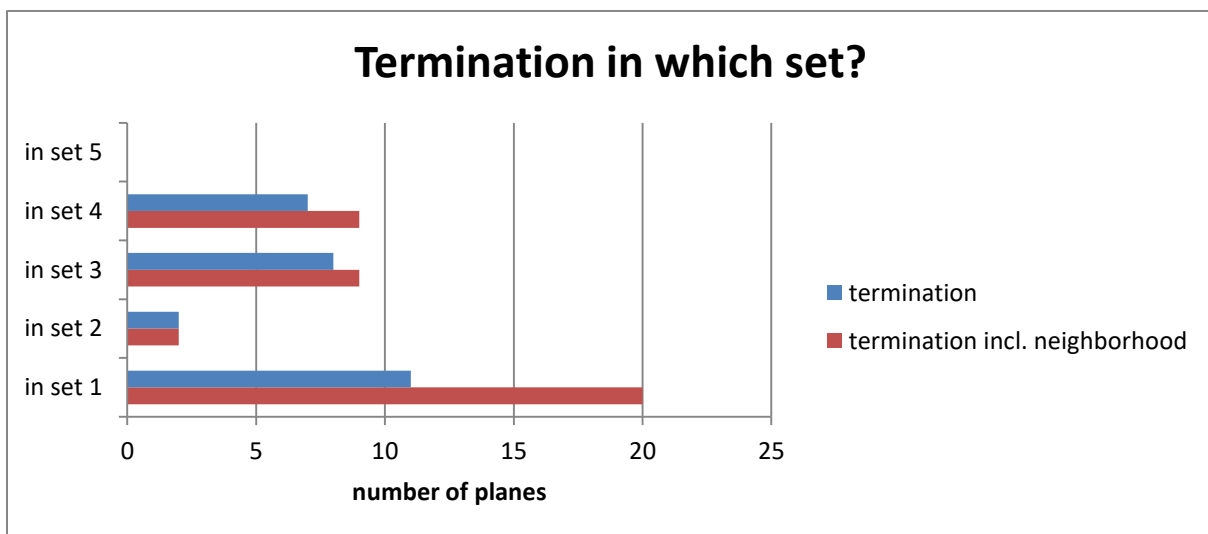


Figure 52: Termination of set 5

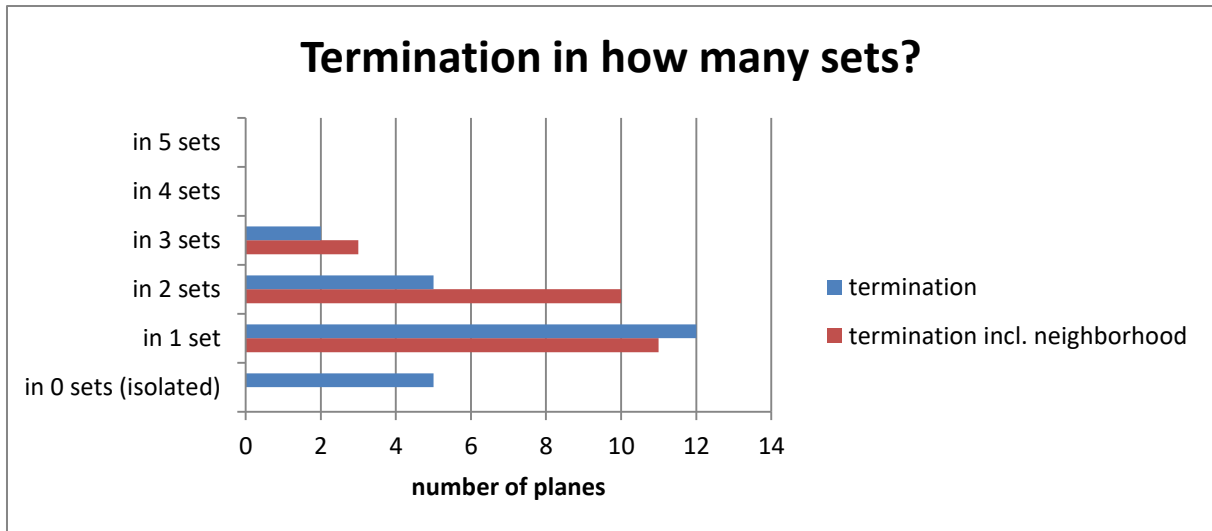


Figure 53: Termination of set 5

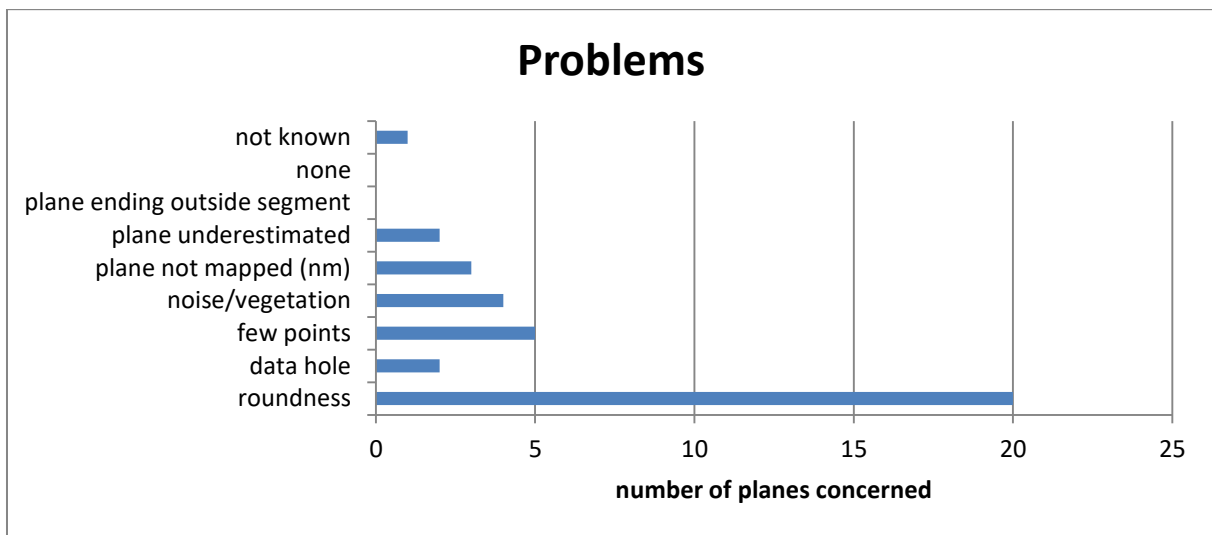


Figure 54: Problems for plane fitting in set 5

5.2.3 Sets in segment 2 (BI-part 2)

Segment 2 is located in the center of the dam site (see Figure 3). It is shown in RGB colors in Figure 55. Empirically, the best clustering results are achieved for six clusters with an average silhouette width of 0.6, although the average silhouette width for five clusters is higher (0.63). The numbers of points in the clusters as well as the average silhouette widths of the clusters are given in the silhouette plot in Figure 56. The minimum silhouette value is -0.2695, the maximum is 0.8956. The first quartile is 0.4317, the median 0.6904, the mean 0.6011, and the third quartile 0.8178. The third quartile value and the maximum value are higher for six clusters than for five clusters (third quartile: 0.8037, maximum: 0.8951), the other values are lower for six clusters. The minimum value for five clusters is -0.1782, the first quartile 0.5238, the median 0.7267, and the mean 0.6348. In comparison to a classification into seven clusters, the median value for six clusters is higher (six clusters:

0.6904, seven clusters: 0.6876). The silhouette plot statistics for seven clusters are: Minimum value -0.2790, first quartile 0.4321, median 0.6876, mean 0.6018, third quartile 0.8228, maximum value 0.8990. The negative silhouette widths are to be expected, as in segment 1.



Figure 55: Segment 2, RGB colors (shown in CloudCompare, 2019)

Therefore, the data is classified into six clusters. Cluster 1 contains the most points, which represent the very steeply dipping set about parallel to this page in Figure 55. Due to the steep dip of this set, it is split apart in two clusters and also represented in cluster 3. This has been demonstrated above for set 1 in segment 1 (Figure 20, set 1 marked by orange circles). An oblique set is classified into cluster 2. In cluster 4, two sets are mixed: another oblique one, and a nearly vertical one with small surfaces. This cluster is reclustered into two clusters to separate the sets (average silhouette width: 0.65). Cluster 5 contains a set which is oriented vertically about 90° to the set in cluster 1, and cluster 6 contains another very noisy set.

Five sets with the orientation statistics given in Table 7 are identified in the six clusters. Set a is the set parallel to this page, consisting of the points of cluster 1 and 3. Set a contains the most points of all sets in segment 2. Set b, which appeared as the very noisy set in cluster 6, loses many points to the noise. Its planes might be bigger than the mapped planes, but this is concealed by vegetation. Set c+f was at first thought to be two extra sets (c and f), but appeared to belong together during the plane fitting procedure. This is supported by the steep dip, which causes the same splitting in two clusters due to the dip direction as in set a, and the overlapping of the c- and f-planes, which clearly belong to one surface according to

the RGB point cloud. The planes have been corrected and the orientation statistics have been calculated again. Set d comes from cluster 2. Set e is the set with the small, vertical surfaces in one cluster of the reclustered cluster 4.

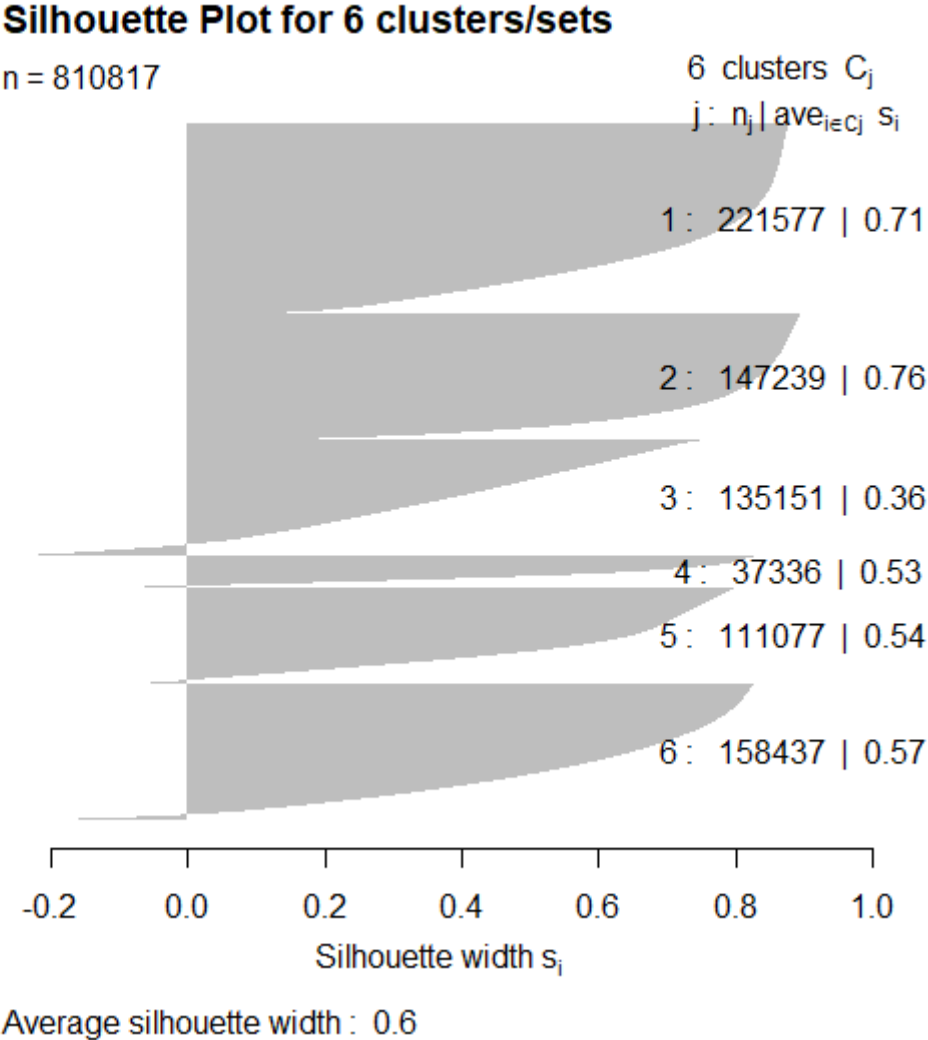


Figure 56: Silhouette plot for segment 2

Table 7: Orientation statistics for segment 2. The angles are given in degrees.

	number of values	mean dip dir. ("major axis")	mean dip ("major axis")	Fisher k	variability angle (95.4%)	confidence angle (95.4%)
set a	343361	230.3090	84.9710	12.7854	40.6090	0.0707
set b	152964	250.1180	48.5650	20.9725	31.4404	0.0813
set c	14435	143.2760	76.4750	29.2710	26.5164	0.2226
set d	147231	293.8000	33.1690	18.9773	33.0970	0.0874
set e	17374	317.8360	70.4620	27.7350	27.2545	0.2086
set f	107341	108.3480	84.7630	15.9328	36.2210	0.1123
set c+f	121776	112.3420	83.6380	12.7967	40.5902	0.1186

The points of each set are given in Figure 57 to Figure 61, extracted via the Facets Plugin (Dewez et al., 2016) and cleaned by SOR. Nevertheless, a certain amount of noise cannot be eliminated. Sets a and c+f show two dip direction colors, which is due to the steep dip. The fracture pattern in terms of the fitted planes is shown in Figure 62 to Figure 66. Set e's surfaces are too small for the plane fitting ($<1 \text{ m}^2$). Therefore, set e is not represented by any plane.

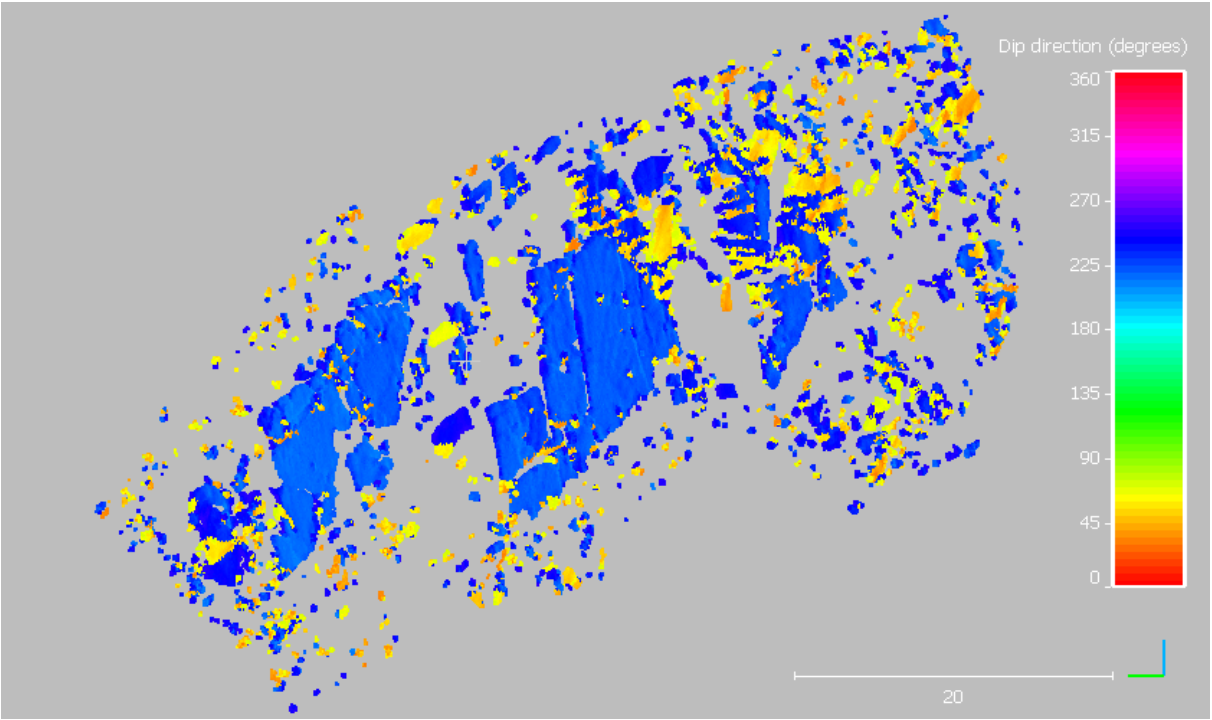


Figure 57: Points of set a. Software used: CloudCompare (2019).

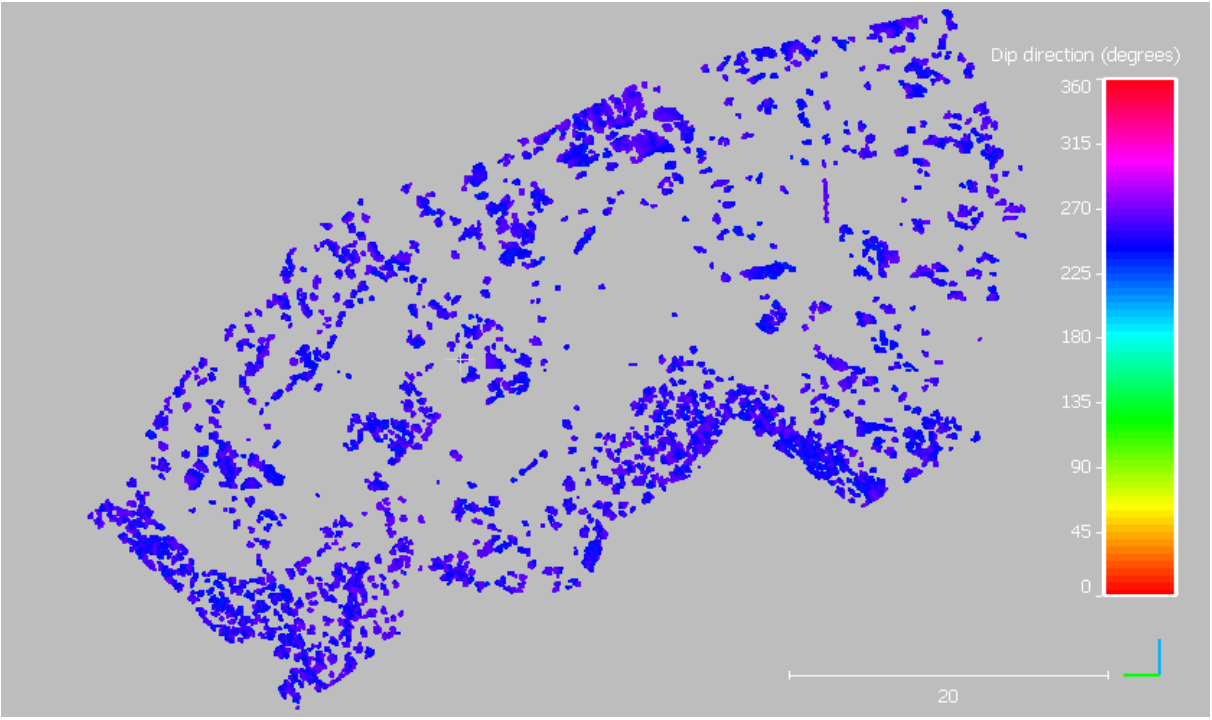


Figure 58: Points of set b. Software used: CloudCompare (2019).

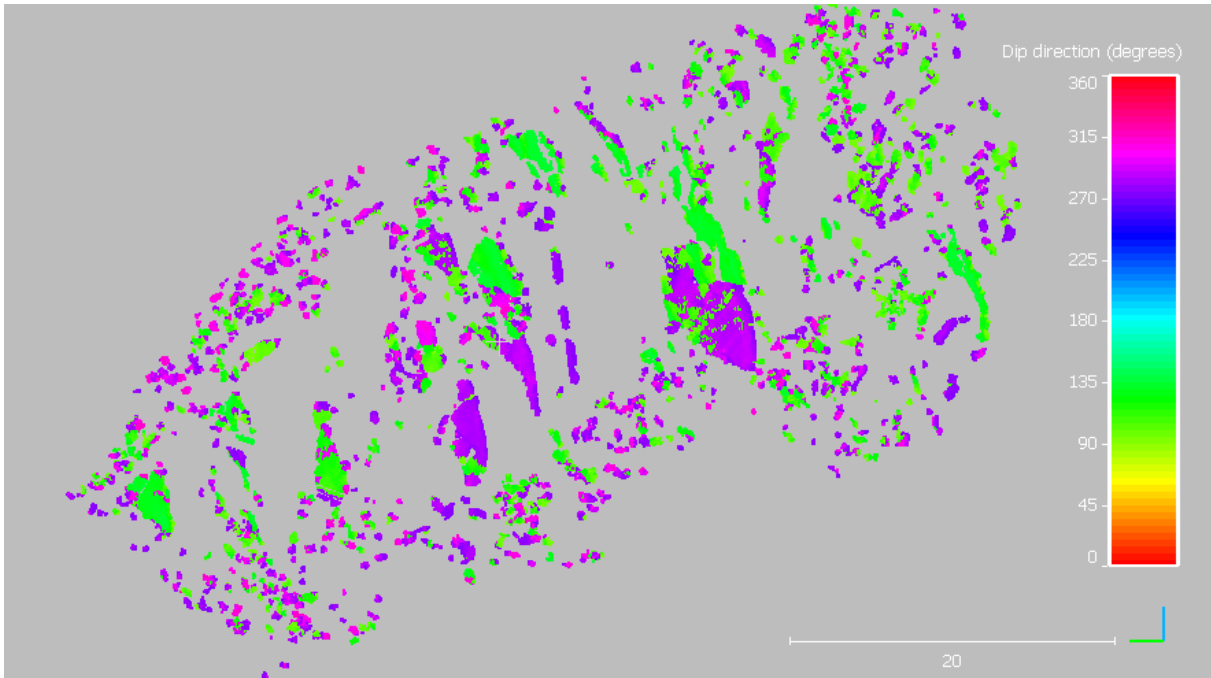


Figure 59: Points of set c+f. Software used: CloudCompare (2019).

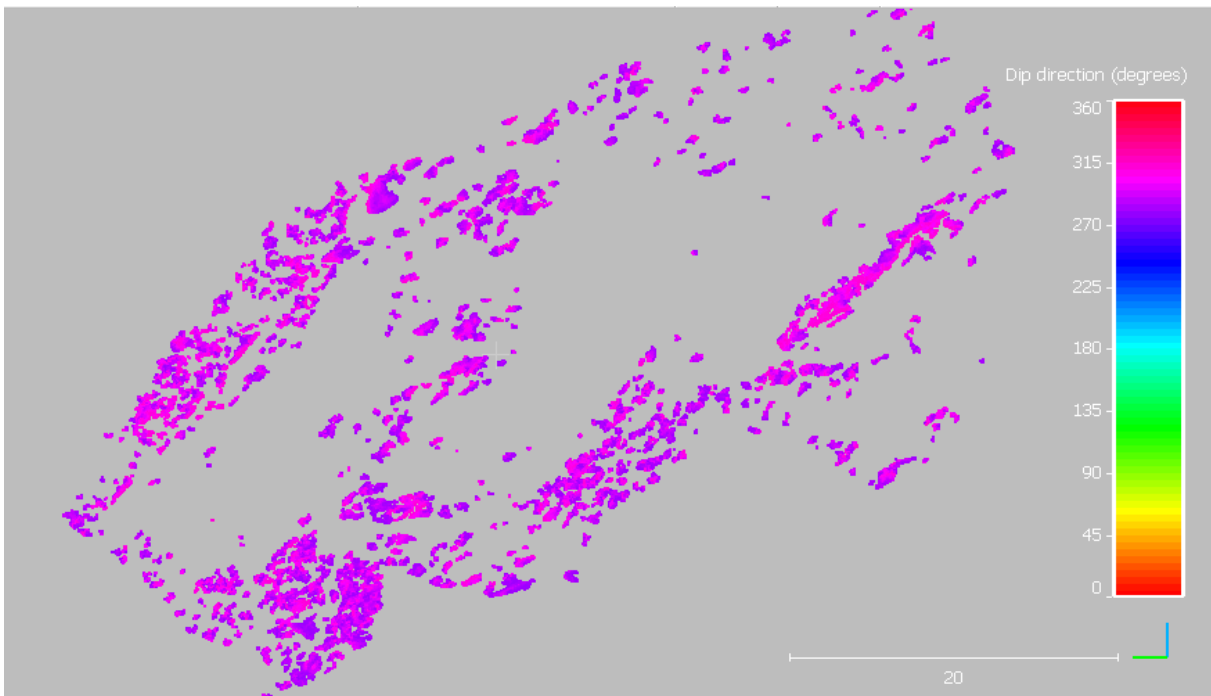


Figure 60: Points of set d. Software used: CloudCompare (2019).

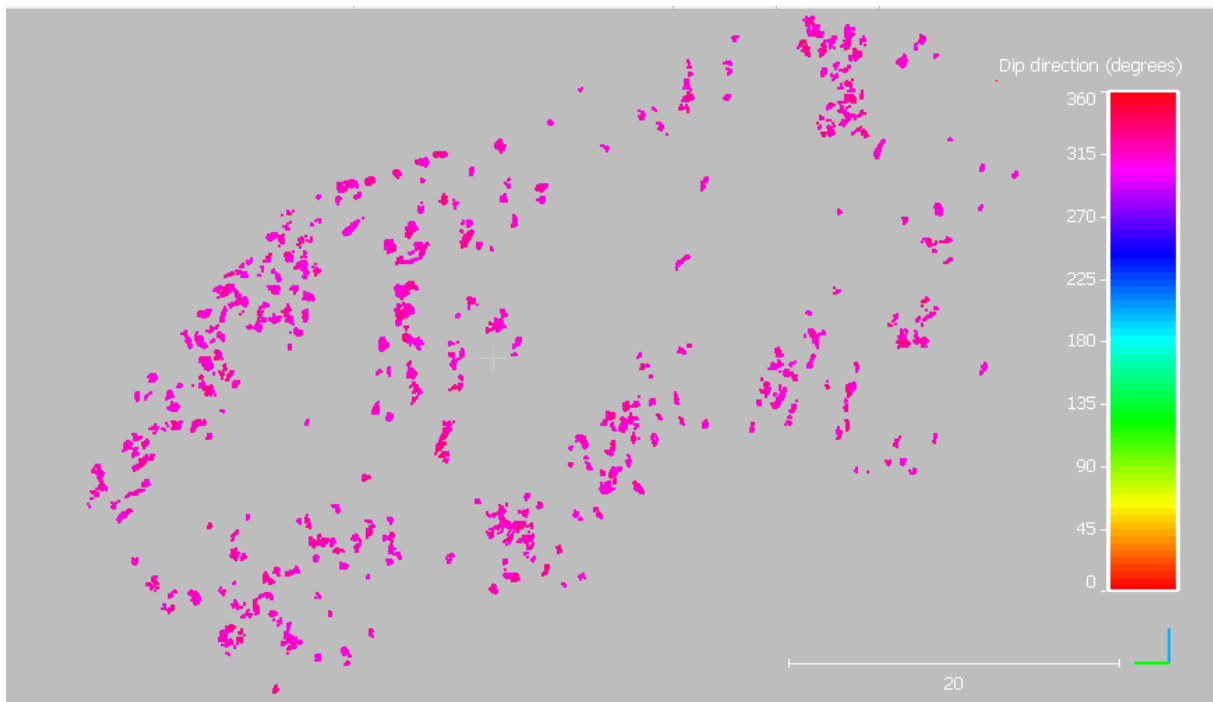


Figure 61: Points of set e. Software used: CloudCompare (2019).

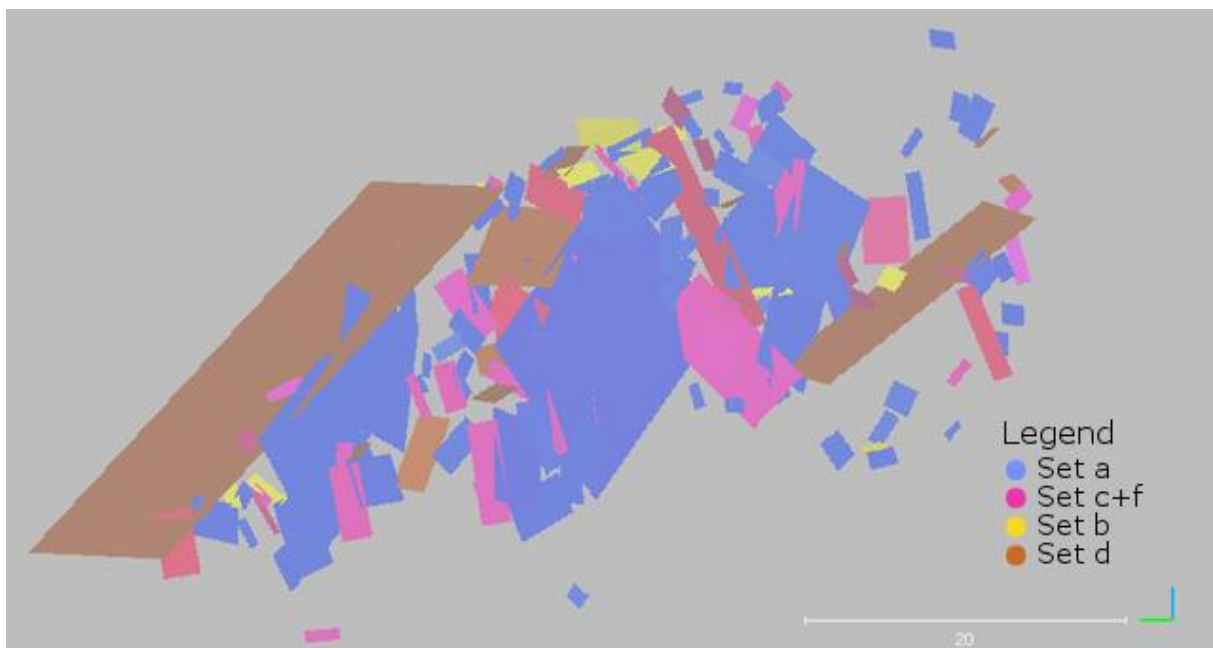


Figure 62: Fracture pattern in frontal view. Software used: CloudCompare (2019).

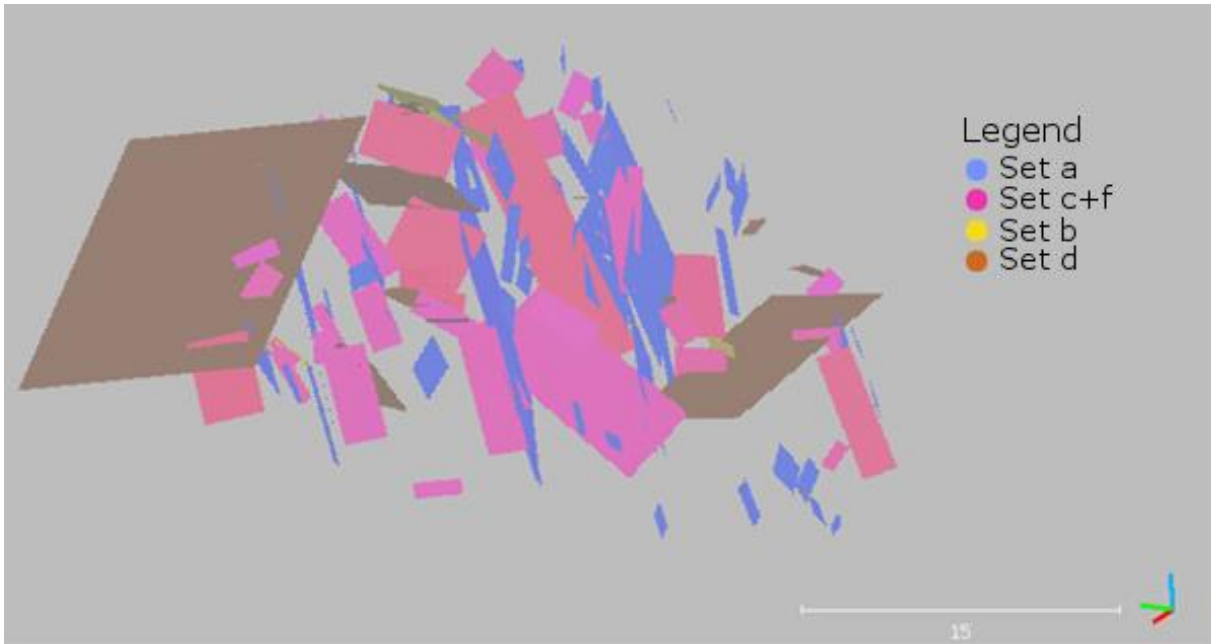


Figure 63: Fracture pattern in side view (left side from viewer's point). Software used: CloudCompare (2019).

As can be seen in Figure 64 and Figure 65, the planes fit well to the RGB point cloud. The plane elongation is fitted automatically to the segmented surfaces and does not necessarily correspond to the fracture set's elongation. However, for set d, for example, the plane elongation indicates the fracture form at least. Figure 66 provides a better view of sets b, c+f, and d. In some cases, set d is concealed by vegetation which makes it necessary to estimate the plane over a lot of noise. This has been done for the four biggest d-planes, for example.

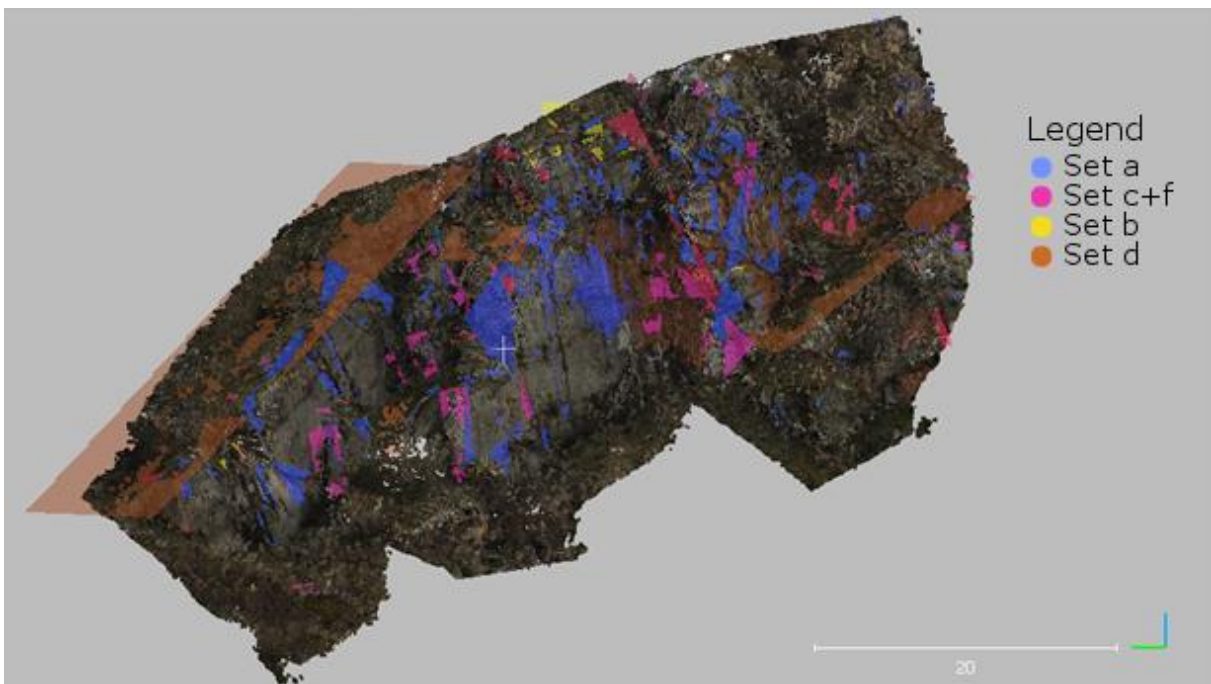


Figure 64: Fracture pattern over the RGB point cloud, frontal view. Software used: CloudCompare (2019).

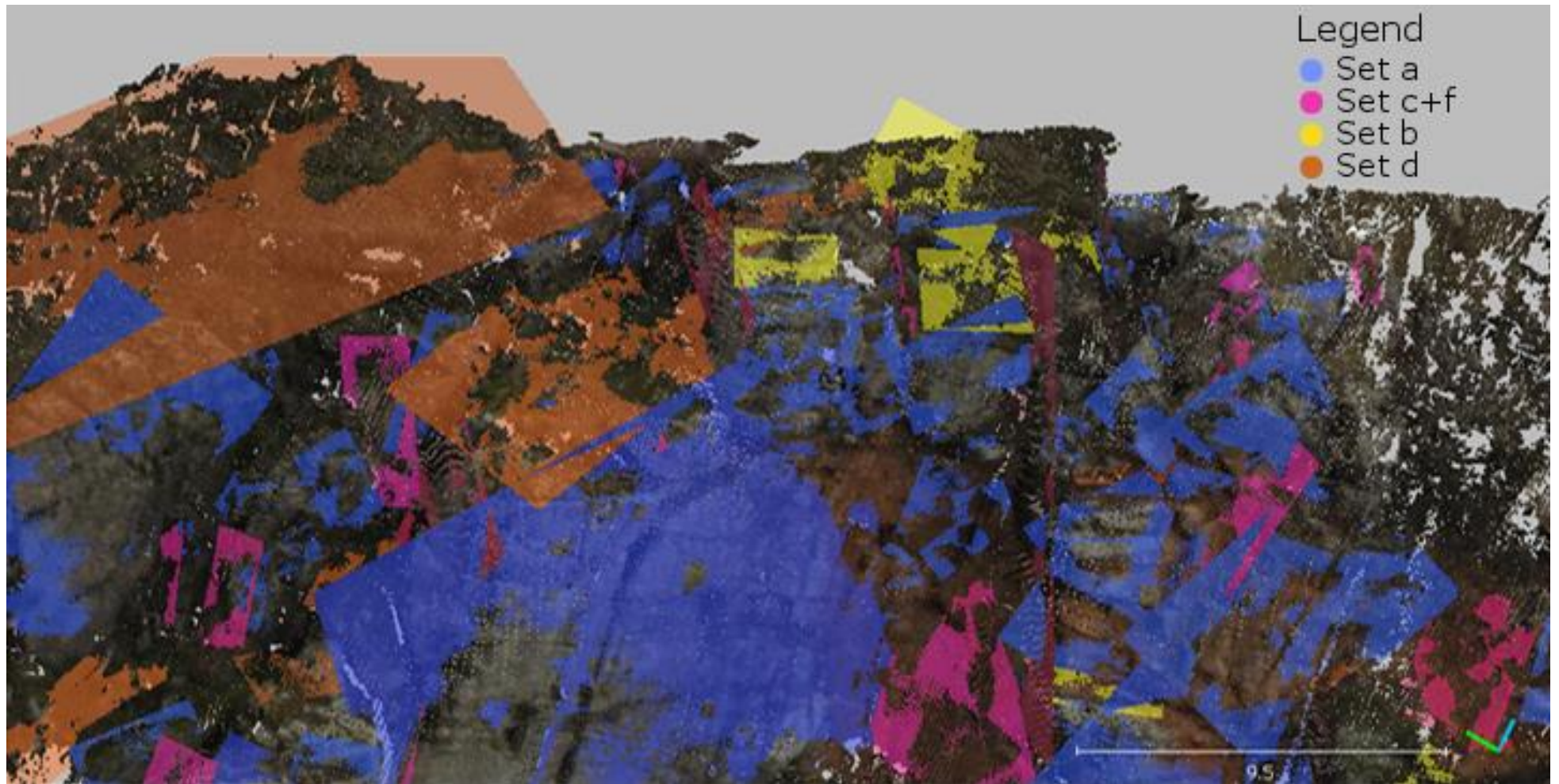


Figure 65: Fracture pattern in detail over the RGB point cloud. Software used: CloudCompare (2019).



Figure 66: Fracture pattern in frontal view, without set a. Software used: CloudCompare (2019).

The planes poles' are shown in Figure 67 in comparison to the orientation statistics plots from FracMan (Golder Associates Inc., 2019). The latter are also plotted for set e, of course. The stereograms show the same trends as already described above for segment 1: The plane poles' distribution is similar to the point cloud normals distribution, but narrower which is due to the filtering process with Facets (Dewez et al., 2016). As the result's plot of the planes (right) corresponds to the initial plot of the point cloud normals (left), the calculation (middle) appears to be a good base for the plane fitting.

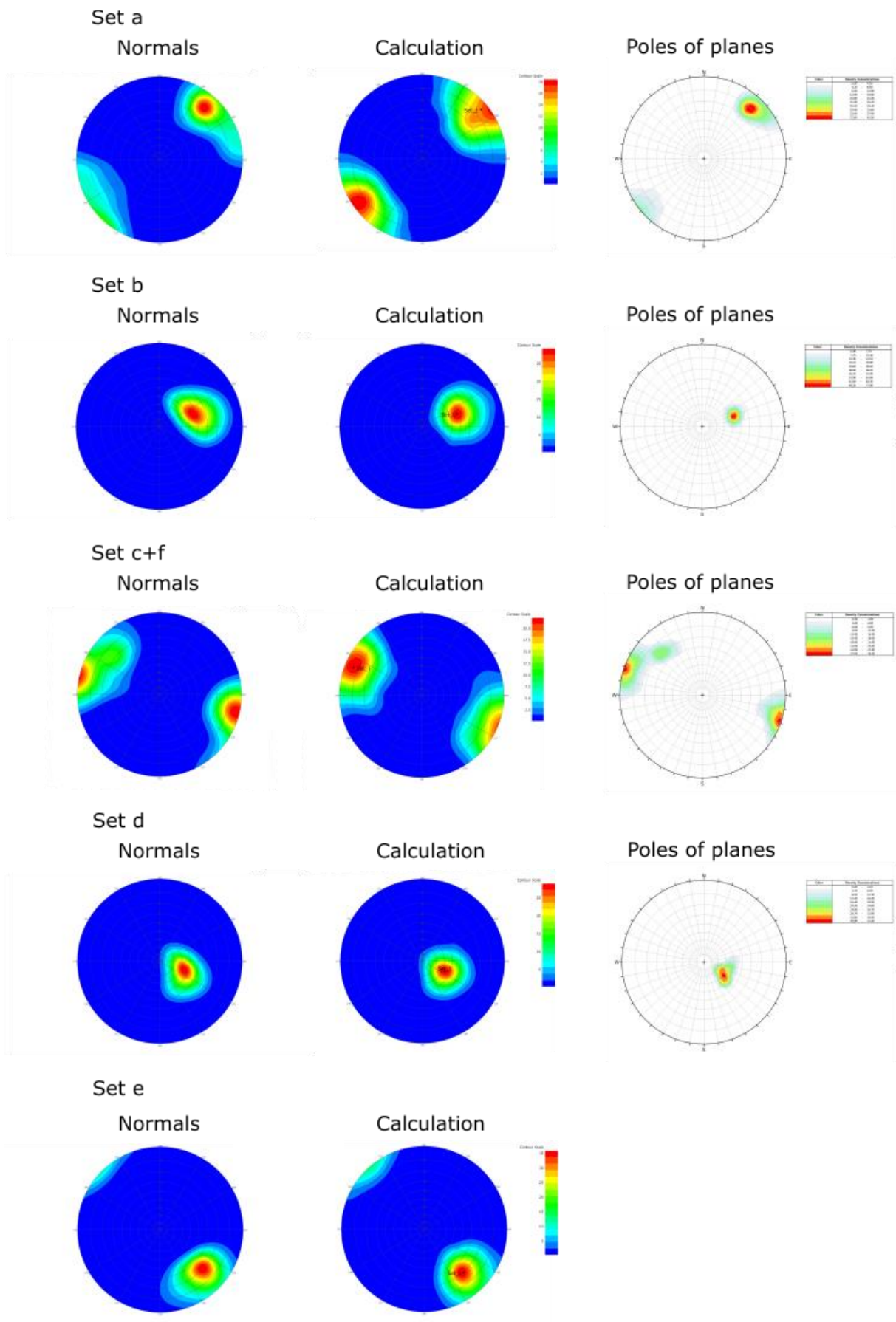


Figure 67: Stereograms for segment 2's sets of the point cloud (left, middle; FracMan (Golder Associates Inc., 2018)) and the plane data (right; Dips (Rocscience Inc., 2018))

At first sight, set a has very big planes. Set d also has big planes, but the four biggest ones are estimated. Sets b and c+f seem to have medium to small plane sizes. Table 8 gives the mean, median, maximum, and minimum of the plane sizes, along with data about the planes <1 m². These should not have been mapped actually, but the true plane size is difficult to estimate in some cases. In doubt whether the concerned surface is <1 m², the planes have been mapped. However, in this segment, very few planes are <1 m². Therefore, the mean and median do not vary much in the calculations with and without the planes <1 m². Sets b and d do not include any plane <1 m². The calculated plane sizes show that the maximum plane size is reached in set d, but this is the estimated plane concealed by vegetation. Set d's four biggest planes are estimated, all smaller ones are not estimated. The biggest non-estimated d-plane has 7.4772 m², which is by far smaller than the maximum plane size of set a. Therefore, set a has the highest mean and median of the non-estimated planes, which is of course exceeded by set d when the estimated planes are included. The median value is always smaller than the mean value which is due to the relatively higher amount of smaller planes than bigger planes. This trend is also shown in plane size histograms and even better by the added density lines (Figure 68 to Figure 71). In the histograms, high plane sizes as in set a and d are shown as logarithmic to the base 10. As already mentioned above, set e has too small surfaces for plane fitting (<1 m²). However, set e is identifiable in the outcrop and also detected by the clustering.

Table 8: Planes sizes in segment 2

	Set a	Set b	Set c+f	Set d
Mean	9.3244	3.8506	6.0248	52.9874
Mean (>1m²)	9.6204	3.8506	6.1433	52.9874
Median	3.1149	2.7211	2.5410	5.4573
Median (>1m²)	3.1821	2.7211	2.6019	5.4573
Maximum	225.9891	11.7653	42.9598	440.2808
Minimum	0.7103	1.1637	0.9301	1.0042
Number of planes	89	11	44	12
Number of planes <1m², total	3	0	1	0
Number of planes <1m², %	3.3708	0	2.2727	0

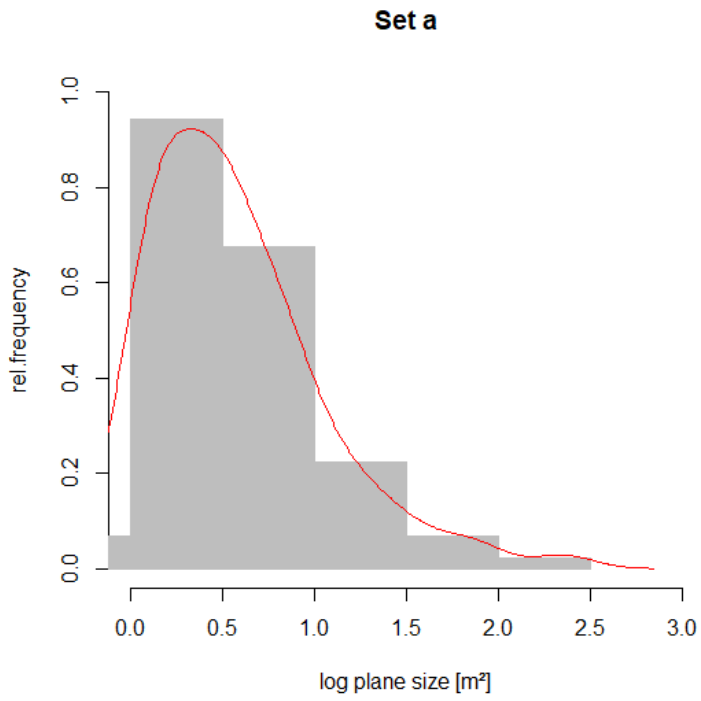


Figure 68: Plane sizes of set a, density line shown in red

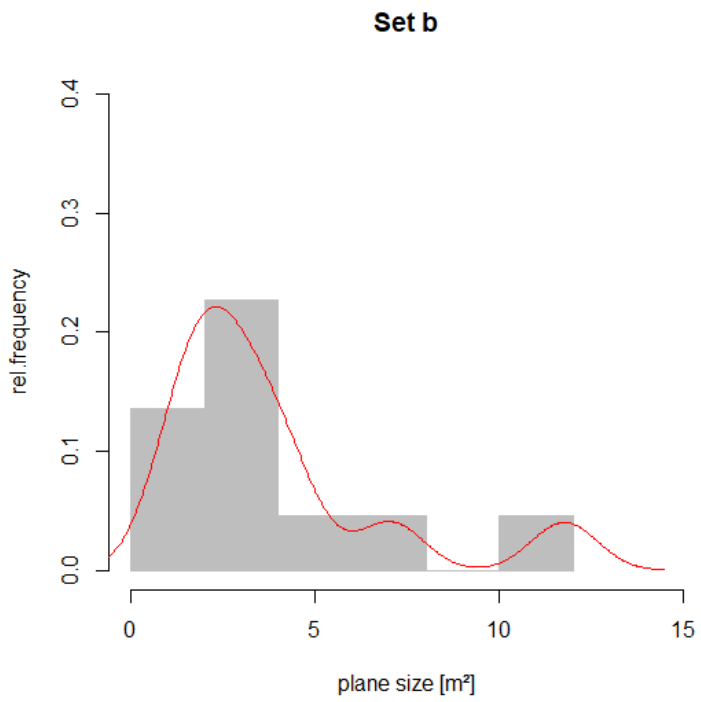


Figure 69: Plane sizes of set b, density line shown in red

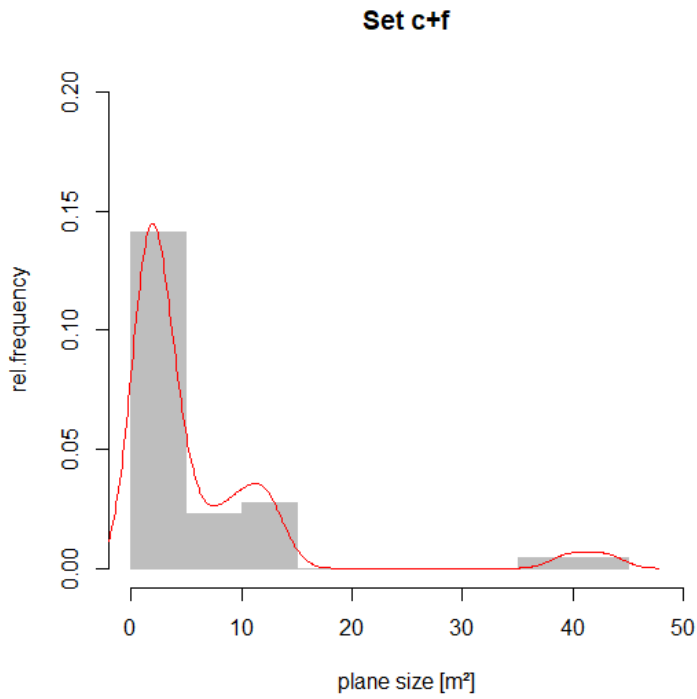


Figure 70: Plane sizes of set c+f, density line shown in red

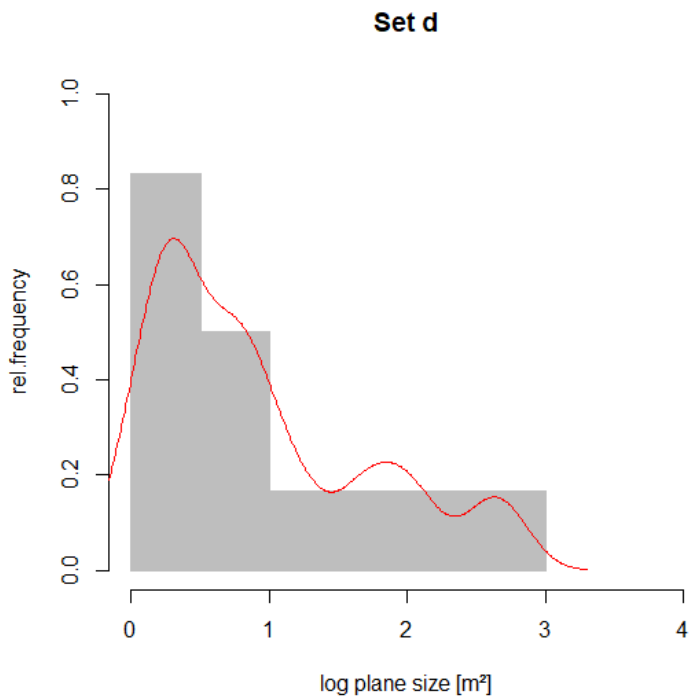


Figure 71: Plane sizes of set d, density line shown in red. The four biggest planes are estimated.

The termination describes the spatial relation of the sets and represents the connections in the fracture pattern. For each set, the termination in which sets and in how many sets as well as the problems faced during the plane fitting procedure are plotted (Figure 72 to Figure 83). Further details are given in the appendix. In this segment, sets a and b are classified as sheeting joint sets due to the orientation, appearance in the point cloud, plane size, and waviness. This will be further explained and interpreted in chapters 6.1 interpretation – joint sets, and 7.2 discussion – results.

As can be seen in Figure 72, set a mostly terminates in itself or in set c+f, but also in set d and b. Including the neighborhood raises the overall number of terminations, but the relations in which sets set a terminates stay the same. The termination in itself means that set a has a high waviness which causes the planes to be mapped separately although they might form one huge, wavy plane. Concerning the number of connected sets, isolated planes (Figure 73) do not exist when the neighborhood is taken into account. Set a connects with one to four sets, where the fourth set is set a itself. Set e is not investigated as it does not have any fitted planes. Most of set a planes terminate in two sets. The most common plane fitting problem is the roundness of the rock, followed by holes in the point cloud and noise or vegetation (Figure 74).

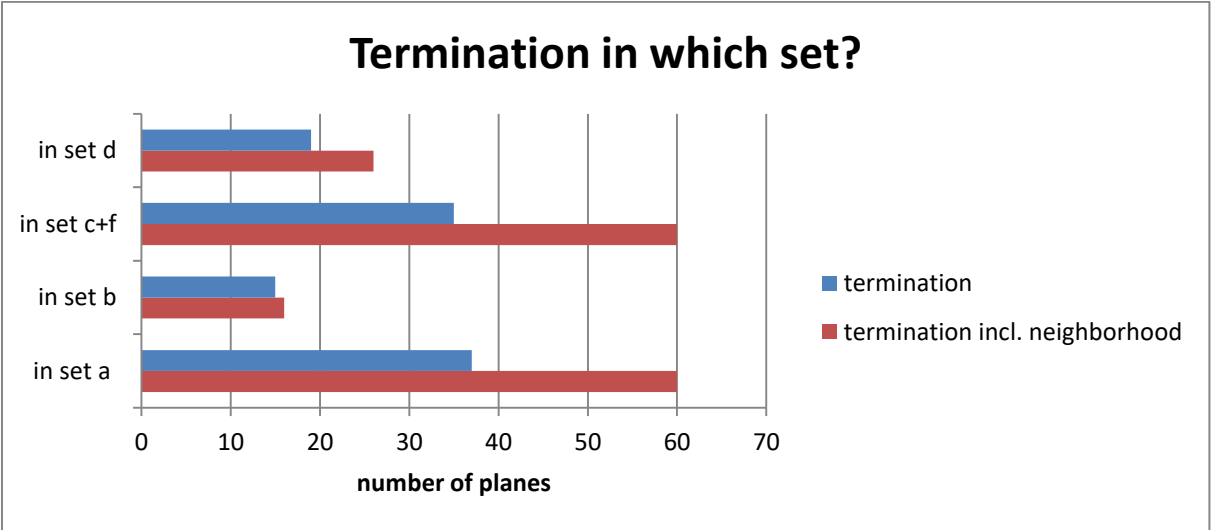


Figure 72: Termination of set a

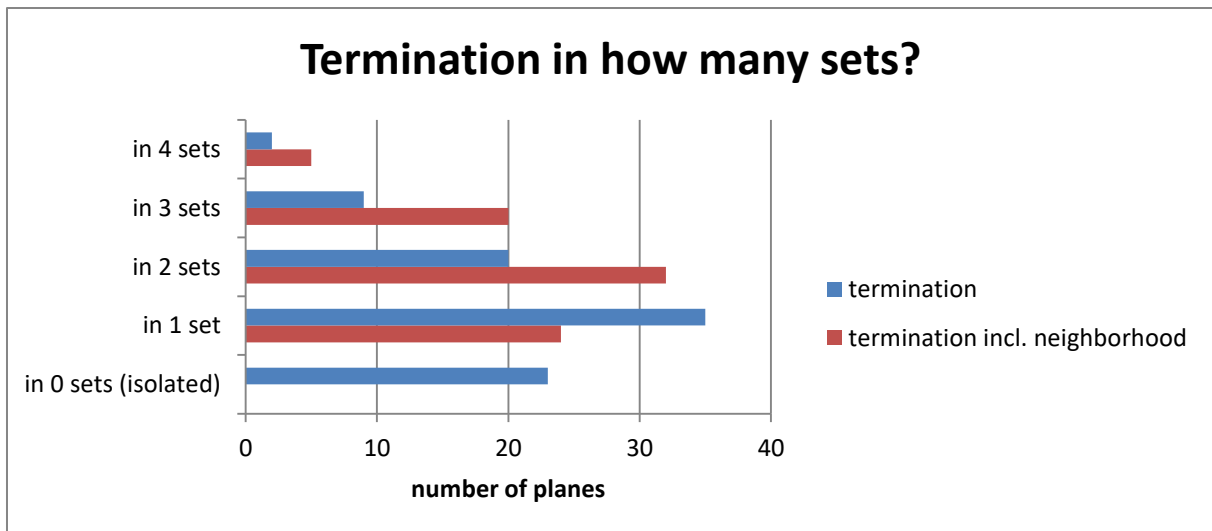


Figure 73: Termination of set a

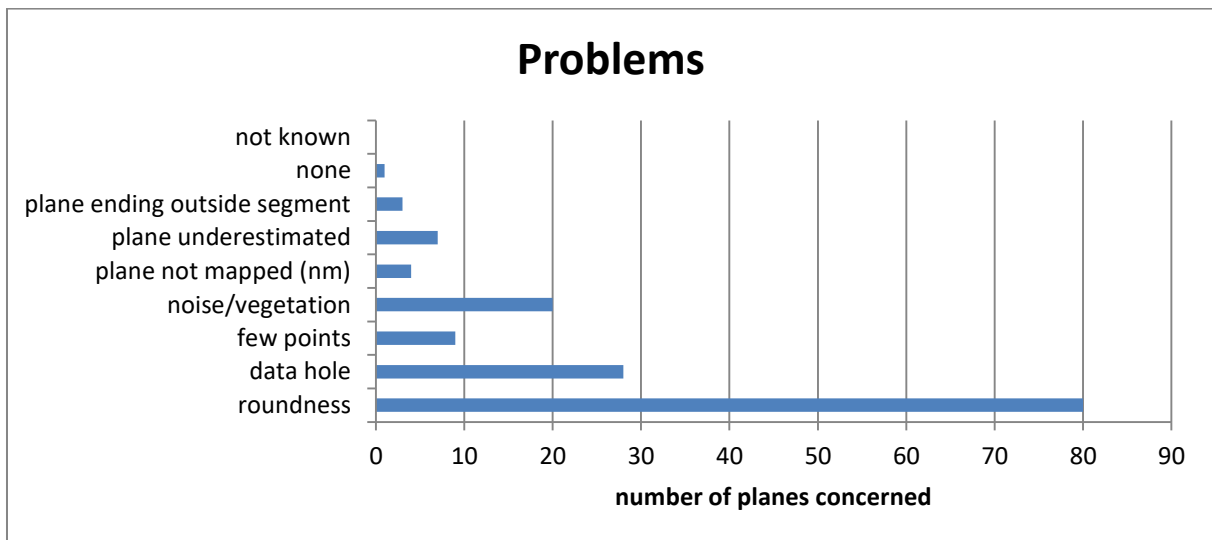


Figure 74: Problems for planes fitting in set a

Set b never terminates in itself, but in all other sets (Figure 75). This trend does not even change when the neighborhood is taken into account, although the absolute number of terminations increases. Most of set b planes terminate in set a planes. As set b never terminates in itself, it cannot terminate in four sets (Figure 76). However, it connects with up to three sets if the neighborhood is included. Else, it shows isolated planes or connects with one or two other sets. Similar to set a, the most common plane fitting problems are the roundness and data holes (Figure 77).

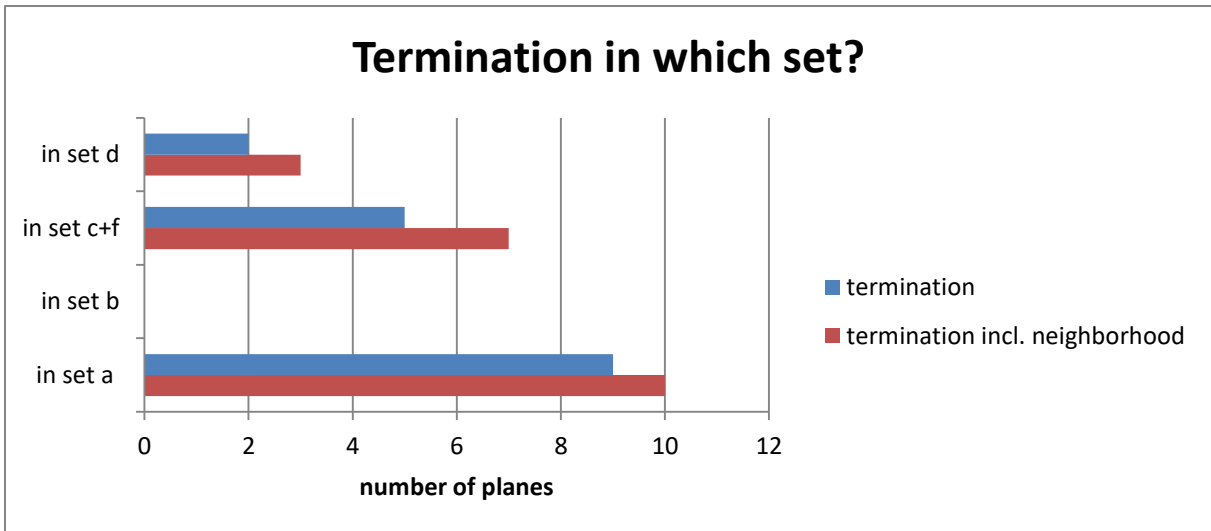


Figure 75: Termination of set b

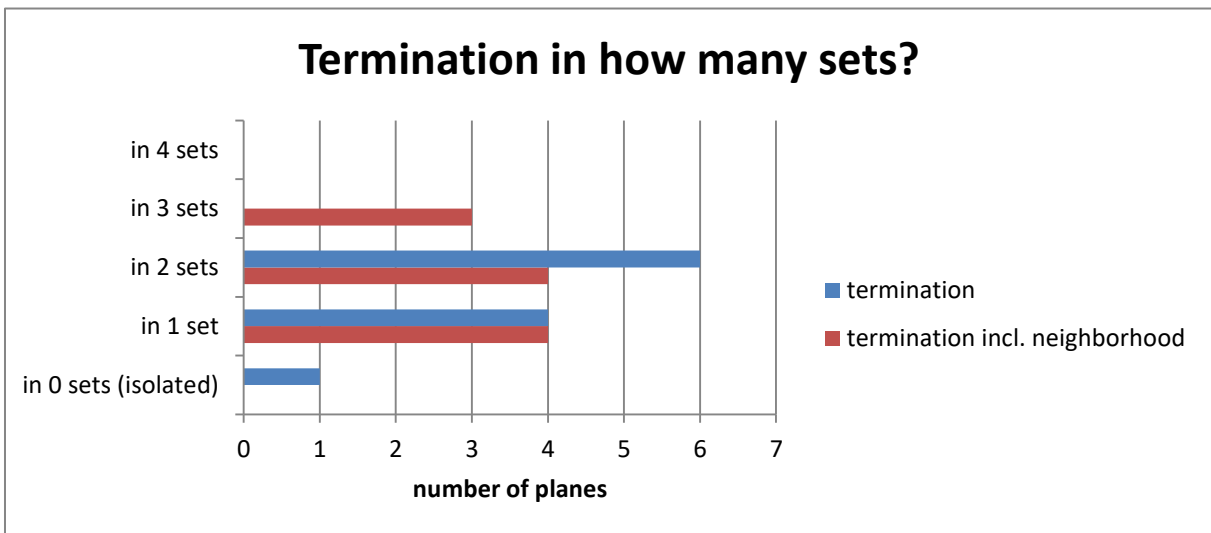


Figure 76: Termination of set b

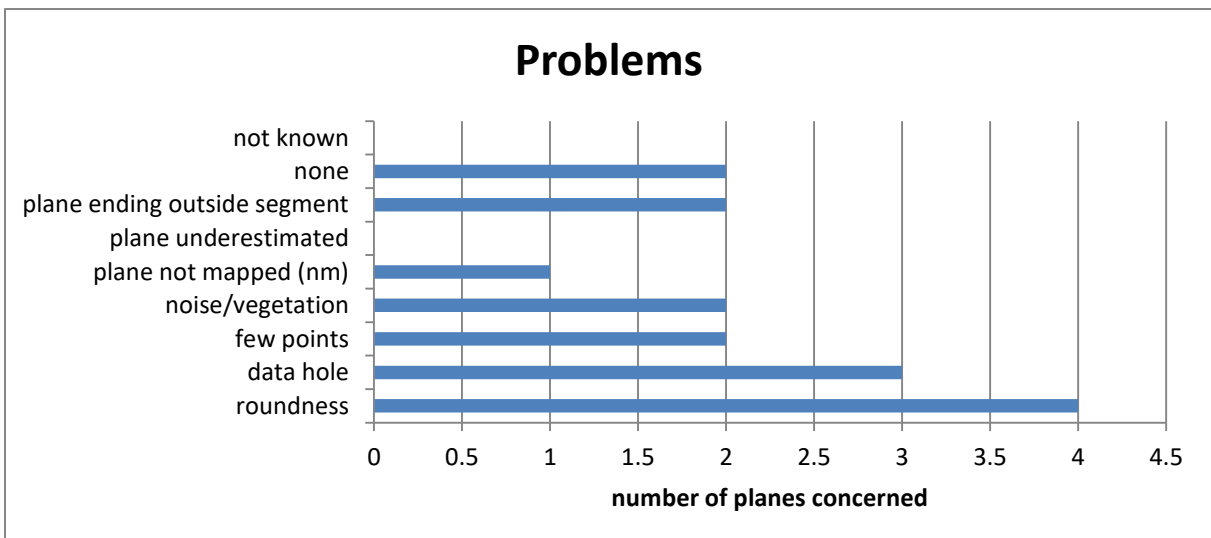


Figure 77: Problems for plane fitting in set b

Set c+f mostly terminates in set a, but also in set d, itself, and in set b (Figure 78). The consideration of the neighborhood does not change the relative abundance of terminations in the sets, but the absolute number of terminations. As for sets a and b, there are some isolated planes at first sight (Figure 79) which turn out to actually connect to other planes when the neighborhood is considered. Then, most of the set c+f planes connect with two sets. The dominating problem is the roundness, followed by data holes and noise or vegetation (Figure 80).

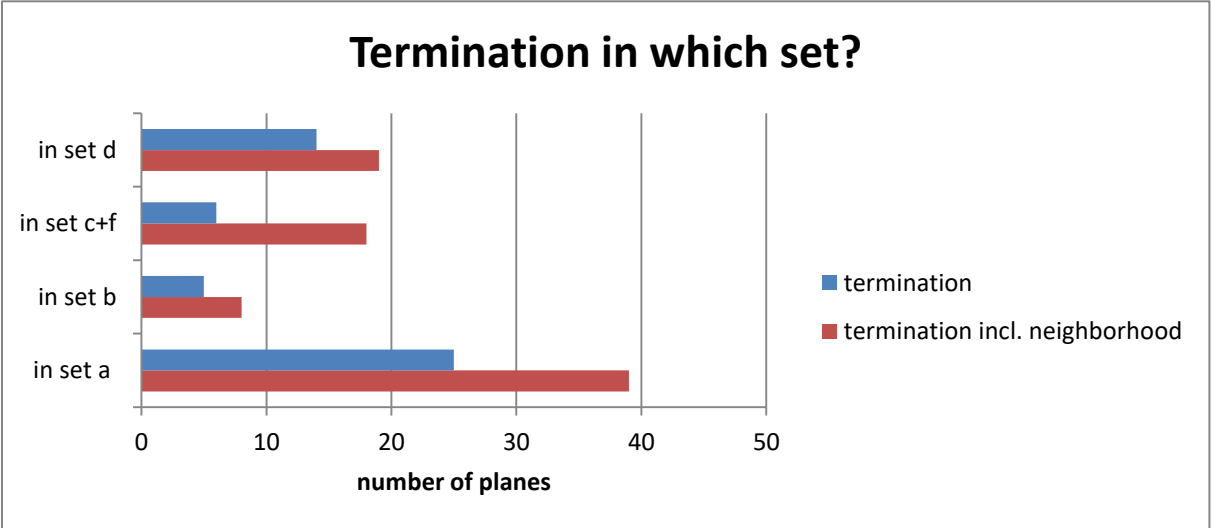


Figure 78: Termination of set c+f

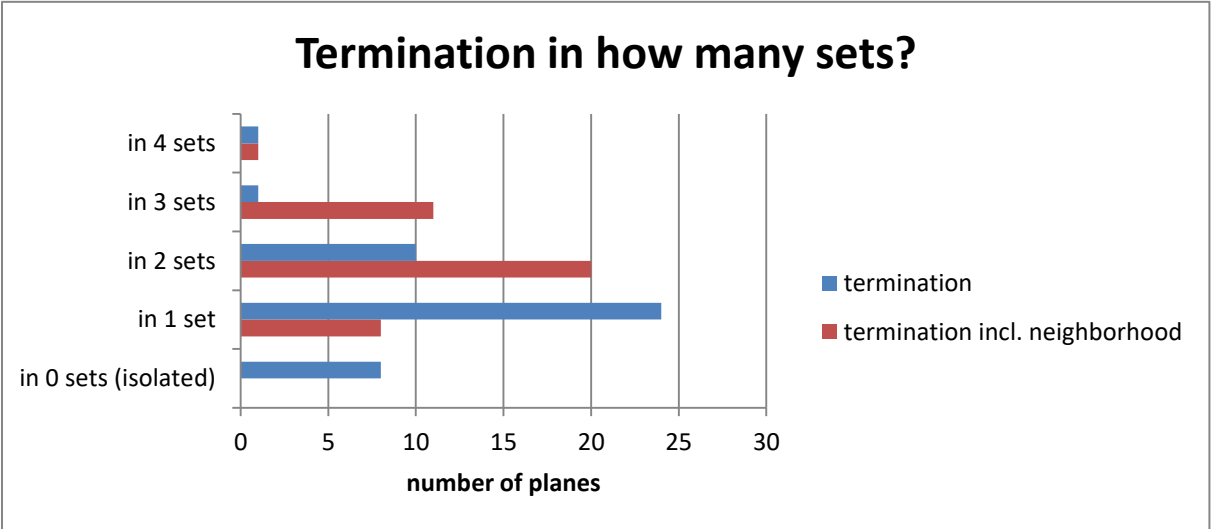


Figure 79: Termination of set c+f

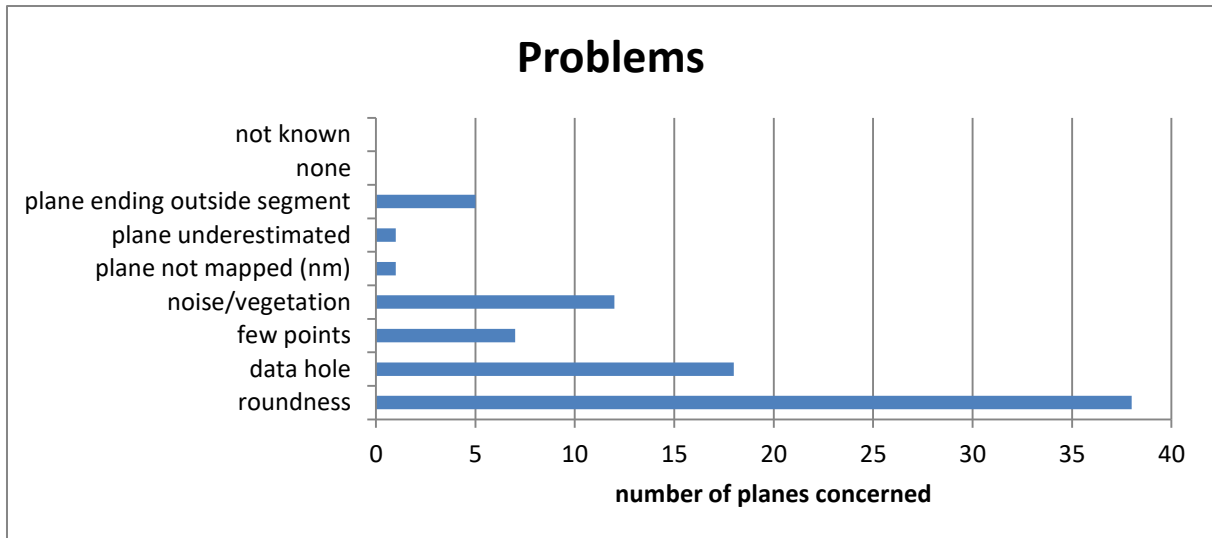


Figure 80: Problems for plane fitting in set c+f

Set d's termination is shown in Figure 81 and Figure 82. Set d terminates in set c+f or in set a. In two cases, set d terminates in set b. The consideration of the neighborhood does not cause major changes. Set d never terminates in itself and therefore it never connects with four sets. As in the other sets in this segment, isolated planes actually do connect to other planes. Set d planes connect with up to three sets, while the majority of the planes terminate in two sets. Roundness and noise or vegetation concern the most planes and cause the difference in the neighborhood considerations (Figure 83). The estimation of the four biggest planes is also shown as a problem in the plot.

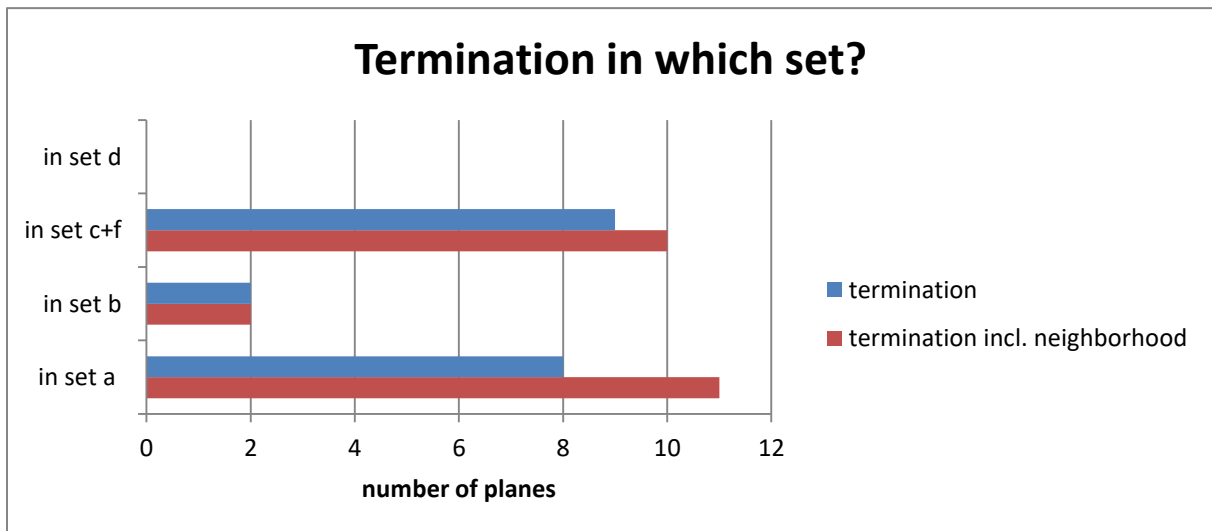


Figure 81: Termination of set d

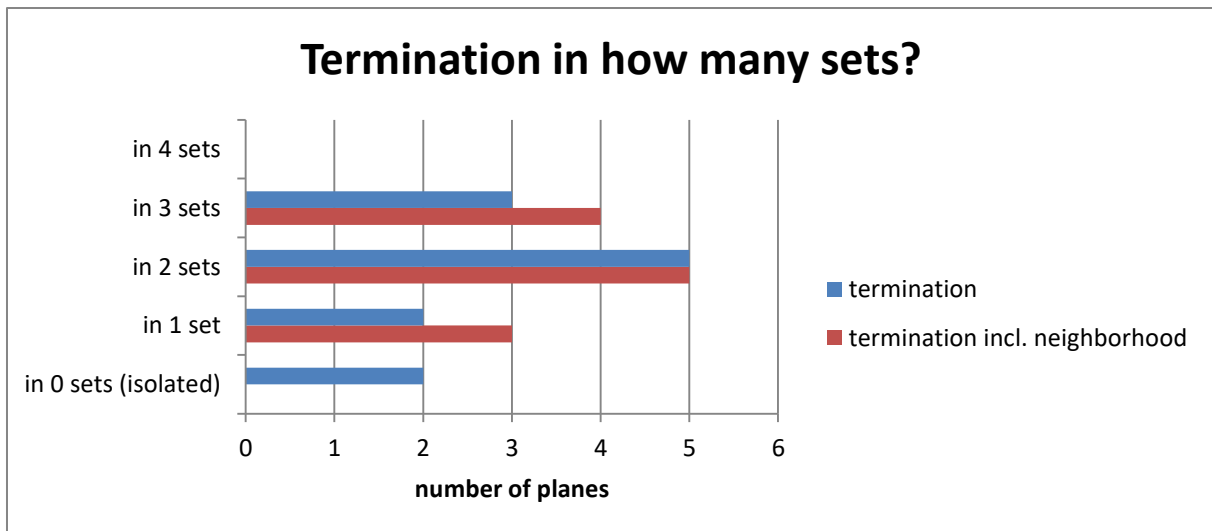


Figure 82: Termination of set d

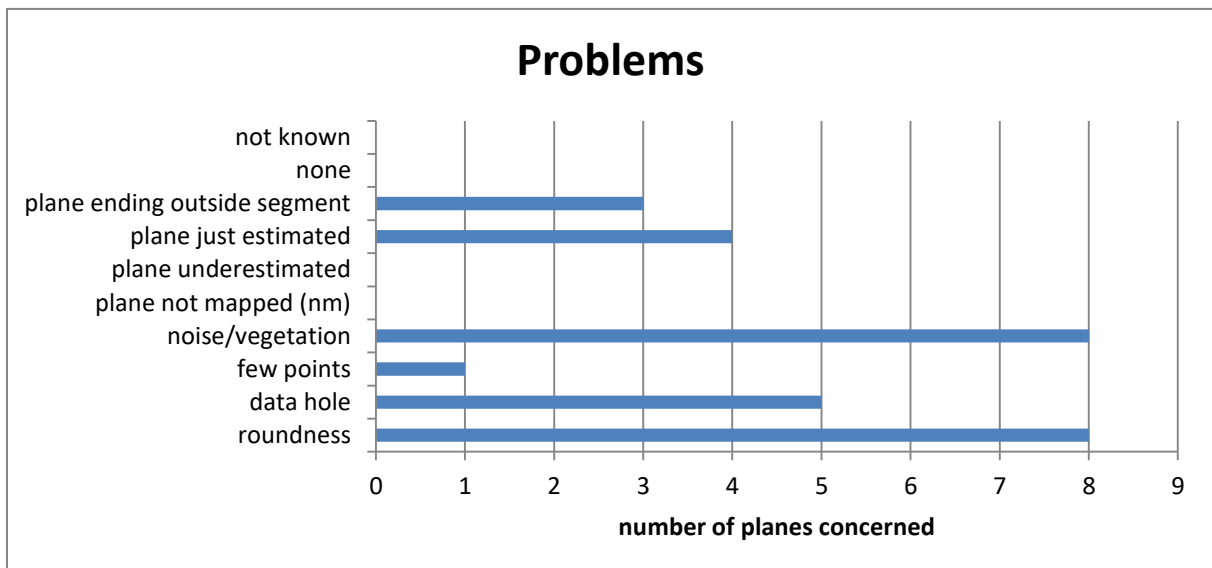


Figure 83: Problems for plane fitting in set d

5.2.3 Sets in segment 3 (BI-part 1)

Segment 3 is shown in Figure 84. At first sight, a big problem of this dataset is already revealed: There are many data holes, although the area has been scanned with a higher resolution than its surroundings. The difference in resolution can be seen at the borders of the segment where the point density abruptly decreases. The data holes seem to have been caused by shadowing of vegetation or of the rock mass itself. The line of sight seems to have been in some distance of the segment at the left as the data holes are mostly on the right “behind” edges. However, the rock mass structure is identifiable.

As segments 1 and 2, segment 3 is classified into six clusters. The silhouette plot is shown in Figure 85. The average silhouette width is 0.62. A classification into 5 clusters produces a higher average silhouette width (0.64), but slightly worse set differentiation results. For six clusters, the minimum individual silhouette width is -0.1723, the maximum is 0.8956. The first

quartile is 0.4713, the median 0.7113, the mean 0.6225, and the third quartile 0.8205. For five clusters, the minimum is -0.2508, the maximum is 0.8740. The first quartile is 0.5306, the median 0.7409, the mean 0.6413, and the third quartile 0.8136. Therefore, the first quartile, the median and the mean have higher values for five clusters. The third quartile, the maximum and the minimum individual silhouette widths are higher for six clusters.

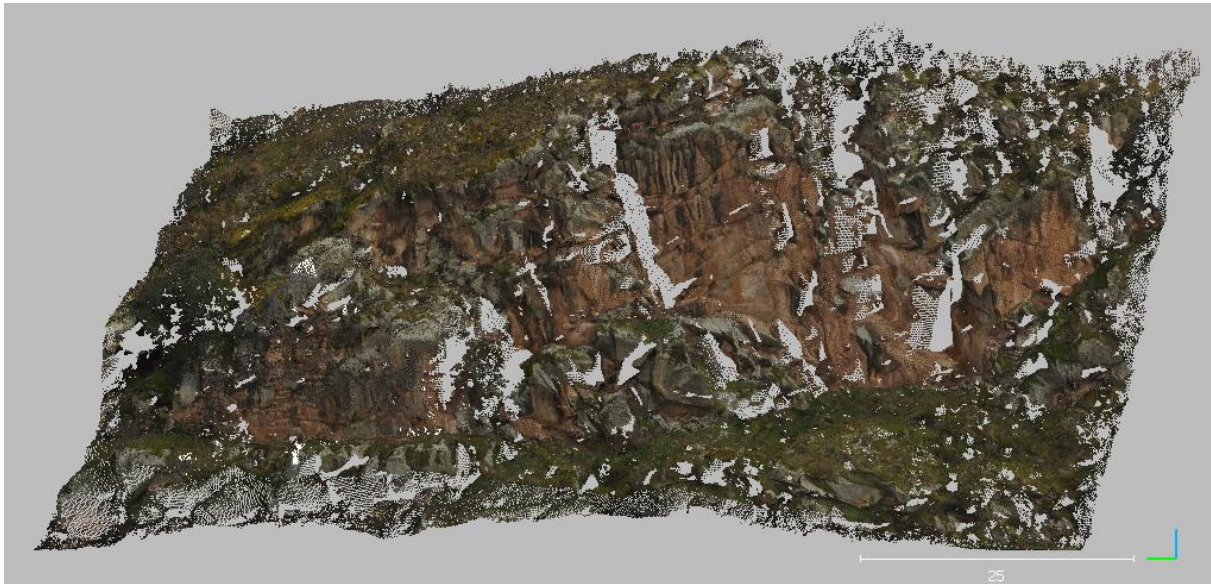
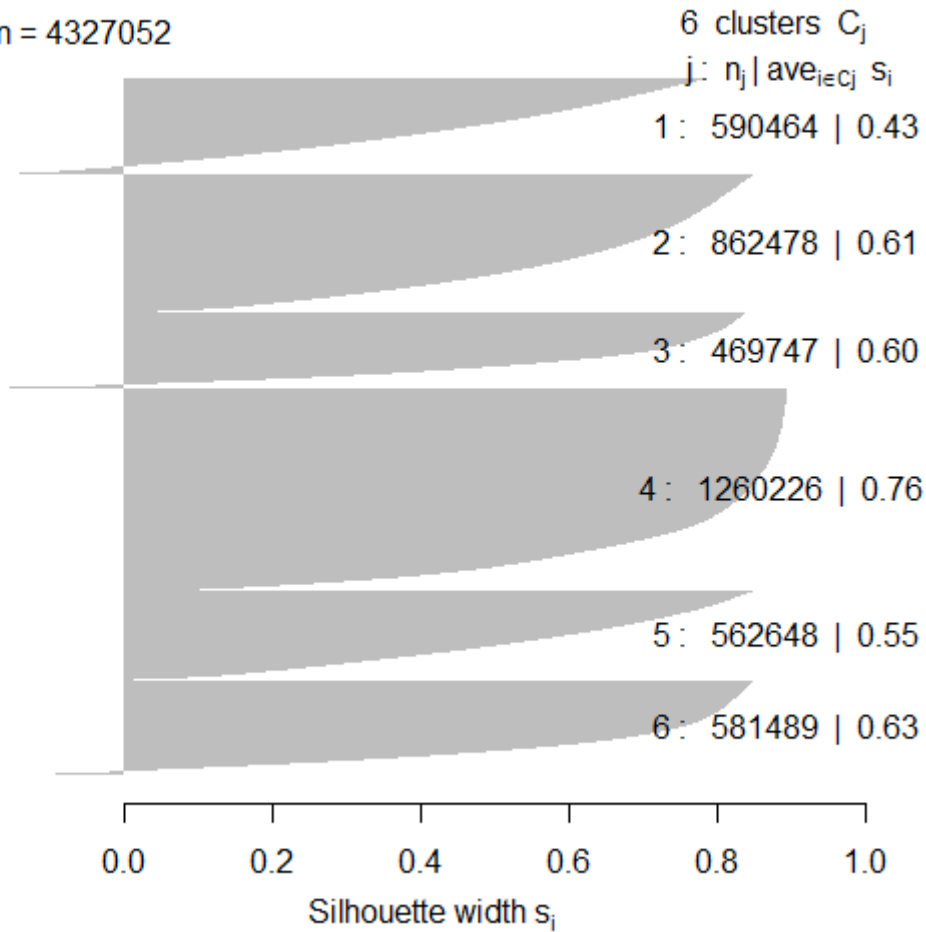


Figure 84: Segment 3, RGB colors (shown in CloudCompare, 2019)

Cluster 1 of the six clusters contains parts of a slightly oblique set. The rest of this set is classified to cluster 5. These two clusters have to be merged manually. However, a classification into five clusters by the R (R Core Team, 2018) clustering algorithm would neither have classified this set into one cluster. The normals classified into cluster 2 also belong to this set, but the rock mass' roundness caused the splitting into another cluster. This part of the set has been treated separately in the orientation statistics at first because the togetherness of all three clusters has just been detected by the help of the planes (see below). Cluster 3 and cluster 6 contain two other oblique sets. The most prominent set is a steeply dipping set represented by cluster 4.

Silhouette Plot for 6 clusters/sets

$n = 4327052$



Average silhouette width : 0.62

Figure 85: Silhouette plot of segment 3 for six clusters

Therefore, four sets can be identified – although, as mentioned above, one set was initially split apart and the rock mass appeared to feature five sets: A, B, C, D, and E. Set A has not been cleaned by SOR as one surface would have been lost. By evaluating the fitted planes, sets C and D appeared to belong together. The orientation statistics are shown in Table 9. The statistical parameters for the sets C and D together have been calculated subsequently, but for plane fitting, the individual parameters of the so-called sets C and D have been used. Set C+D consists of even more points than the steeply dipping set E. Sets A and B are relatively smaller concerning the number of values i.e. normals. The variability angle is higher for set C+D than for the two parts of this set, of course. 44.8933° is a very high variability angle which is caused by the rock mass' roundness. Fisher's concentration parameter k is also lowest for set C+D. However, due to the very high number of values, the confidence angle is in the middle of the value range in comparison to the other sets. The k parameter is higher and the variability angle is lower for sets A, B, and E.

Table 9: Orientation statistics for segment 3. The angles are given in degrees.

set	number of values	mean dip direction ("major axis")	mean dip ("major axis")	Fisher k	variability angle (95.4%)	confidence angle (95.4%)
set A	451121	149.0030	78.8940	17.4851	34.5228	0.0521
set B	563414	257.4160	56.0670	16.7730	35.2716	0.0477
set C	862478	293.0800	25.8330	30.9843	25.7599	0.0280
set D	1105773	322.7130	50.9930	11.7922	42.3634	0.0412
set E	1260207	102.7330	80.8470	23.4832	29.6712	0.0267
set C+D	1968251	313.4540	38.8260	10.5602	44.8933	0.0328

The points of sets A, B, C+D, and E (Figure 86 to Figure 89) are extracted via the Facets Plugin (Dewez et al., 2016) and cleaned by SOR. As already mentioned above, no SOR has been applied on set A. The plane fitting result is shown in Figure 90 to Figure 94. As vegetation conceals the true rock surface, six of the 138 planes of set C+D are estimations of the set plane. Among them are the two biggest planes of set C+D.

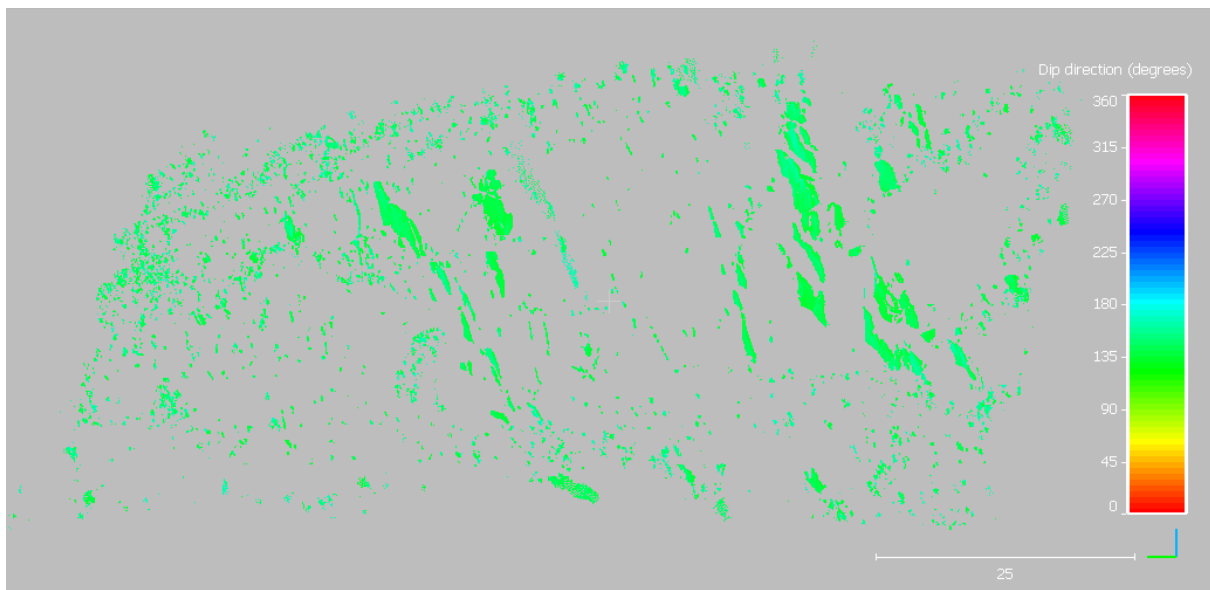


Figure 86: Points of set A. Software used: CloudCompare (2019).

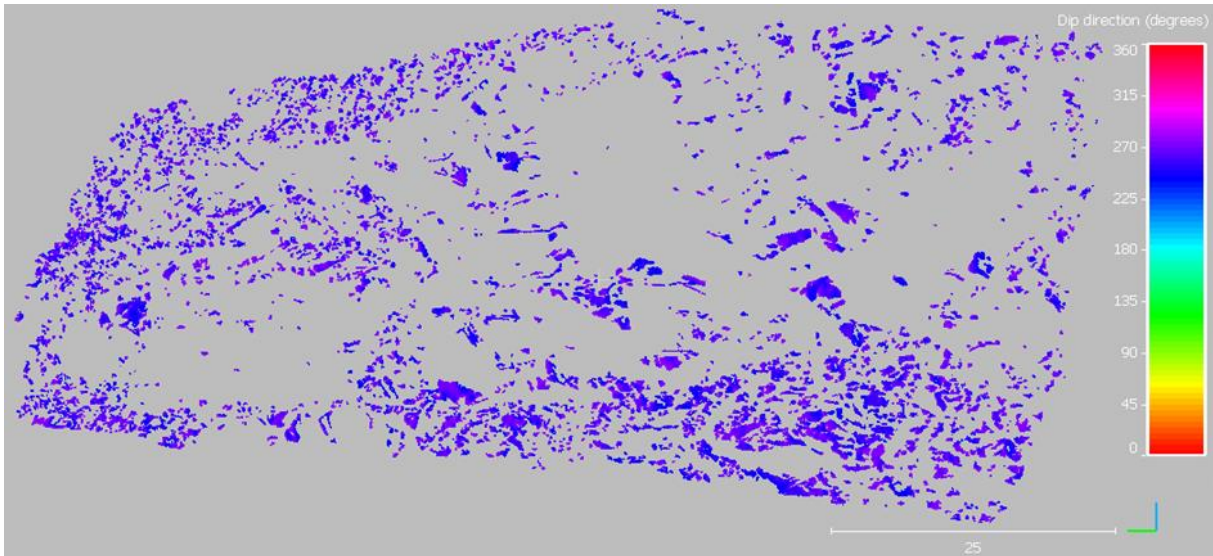


Figure 87: Points of set B. Software used: CloudCompare (2019).

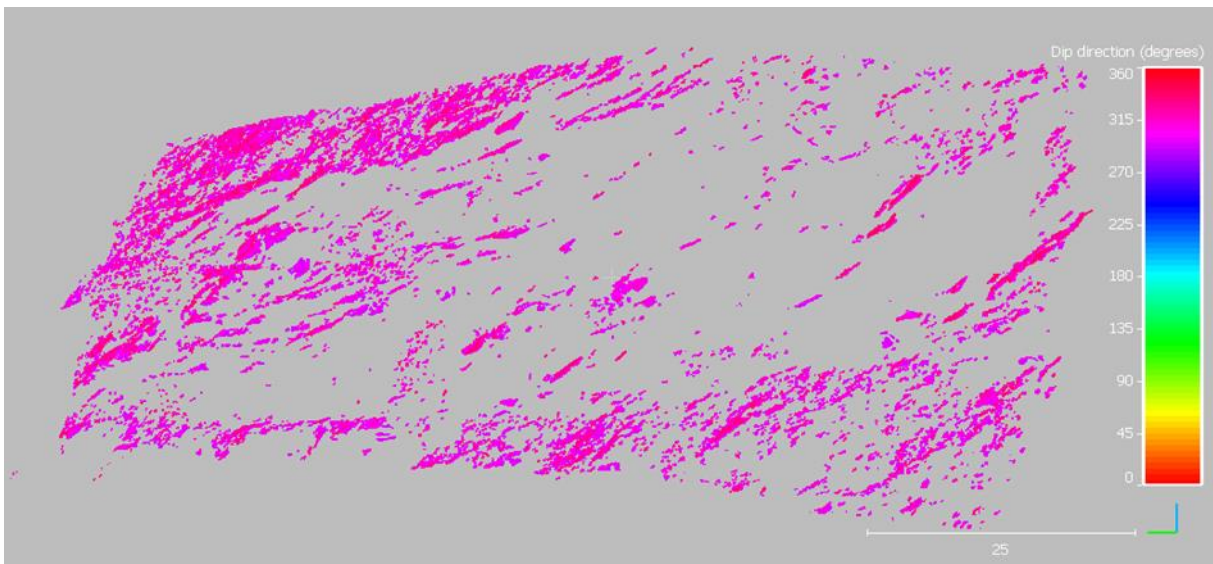


Figure 88: Points of set C+D. Software used: CloudCompare (2019).

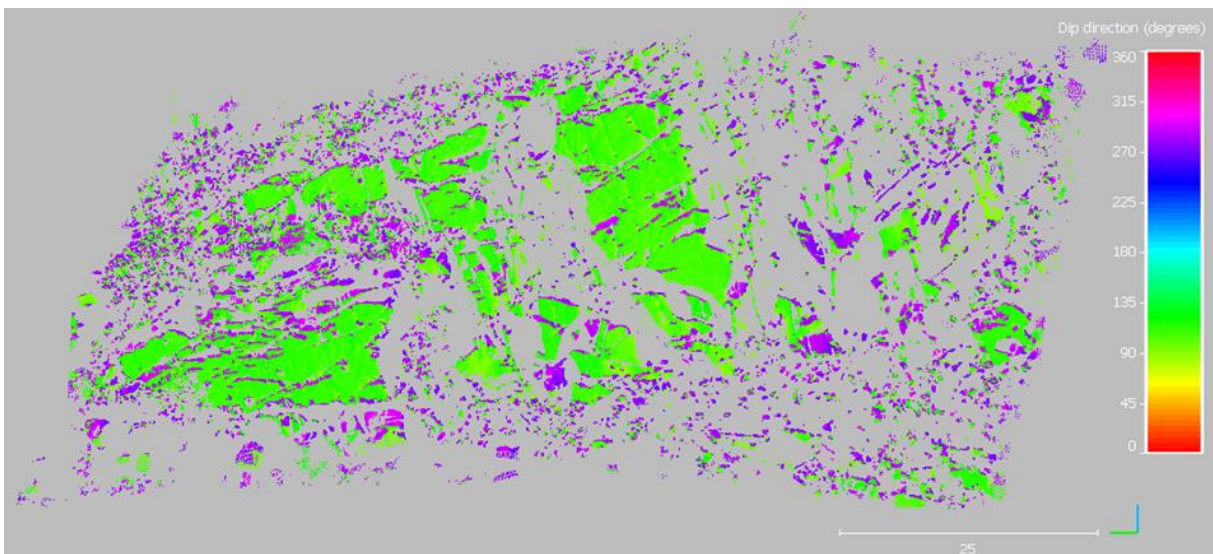


Figure 89: Points of set E. Software used: CloudCompare (2019).

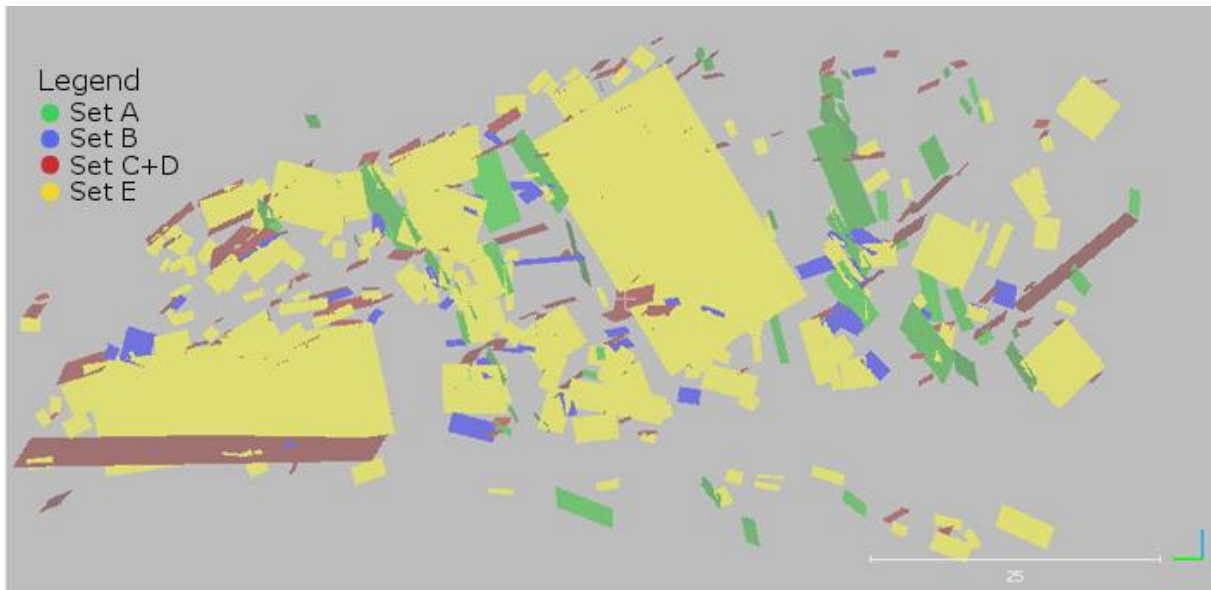


Figure 90: Fracture pattern in frontal view. Software used: CloudCompare (2019).

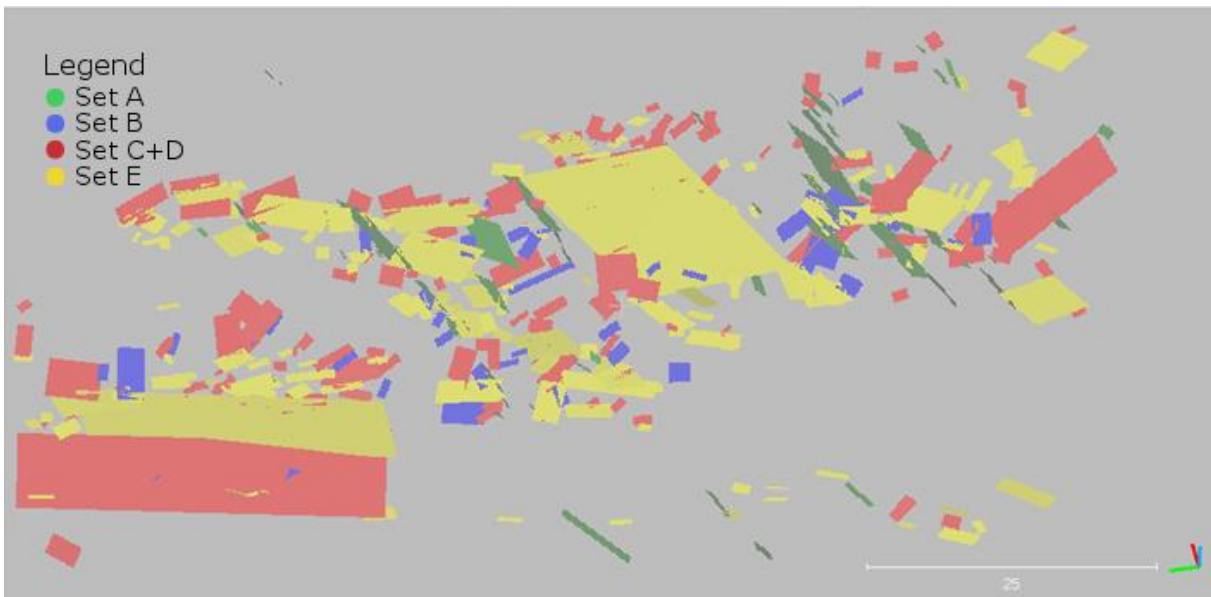


Figure 91: Fracture pattern in birds-eye-view. Software used: CloudCompare (2019).

Laid above the RGB point cloud (Figure 92 to Figure 94), the planes appear to fit quite well to the rock mass' surface despite the data holes and the vegetation. However, without these obstacles, several planes of the four sets might additionally appear in the fracture pattern. This particularly concerns set A.

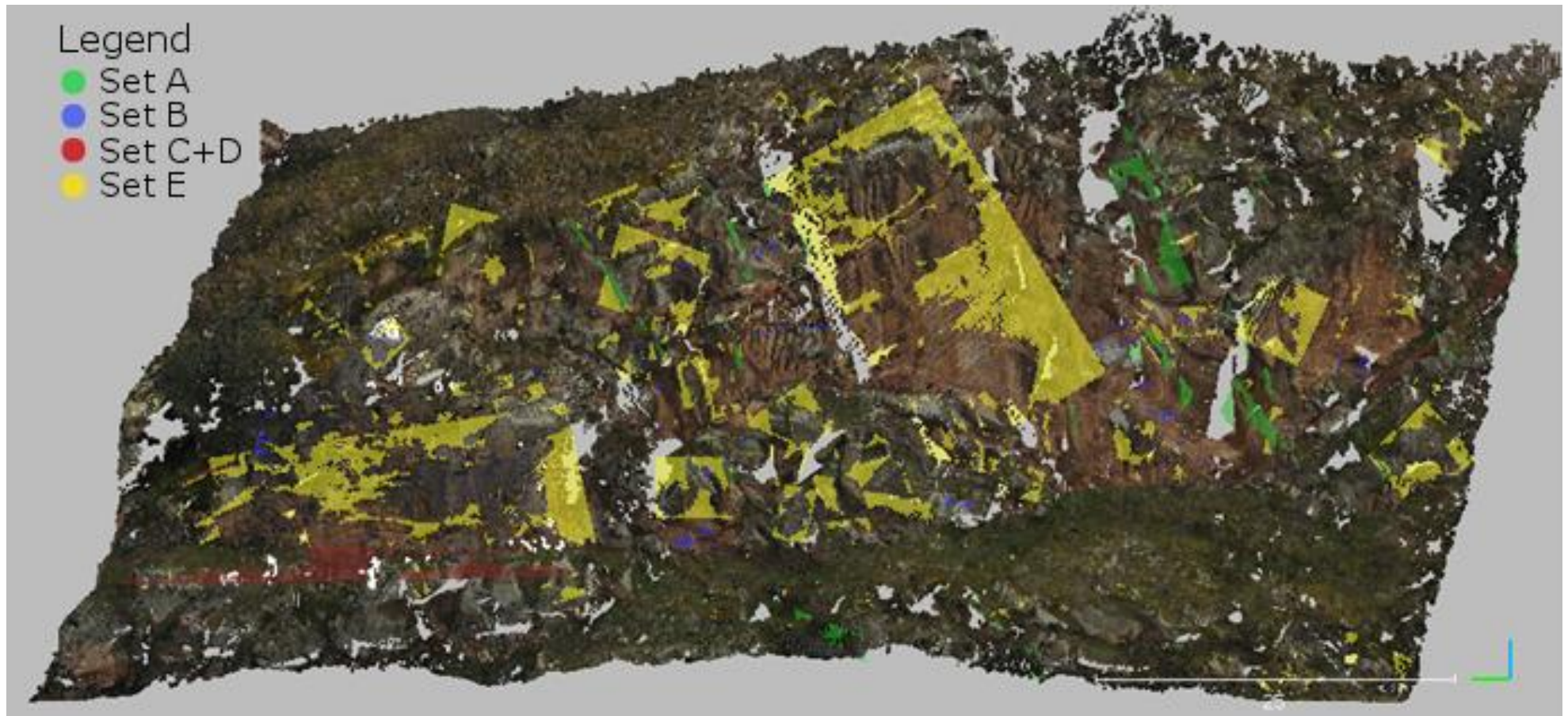


Figure 92: Fracture pattern over the RGB point cloud in frontal view. Software used: CloudCompare (2019).

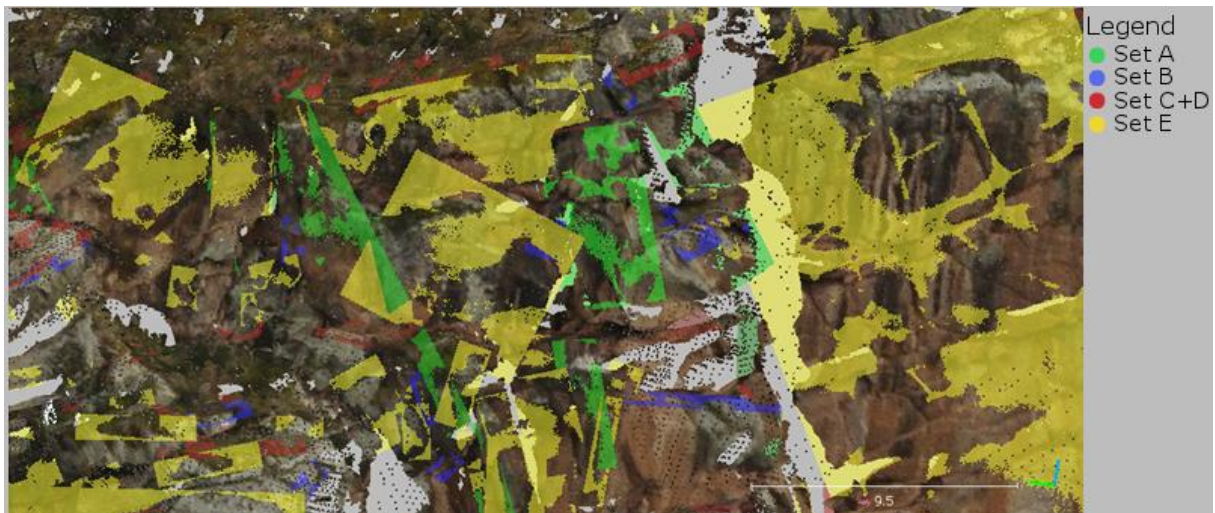


Figure 93: Fracture pattern over the RGB point cloud in detail. Software used: CloudCompare (2019).

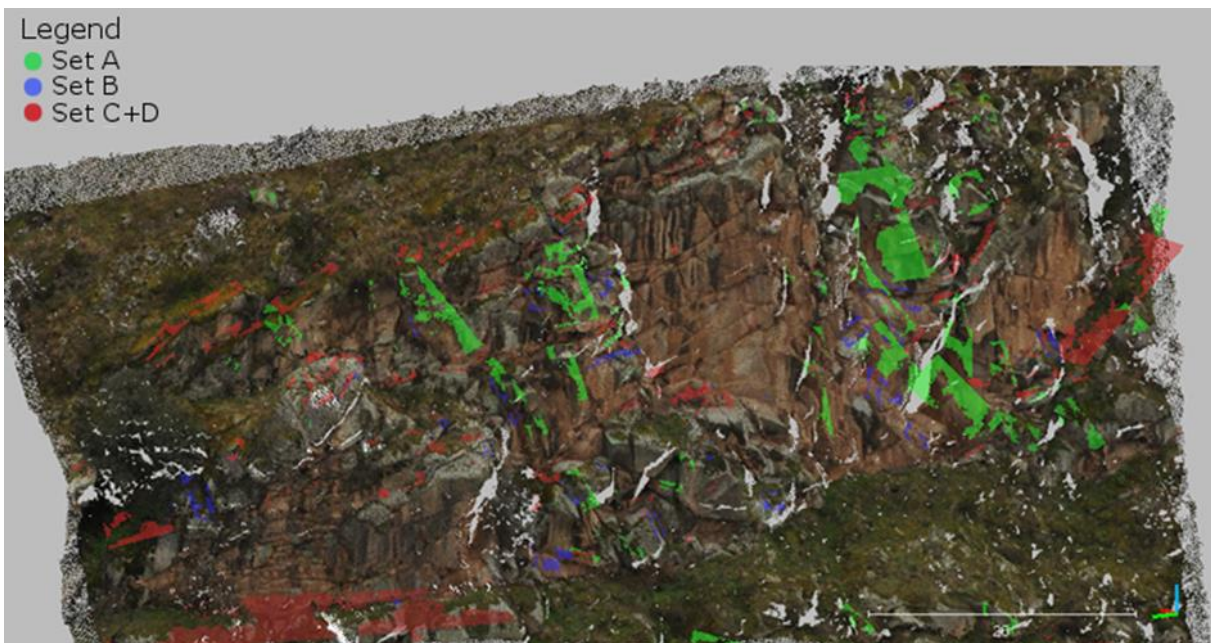


Figure 94: Fracture pattern over the RGB point cloud, without set E. Software used: CloudCompare (2019).

The plane poles' stereograms are compared to the point cloud normals' stereograms and the Fisher distribution calculations for the sets (Figure 95). The set A planes concentrate around a very narrow mean orientation although the normals are split apart by 180° due to the steep dip. All three stereograms of sets B and E correspond well. The set C+D planes show the two sub-clusters which originally caused the separation into two sets. The calculation of set C+D corresponds very well to the normals. The difference to the plane poles stereogram, i.e. the two sub-clusters, is caused by the separate Facets (Dewez et al., 2016) extraction.

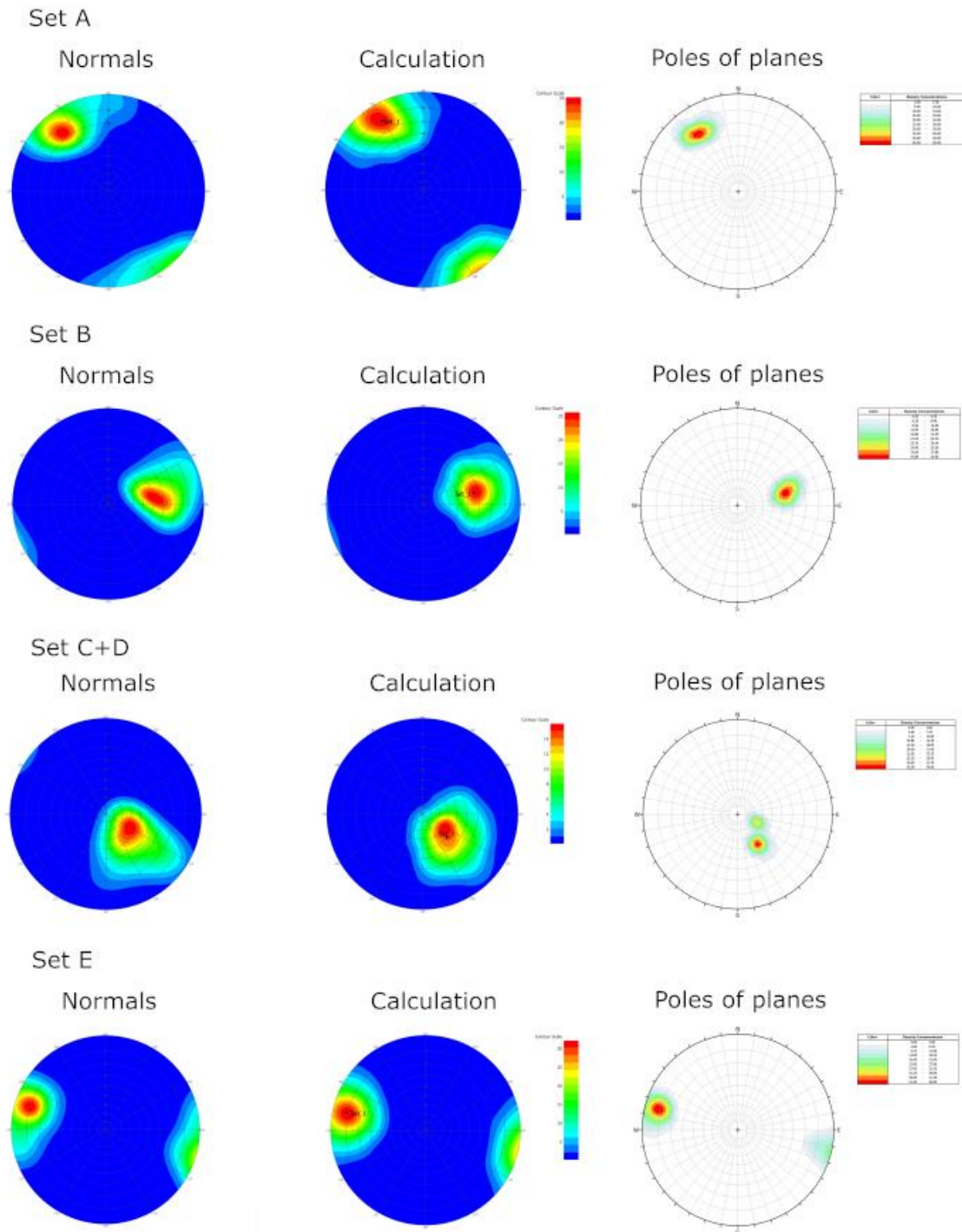


Figure 95: Stereograms for segment 3's sets of the point cloud (left, middle; FracMan (Golder Associates Inc., 2018)) and the plane data (right; Dips (Rocscience Inc., 2018))

At first sight, set E has the highest number of big planes. Except of the estimated planes, set C+D shows relatively smaller plane sizes, as set B does. Set A's planes are moderate in size. The calculated plane sizes for segment 3 are given in Table 10. Set E has the highest mean and median plane size, which supports the appearance at first sight. The only exception is set A's median plane size of planes $>1 \text{ m}^2$, which is the highest of all sets in this

segment. The high amount of planes $<1 \text{ m}^2$ in sets A and C+D causes the relatively high difference in mean and mean $>1 \text{ m}^2$. This is also true for the median. The maximum plane size of set C+D is that of an estimated plane. However, set E's maximum plane size is not related to an estimated plane. The overall trend of a higher amount of small planes and relatively few big planes also appears in this segment, as in segments 1 and 2. This trend is shown for each set in the plane size histograms with density lines in Figure 96 to Figure 99. High plane sizes are plotted as logarithmic to the base 10 (sets A, C+D, and E).

Table 10: Plane sizes in segment 3

	Set A	Set B	Set C+D	Set E
Mean	5.3415	2.4304	4.4553	8.5511
Mean ($>1 \text{ m}^2$)	7.5964	2.8377	6.3551	9.4576
Median	1.9433	1.6356	1.5547	2.0998
Median ($>1 \text{ m}^2$)	3.7863	1.8275	2.2439	2.4102
Maximum	48.3264	11.3728	217.4984	339.9287
Minimum	0.0826	0.2743	0.1934	0.3196
Number of planes	75	43	138	154
Number of planes $<1 \text{ m}^2$, total	24	8	46	16
Number of planes $<1 \text{ m}^2$, %	32	18.6047	33.3333	10.3896

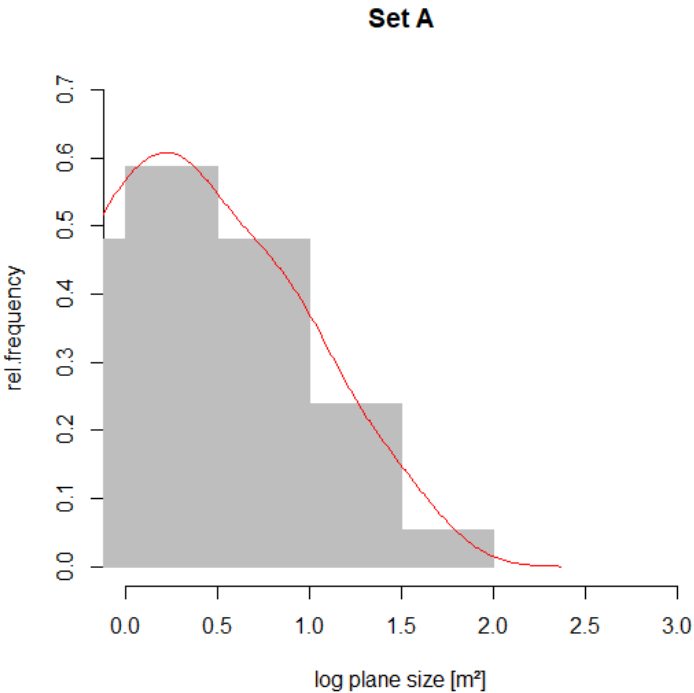


Figure 96: Plane sizes of set A, density line shown in red

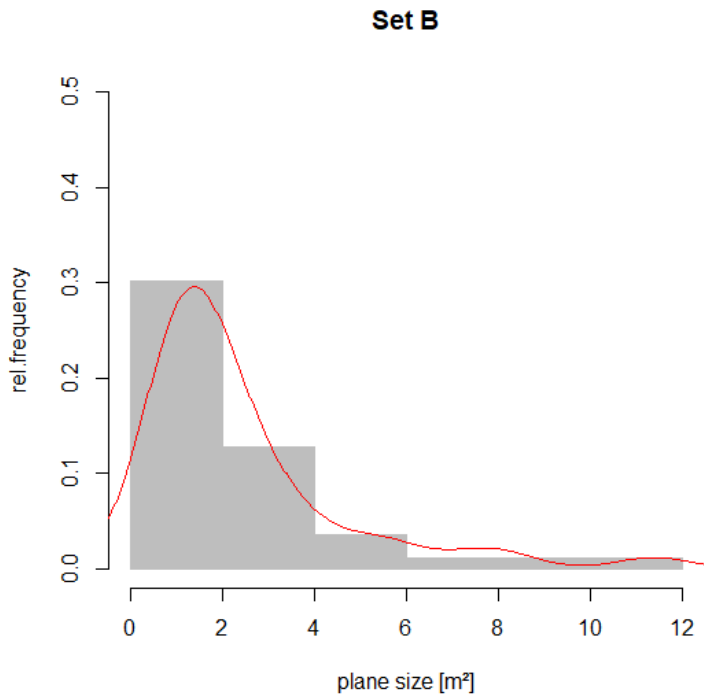


Figure 97: Plane sizes of set B, density line shown in red

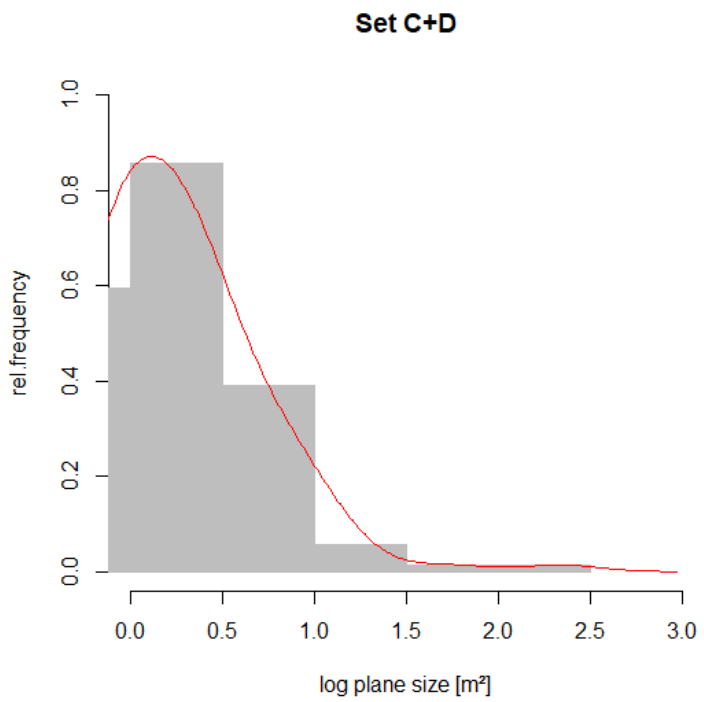


Figure 98: Plane sizes of set C+D, density line shown in red

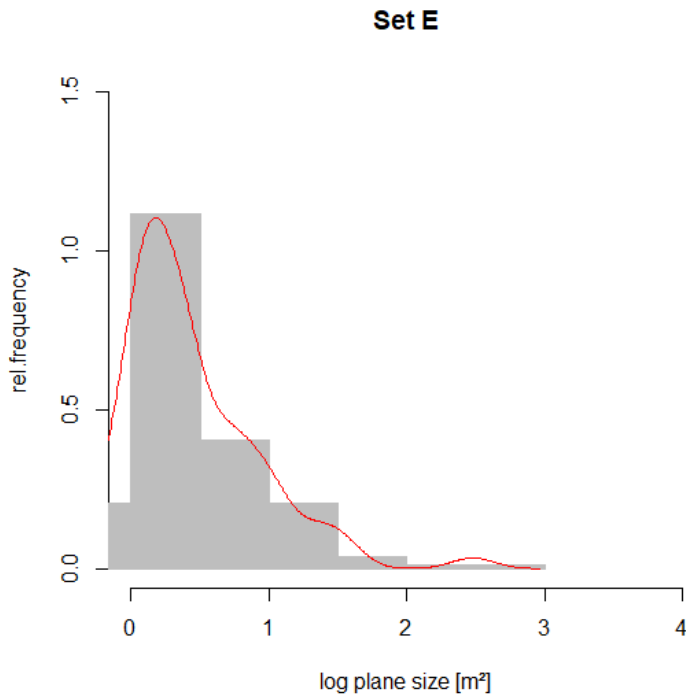


Figure 99: Plane sizes of set E, density line shown in red

The termination is investigated for each set: A, B, C+D, and E. The results are shown in Figure 100 to Figure 111. The plots are based on tables which are given in the appendix. According to the set characteristics, sets B and E are classified as sheeting joint sets, which will be further interpreted and explained in chapters 6.1 interpretation – joint sets, and 7.2 discussion – results.

Set A mostly terminates in set E and in set C+D (Figure 100). This trend appears in the plane termination as well as in the termination estimation when the plane's neighborhood is taken into account. The isolated planes (Figure 101) actually do terminate in other sets. Most set A planes terminate in one or two sets. The maximum shifts from one set (termination) to two sets when the neighborhood is considered in the investigation. This difference is primarily caused by roundness and data holes (Figure 102).

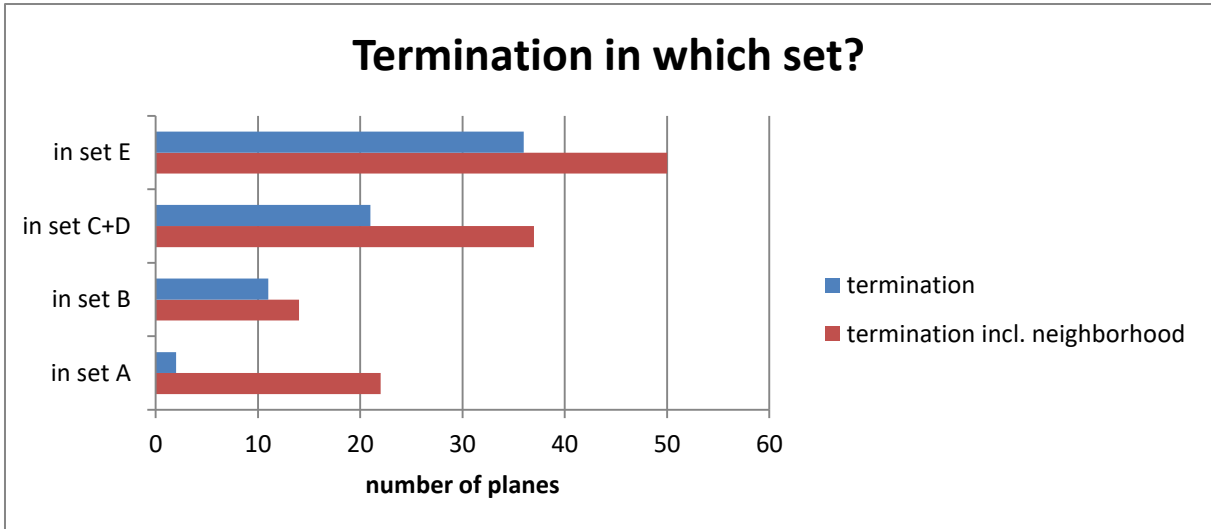


Figure 100: Termination of set A

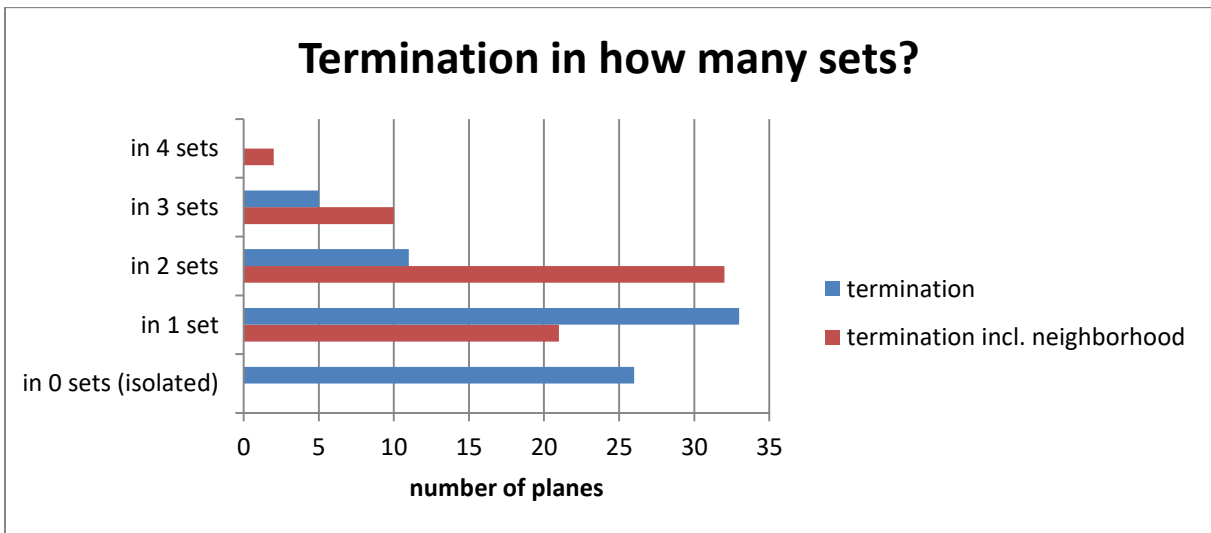


Figure 101: Termination of set A

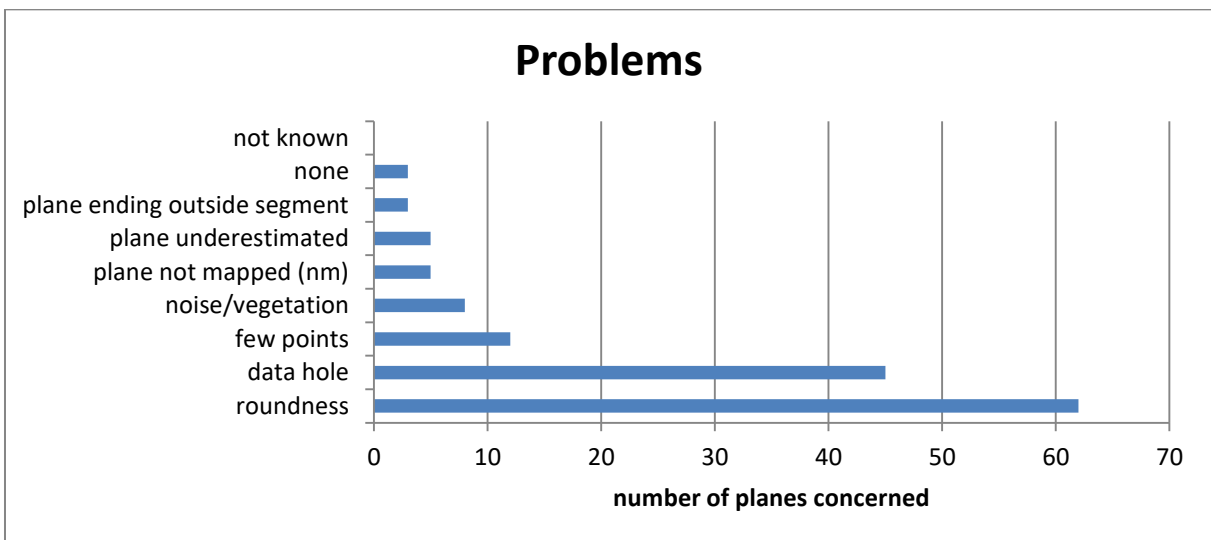


Figure 102: Problems for plane fitting in set A

Set B mostly terminates in set E and set C+D, and often in set A (Figure 103). The neighborhood only changes the absolute number of terminations, but the relations of the set terminations stay the same. As above in set A, there are no isolated planes in this set when the neighborhood is considered (Figure 104). Most of set B planes terminate in one or two sets. The neighborhood consideration significantly raises the termination in three sets. Roundness, data holes, and a low point density decrease the plane fitting quality and the plane networking with neighboring planes (Figure 105).

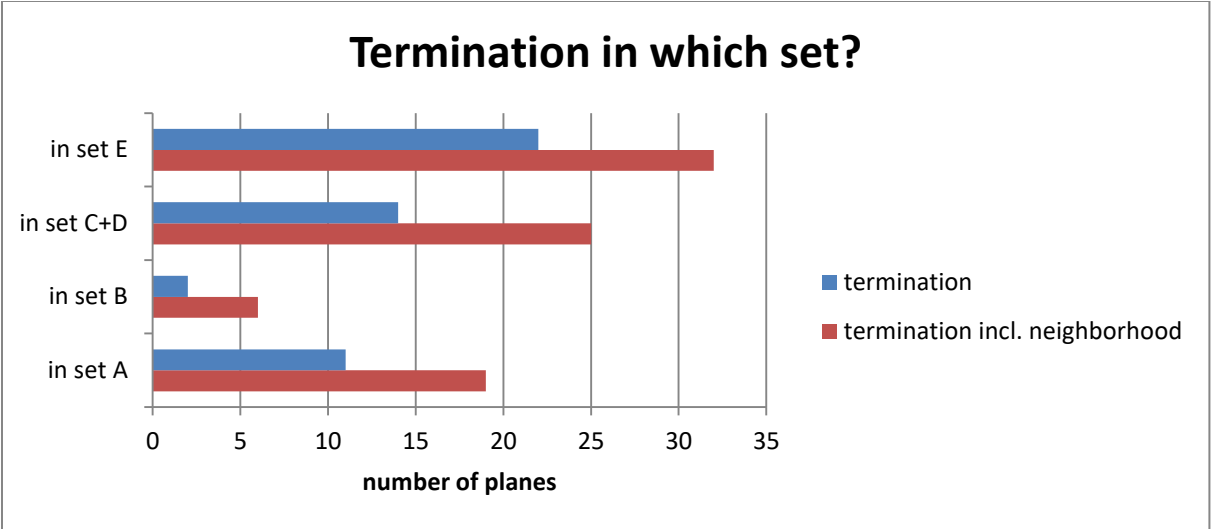


Figure 103: Termination of set B

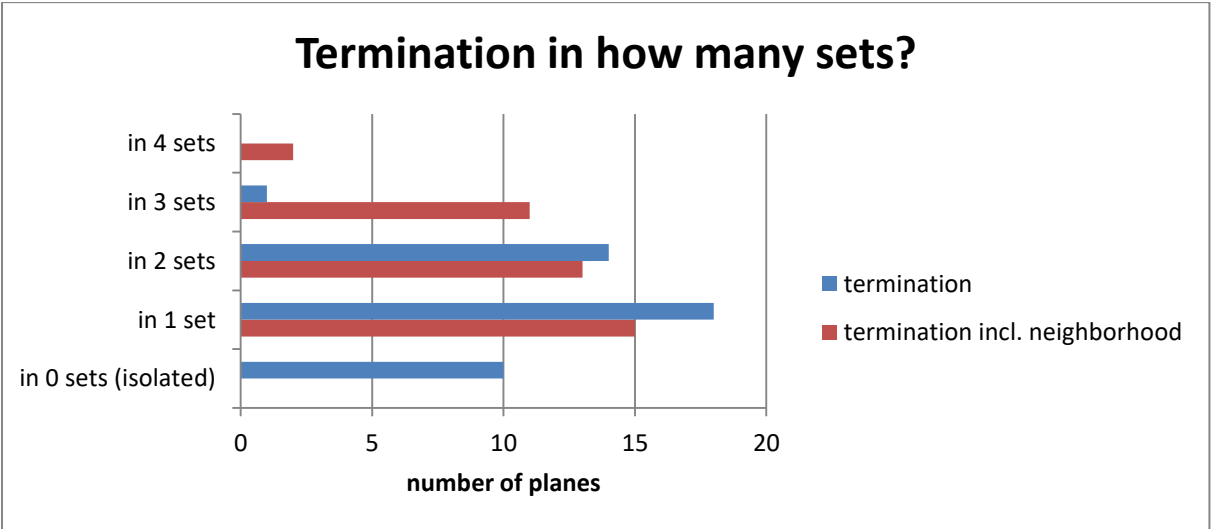


Figure 104: Termination of set B

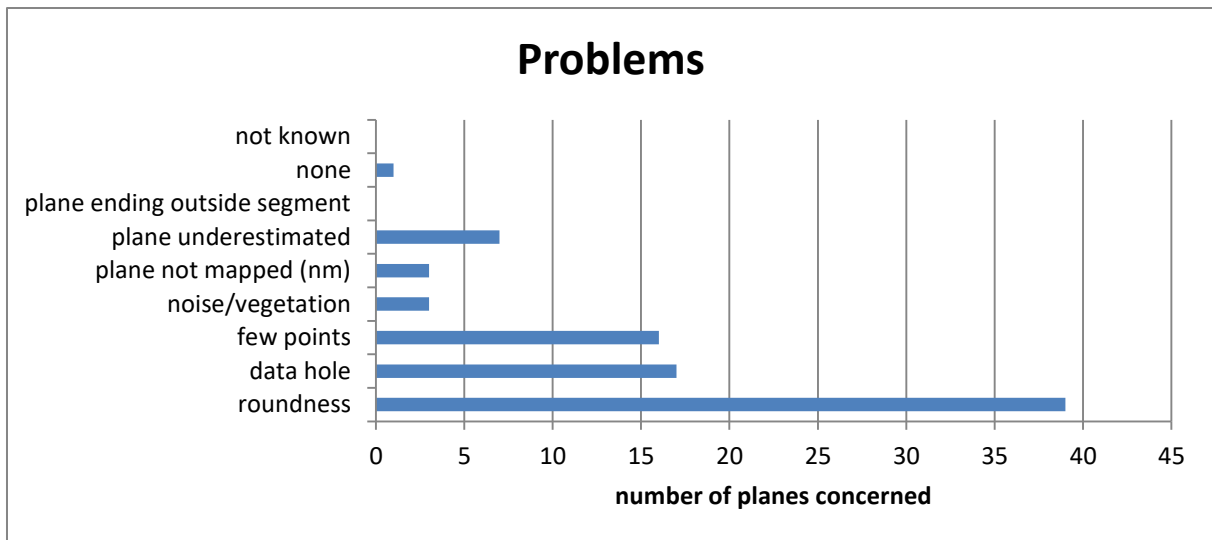


Figure 105: Problems for plane fitting in set B

Set C+D tends to terminate in set E (Figure 106). Several planes also terminate in set C+D itself, which might be caused by the biggest plane fitting problem in this set, the roundness (Figure 108). Other problems are data holes and noise or vegetation. The number of sets in which set C+D planes terminate (Figure 107) follows the same trend as in sets A and B. There are no isolated planes actually, and most of the planes terminate in one or two sets.

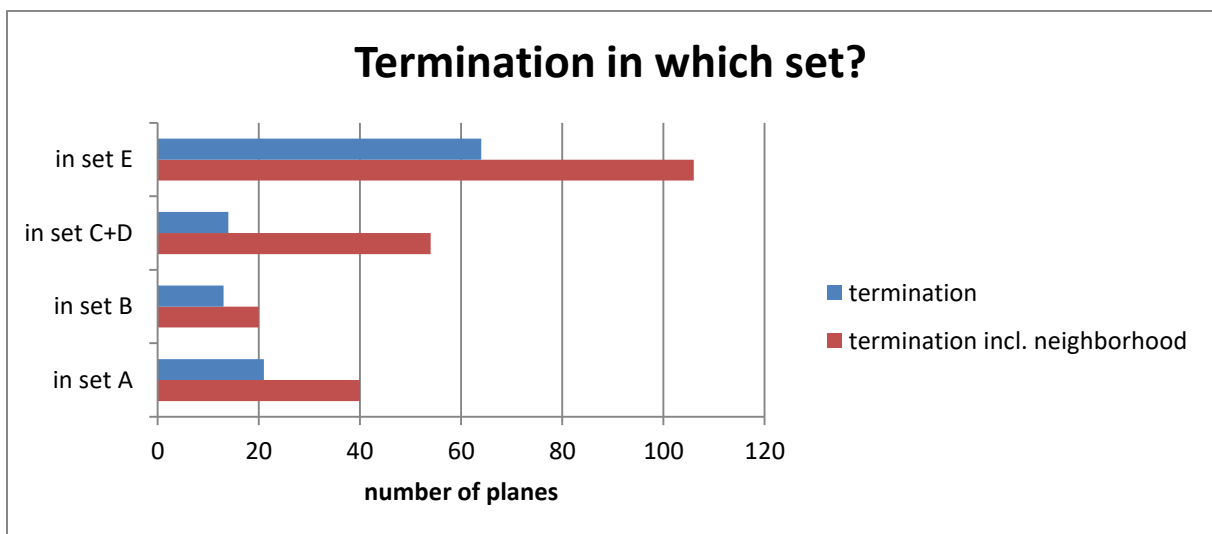


Figure 106: Termination of set C+D

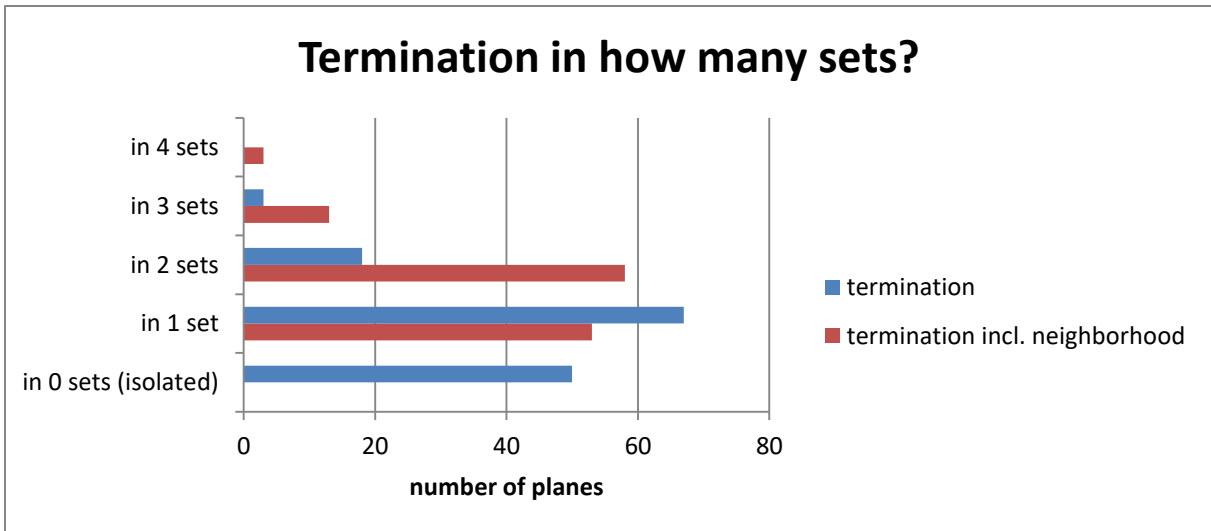


Figure 107: Termination of set C+D

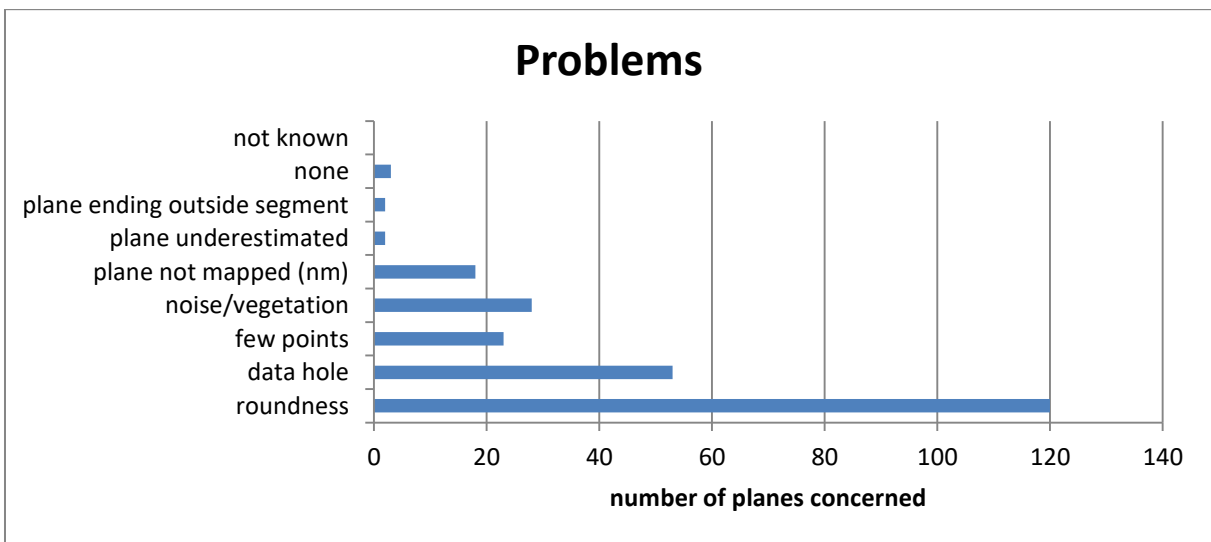


Figure 108: Problems for plane fitting in set C+D

Set E terminates in sets C+D, in itself, in set A, and in set B (Figure 109). Concerning the number of sets in which set E terminates (Figure 110), the actual number of isolated set planes is 0, and most planes terminate in one or two sets. This is the same behavior as in all other sets of this segment. The most common plane fitting problems are roundness, data holes, and a low point density (Figure 111).

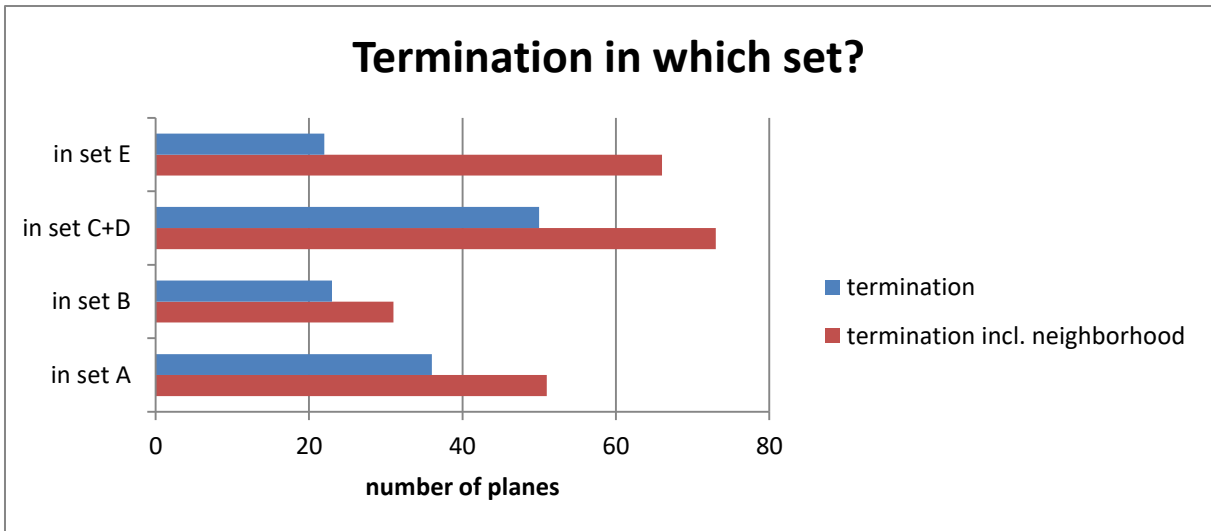


Figure 109: Termination of set E

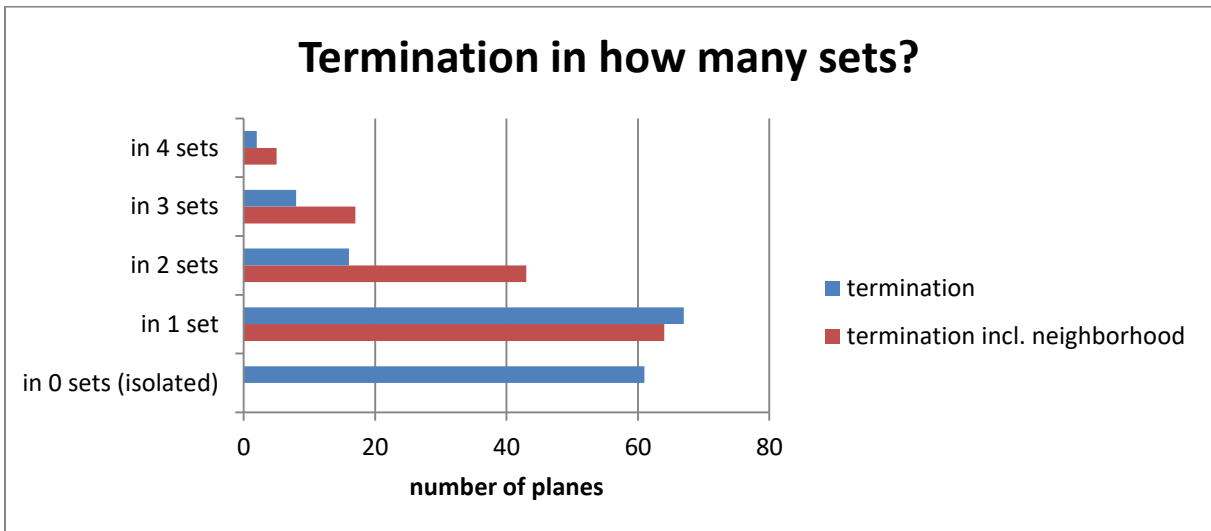


Figure 110: Termination of set E

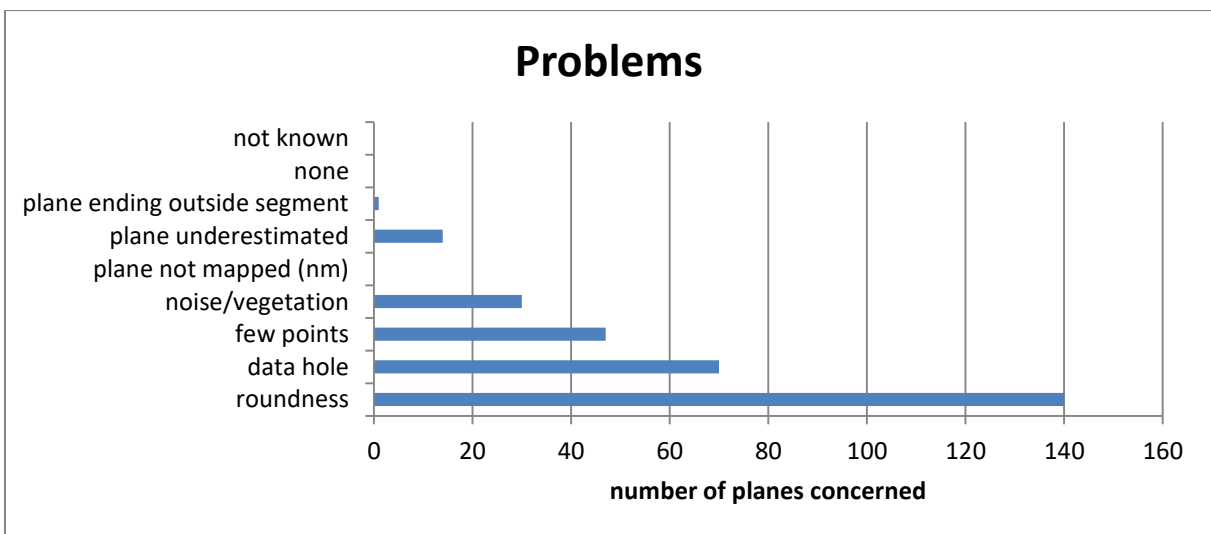


Figure 111: Problems for plane fitting in set E

5.2.4 Sets in segment 4 (WG)

Segment 4 is shown in RGB colors in Figure 112. Some parts of the rock surface at the bottom are concealed due to shotcrete, which lines the plunge pool in some areas. The overall slope orientation varies more than in the other segments. The best clustering results are produced for a classification into six clusters (Figure 113), with a corresponding average silhouette width of 0.56. The calculated statistical parameters are as follows: minimum individual silhouette width -0.4562, maximum individual silhouette width 0.8989; first quartile 0.4188, median 0.6389, mean 0.5612, third quartile 0.7705. If the data is classified into five clusters, the average silhouette width is the same as for six clusters (0.56). The minimum individual silhouette width for five clusters is -0.4186, the maximum is 0.8513. The first quartile is 0.4311, the median 0.6330, the mean 0.5626, and the third quartile 0.7534. Therefore, for five clusters, the minimum individual silhouette width, the first quartile and the mean are higher, while the maximum individual silhouette width, the median, and the third quartile are lower.



Figure 112: Segment 4, RGB colors (shown in CloudCompare, 2019)

Silhouette Plot for 6 clusters/sets

n = 1349513

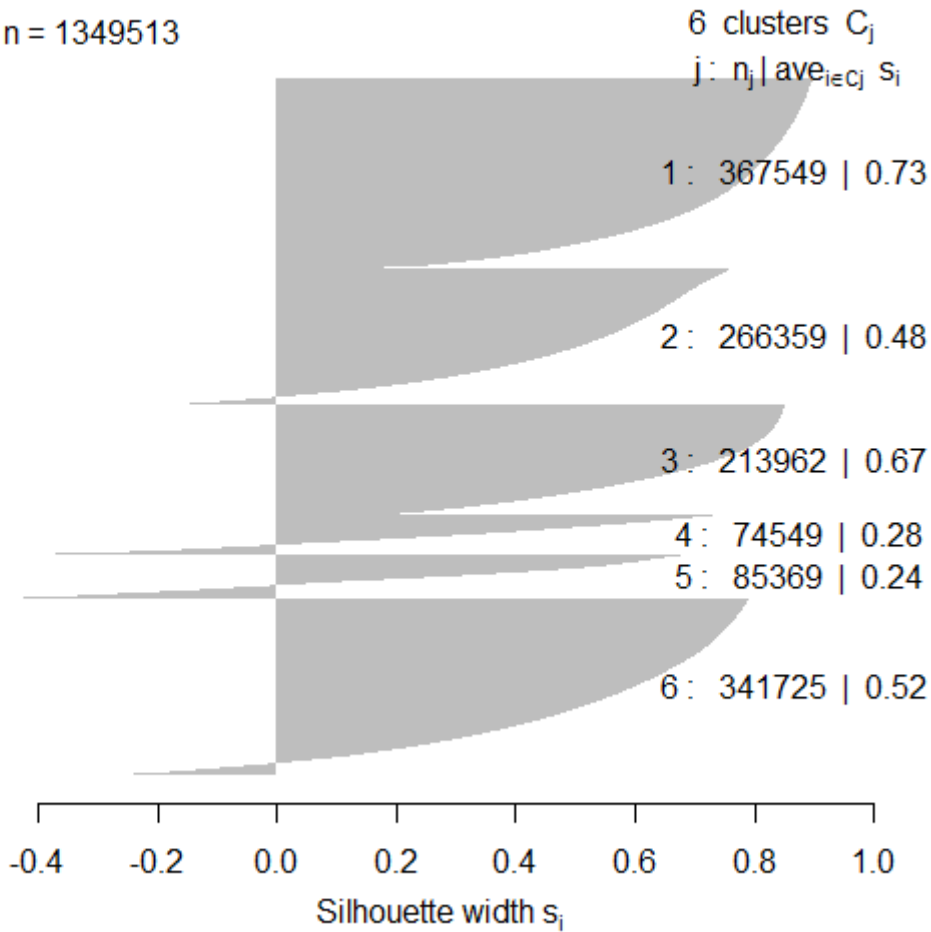


Figure 113: Silhouette plot for segment 4

Due to the varying slope orientation, there is not only one dominating set as in segments 1, 2, and 3, but there are several steeply dipping joint sets. These sets are contained in clusters 1, 2, 3, and 6. Clusters 4 and 5 consist of two sets each, which causes their re-clustering into two clusters each to separate the sets. Cluster 4 is separated into two oblique sets, while cluster 5 is classified into two steeply dipping sets which seem to compliment the steeply dipping sets mentioned above.

Therefore, eight sets can be identified. They are numbered from I to VIII. Table 11 gives the orientation statistical parameters for these sets. No set dips so steep that its dip direction distribution can be supposed to be split apart by 180° . The Fisher concentration parameter k is quite high for all sets, with an outstanding k of 45.4900 for set V. Consequently, set V's variability angle is as low as 21.2018° . The confidence angles of sets I, II, III, and VIII are remarkably higher than the ones of the other sets in this segment. This might be caused by the relatively low amount of values in these sets paired with a slightly lower Fisher k . An exception is set VIII, which has a quite high k , but still consists of very few values.

Table 11: Orientation statistics for segment 4. The angles are given in degrees.

set	number of values	mean dip direction ("major axis")	mean dip ("major axis")	Fisher k	variability angle (95.4%)	confidence angle (95.4%)
set I	24919	172.9120	70.5590	19.9416	32.2644	0.2070
set II	30044	127.8690	61.8220	20.4584	31.8433	0.1860
set III	28828	10.9300	76.6630	19.6890	32.4764	0.1937
set IV	320232	254.7600	68.5870	22.5687	30.2805	0.0541
set V	367549	290.4080	74.0750	45.4900	21.2018	0.0352
set VI	213962	315.3970	74.1380	35.7334	23.9598	0.0522
set VII	250662	315.3750	43.6910	22.4151	30.3866	0.0614
set VIII	25044	95.8660	72.1410	29.0700	26.6096	0.1696

The points of the eight sets are shown in Figure 114 to Figure 121, and the planes are shown in Figure 122 to Figure 125. The fracture pattern (Figure 122) is easier to identify over the RGB point cloud (Figure 123, Figure 124). Figure 124 excludes sets I, II, and III in the visualization. Figure 125 only shows sets I and III to illustrate their connection which is concealed by the big magenta plane in the other fracture pattern figures.

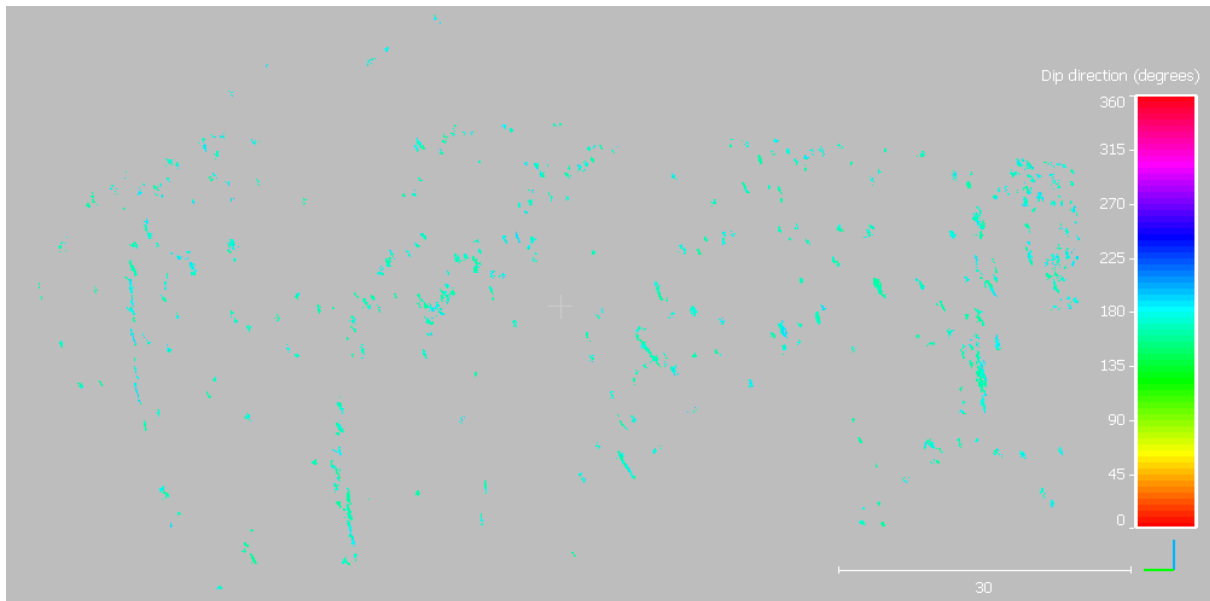


Figure 114: Points of set I. Software used: CloudCompare (2019).

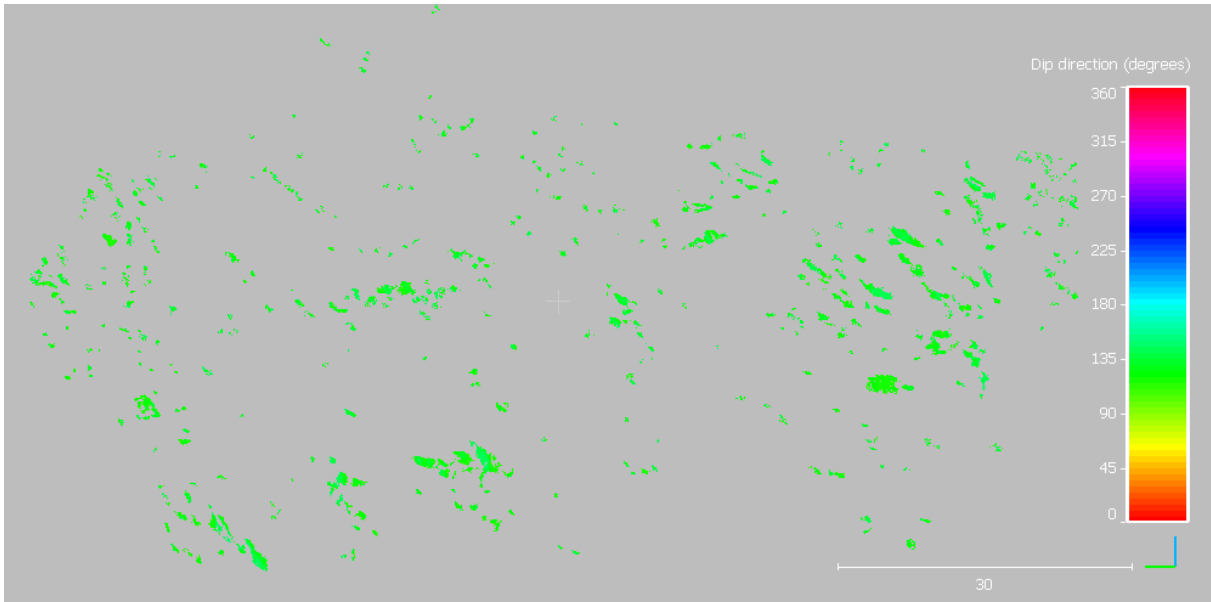


Figure 115: Points of set II. Software used: CloudCompare (2019).

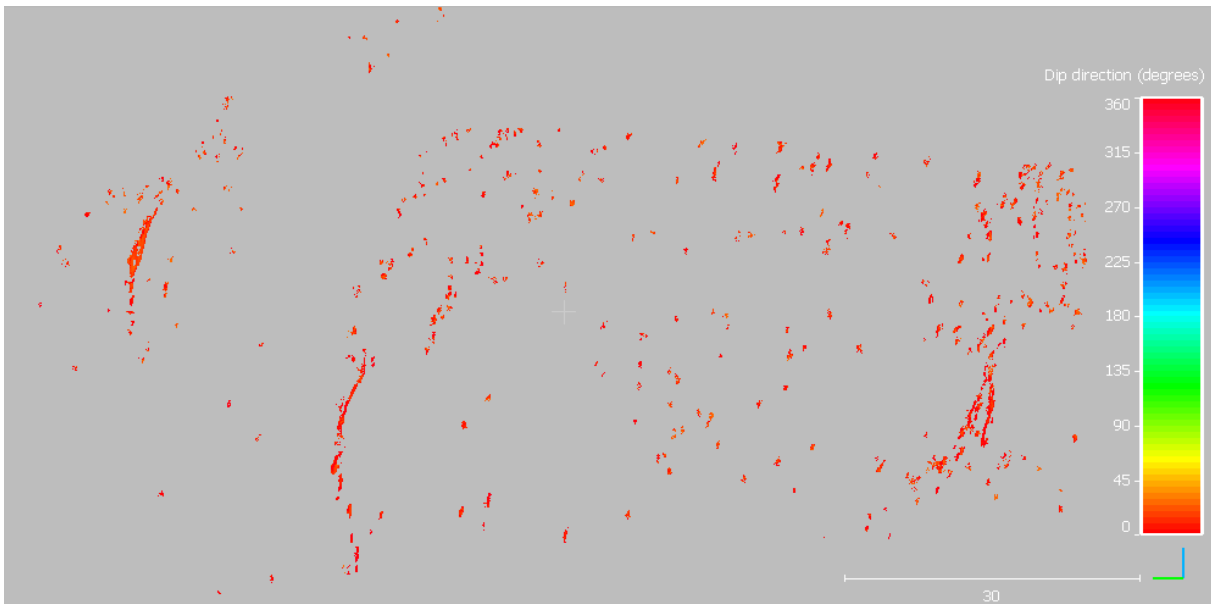


Figure 116: Points of set III. Software used: CloudCompare (2019).

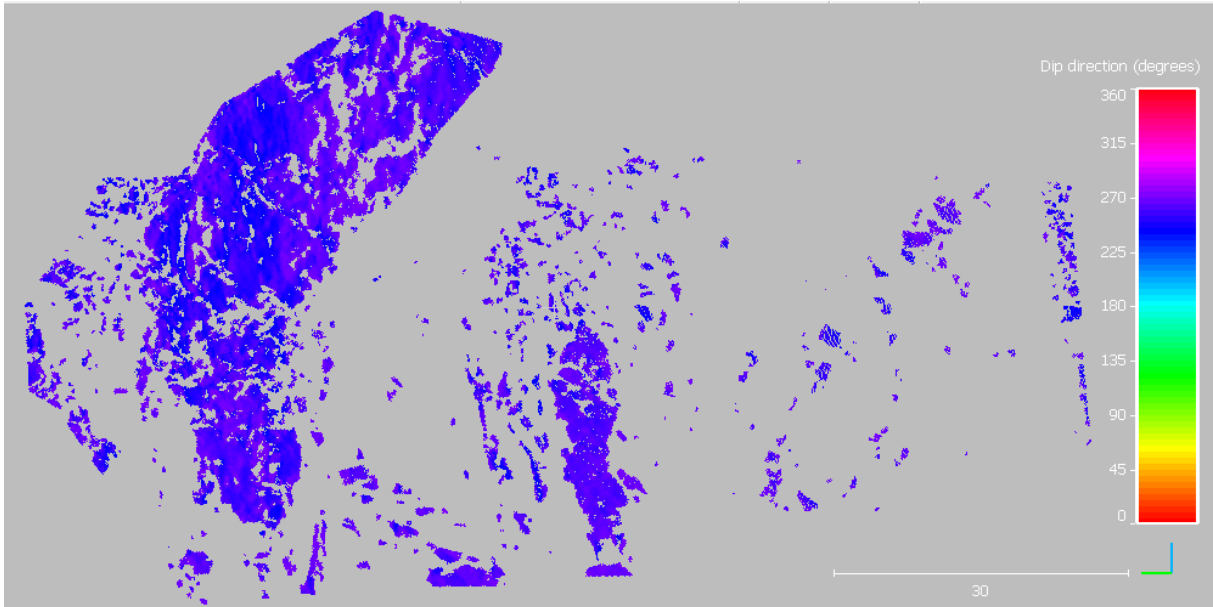


Figure 117: Points of set IV. Software used: CloudCompare (2019).

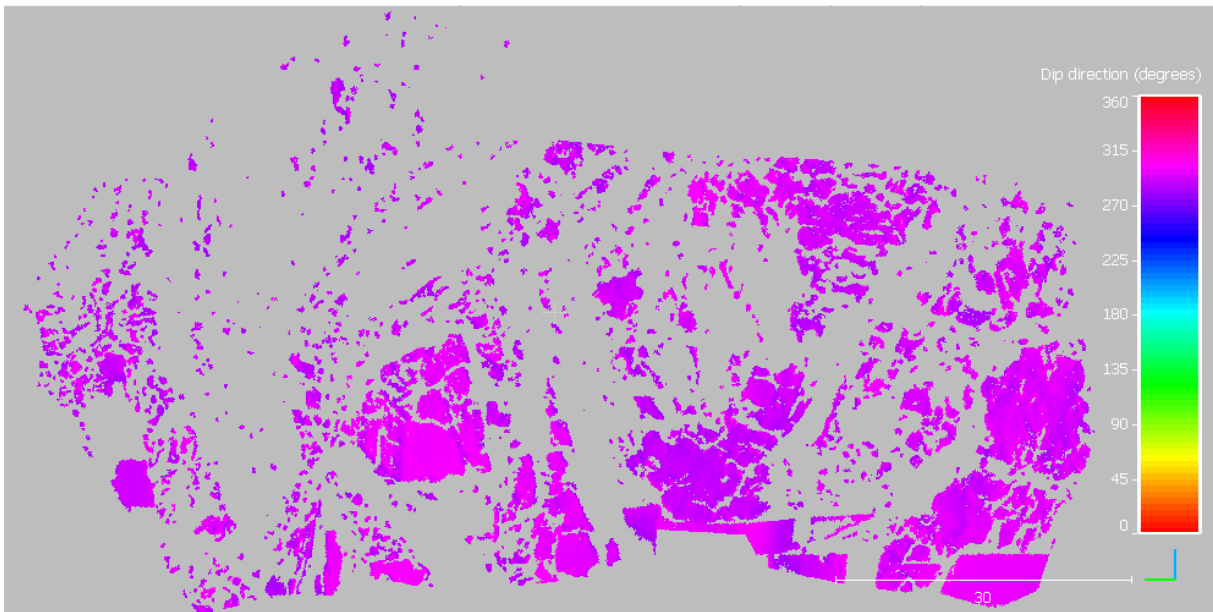


Figure 118: Points of set V. Software used: CloudCompare (2019).

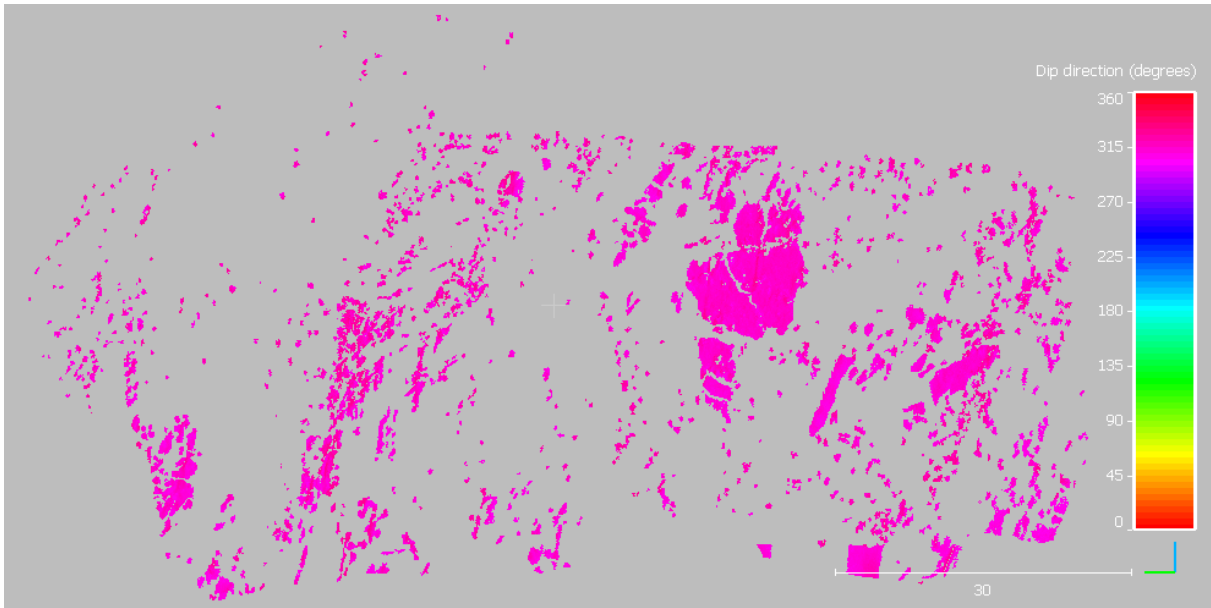


Figure 119: Points of set VI. Software used: CloudCompare (2019).

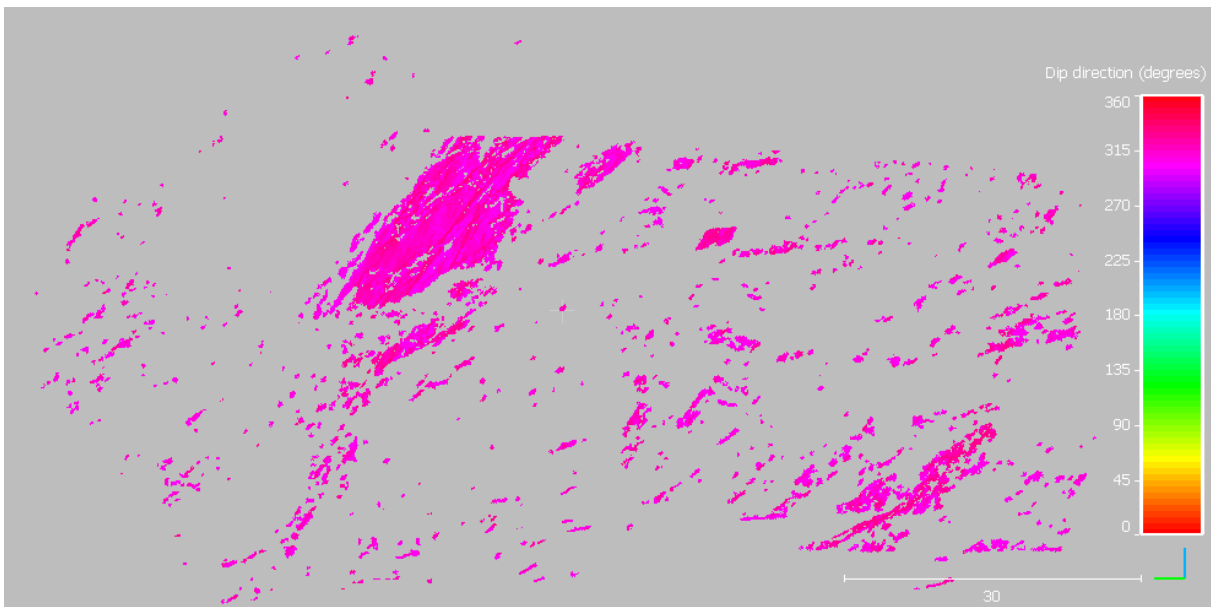


Figure 120: Points of set VII. Software used: CloudCompare (2019).

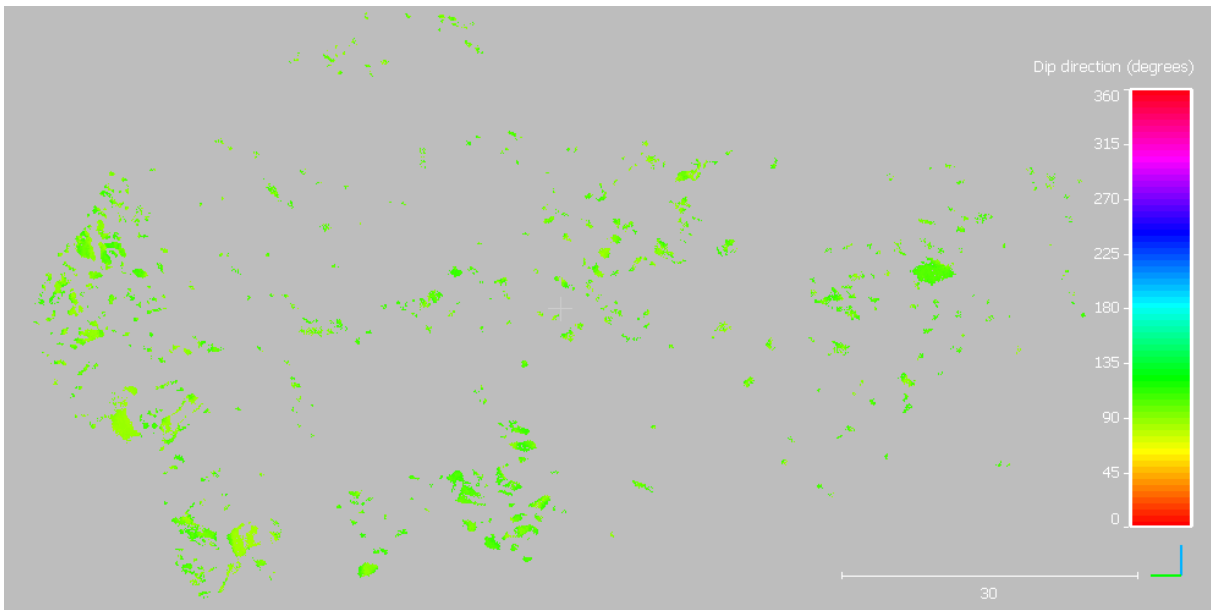


Figure 121: Points of set VIII. Software used: CloudCompare (2019).

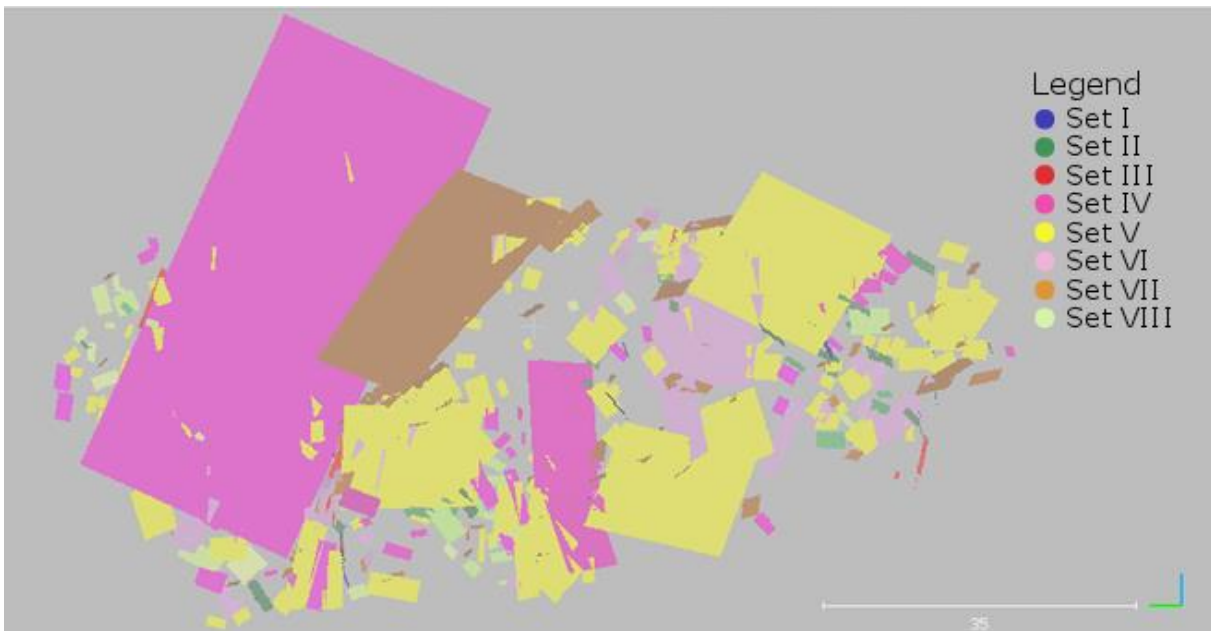


Figure 122: Fracture pattern in frontal view. Software used: CloudCompare (2019).

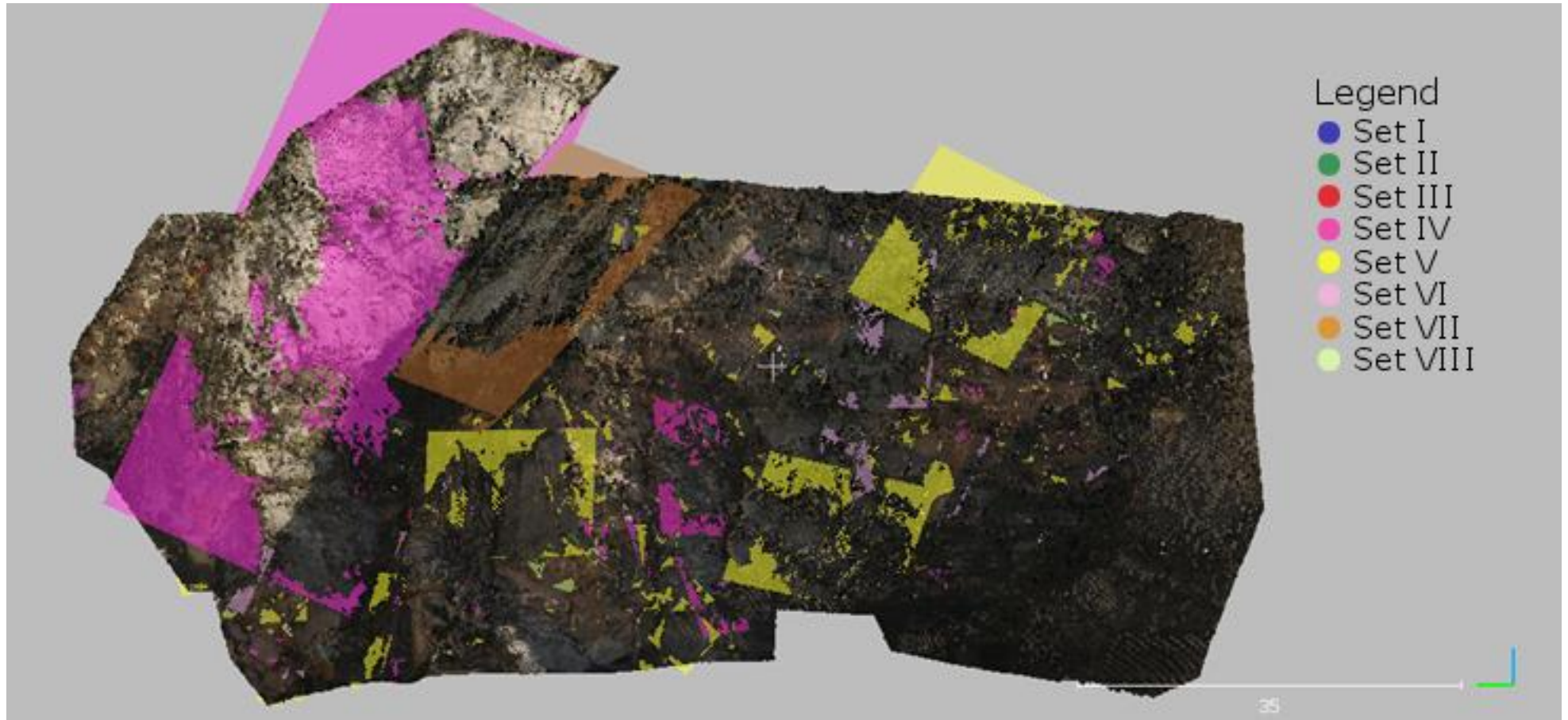


Figure 123: Fracture pattern in frontal view over the RGB point cloud. Software used: CloudCompare (2019).

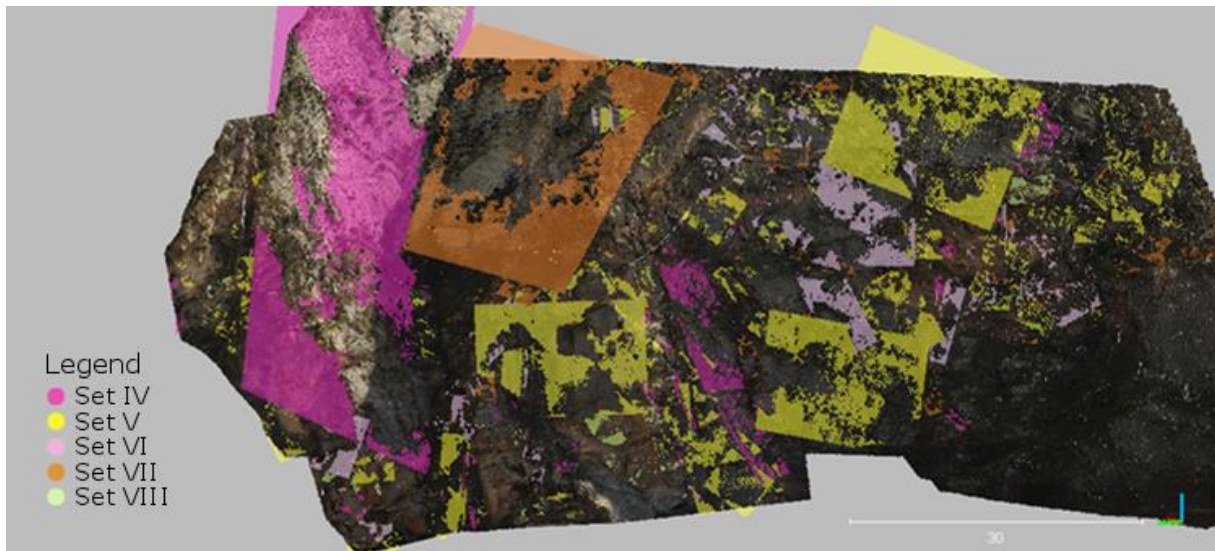


Figure 124: Fracture pattern over the RGB point cloud, without sets I, II, and III. Software used: CloudCompare (2019).



Figure 125: Fracture pattern of set I and III in detail over the RGB point cloud, left border of the big magenta plane in the figures above. Software used: CloudCompare (2019).

The planes' poles are plotted in a stereogram, which is compared with the stereograms from the point cloud normals and from the Fisher distribution calculation (Figure 126, Figure 127). The mean orientation of the set planes corresponds to the one of the point cloud normals as well as to the one of the Fisher distribution calculation. However, the set planes show a narrower distribution, which might be due to the filtering process. This is the same for this segment as for the previous segments. The shape of the density peak in the contour plot of the plane orientation does resemble both, the normals plot and the Fisher calculated plot.

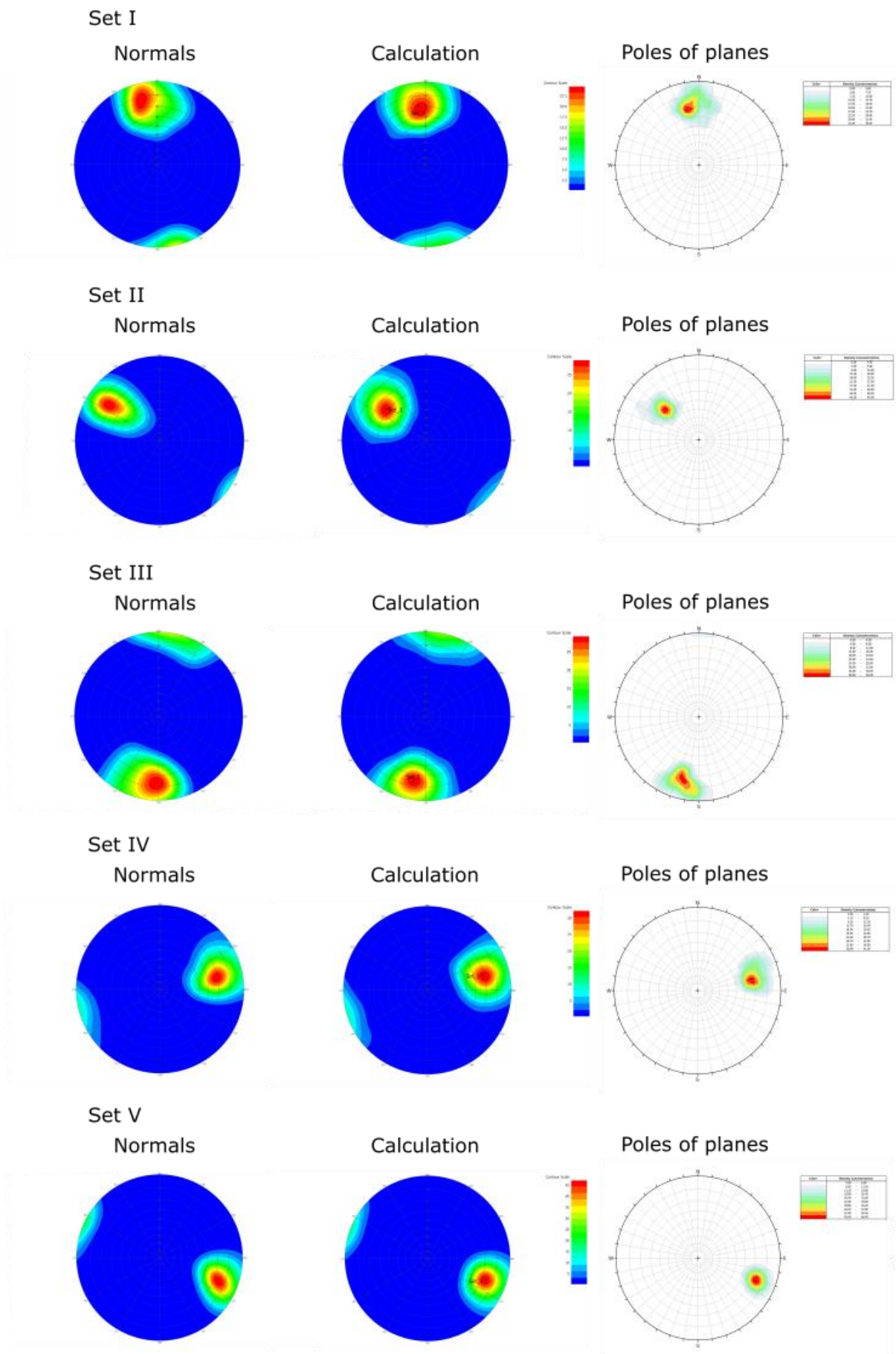


Figure 126: Stereograms for segment 4's sets I to V, of the point cloud (left, middle; FracMan (Golder Associates Inc., 2018)) and the plane data (right; Dips (Rocscience Inc., 2018))

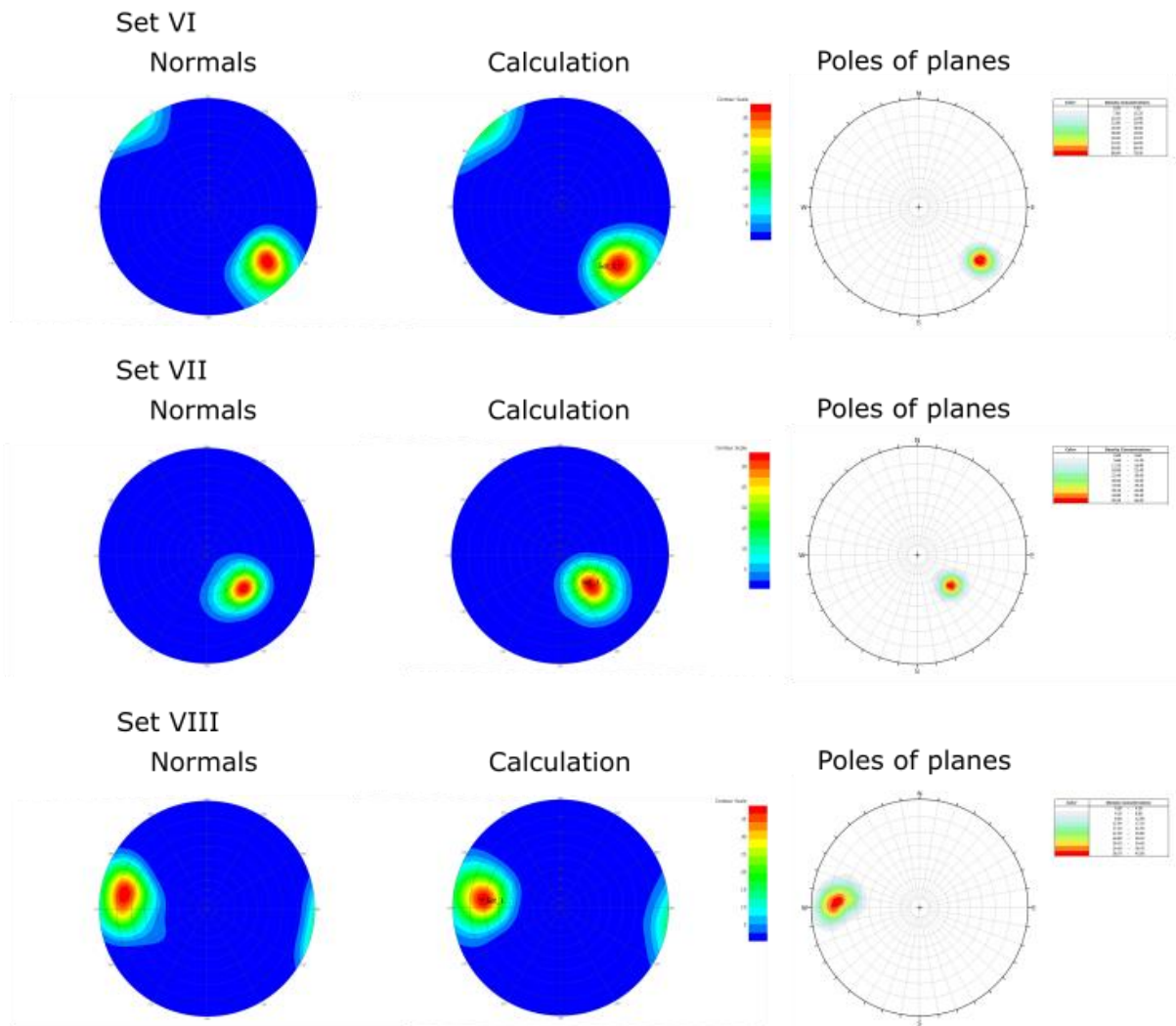


Figure 127: Stereograms for segment 4's sets VI to VIII, of the point cloud (left, middle; FracMan (Golder Associates Inc., 2018)) and the plane data (right; Dips (Rocscience Inc., 2018))

Concerning the plane size, sets IV, V, and VII seem to feature the biggest planes (Figure 122 to Figure 124, above). This is confirmed by the area calculation given in Table 12. The high difference between mean and median of sets IV, V, and VII is caused by the few big planes. The number of planes $<1 \text{ m}^2$ is relatively low for all sets, except for set I and set VIII. This causes the low difference of mean and median to mean and median of the planes $>1 \text{ m}^2$. The trend to a higher amount of small planes and just a few bigger planes is visualized for each set in the plane size histograms with density lines in Figure 128 to Figure 135. As in segments 1, 2, and 3, high plane sizes are plotted as logarithmic to the base 10 in the histograms. This is the case for sets IV, V, VI, and VII.

Table 12: Plane sizes in segment 4

	Set I	Set II	Set III	Set IV	Set V	Set VI	Set VII	Set VIII
Mean	1.8676	3.2928	3.8144	41.7490	13.1422	9.0315	13.6389	3.6188
Mean >1 m²	2.0956	3.5700	4.2394	45.6565	13.2536	9.3280	15.3817	4.3816
Median	1.3928	2.8457	1.6863	2.9295	3.6068	3.1880	2.1857	2.2630
Median >1 m²	1.5668	3.1438	1.8195	3.4011	3.7397	3.2869	2.7009	2.8790
Maximum	6.9901	7.3542	25.4932	1550.0942	301.2186	165.9936	644.8263	13.4281
Minimum	0.5576	0.7357	0.6857	0.6539	0.5593	0.7778	0.5534	0.4430
Number of planes	23	30	16	46	114	57	67	33
Number of planes <1 m², total	4	3	2	4	1	2	8	7
Number of planes <1 m², %	17.3913	10	12.5000	8.6957	0.8772	3.5088	11.9403	21.2121

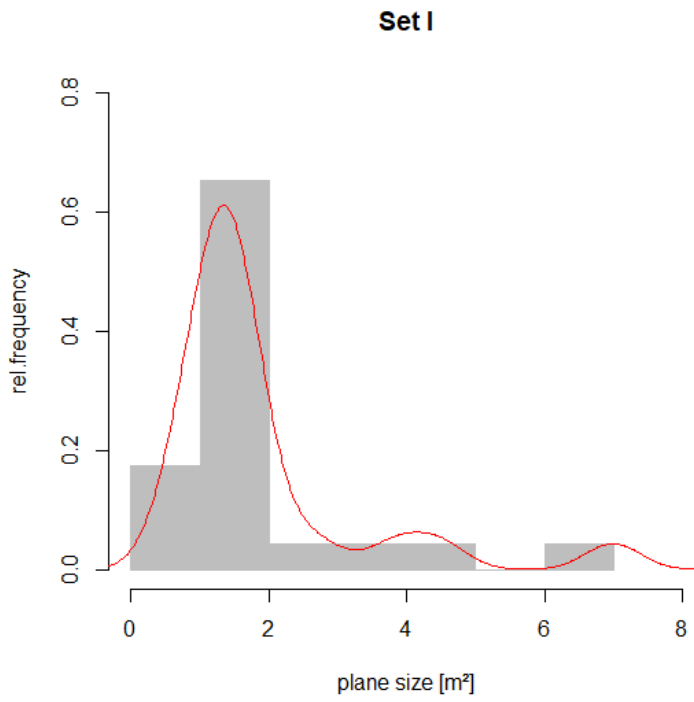


Figure 128: Plane sizes of set I, density line shown in red

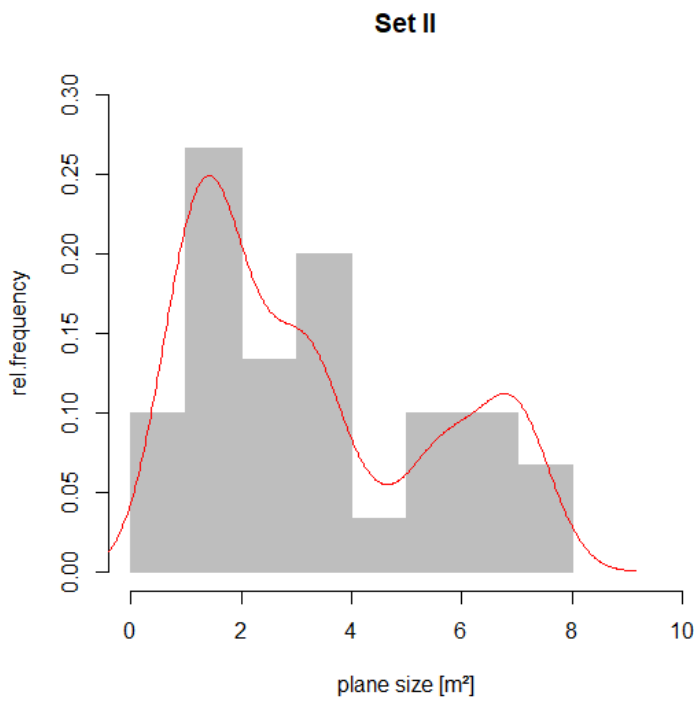


Figure 129: Plane sizes of set II, density line shown in red

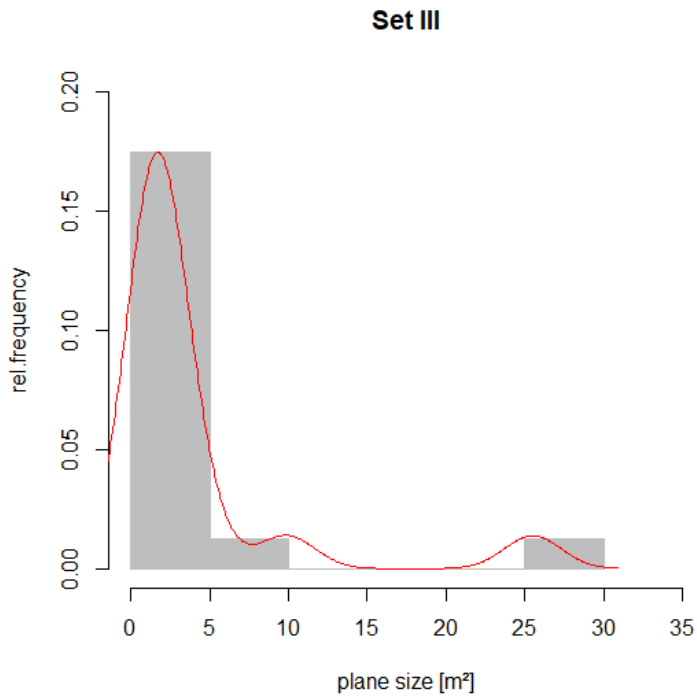


Figure 130: Plane sizes of set III, density line shown in red

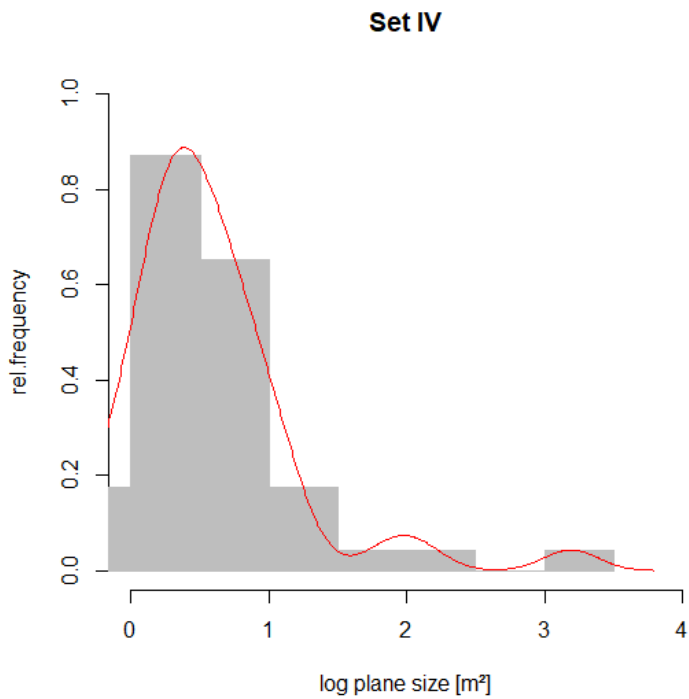


Figure 131: Plane sizes of set IV, density line shown in red

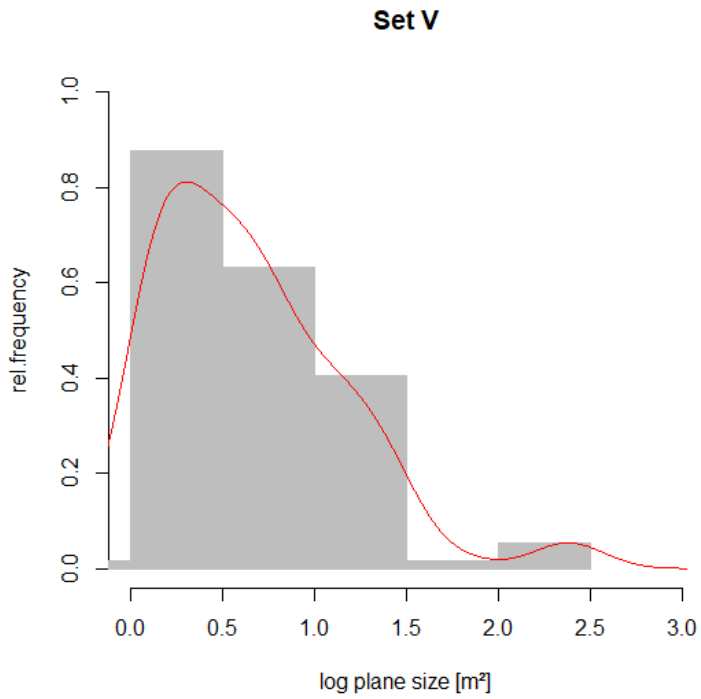


Figure 132: Plane sizes of set V, density line shown in red

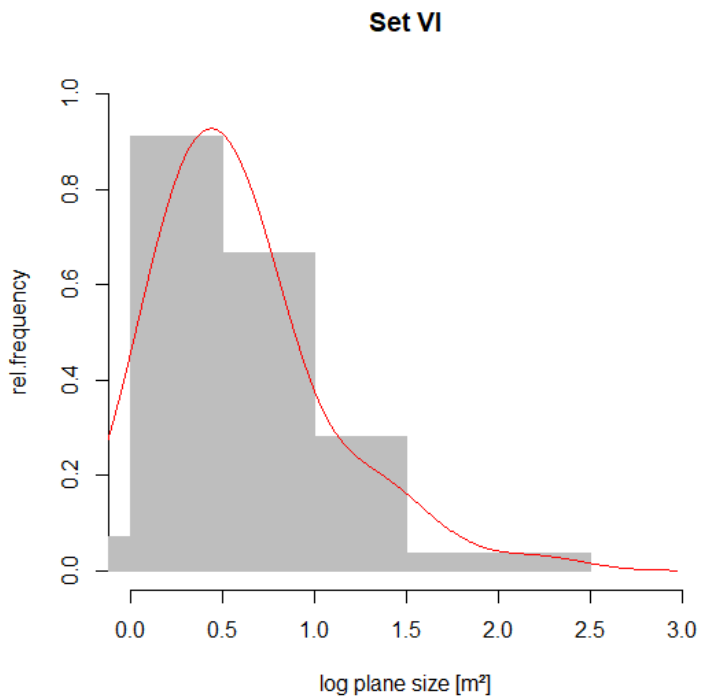


Figure 133: Plane sizes of set VI, density line shown in red

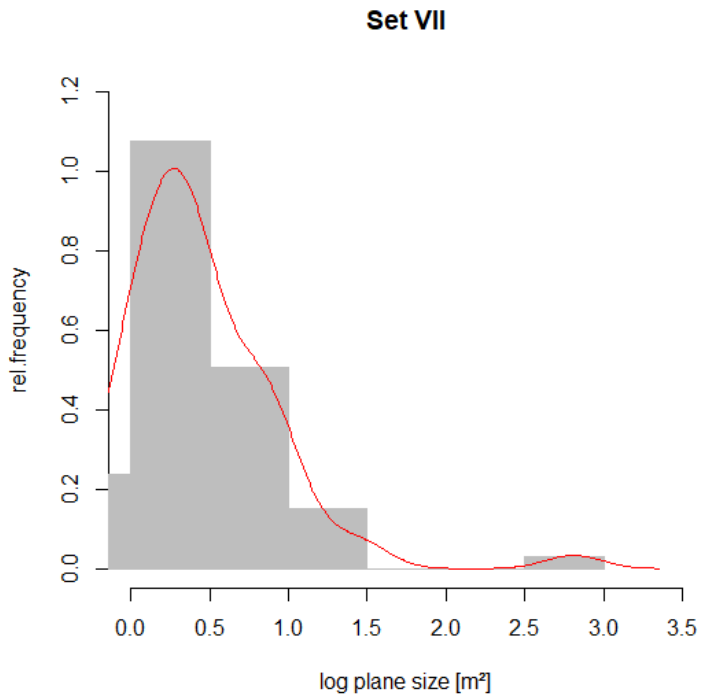


Figure 134: Plane sizes of set VII, density line shown in red

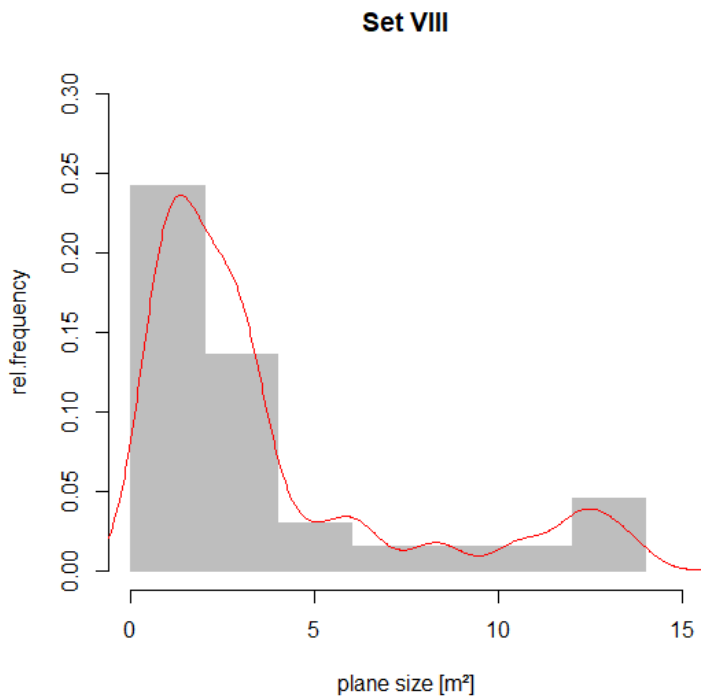


Figure 135: Plane sizes of set VIII, density line shown in red

The termination of the sets is investigated as in the segments before. However, the plot of the number of connected sets (“Termination in how many sets?”) differs: It summarizes sets IV, V, VI, VII, and VIII as sheeting joint (“SJ”). Therefore, a set may connect to non-SJ-sets only (I, II and/or III), to SJ-sets only, or to both. The plot would have lost any clarity without this simplification. The decision about the SJ-sets is based on the visual investigation of the rock face, combined with the orientation and the plane sizes. Further information about the sheeting joint sets is given in chapters 6.1 interpretation – joint sets, and 7.2 discussion – results. The tables, upon which the termination diagrams are based, are given in the appendix.

Set I, a non-SJ-set, terminates in sets V, II, III, and IV (Figure 136). The neighborhood changes the termination pattern in relative and in absolute terms. The isolated planes of set I are connected to other planes, actually (Figure 137). Set I mostly terminates in SJ-sets, but there are also some planes which do not connect with any SJ-set, and some which connect with both, SJ-sets and non-SJ-sets. The main problem for the plane fitting process is the roundness of the rock mass (Figure 138).

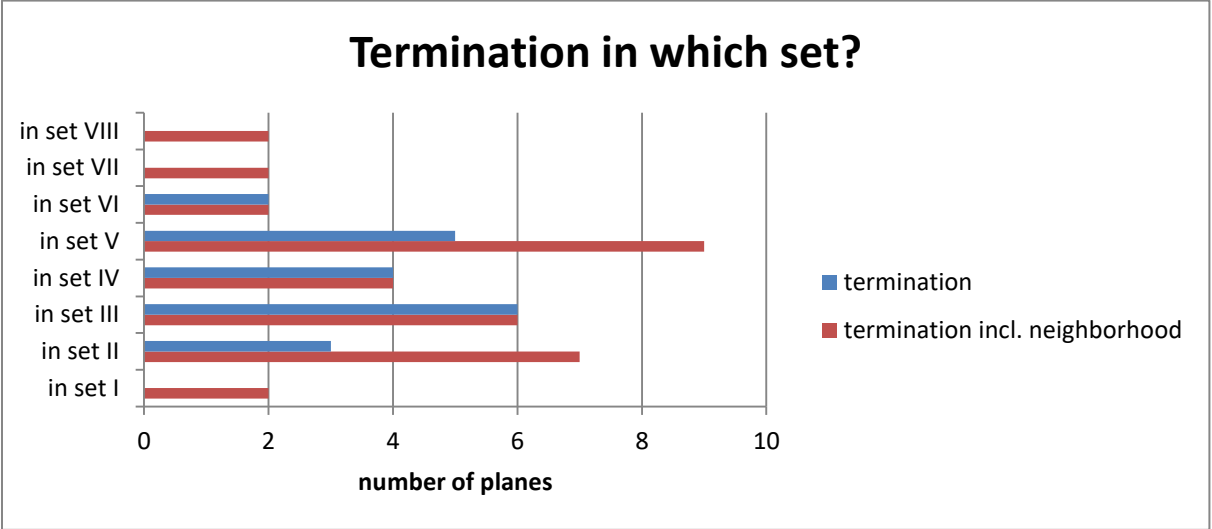


Figure 136: Termination of set I

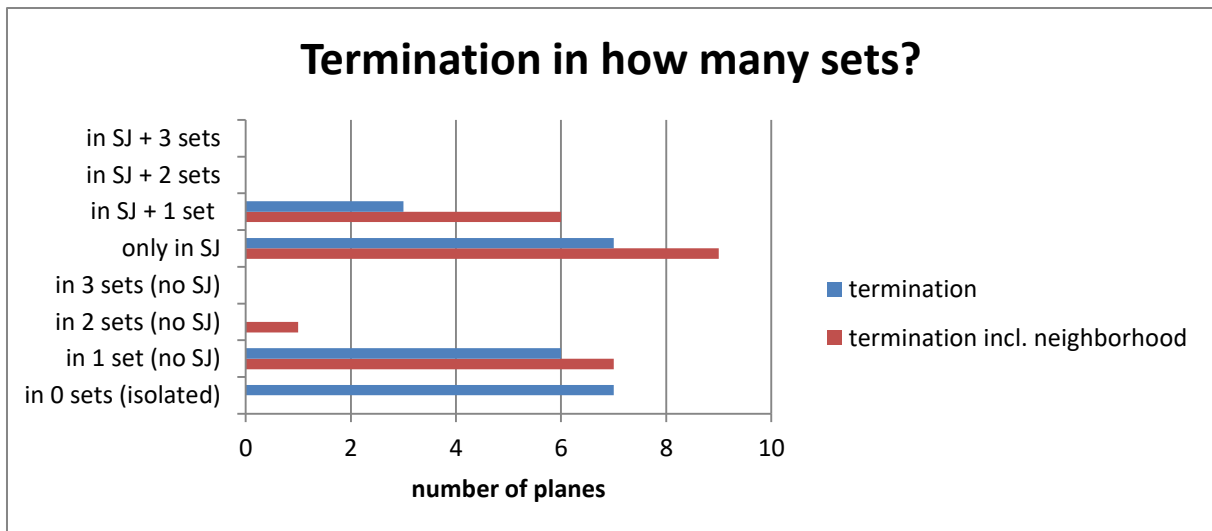


Figure 137: Termination of set I

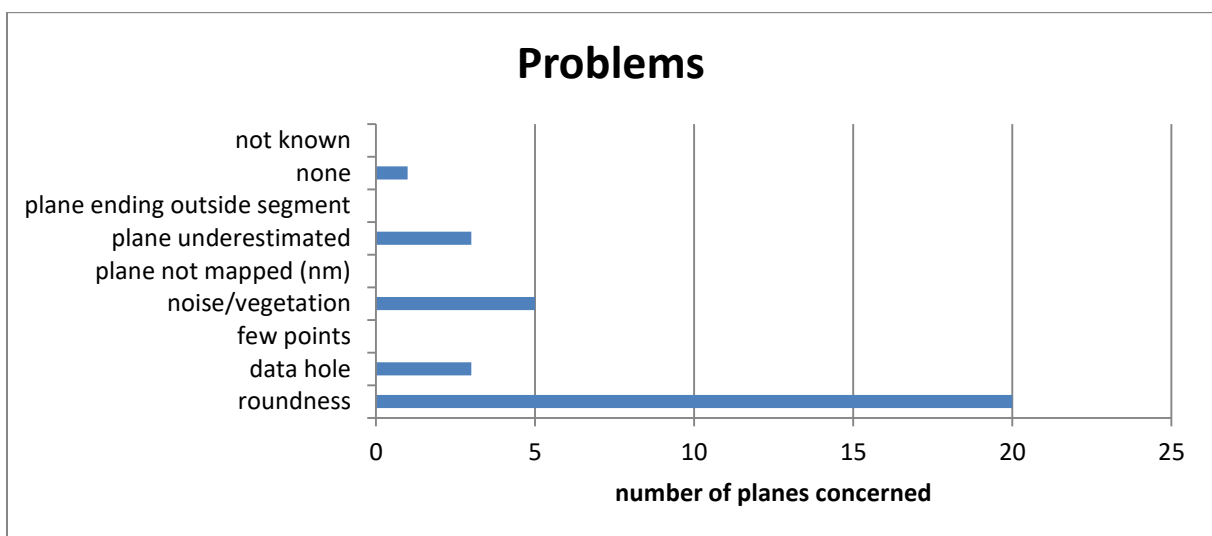


Figure 138: Problems for plane fitting in set I

Set II is a non-SJ-set. It mostly terminates in SJ-sets (set V, set VI, set VIII, set IV), but several planes also terminate in set I (Figure 139). If the neighborhood is not taken into account, set II does not terminate in set III or in itself. However, the neighborhood consideration changes this. The majority of set II planes end in SJ-sets, this is also visualized in Figure 140. In some cases, set II planes also connect with up to two non-SJ-sets. The most common plane fitting problem is roundness, but noise or vegetation also poses a challenge (Figure 141).

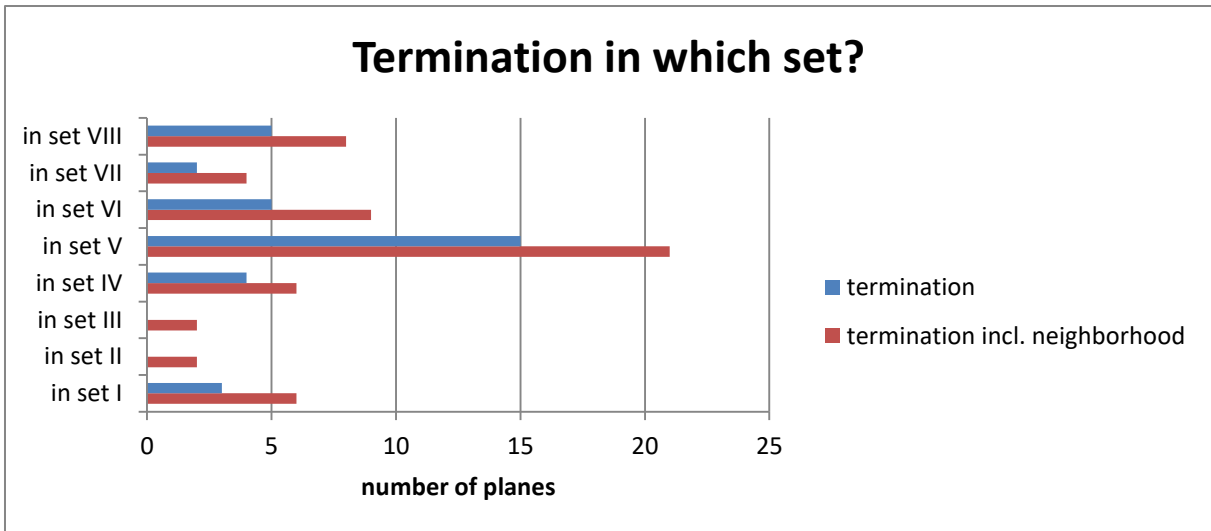


Figure 139: Termination of set II

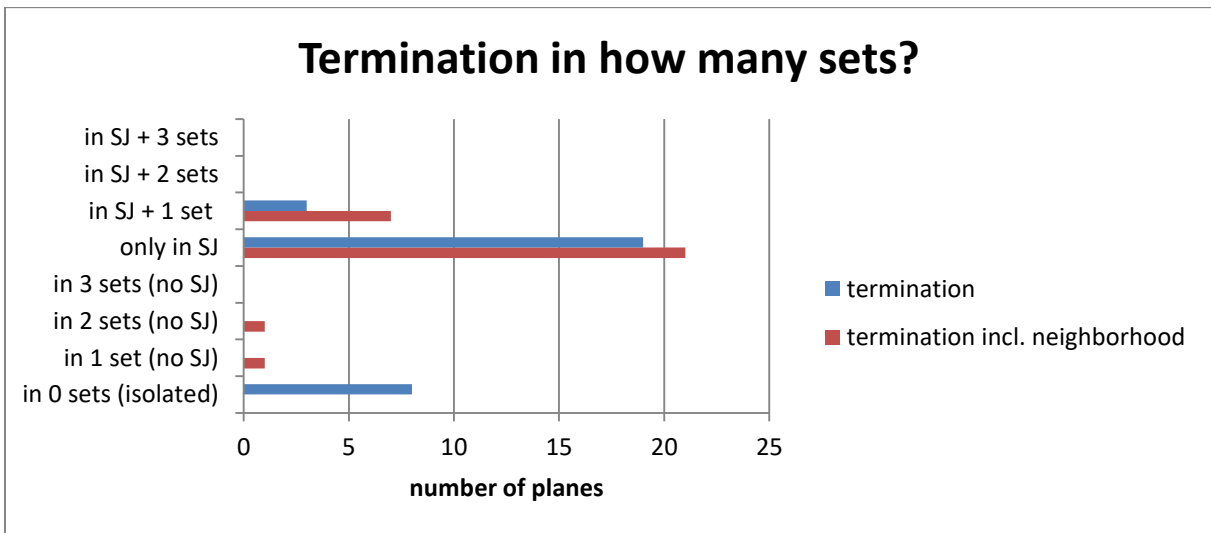


Figure 140: Termination of set II

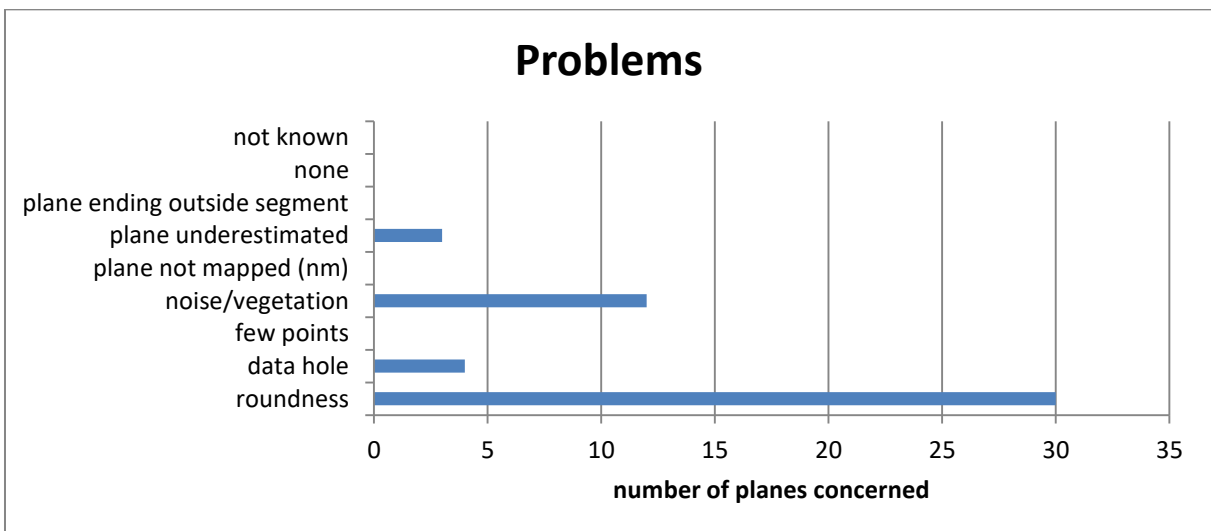


Figure 141: Problems for plane fitting in set II

Set III is a non-SJ-set. It mostly terminates in set I, but also in sets V and VI (Figure 142). Set III never terminates in set VIII. The isolated planes in Figure 143 appear to actually connect to other planes when the neighborhood is considered. The majority of planes connect to SJ-sets, to one non-SJ-set, or to SJ-sets and one non-SJ-set. The main problems concerning this set are roundness and, of a much lesser extent, noise or vegetation (Figure 144).

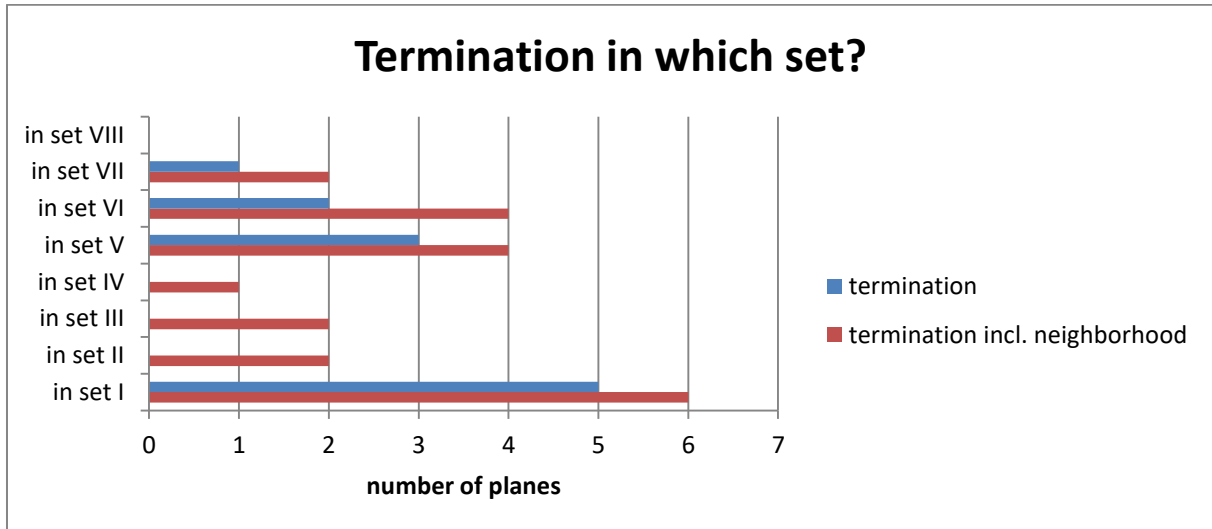


Figure 142: Termination of set III

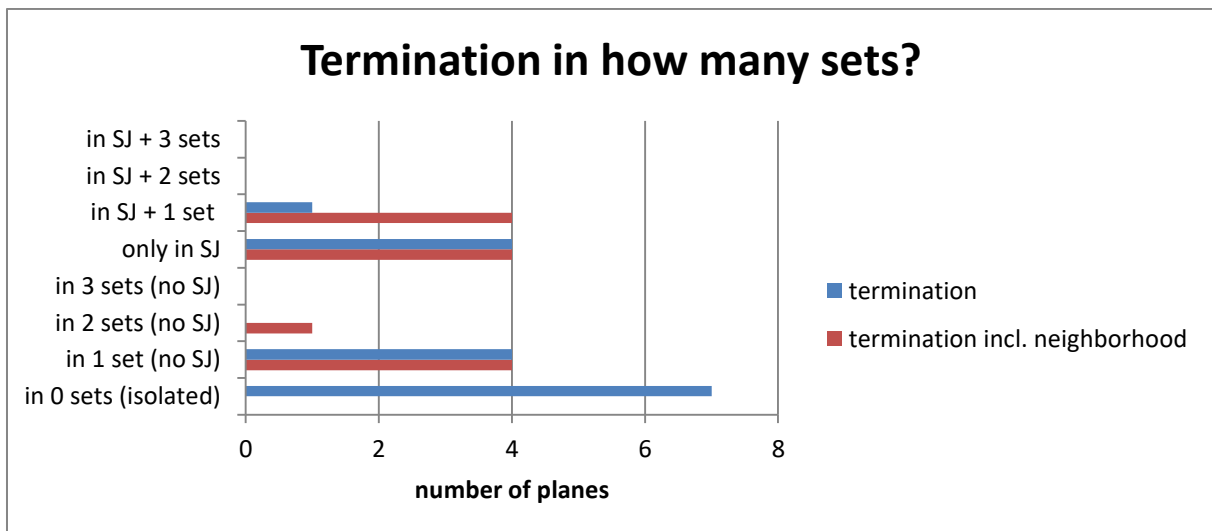


Figure 143: Termination of set III

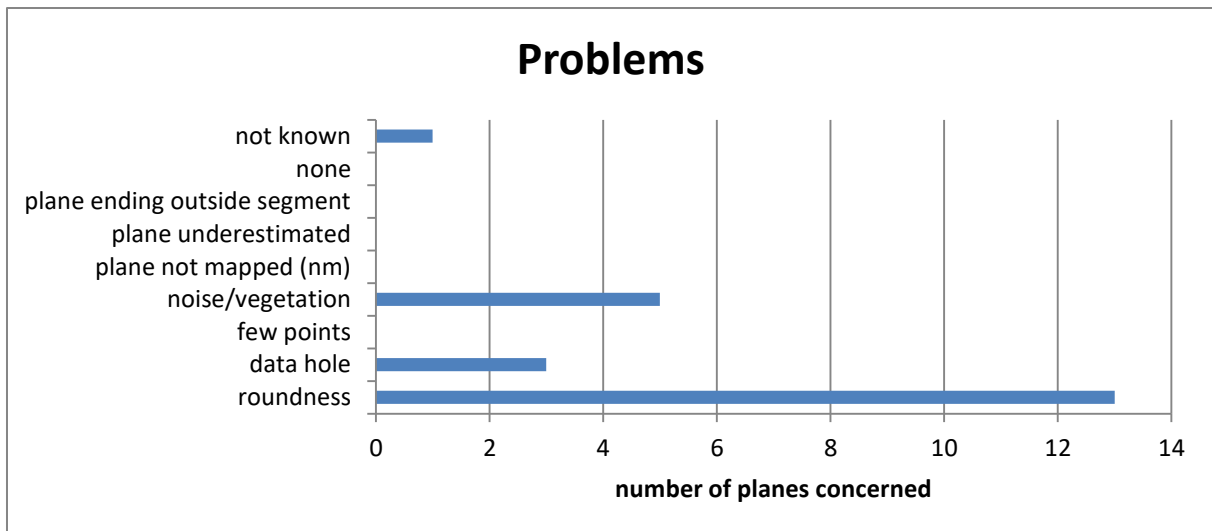


Figure 144: Problems for plane fitting in set III

The majority of set IV planes terminate in SJ-sets, including itself (Figure 145). A very low amount of planes also terminates in non-SJ planes. This trend is also shown in Figure 146, which further outlines that no set IV plane terminates in all non-SJ-sets at the same time. As for the previous sets of this segment, the major plane fitting problems are roundness and noise or vegetation (Figure 147).

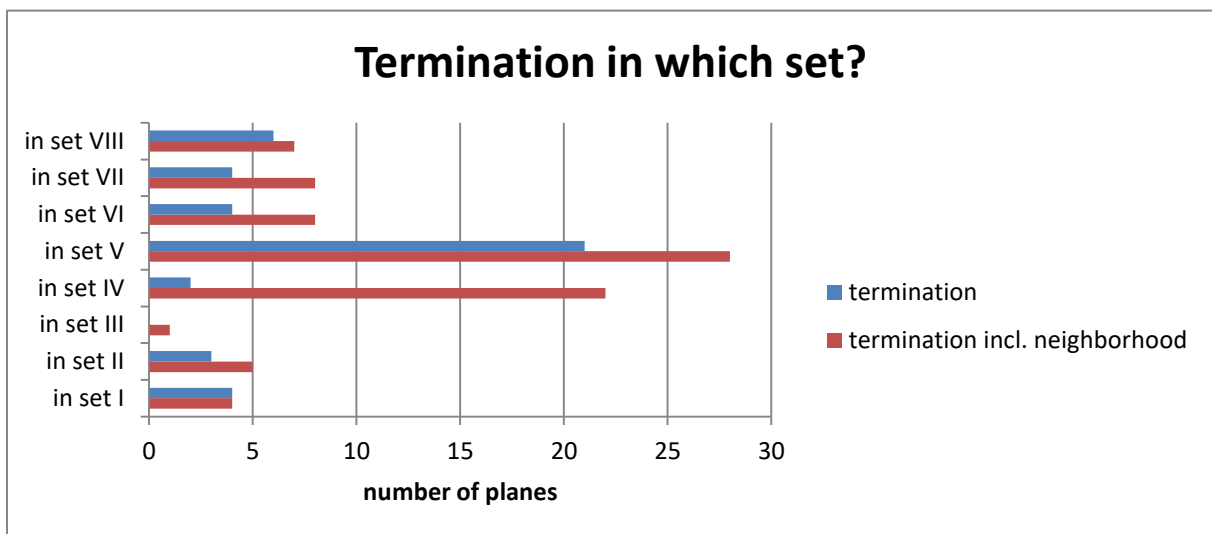


Figure 145: Termination of set IV

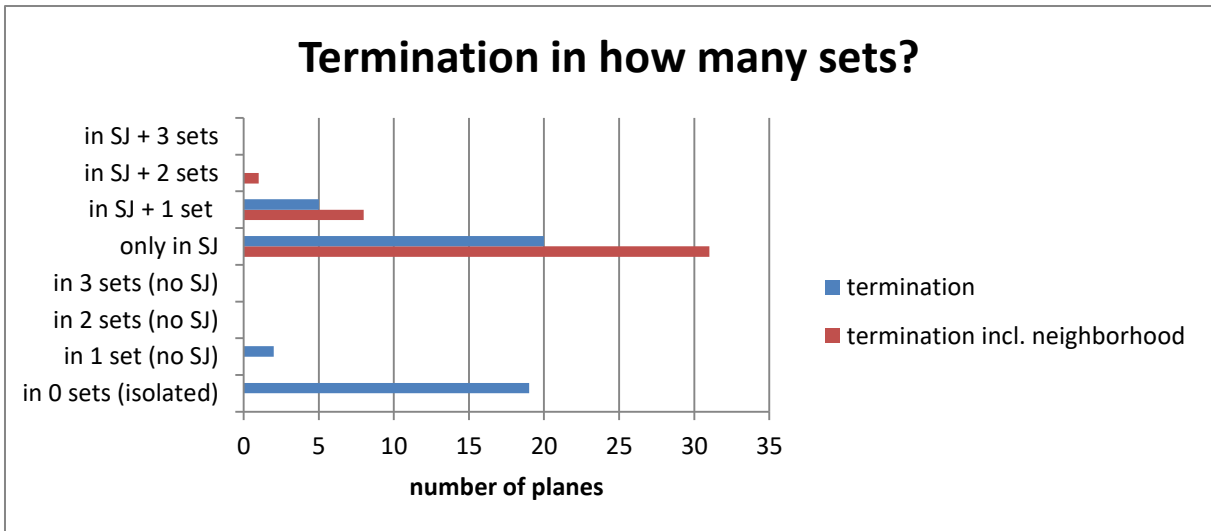


Figure 146: Termination of set IV

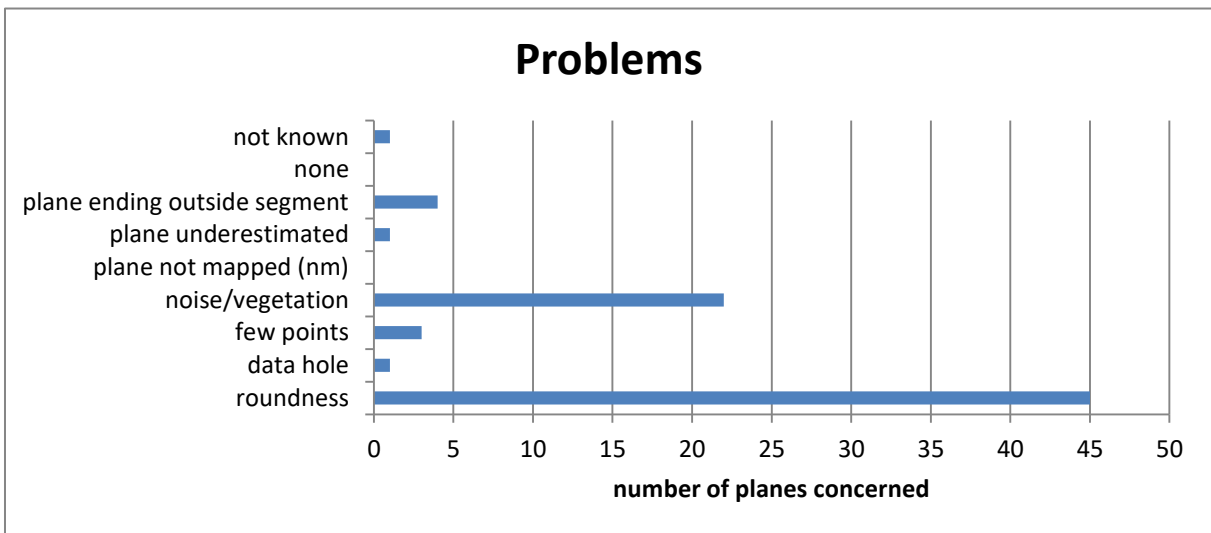


Figure 147: Problems for plane fitting in set IV

Set V's termination is described in Figure 148 to Figure 150. It terminates in all sets, including itself. The most terminations occur in sets VI, VII, IV, and V. This set never terminates in three non-SJ-sets (Figure 149). A peak in frequency is observable for termination in SJ-sets only. Roundness and noise or vegetation are the major problems for plane fitting in this set (Figure 150).

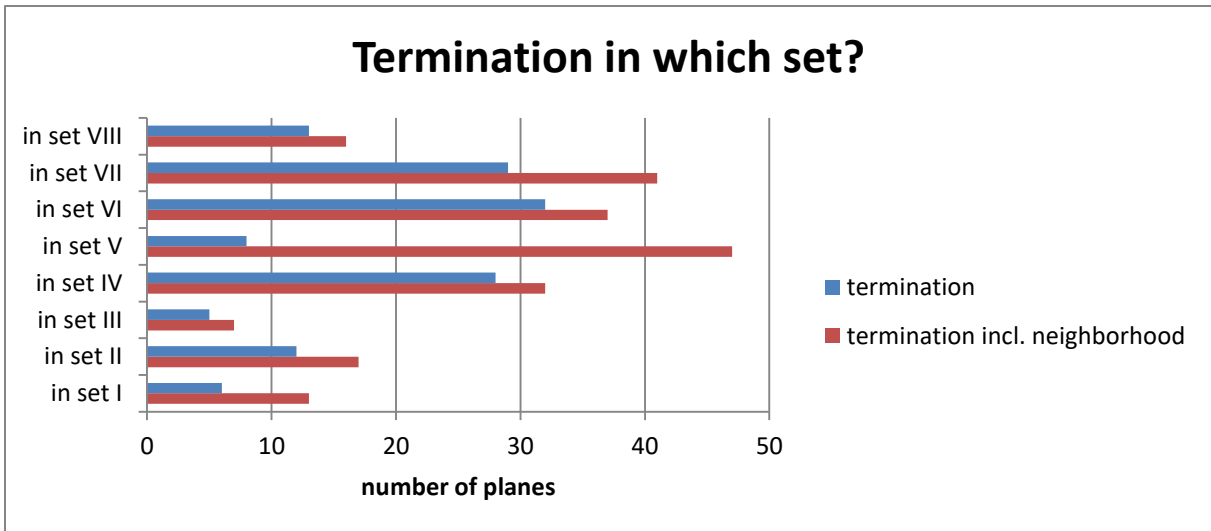


Figure 148: Termination of set V

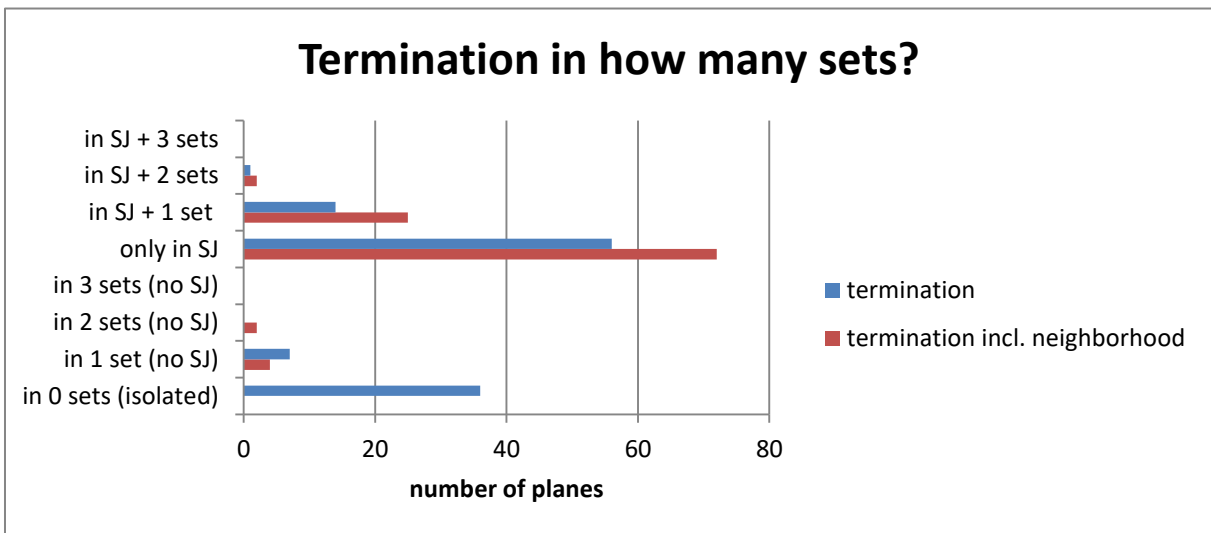


Figure 149: Termination of set V

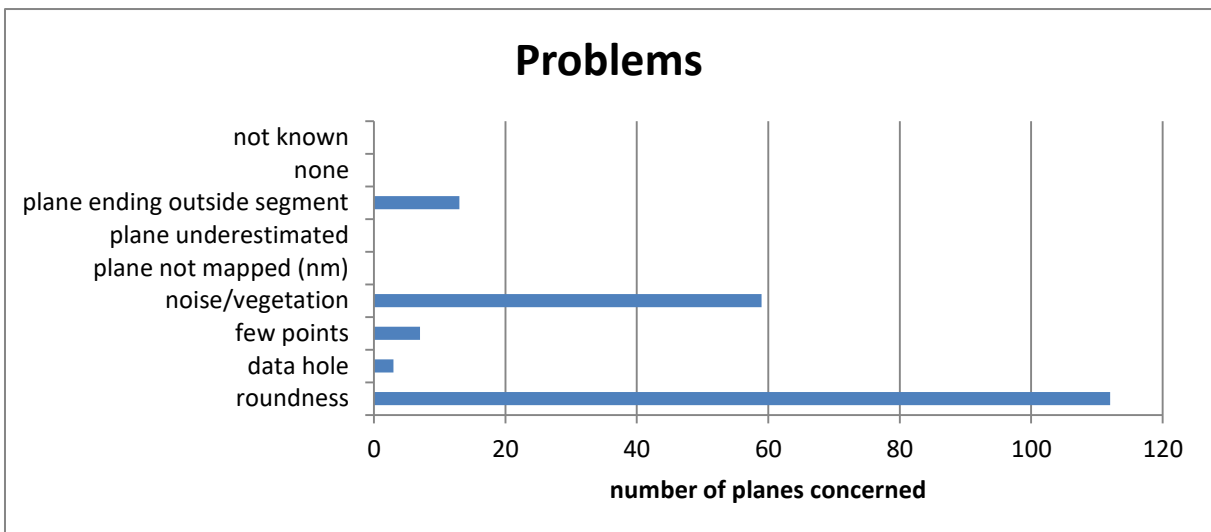


Figure 150: Problems for plane fitting in set V

Set VI, another SJ-set, tends to terminate in other SJ-sets, namely in sets V and VII (Figure 151). This tendency is also shown in Figure 152: The majority of set VI-planes connect with other SJ-planes. In addition, set VI connects with up to two non-SJ-sets. The most common problems which are faced during the plane fitting procedure are roundness and noise or vegetation (Figure 153).

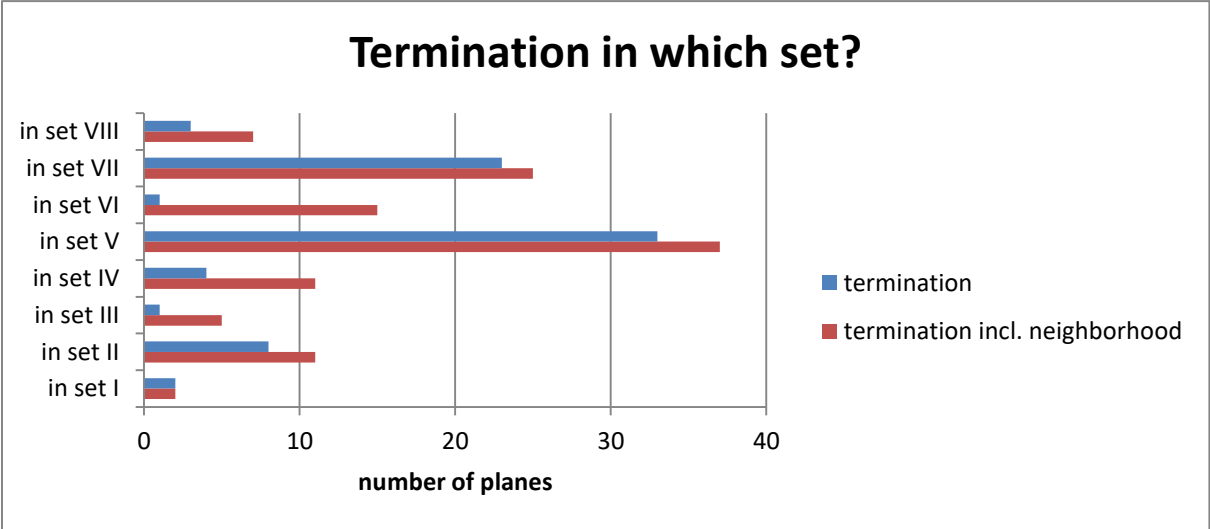


Figure 151: Termination of set VI

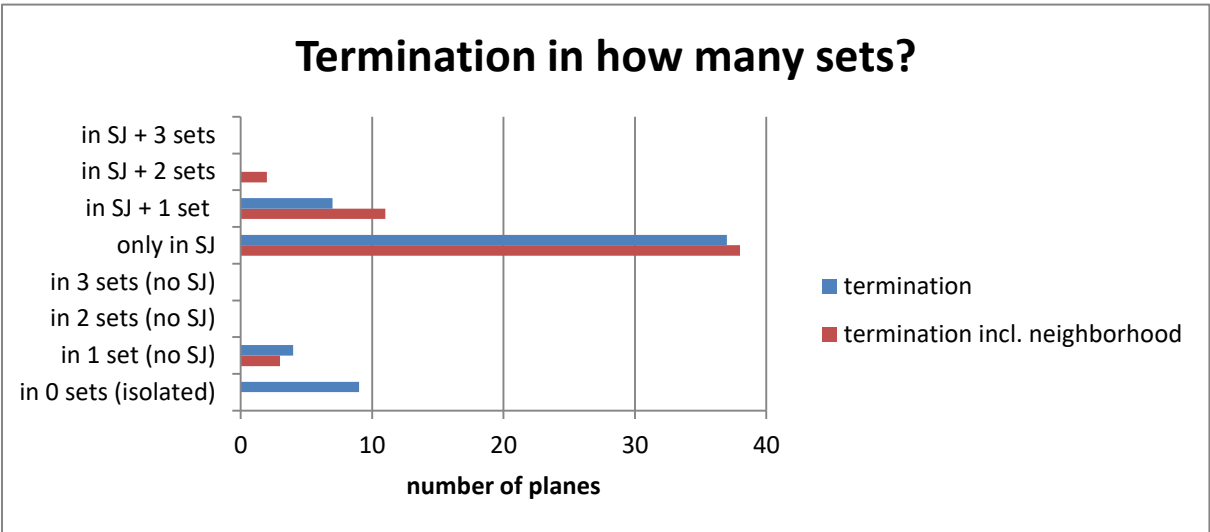


Figure 152: Termination of set VI

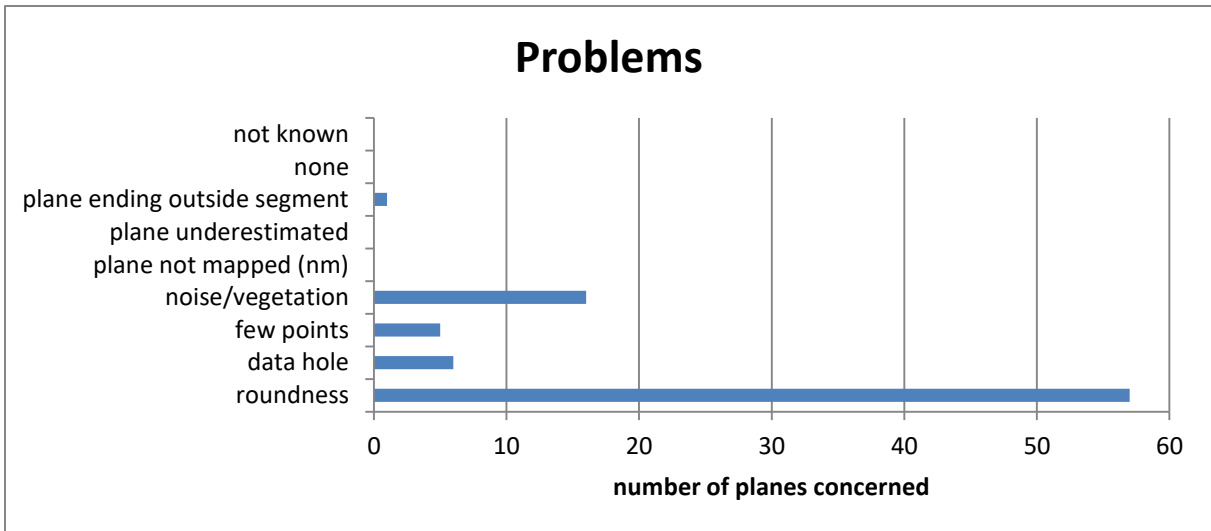


Figure 153: Problems for plane fitting in set VI

Set VII also tends to terminate in SJ-sets, mainly in sets V and VI (Figure 154). When the neighborhood is considered, set VII also terminates in the non-SJ-sets I, II, and III. However, as can be seen in Figure 155, set VII-planes connecting with non-SJ-planes also connect to SJ-planes. The majority of set VII planes terminate in SJ-planes only. As for all previous sets of this segment, the main plane fitting problem is roundness, followed by noise or vegetation (Figure 156).

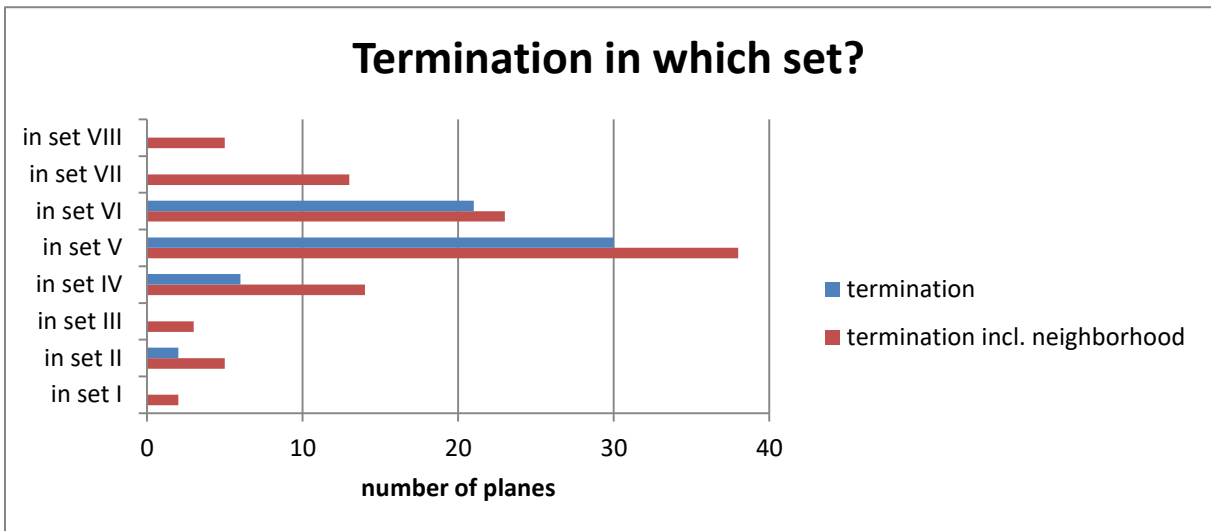


Figure 154: Termination of set VII

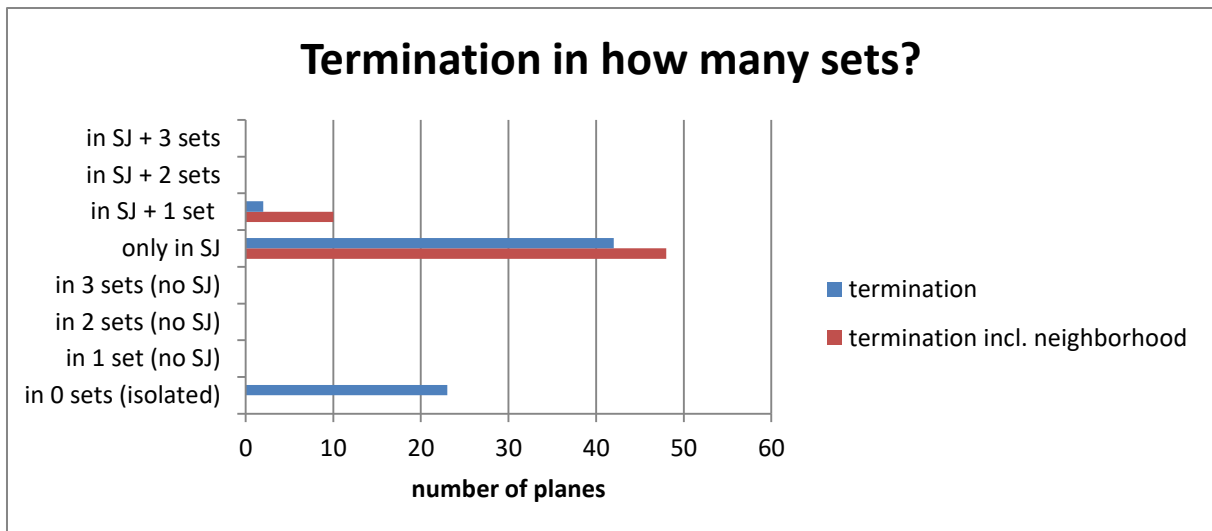


Figure 155: Termination of set VII

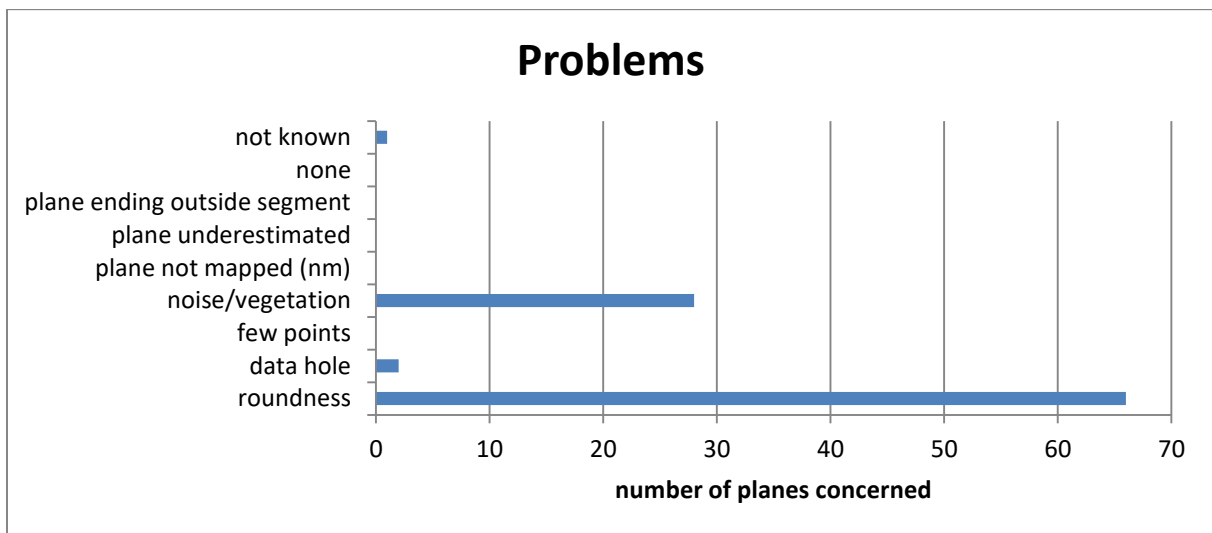


Figure 156: Problems for plane fitting in set VII

Set VIII is a SJ-set, too. It terminates in other SJ-sets, primarily in set V (Figure 157). Set VIII never terminates in set III or in more than one non-SJ-set. This is visualized in Figure 158. The majority of set VIII-planes only connect with other SJ-planes. The biggest problems for plane fitting in this set are the same as in every other set of this segment: roundness and noise or vegetation (Figure 159).

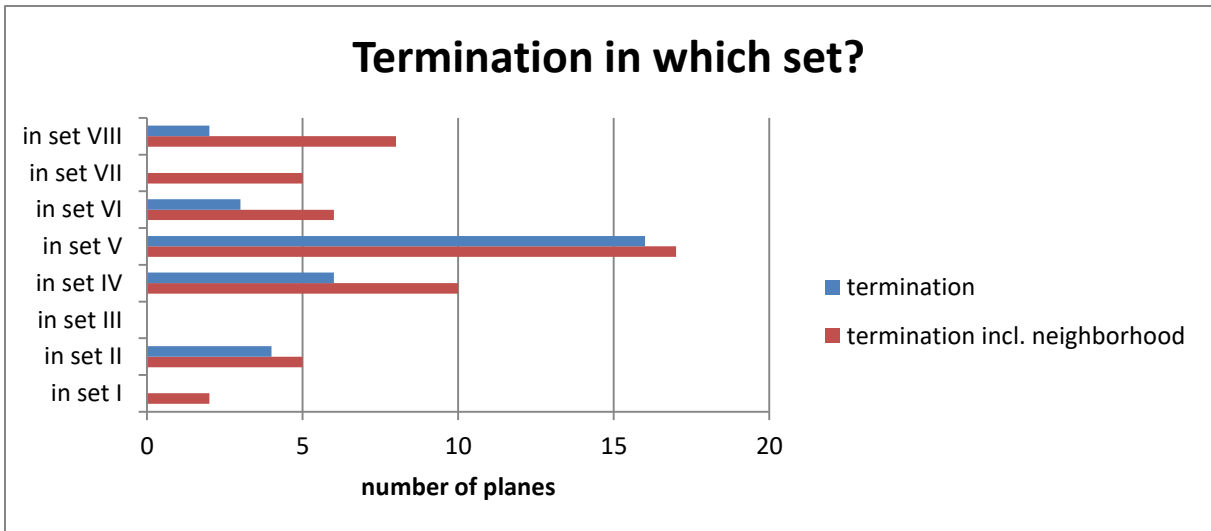


Figure 157: Termination of set VIII

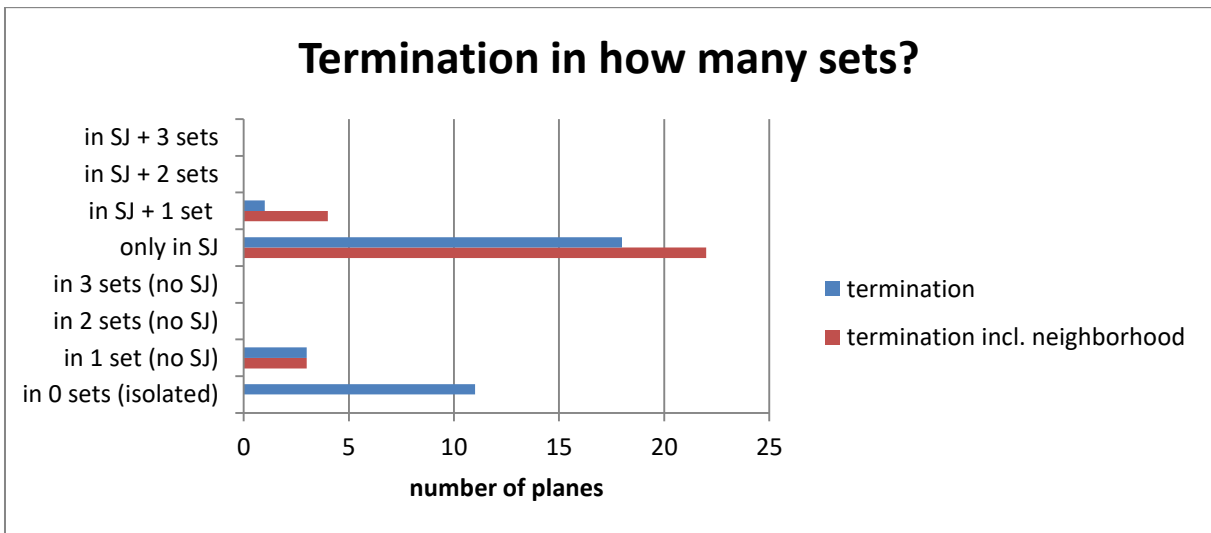


Figure 158: Termination of set VIII

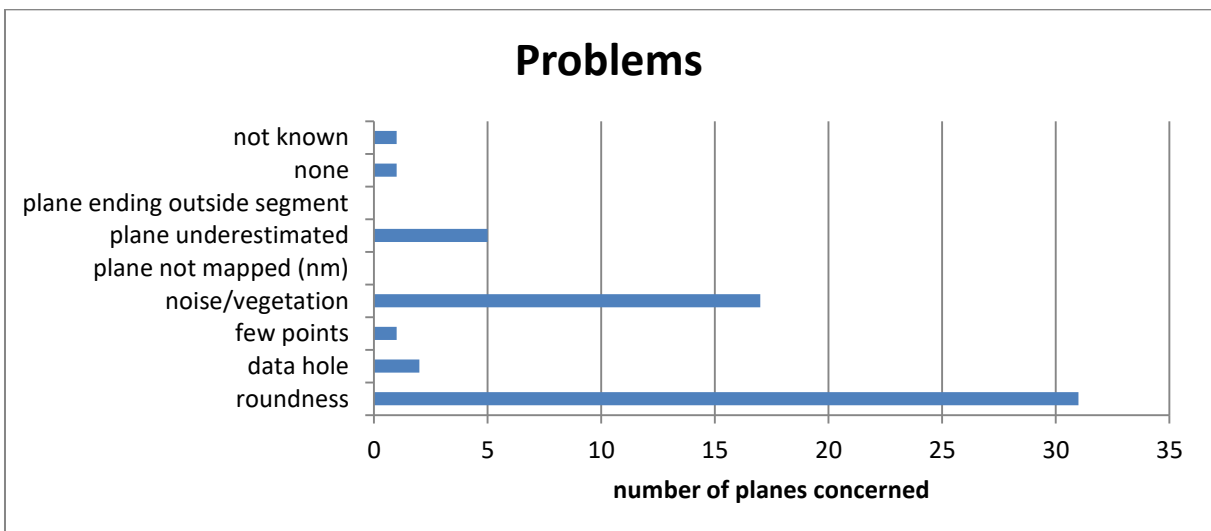


Figure 159: Problems for plane fitting of set VIII

6 Interpretation

6.1 Joint sets

The presence of sheeting joints has been anticipated in the previous chapter. In general, according to Hencher et al. (2011 – review paper, so references therein are always included in the citation), sheeting joints are characterized by their slope-parallel run and their long persistence without rock bridges. They occur in shallow depths (Martel, 2017, and references therein) in steep and flat lying terrain (Hencher et al., 2011), which is convex in at least one direction (Martel, 2017, and references therein). Sheeting joints are common in granite (Hencher et al., 2011). Their dip varies according to the slope's dip from horizontal to vertical or even to overhanging (Martel, 2017, and references therein). Another important characteristic of sheeting joints is their curvature and their occurrence in collections (Martel, 2017). Their spacing increases with depth, while being relatively small in relation to the plane extent and curvature, as well as not being constant, i.e. the joints often (partly) overlap and tend to round off corners. As sheeting joints typically are younger than other discontinuities, they tend to cut the latter, causing the high number of terminations in the sheeting joint set of all other sets (Martel, 2017, and references therein). However, there are also older sheeting joints which often show a high degree of weathering (Hencher et al., 2011). In case of failure or erosion, new sheeting joints develop. After calculations of an example of sheeting joints in granite in Korea, the erosion rate of slopes concerned by sheeting joints is higher than in the surroundings without sheeting joints (Hencher et al., 2011). Sheeting joints show a typical roughness and waviness, even superimposed by smaller roughness and steps (Hencher et al., 2011). The steps develop because of the interaction with other joints or during the development of the sheeting joint in terms of interaction and overlapping (Hencher et al., 2011).

Concerning segment 1, the joint set with the highest plane size and persistence is set 1. Its orientation dictates the slope face appearance. As already outlined above, the roundness of the rock face poses the biggest challenge. This corresponds to the description of sheeting joints in Hencher et al. (2011) in terms of a stepped rock face as a small waviness feature. Concerning the termination of this sheeting joint set, the majority of terminations has been mapped as “in set 1”. This is due to the waviness and stepping. Set 2 can also be counted as sheeting joint set due to its conforming dip direction as well as the 3D development of sheeting joints, i.e. their curvature. The orientation of the sheeting joints is unstable and varies with topography (see also: Figure 164). Flat-lying joints in the slope can be interpreted as sheeting joints if the slope recedes uphill, which is the case in segment 1. Sets 3, 4, and 5 do not belong to the sheeting joints. Sets 3 and 4 are conjugated sets. According to their appearance, especially as set planes laid over the RGB point cloud, sets 3 and 4 can be

interpreted to pre-date the sheeting joint sets. The set planes can be traced across sheeting joint plane boundaries. In addition, sets 3 and 4 influence the termination of the sheeting joint. This relation is also described in Hencher et al. (2011). The intersection angle of set 3 and the sheeting joint (set 1) is 72.55° , the one of set 4 and the sheeting joint (set 1) is 82.17° . Sets 3 and 4 intersect each other with an angle of 74.25° . Set 5, however, post-dates the sheeting joint. Its set planes are restricted to one tabular slab and do not exceed over several sheeting joint planes. Some set 5 planes terminate in one single sheeting joint plane only. Therefore, set 5 does not really influence the sheeting joint set's termination, which is another indication for the post-dating (Hencher et al., 2011). Martel (2017) gives an example of post-sheeting joint fractures, and describes the generated pattern as "masonry wall" due to the high intersection angle and the termination of the set in relation to the sheeting joint. The measured intersection angle between set 5 and the sheeting joint (set 1) is as high as 71.22° .

In segment 2, set a shows the typical sheeting joint characteristics: high plane size, i.e. high persistence, slope-defining orientation, steep dip. As set 1 in segment 1, the fitted planes often terminate in the set itself, which indicates the high waviness and stepping. Set b also belongs to the sheeting joint. Its dip direction is similar to set a's, but set b has a medium dip. The development principle is the same as for set 2 in segment 1. The difference between set 2 and set b lies in set b's more exposed position in direction of the vertical slope face, i.e. set b is closer to the sheeting joint's transition into the typical very steeply dipping joints. Set b also shows this transitioning behavior by its frequent termination in set a. Set a however terminates more often in itself than in set b, which might also be caused by set b's low amount of acquired planes. A similar number of terminations of set a as in itself is reached in set c+f, which is also steeply dipping. This high number of intersections is also visible in set c+f's termination plot (Figure 78). However, set c+f limits the sheeting joint plane size (set a) and strongly influences set a's termination. Therefore, set c+f seems to pre-date set a. Its intersection angle with set a is 68.78° . Set d also pre-dates the sheeting joint, as it forms the bottom and top borders for set a's planes. This relation is also true for set c+f planes, i.e. set d even pre-dates set c+f. These relations are visualized in the termination plots, which show that set d mainly terminates in sets a and c+f (Figure 81). The intersection angle of sets d and a is 75.26° . The conjugated sets c+f and d intersect each other with an angle of 64.02° . Although set e does not feature any planes, its role in the local development is investigated from the point cloud's normals directly. Its small surfaces are highly influenced by noise, but it seems to post-date all other sets in this segment (Figure 160). Therefore, the sets in this segment developed in the following order: set d - set c+f - set a and set b - set e.

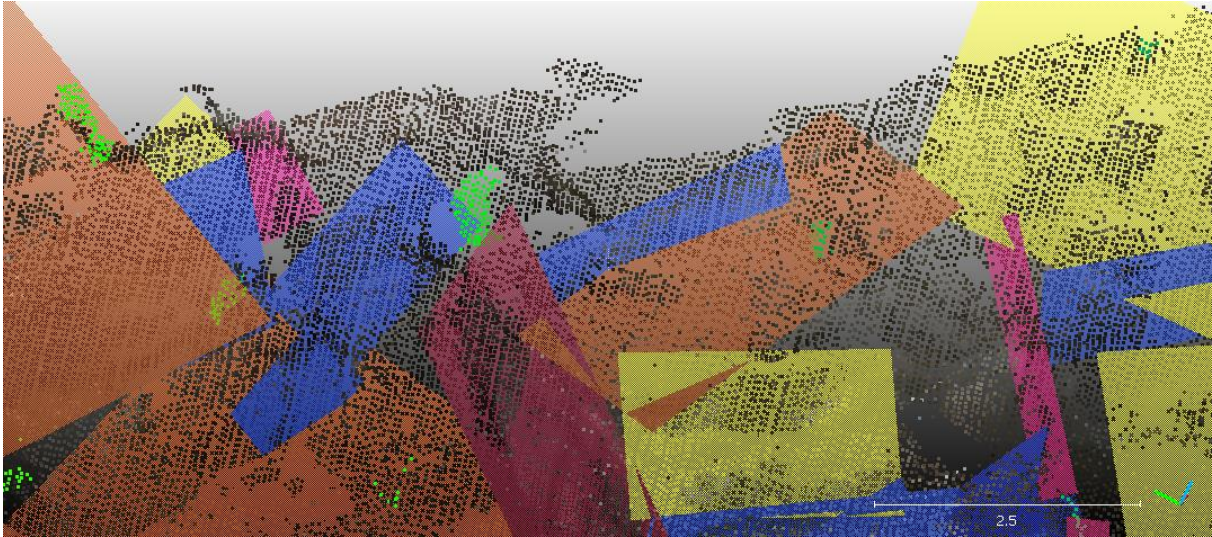


Figure 160: Segment 2's sets a (blue), b (yellow), c+f (magenta), d (orange), and e (green points). Software used: CloudCompare (2019)

In segment 3, set E represents the sub-vertical sheeting joint set, fulfilling the characteristics of slope-parallel orientation, big plane sizes and high persistence. Set B represents the transition to a shallower dipping sheeting joint, which is supported by its termination mainly in set E as well as by its dip direction which is similar to set E's. The orientation restriction limits set B's plane sizes, as it mainly represents a part of the sheeting joint's transition to a vertical run. Set E mainly terminates in itself, which might be caused by its waviness, and in set C+D. The intersection angle of these sets is 65.13° . The roundness concerns about 91% of all set B and set E planes, while the roundness problems of sets A and C+D concern 83% and 87% of the set planes. The conjugated sets A and C+D intersect with an angle of 72.51° . Set C+D confines set E's but also set A's planes, so it is supposed to pre-date the sheeting joint and set A. Set E's tendency to terminate in set C+D supports this development order. Set A also pre-dates set E, as it intersects set E's planes (intersection angle: 43.96°). Therefore, set C+D is the oldest set, followed by set A. The youngest set is the sheeting joint, represented in two inclinations by sets B and E.

Segment 4's sheeting joint sets are sets IV, V, VI, VII, and VIII. Some of these sets show very high plane sizes, namely sets IV, V, VI, and VII. Their orientation dictates the slope face. According to Martel (2017, review paper – always includes references therein), a very important characteristic of sheeting joints is their curvature. In this segment, the curvature is represented by the classification into different sets. In combination with the roundness of the discontinuities, which has been identified as the major problem for plane fitting, the sheeting joint is divided into several parts, i.e. sets. Sets I and III show smaller plane sizes and often terminate in each other. They are conjugated sets pre-dating the sheeting joint, intersecting each other at an angle of 37.45° . Set I intersects the sheeting joint sets by angles of 57.01° (set VI) to 77.38° (set VII), set III by angles of 60.66° (set VII) to 79.85° (set V). The sheeting

joint sets show a similar termination behavior with the majority of terminations in other sheeting joint planes, while sets I and III less often terminate in sheeting joint planes. However, their connection to each other is more pronounced than the connection of sheeting joint planes to these sets I and III. Set II neither is a sheeting joint set and post-dates the sheeting joints. This is indicated by the contact between set II and the sheeting joint, where set II does not limit the sheeting joint's plane extension, but vice versa. On some sheet surfaces, set II can be traced, but it does not cut the tabular sheet. Concerning the intersection angles of set II and the sheeting joint sets with the highest plane sizes (IV, V, VI, VII), these angles range from 49.01° (set VI) to 79.05° (set VII). Compared to sheeting joint sets, set II shows a higher percentage of terminations in sets I and III. According to photos taken by Kaspar (2012) on site, the lower leftmost part of segment 4 seems to be concealed by shotcrete. This is supported by the surface color and its condition in the point cloud which are quite similar to the photos.

Table 13 compares the sheeting joint characteristics of all segments. The mean orientation of the point cloud normals has been calculated by FracMan (Golder Associates Inc., 2018), while the mean orientation of the planes fitted in CloudCompare (2019) has been assessed by Dips (Rocscience Inc., 2018). Concerning the orientation, each segment contains sheeting joints of varying dip which is caused by the curvature. The orientations of segments 1, 2, and 3 correspond very well. Segment 4 shows a higher variation in dip direction, but still fits in a wider sheeting joint dip direction range of 50° to 102° and 254° to 315 °. The most flat-lying part of the sheeting joint is located in segment 1 (set 2, dip angle 28.3890°), as well as the steepest part (set 1, dip angle 86.6400°). Segments 2 to 4's minimum and maximum dips are in between. Figure 161 shows the mean plane poles of all segments' sheeting joints, outlining the trend in dip direction as well as the varying dip. In each segment, at least one sheeting joint set shows very high plane sizes raising the mean set plane size. In comparison to non-sheeting joint set plane sizes, the sheeting joint sets differ in a high mean plane size, but an unremarkable median plane size. Non-sheeting joint sets featuring bigger set planes in general show both a high mean and median plane size.

Table 13: Sheeting joints of all segments

	Segment 1 – set 1+2	Segment 2 – set a+b	Segment 3 – set B+E	Segment 4 – set IV+V+VI+VII+VIII
Mean orientation, normals	1: 74.4690/86.6400 2: 287.1220/28.3890	a: 230.3090/84.9710 b: 250.1180/48.5650	B: 257.4160/56.0670 E: 102.7330/80.8470	IV: 254.7600/68.5870 V: 290.4080/74.0750 VI: 315.3970/74.1380 VII: 315.3750/43.6910 VIII: 95.8660/72.1410
Mean orientation, planes	1: 74.3900/89.3400 2: 286.4600/18.0200	a: 227.2600/84.7200 b: 251.3900/44.1000	B: 255.5500/54.8800 E: 102.9000/84.8600	IV: 254.8200/68.9500 V: 290.8700/74.2400 VI: 311.2200/73.6500 VII: 313.3000/43.6300 VIII: 94.3700/72.5800
Mean plane size (> 1m²)	1: 13.6214 2: 3.9828	a: 9.6204 b: 3.8506	B: 2.8377 E: 9.4576	IV: 45.6565 V: 13.2536 VI: 9.3280 VII: 15.3817 VIII: 4.3816
Median plane size (>1 m²)	1: 4.5918 2: 4.0200	a: 3.1821 b: 2.7211	B: 1.8275 E: 2.4102	IV: 3.4011 V: 3.7397 VI: 3.2869 VII: 2.7009 VIII: 2.8790
Pre-dating sets	3,4	d, c+f	C+D, A	I, III
Post-dating sets	5	e	-	II

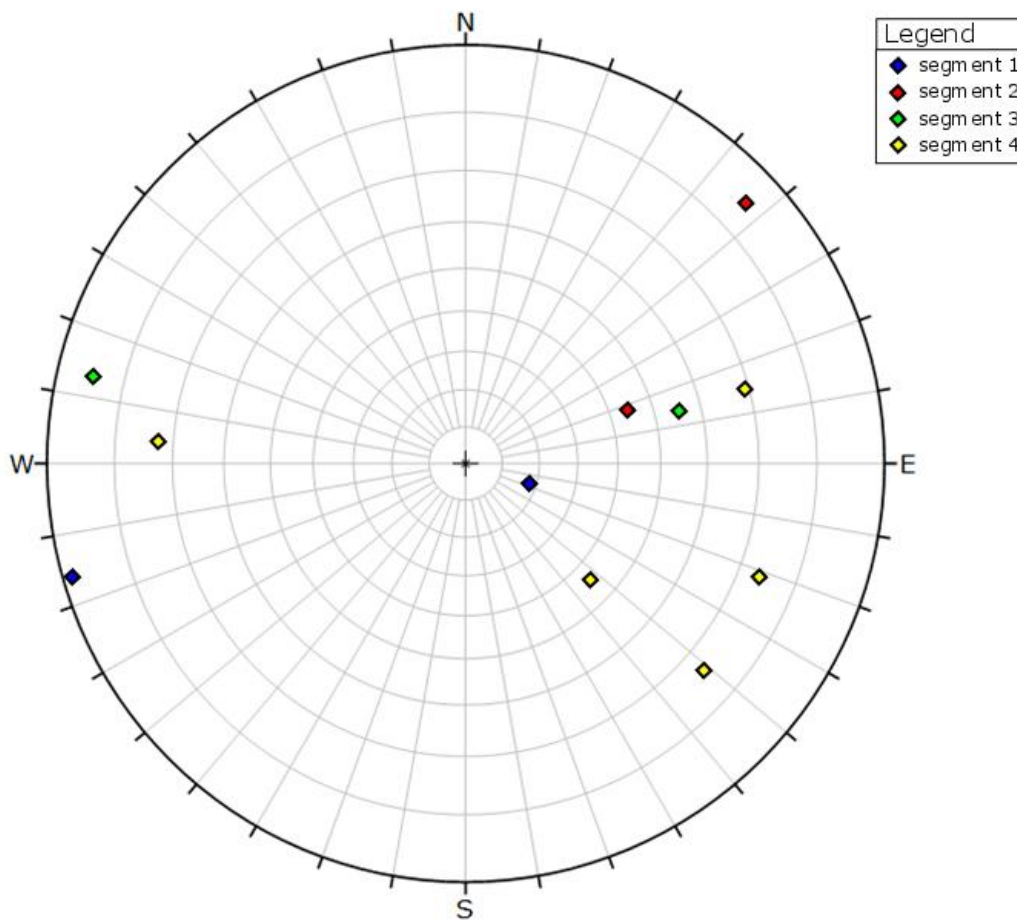


Figure 161: Mean plane poles of all sheeting joint sets. Software used: Dips (Rocscience Inc., 2018)

The characteristics of the sets pre- and post-dating the sheeting joints are compared in Table 14 and Table 15. This leads to the identification of sets corresponding to each other in the four segments. Concerning the orientation, one has to keep in mind that the values given in the tables below are mean orientations. The orientation of set 3 (segment 1) and set I (segment 4), for example, are similar (Figure 162). Although their plane sizes differ, their termination patterns resemble each other in terms of the number of sets in which they terminate (1 to 2) and of their termination in the conjugated set (4, III) as well as in the youngest set which post-dates the sheeting joint (5, II). Set A (segment 3) also corresponds quite well to sets 3 and I. Its mean and median plane size are similar to set 3's. Besides that no post-dating set has been identified in segment 3, set A's termination pattern is similar to the one of sets 3 and I in terms of its connection with the conjugated set. Set c+f (segment 2) somewhat differs in dip direction, but its dip resembles that of sets 3, A, and I. In addition, its dip direction is more similar to the dip directions of the already mentioned sets than of the other sets pre-dating the sheeting joints. The c-part of this set (orientation 143.2760/76.4750) is closer to the other segments' sets than the f-part (orientation 108.3480/84.7630). Set c+f's termination resembles that of set A: the majority of terminations are in the sheeting joint,

followed by the conjugated set and the concerned set itself. The intersection angles in relation to the local sheeting joint range from 43.96° (A to E) to 77.38° (I to VII). However, sets 3, c+f, A, and I are interpreted to correspond to each other in the four segments. The point of similar orientation (Figure 162) and termination can be also made for sets 4, d, and C+D. Set III shows a similar termination pattern, but its dip is steeper. However, the variance of the mean dip direction of the normals (variance: ~77°) is just ~7° above the one of segments 3, c+f, A, and I (variance: ~70°). In addition, set III is conjugated to set I, as set 4 to set 3, for example. Therefore, sets 4, d, C+D, and III are also corresponding sets in the various segments. The intersection angles with the local sheeting joints lie between 60.66° (III to VII) and 82.17° (4 to 1). In the plot in Figure 162, the corresponding sets 3, c+f, A, and I are visualized in darker colors, while sets 4, d, C+D, and III are represented by warmer colors. The conjugated sets of each segment intersect by angles of 64.02° (c+f to d), 72.51° (A to C+D), and 74.25° (3 to 4). With an intersection angle of 37.45°, the angular relation of segment 4's sets I and III is quite far from that. This can also be read from Figure 162.

Table 14: Comparison of sets pre-dating the sheeting joint

	Segment 1 – sets 3, 4	Segment 2 – sets c+f, d	Segment 3 – sets A, C+D	Segment 4 – sets I, III
Mean orientation, normals	3: 182.2950/71.8200 4: 359.9710/38.8400	c+f: 112.3420/83.6380 d: 293.8000/33.1690	A: 149.0030/78.8940 C+D: 313.4540/38.8260	I: 172.9120/70.5590 III: 10.9300/76.6630
Mean orientation, planes	3: 183.2900/70.2900 4: 355.7200/35.8400	c+f: 114.5300/84.500 d: 297.1100/31.8400	A: 146.4100/72.3600 C+D: 316.1800/35.7300	I: 175.6100/69.9800 III: 14.0200/76.7100
Mean plane size (>1 m²)	3: 6.6922 4: 10.3901	c+f: 6.1433 d: 52.9874	A: 7.5964 C+D: 6.3551	I: 2.0956 III: 4.2394
Median plane size (>1 m²)	3: 3.3434 4: 7.1739	c+f: 2.6019 d: 5.4573	A: 3.7863 C+D: 2.2439	I: 1.5668 III: 1.8195
Termination pattern, with neighborhood	3: most SJ, also sets 4, 5. In 1 to 2 sets 4: most SJ, also sets 3, 4. In 2 sets	c+f: most SJ, also set d, c+f. In 2 sets d: most SJ, also set c+f. In 2 to 3 sets	A: most SJ, also sets C+D, A. In 2 sets C+D: most SJ, also sets C+D, A. In 1 to 2 sets	I: most SJ, also sets II, III. In SJ, SJ+1, 1 set III: most I, also SJ. In SJ, SJ+1, 1 set

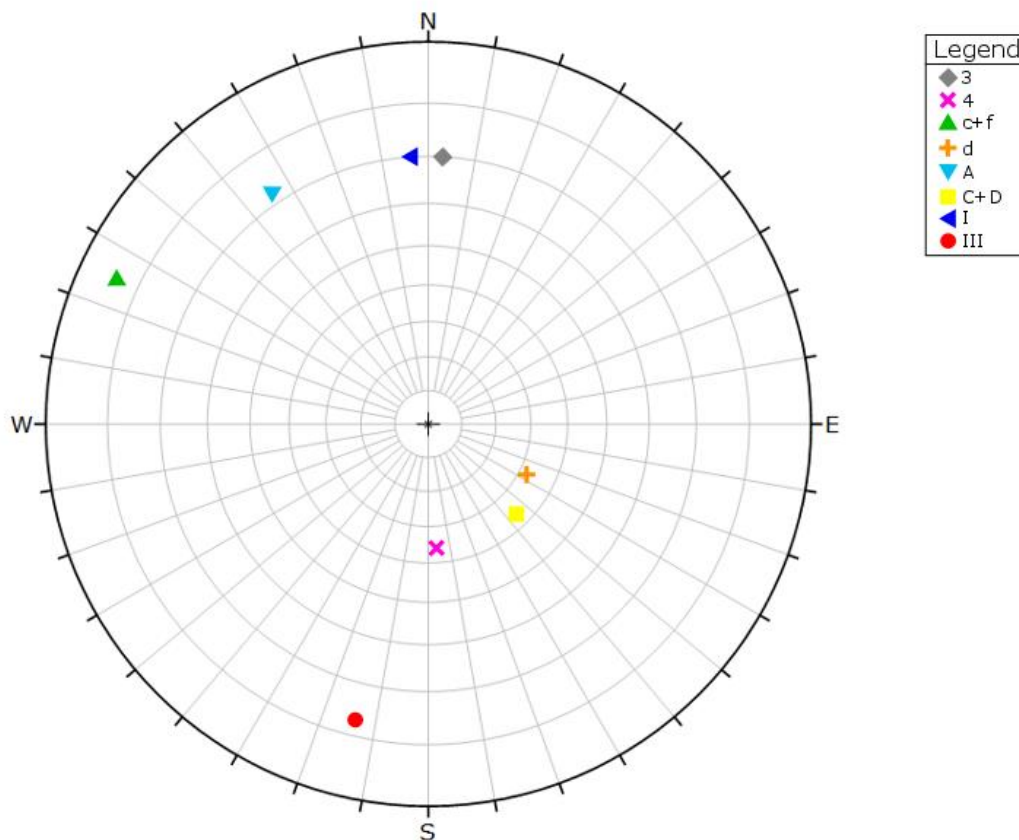


Figure 162: Stereogram plot of all sets (mean plane poles) pre-dating the sheeting joint. Software used: Dips (Rocscience Inc., 2018)

Table 15 compares the sets post-dating the sheeting joint, Figure 163 visualizes their orientation. A correspondence is visible for sets 5 (segment 1) and e (segment 2), although set e does not feature any fitted planes due to the small surface areas. However, both post-date the sheeting joint and are similarly oriented. Segment 5's planes are the smallest in segment 1, in terms of mean and median of the planes $>1 \text{ m}^2$. The similarity in orientation is also visualized in Figure 163. In segment 3, no set has been identified to post-date the sheeting joint. With the small plane sizes of the possibly corresponding sets kept in mind, the roundness, data holes, or noise could have obscured the set surfaces, i.e. a post-sheeting joint set might also be present in segment 3 but might not have been acquired. Segment 4's set II includes planes of higher mean and median plane sizes, and its orientation varies from set 5's and e's (Figure 163). At least the dip is somewhat similar. The only shared characteristic of set II, 5, and e, is the age in relation to the sheeting joint and the termination pattern (sheeting joint and conjugated sets, number of sets).

Table 15: Comparison of sets post-dating the sheeting joint

	Segment 1 – set 5	Segment 2 – set e	Segment 3	Segment 4 – set II
Mean orientation, normals	323.6080/77.3450	317.8360/70.4620	-	127.8690/61.8220
Mean orientation, planes	323.5000/73.0900	-	-	130.1400/57.1400
Mean plane size (>1 m²)	2.5270	-	-	3.5700
Median plane size (>1 m²)	1.6716	-	-	3.1438
Termination pattern, with neighborhood	Most SJ, also sets 3, 4. In 1 to 2 sets	-	-	Most SJ, also sets I, II, III. In SJ, SJ+1 set

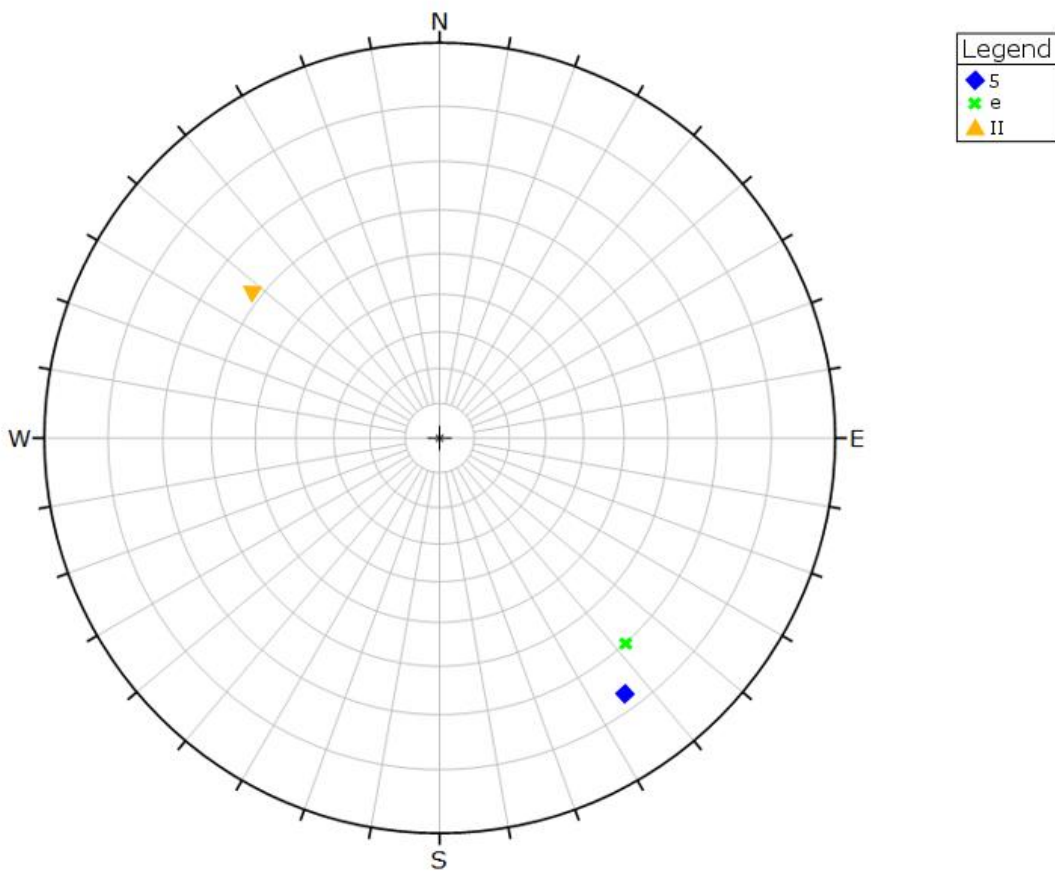


Figure 163: Stereogram plot of all sets (mean point cloud normals) post-dating the sheeting joints. Software used: Dips (Rocscience Inc., 2018)

As outlined in the geology chapter above, there are just two discontinuity systems post-dating the granite intrusion (González Clavijo and Martínez Catalán, 2002): the Villalcampo Shear System and subvertical faults. The latter commonly run NE-SW in the Ricobayo granites, with NW-SE running conjugated faults. The Villalcampo Shear System trends 130° SE and dips steeply. The system is a dextral strike-slip zone with a displacement of 3 to 4 km. Its conjugated, sinistral shear bands trend 70°-110° ENE-ESE (González Clavijo and Martínez Catalán, 2002). Written as azimuth values, the subvertical faults' dip direction would be about 135° or 315°, with a steep dip. However, "NE-SW" is quite imprecise, as "subvertical" is. Therefore, significant variation around the dip direction has to be expected and any steep dip is acceptable. The same is true for the conjugated, NW-SE striking faults. The dip direction would be around 45° or 225°. The Villalcampo shear system would be characterized by a dip direction of 40° or 220° and a steep dip, its conjugated shear bands by a dip direction of 160°-200°.

The sets pre-dating the sheeting joint might represent the subvertical faults. This is supported by a nearly perfect fit of the second largest plane in set c+f (segment 2) which is oriented (134/71). It terminates in the sheeting joint of segment 2 (sets a and b). As the sets 3, A, and I have been identified as corresponding sets to set c+f (Figure 162), these are also interpreted as representations of the NE-SW running subvertical faults mentioned by González Clavijo and Martínez Catalán (2002). In addition, the four mentioned sets have conjugated sets, namely sets 4, d, C+D, and III. However, only set III shows a "subvertical" dip. Together with the conjugation with the identified NE-SW subvertical faults and without any further information about these faults, sets 4, d, C+D, and III are interpreted as conjugated faults striking NE-SW. The mentioned NW-SE running faults are not present in the segments. The Villalcampo Shear System seems not to be represented by any features in the data. Moreover, González Clavijo and Martínez Catalán (2002) do not mention any occurrence at the Ricobayo Reservoir or the Río Esla, in contrast to the statement concerning the subvertical faults.

As already mentioned, the sheeting joints are younger than the subvertical faults. Concerning their formation, Hencher et al. (2011) state that in steep slopes, the maximum compressive stress caused by gravity runs parallel to the slope. Therefore, sheeting joints develop as slope-parallel, tensile fractures (Figure 164; Hencher et al., 2011). Martel (2017) also states high compressive stresses (several MPa or greater) parallel to the surface at locations with young sheeting joints, and low compressive stresses (<1 MPa) perpendicular to the surface. This is caused by the low or lacking overburden. Using a fracture mechanics approach, Martel (2017) identifies the topography's shape, the compressive stress state parallel to the surface, gravity, and groundwater pressure as important factors for sheeting joint initiation,

propagation, and termination. He rejects several “simpler” theses, e.g. that the removal of overburden would be the only reason for sheeting joints. Pre-existing fractures could enhance the formation of deep sheeting joints by acting as water conducts, but they could also hinder the formation as an already intensely fractured rock mass may not be able to sustain the magnitude of stresses needed for sheeting joint formation (Martel, 2017). Obviously, the rock mass has not been intensely fractured by the conjugated sets pre-dating the sheeting joints. Their influence as possible water conducts cannot be determined by the evaluation of the TLS data sets. The origin of the sets post-dating the sheeting joint is not clear. However, Martel (2017) mentions the possible presence of systematic fractures which are younger than sheeting joints and further decrease the rock mass strength by acting as a mechanical link of the sheeting joints. The young joints are oriented perpendicular to the sheeting joints and terminate against the latter (Martel, 2017). This pattern seems to fit for sets 5 and e, which are identified as post-sheeting joint.

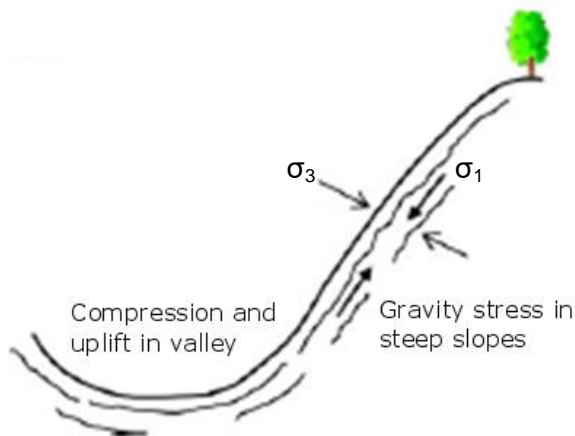


Figure 164: Sheeting joint development (modified after Hencher et al., 2011)

6.2 Plane fitting problems

As already mentioned in the results chapter, there are several problems which inhibit a “perfect” plane fitting process. The main problems are the roundness of the rock mass and the vegetation. The roundness causes the edges of joint sets to become blurred and influences the whole fracture pattern, as well as the termination. Since the whole rock face is affected by weathering, the roundness problem concerns a very high amount of planes. Another facet of this roundness is given by the sheeting joint’s curvature and waviness. The interaction of different sheeting joint planes might intensify the weathering in the concerned parts of the tabular blocks and increase the roundness. The clustering and plane fitting becomes more difficult, as rounded edges cannot be identified as belongings of a set by the algorithm. CloudCompare’s (2019) tendency to overestimate the planes compensates for this roundness to a certain extent, but the termination might be biased nevertheless. This is the reason why the so-called neighborhood, i.e. the evaluation of the local roundness, is an

important part when the termination is investigated. The RGB point cloud as well as the dip and dip direction scalar fields help with the evaluation of the fitted plane's true size. The second problem mentioned here is the vegetation, which might cause a shadowing effect in the point cloud resulting in a data hole, conceal the true joint surface (especially low vegetation like grass or moss), or increase the noise surrounding a joint surface. In addition, vegetation is represented by many points in the point cloud which might decrease the clustering and surface extraction quality.

In general, joint sets in the point cloud will never be perfectly clustered due to noise, vegetation, asperities on the joint planes, and the roundness in granite. Several other problems like data holes caused by shadowing or other reasons, statistical removal because of a too high variation in dip direction, or overlooking of some planes, might also occur. Nevertheless, the applied procedure is quite quick, effective, and produces reasonable results. Additionally, it provides several steps of result validation, e.g. through the comparison of point cloud normals and calculated orientation statistics, of the RGB point cloud and the planes, and of point cloud normals and fitted planes stereograms.

7 Discussion

7.1 Method

The applied method tries to use free, open-source software for discontinuity extraction out of a point cloud. It makes use of CloudCompare's (2019) potential which exceeds the cleaning of a point cloud in order to continue the work with another software, for example.

For the normals computation, the parameter settings appear to be well chosen. Concerning the Hough Normals Computation Plugin (Boulch and Marlet, 2016), it has to be noted that the plugin seems to barely respond to parameter changes in the tests with the geometric forms. However, it has been used for the methodology here as the plugin's power lies in the application on point clouds of varying density and with higher noise (Boulch and Marlet, 2016, slides) like the Ricobayo TLS data. The normals computation results confirm this expectation in comparison to the straight-forward normals computation.

The clustering method used here is a hard partition skmeans clustering (Hornik et al., 2017) conducted in R (R Core Team, 2018). Assali et al. (2014) also used the combination of R and skmeans clustering (references in Assali et al., 2014). Chen et al. (2016), for example, improved the skmeans algorithm for use in noisy data in terms of a density-based clustering centroid detection. Riquelme et al. (2014) use a kernel density estimation to determine the density peaks, which correspond to the main discontinuity sets. Afterwards, the user applies a filter which identifies the peaks representing sets. Guo et al. (2017) apply two different algorithms: the firefly algorithm and the fuzzy c-means algorithm (references in Guo et al., 2017). The primary characteristic of "fuzzy" clustering is that data points may belong to more than one cluster at the same time (Matteucci, 2019). In a hard partition k-means clustering, each data point belongs to one cluster only and it is vital for good clustering results to choose the initial clustering centers wisely, i.e. the furthest possible away from each other (Matteucci, 2019). The firefly algorithm used in Guo et al. (2017, including references for the algorithm) can reveal the best cluster centers. Based on the function behind the algorithms given by Matteucci (2019), the k-means and the c-means calculation principles show similarities. The clustering method used by Riquelme et al. (2014) is a probability based approach, which has also been used by Buyer and Schubert (2016). Matteucci (2019) explains that clusters can be seen as Gaussian distributions with their cluster center located in the distribution's centroid. Probabilistic distributions provide the possibility for soft partitions, too. If a clustering algorithm is applied on geological data, one has to keep in mind that each plane belongs to one set only. This contradicts any fuzzy approach. However, the Ricobayo data features rounded edges and corners, which could have been better clustered by a fuzzy algorithm, as the points could have been counted to both surfaces contributing to

the edges. The normals at rounded edges are oriented to somewhere in between the orientations of the planes by which they are bordered. Although the edges do not represent an individual set, a hard partition could classify them into a separate cluster if they are common in the outcrop. The user's estimation about the number of clusters would be wrong in that case because one cluster would have been unintentionally occupied. Therefore, a fuzzy algorithm could be better suited for outcrops with a pronounced roundness. In a user-guided clustering process, the user can correct any misclassified normals, of course. This has also been done here and appeared to be thoroughly feasible, but some improvements of the used clustering algorithm and their effects on the classification quality should be investigated. A possibility is to use the *skmeans* package (Hornik et al., 2017) in R (R Core Team, 2018), as done in this thesis, but to soften the partition by setting the parameter *m*, which governs the fuzziness like in a *c-means* clustering, to >1 . The need for the spherical version of the clustering algorithm is obvious due to the 3D orientation of the normals. Through the implementation of the firefly algorithm (references see Guo et al., 2017), the clustering results could be improved by optimizing the cluster centers beforehand. It is obvious that the method is not fully automated, being aware of the advantages and drawbacks of the user's involvement, which most importantly are keeping the overall control but also introducing a bit of subjectivity. This is particularly visible if this thesis' workflow is compared with the one proposed in Chen et al. (2016). Although the workflow used here is more time-consuming than the automated one of Chen et al. (2016), this thesis' one does not completely rely on the silhouette plot's (Rousseeuw, 1987) highest average silhouette width. Generally, the silhouette concept (Rousseeuw, 1987) has not only been used in this methodology, but also by Assali et al. (2014) and Chen et al. (2016), for example. From the results generated within this thesis' work, the silhouette plot is thoroughly applicable to geological datasets, but it has to be interpreted with care. The highest average silhouette width does not seem to be suited as the deciding value of the number of clusters as in Chen et al. (2016), because the maximum average silhouette width does not always match the best clustering results for the Ricobayo TLS datasets. The maximum and third quartile values, maybe together with the median value, appear to be more significant. At relatively higher values, they seem to ensure a better clustering result. Alternatively to the silhouette index (Rousseeuw, 1987), Guo et al. (2017) used the Xie-Beni Index (Xie and Beni, 1991), for example, to evaluate the clustering results. The Xie-Beni Index is suited for fuzzy *c*-clustering (Xie and Beni, 1991). The validity function is defined to evaluate the cluster compactness and separation, i.e. the distance between cluster centroids. In the optimal fuzzy *c*-means partition, the validity function reaches its minimum due to compact and separated clusters. In Xie and Beni (1991), several clustering validity criteria are mentioned. The Xie-Beni Index (Xie and Beni, 1991) can be seen as an alternative to the silhouette index, but the

former is restricted to fuzzy c-partitions. The Xie-Beni Index can be realized in R (R Core Team, 2018) via the fuzzy clustering package "fclust" (Giordani et al., 2018). However, a semi-automatic approach appears to be better suited for the investigation of geological data than a fully automated method, as the uncertainties, irregularities, and noise of geological surfaces probably make some educated user decisions necessary. In addition, not all parallel discontinuities must belong to the same set, as they could differ in their genesis. Only a semi-automatic approach can differentiate these discontinuities.

The use of the commercial application FracMan (Golder Associates Inc., 2018) contradicts the open-software approach of this methodology. It is of course possible to write a code for orientation statistics in R (R Core Team, 2018), but this was not possible during this thesis due to time constraints. The statistics should be based on the eigenvalue method (see e.g. Woodcock and Naylor, 1983; Scheidegger, 1965; Wallbrecher, 1986), which is also used in Dips (Rocscience Inc., 2018). The eigenvector which corresponds to the largest eigenvalue represents the mean orientation (see e.g. Scheidegger, 1965). Woodcock and Naylor (1983) propose an eigenvalue-ratio graph (Figure 165) to graphically investigate the sample shape. Therefore, a cluster shaped sample is characterized by one very high eigenvalue ("S1" in Figure 165) and two far lower eigenvalues ("S2" and "S3" in Figure 165). The higher eigenvalue "S1" in relation to the other eigenvalues, the more pronounced is the cluster. The assumption of a theoretical distribution for the sets, e.g. Fisher or Bingham distribution, is criticized by Woodcock and Naylor (1983), because geological data does "not usually conform well to available ideal distributions". However, in the Ricobayo data, the assumption of a cluster shape for the set orientation distributions, represented by a Fisher distribution, has appeared to be a good decision. This is proven by the good conformity of the visual inspection of the dip and dip direction point clouds in CloudCompare (2019), the clustering results, the orientation statistics and their stereogram plots (FracMan, Golder Associates Inc., 2018), the data extraction success (Facets, Dewez et al., 2016), and finally the plane orientation stereograms and statistics (Dips, Rocscience Inc., 2018). The orientation statistics calculation in FracMan (Golder Associates Inc., 2018) combined with the data extraction by the Facets Plugin (Dewez et al., 2016) is well suited for cluster-distributed data. After all, the Dips (Rocscience Inc., 2018) calculation showed one high and two low eigenvalues as expected for clusters. An eigenvalue analysis in R (R Core Team, 2018) instead of the FracMan (Golder Associates Inc., 2018) calculation would nevertheless be preferable as it minimizes assumptions concerning theoretical distributions and enhances objectivity. The calculation of the variability and the confidence angles could be added to the eigenvalue analysis code in order to improve this workflow's effectivity. A detailed description of the calculation process has been given above in the methodology chapter. The probability of 95.4% has excluded some surfaces from the feature extraction with Facets (Dewez et al.,

2016), but this does not influence the overall discontinuity pattern. In addition, this does not concern any big surfaces. A higher probability would have raised the variability angle to unreasonable values contradicting any assumed parallelism of set surfaces. The confidence angles are very low, which is caused by the high amount of values per sample, i.e. by the amount of normals per set. The low angles are expectable after consideration of the angle's calculation equation (4, chapter 4). The successful surface extraction with Facets (Dewez et al., 2016) needs the variability angle only.

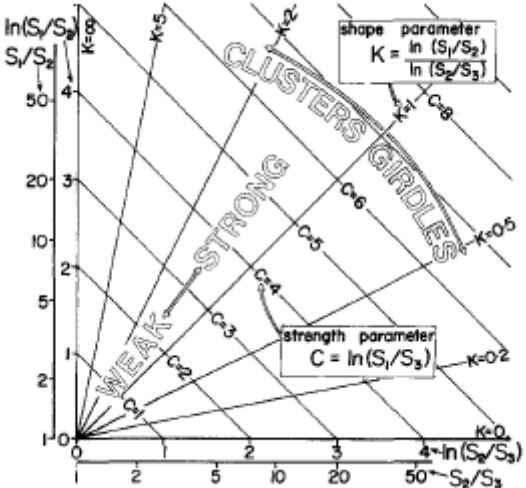


Figure 165: The eigenvalue ratio graph by Woodcock and Naylor (1983)

The idea of a minimum plane size as well as a reclassification, implemented here by the re-clustering, are also needed for the methodology of Chen et al. (2016). However, the minimum plane size is bounded to a minimum number of facets per plane, which is not necessary here as this is the user's decision. The minimum plane size of >1 m² has been justified above and seems to be reasonable in consideration of the results. Nevertheless, the sets post-dating the sheeting joint could have been eliminated in some segments by this plane size limit. For the reconstruction of the geological evolution, this is much worse than from an engineering geological point of view, because these planes are just not significant to the rock mass behavior. In general, the segmentation and plane fitting part of the workflow probably is the most time-consuming one. An algorithm telling CloudCompare (2019) to segment each surface >1 m² would be very helpful. However, the result should be evaluated by the user before the plane fitting in order to ensure the segmentation of geologically true surfaces.

As already mentioned above, CloudCompare (2019) fits rectangular planes over the segmented surfaces. Although the mean set plane orientation corresponds very well to the mean normal orientation of a set, the rectangular shape often leads to an overestimation of the planes. As the artificially added plane area is within reason, the relative plane size in one

set and in comparison to other sets is barely affected. In addition, the overestimation effect is compensated for by the TLS data set's problems. Vegetation and horizontal surfaces have caused shadowing during the data acquisition, which has resulted in data holes or areas of a lower point cloud density. Many of these problems have been taken into account and the result has been corrected by the "neighborhood". This introduces some subjectivity into the analysis, whose impact remains reasonable as long as the neighborhood interpretation only includes quite obvious problems and effects. In general, the point cloud density varies over the whole TLS data sets, i.e. beyond the segments which show a higher resolution. The amount of noise is strongly influenced by the vegetation. In rocky parts, the noise is low and the plane fitting is subject to one problem less. This is also the reason why the structural analysis has been done in the segments only. An evaluation of the whole datasets would not have been worth the effort because the set characteristics outside the segments are widely concealed by vegetation, concrete, or shotcrete, for example. The rock mass' joint sets are best shown in the segments causing the set characteristics to be optimally represented in these parts of the whole datasets. Concerning the set persistence, this parameter could also be influenced by the data acquisition itself. As already mentioned above, the position of the laser scanner relative to the discontinuity or slope surface can cause shadowing. In case a discontinuity surface is fragmented into parts by this effect, the persistence seems to be lower. The consideration of the "neighborhood" can solve this problem, too.

The proposed methodology is not only applicable to joint sets, but also to other types of discontinuities like schistosity, foliation or bedding planes. The only vital characteristic for the application is the (sub-) parallelism of the set planes. A fold, for example, could pose severe problems by its varying orientation. Fractures due to blasting or geomorphological strains like land sliding or creeping are not necessarily parallel to each other (Price, 2009) which may frustrate any classification into sets by this methodology. In case of a fault present in the outcrop, any non-translational movement could modify the fracture pattern orientation and conceal actually parallel discontinuity sets. In case there are small surfaces in an outcrop which should be mapped as distinctive planes, it is important to keep the noise low. High noise conceals surfaces, getting worse with decreasing surface or plane size. It is assumed that there is a limit to minimum plane size caused by noise in a TLS data set.

7.2 Results

The joint sets identified in this thesis consist of sheeting joints, two conjugated sets pre-dating the sheeting joints, and one set post-dating the sheeting joints. Segments 1, 2, and 3 have shown similar fracture patterns of a good correspondence. Concerning segment 4, the sheeting joint sets not only show a quite wide variety of dip, but also of dip direction. Set IV

has been interpreted as a sheeting joint surface mostly due to its plane extent. However, its true meaning remains doubtful. The dip of set III differs from its corresponding sets', but this has already been discussed above (chapter interpretation). Set II poses questions about its orientation and plane size in comparison to the other post-sheeting joint sets (5 and e), which is why its tectonic evolution is difficult to interpret. However, set II has been classified as post-sheeting joint based on a visual point cloud inspection revealing its appearance in the outcrop in relation to the other joint sets.

Nevertheless, the tectonic evolution seems quite clear. The regional compressive stress state resulted in a shortening in deformation event D3 (González Clavijo and Martínez Catalán, 2007). After the placement of the syn-D3 Ricobayo batholith at 307 Ma (Gutierrez-Alonso et al., 2013) during the formation of upright folds, subvertical faults developed in the Ricobayo granites (González Clavijo and Martínez Catalán, 2007). These faults strike NE-SW and define the fluvial system in the area. On a regional scale, the Villalcampo Shear System, which pre-dates the subvertical faults, appears as a dextral strike slip shear zone with a displacement of three to four kilometers (González Clavijo and Martínez Catalán, 2007). However, it seems not to appear in the Ricobayo granites, and has not been mentioned in connection with the latter in literature. The same is true for the conjugated NW-SE striking faults of the subvertical, NE-SW running faults of the Ricobayo granites (González Clavijo and Martínez Catalán, 2007). The stress state is still compressive (González Clavijo and Martínez Catalán, 2007). The sheeting joints are younger features, which is also generally stated in Hencher et al. (2011) and Martel (2017). The age of the individual sheeting joints decreases with depth from the surface (Martel, 2017, and references therein). Their development might be caused by several factors including the topography, the regional horizontal stress state, gravity, and groundwater pressure (Martel, 2017). As an even younger set, sets 5 and e, and set II evolved. Their true development is obscure, but could be related to further, later shortening events. According to González Clavijo and Martínez Catalán (2007), the area has been a craton since the end of the shortening.

The Ricobayo dam site has already been investigated in a field survey by Kaspar (2012) and Coelho Rocha (2012), and through the same TLS data set as used for this thesis by Liu (2013), who investigated the area of segment 1 by using another methodology. Liu (2013) identified five sets. Table 16 compares the orientation data from Kaspar (2012), which is the same as in Coelho Rocha (2012), Liu (2013) and segment 1, representing this thesis' results. In segment 1, the conjugated sets are sets 3 and 4. While the dip direction is similar to the conjugated sets' dip direction in Liu (2013), set 3 dips steeper and set 4 dips flatter. However, a certain variation of these conjugated sets is also visible in the different segments.

The sheeting joint sets (sets 1 and 2) are called “sheeting joint” and “flat” by Liu (2013). Their orientation corresponds quite well. Set 5 can be connected to the set “vertical” by Liu (2013). The connection to the sets identified by Kaspar (2012) and Coelho Rocha (2012) is more difficult. Kaspar (2012) states that set J1 is the most dominant set, while it is interpreted as the youngest set. Based on its orientation and the photos in Kaspar (2012), J1 might be assigned to set 4, in combination with set J4, i.e. set 3. However, this contradicts the development of the sets proposed by Kaspar (2012). According to a trace map given in Coelho Rocha (2012), it is quite certain that set J1 corresponds to set 4. Furthermore, Kaspar (2012) mentions set J1 in combination with set J5, whose orientation does not correspond to any set identified in segment 1 neither in Liu (2013). Set J3 can be assigned to set 1, although the TLS data is dominated by set 1 and set J3 is not mentioned to be especially common. The steep dip causes the difference in dip direction. Set J2’s orientation resembles the one of set 3’s corresponding sets in segments 2 to 4, but this connection is very uncertain. As Coelho Rocha (2012) mentions sets J2, J3, and J4 to define the plunge pool’s walls, which would correspond to sets 1 (sheeting joint, J3) and 3 (pre-sheeting joint, J4; less influence on slope direction), J2 could be interpreted as another sheeting joint set. Its steep dip and the slope-controlling behavior over wide areas might be the key features.

Table 16: Joint set comparison

Kaspar (2012) , Coelho Rocha (2012)	Liu (2013)	Segment 1
J1 (340/31)	Sheeting joint (77/81)	Set 1 (74/89)
J2 (132/85)	Conjugated 1 (328/74)	Set 2 (286/18)
J3 (248/88)	Conjugated 2 (171/58)	Set 3 (183/70)
J4 (192/85)	Flat (263/19)	Set 4 (356/36)
J5 (155/19)	Vertical (343/79)	Set 5 (324/73)

According to a scanline survey conducted by Kaspar (2012), the spacing ranges between 0.2 m and 2 m, although some joints show a spacing of up to 6 m. Coelho Rocha (2012) gives a similar mean spacing and observed very high persistent sets downstream from the Ricobayo dam. A rough estimation from the TLS point cloud reveals spacing values in the range of several meters. For set 1 in segment 1, for example, a spacing of about 2 to 4 m is quite common. According to Martel (2017), the spacing of sheeting joints is usually small in comparison to the extent of the sheeting joint plane, causing tabular slabs of one to ten meters thickness (Hencher et al., 2011, citation always includes references therein). The spacing is mentioned here in the discussion instead of in the results due to its parallelism problem (see chapter methodology) and consequently high variation, which is also visible in the spacing calculations by Kaspar (2012) and Coelho Rocha (2012). However, a TLS point cloud can provide at least the order of magnitude of the spacing. In addition, Martel (2017) states that sheeting joints show a rather frequent spacing, which is also observable in the TLS point cloud in segment 1, for example, as well as that the sheeting joints’ spacing

increases with depth from the surface. An exception are the hook-shaped ends of sheeting joints where planes overlap and terminate into each other (Martel, 2017, and references therein). The spacing of the main sheeting joint in segment 2 (set a) is about 3 to 5 m, in segment 3 2 to 4 m (set E), and in segment 4 about 2 m (estimated over all SJ sets together). Concerning the conjugated sets pre-dating the sheeting joint, their spacing ranges from 2 to 4 m (set 4) and 2 to 6 m (set 3). The corresponding sets in segments 2 and 3 show similar spacing values. In segment 4, the spacing is not possible to be estimated due to the low number of planes and their non-overlapping. During a spacing estimation for the set post-dating the sheeting joint, this problem occurs again: a low set persistence, closely related to the set's plane size. As the youngest set shows very small plane sizes, very rarely are direct spacing estimations possible. Most of the time, the plane would have to be elongated to estimate the spacing. However, a set spacing in the range of several meters, similar to the other sets in segment 1, maybe a bit less, can be estimated for set 5. Set II also shows a spacing of about 2 to 3 m.

While Kaspar (2012) identified the local rock as granodiorite, it is referred to as granitoid in Coelho Rocha (2012), and as granite in Fernández-Turiel et al. (1990; 1991). González Clavijo and Martínez Catalán (2002) mention different types of granite, leucogranite and diorite in the Ricobayo batholith. However, the Ricobayo plutonic body has been affected by weathering, e.g. by exfoliation which causes rounded edges and corners in the outcrop (Bell, 2007). The sheeting joints themselves also tend to round off the rock (Martel, 2017). According to Hencher et al. (2011), steep slopes, where sheeting joints usually occur, are subject to higher surface erosion. The warm and temperate climate in Ricobayo provides reasonably good conditions for weathering. Typically, weathering causes granite to deteriorate which ends in granular disintegration and a loss of strength (Vinx, 2015). Although the weathering grade is difficult to investigate in the TLS point cloud, the rock mass can be assumed to be significantly weathered due to its long time exposure. This is consistent with Kaspar (2012), who reported some isolated, rounded blocks, as well as strong discoloration including iron oxide formation and disintegration. The mean intact rock strength is given in Coelho Rocha (2012, and references therein) as well as in Kaspar (2012, and references therein) as 100 MPa (UCS). However, Kaspar (2012) observed that at some locations weathering has decreased the strength to a soil-like consistency despite the original fabric is still present (Kaspar, 2012). These are characteristics of saprolite, which is another typical feature of granite weathering (Vinx, 2015). Therefore, the rock mass appears to be weathered by different extents depending on the location. The roundness problem which occurred during the plane fitting process is probably caused by the sheeting joints' tendency to round off edges and corners, combined with the weathering of the rock mass. Weathering is also important for the development of new sheeting joints. As soon as the rock

mass is intensely fractured or deeply weathered, no further sheeting joints can develop (Hencher et al., 2011). In a depth of 15 m below surface, weathering grades of III to IV (Coelho Rocha, 2012 and reference therein: ISRM, 1981) have been reported, although in the field, the depth of these weathering grades has been observed to be 5 m (Coelho Rocha, 2012, and references therein).

Furthermore, Kaspar (2012) mentions the possibility of water ingress into the rock mass via joints at the Ricobayo dam site. However, Coelho Rocha (2012) states that no flow has been observed on discontinuity surfaces. Concerning the sheeting joints, newly formed ones show walls fitting together perfectly (Hencher et al., 2011). However, the joint's permeability is higher compared to the surrounding non-fractured rock. Therefore, groundwater flow will be channeled along the sheeting joint (Hencher et al., 2011). As already mentioned above, groundwater plays an important role in sheeting joint formation, too (Martel, 2017). In general, drainage along joints shows tortuous flow in distinct channels causing the joint walls to become weathered (Hencher et al., 2011). According to Kaspar (2012), there are joints showing minor water seepage at the Ricobayo dam site, but just a few. Coelho Rocha (2012) did not observe any groundwater flow in underground excavations of the dam site. While most joints are closed, the few which are open show mainly surface staining, but some are filled by clayey or rock powder material (Kaspar, 2012). Additionally, Coelho Rocha (2012) mentions highly weathered discontinuities and slickensides on set J1 (see above). Furthermore, the discontinuity surfaces are mainly planar to undulating with some roughness, the rock mass being blocky to tabular (Coelho Rocha, 2012). Based on this description, an estimation of the friction angle is quite difficult. A clayey infill can decrease the intact rock's peak friction angle significantly from about 40° (granite) to 24° (Hoek, 2007 and reference therein: Barton, 1974). However, with decomposed granite or rock fragments as infillings, the friction angle is similar to the one of intact rock (Hoek, 2007 and reference therein: Barton, 1974). Coelho Rocha (2012) assumed a joint compressive strength (JCS) as high as the UCS and calculated a peak friction angle of about 40°, and a residual friction angle of about 30° for all sets J1 to J5 (see above). Hencher et al. (2011) also state that the weathering condition of sheeting joints is critical for slope stability. As soon as the rock is deeply weathered and weakened enough, the underlying joints' waviness and roughness become ineffective for slope stability. In combination with a rapidly increasing water pressure, this weakening may cause a major hazard (Hencher et al., 2011). According to Hencher et al. (2011), the stability of sheeting joints is mainly due to their waviness and roughness, i.e. by a basic friction which is enhanced by dilation. This is an important characteristic of sheeting joints, as the stability of other types of joints is usually related to rock bridges and the consequently enhanced cohesion. From case studies, Hencher et al. (2011) identified the development of cleft water pressures as key to sheeting joint failures. In

addition, these failures may evolve incrementally over several storm events (Hencher et al., 2011). Therefore, any kinematic analysis is afflicted with doubts due to the uncertainty in friction angle, caused by the unclear aperture and infilling of the joint sets and the effect of dilation on rough (sheeting) joint surfaces. In addition, the possible presence of water on the joint surfaces (minor seepage according to Kaspar, 2012) is not clear. Coelho Rocha (2012) identified planar sliding and wedge sliding as the main failure modes in the area. However, Hencher et al. (2011) state that sheeting joints usually fail by translational sliding of rock slabs, often caused by water pressure, while wedge sliding is less common (Hencher et al., 2011). In all segments, the slope direction is parallel to the local sheeting joint orientation. A slope-parallel planar sliding along the steepest local sheeting joint is thoroughly imaginable. This would mainly concern set 1 (74/89) in segment 1, set a (227/85) in segment 2, set E (103/85) in segment 3, and sets IV (255/69), V (291/74), VI (311/74), and VII (313/44) in the correspondent parts in segment 4. Due to the slope steepness, toppling should also be investigated in a future kinematic analysis after the determination of the friction angle. Wedge sliding of non-sheeting joint sets could also be possible, but seems rather unlikely. Without consideration of the statement about seldom wedge sliding of sheeting joints (Hencher et al., 2011), an intersection of a sheeting joint plane and a non-sheeting joint plane also seems possible. The scour in the plunge pool resulted in several wall failures, including a wedge failure identified by Coelho Rocha (2012), along the intersection of his joint sets J1 and J3, i.e. the sheeting joint set 1 and the non-sheeting joint set 4. As already mentioned above, today's slope orientation around the plunge pool appears to be controlled by sheeting joints. To sum up, the sheeting joint sets appear to be most important for any kinematic analysis.

8 Conclusion

The method developed and applied in this thesis analyzes a 3D point cloud concerning its inherent discontinuity pattern. The first step is the Hough normals computation with the corresponding plugin by Boulch and Marlet (2016) for CloudCompare (2019). These normals are clustered using a skmeans algorithm (Hornik et al., 2017) in R (R Core Team, 2018). The clustering result is evaluated by means of the silhouette index and its plot (Rousseeuw, 1987). The best clustering results appear for the number of clusters which generates the highest third quartile and maximum values in the silhouette plot. The clusters are used to separate discontinuity sets, whose mean orientations are calculated assuming a Fisher distribution in FracMan (Golder Associates Inc., 2018). Afterwards, the variability angle as well as the confidence angle are calculated, using a probability of 95.4% and the Fisher concentration parameter k , which has been determined in FracMan (Golder Associates Inc., 2018). This information is needed for the set extraction with the Facets Plugin (Dewez et al., 2016) in CloudCompare (2019), which considers dip and dip direction of a set at the same time. After the SOR provided by CloudCompare (2019), all set surfaces $>1 \text{ m}^2$ are segmented. It is important to segment surfaces as big as possible, i.e. not to separate any surface artificially. The minimum plane size has been set after literature study, keeping the engineering geological aim of the methodology in mind. The planes are fitted to the segmented surfaces. Their size is deduced automatically, as CloudCompare (2019) only fits rectangular planes. The quality of fit is given by the RMS in CloudCompare (2019), but also by a comparison of the plane poles, the normals, and the calculated Fisher-distributed normals in a stereogram. To test the method, it has been applied on geometric forms (Riquelme et al., 2014) at first. The successful test showed that in smaller datasets with clearly distinguishable sets, the mean set orientations could also be calculated at the same time in one dataset in FracMan (Golder Associates Inc., 2018). For the form's horizontal top plane (dip $\sim 0^\circ$), the dip direction is $0-360^\circ$. The orientation statistics could seem unnecessary for small datasets, but it is vital for bigger data sets as the Ricobayo TLS data in order not to overlook any discontinuity sets. The Facets Plugin (Dewez et al., 2016) performs well whatever the amount of normals in the set.

For the Ricobayo data, four segments have been defined which are assumed to be representative for the whole area. The segments show the rock mass structure very clearly, despite some TLS data problems like data holes or noise. As the set planes, which are generated using the proposed methodology, are laid over the RGB point cloud, their fit can be evaluated. Horizontal surfaces pose problems due to their low surface area and the laser scanner's wide footprint. However, the plane fitting provides good results which allow the determination of the number of sets, the plane size and persistence, the termination, and the

spacing. The termination might need further investigation as point cloud obstacles or high discontinuity plane waviness might conceal the true termination. Therefore, a “neighborhood” parameter is introduced which takes these problems into account. However, the neighborhood has to be evaluated with care in order to minimize subjectivity. The location-based characterization of discontinuity planes is considered in terms of the investigation of each planes’ individual termination. The plane sizes in the Ricobayo data reveal an expectable trend: There are more small planes in a set than big ones. This has been proven by several histograms. Over all sets, the mean set spacing is several meters.

Therefore, four main discontinuity sets have been detected in the Ricobayo data. Two sets are conjugated and correspond to NE-SW striking subvertical faults mentioned by González Clavijo and Martínez Catalán (2002). They developed in a compressive stress state after the development of upright folds due to shortening (D3) and the syn-D3 emplacement of the Ricobayo batholith (González Clavijo and Martínez Catalán, 2002) at 307 Ma (Gutierrez-Alonso et al., 2013). Afterwards, sheeting joints developed. They control the slope appearance throughout the Ricobayo dam site, including the plunge pool, and are thought to have been key to the massive scour which occurred in the last century (Coelho Rocha, 2012). According to Martel (2017), the topography, the regional horizontal stress state, gravity, and water pressure are the most important factors for sheeting joint development. Sheeting joints may vary in dip due to their 3D extent. This is also visible in the Ricobayo sheeting joint sets. The high plane size, i.e. high persistence, and considerable roughness and waviness are further characteristics for sheeting joints (Hencher et al., 2011). However, the surface curvature and roundness, which seems to be partly caused by sheeting joints, pose challenges to the plane fitting process. The roundness might also be due to weathering, which commonly leads to a granular disintegration and strength reduction (Vinx, 2015) in granite. The degree of weathering is not completely clear, but seems to significantly depend on the location. The discontinuity surface weathering ranges from staining to a possible clayey infilling (Kaspar, 2012). Based on these descriptions, a representative friction angle is difficult to estimate. However, the sheeting joint sets seem to be most important for slope kinematics and stability. The fourth discontinuity set which has been detected in the data post-dates the sheeting joints. It shows very small plane sizes and could be due to later shortening before the region became a craton (González Clavijo and Martínez Catalán, 2002).

As desired, the semi-automated method has resulted in the identification of the discontinuity pattern of the Ricobayo dam site. However, several improvements could be implemented. These include the consideration of fuzzy clustering algorithms in case of a rock mass concerned by considerable roundness. The silhouette plot (Rousseeuw, 1987) seems to

correspond to the best clustering results at the highest third quartile and maximum values. To minimize commercial software in this workflow, the orientation statistics could also be calculated with the eigenvalue method (e.g. Scheidegger, 1965) in R (R Core Team, 2018), ideally including the variability and confidence angles calculation. In order to enhance the efficiency of the proposed method, an algorithm for CloudCompare (2019) to automatically segment each surface exceeding a given threshold, e.g. $>1 \text{ m}^2$, would be preferable. However, the user should finally decide about the true geological surfaces before any plane fitting is performed.

Literature

Google Earth. Pro. Version 7.3.2.5776 (64-bit) (2018). Build: 5.3.2019: Google LLC.

CloudCompare. Version 2.10 (Zephyrus) (2019). compiled with MSVC 1916 and Qt 5.9.3.
Available online at www.cloudcompare.org.

Abellán, A.; Oppikofer, T.; Jaboyedoff, M.; Rosser, N. J.; Lim, M.; Lato, M. J. (2014):
Terrestrial laser scanning of rock slope instabilities. In *Earth Surf. Process. Landforms* 39 (1),
pp. 80–97. DOI: 10.1002/esp.3493.

Assali, P.; Grussenmeyer, P.; Villemin, T.; Pollet, N.; Viguié, F. (2014): Surveying and
modeling of rock discontinuities by terrestrial laser scanning and photogrammetry. Semi-
automatic approaches for linear outcrop inspection. In *Journal of Structural Geology* 66,
pp. 102–114. DOI: 10.1016/j.jsg.2014.05.014.

Barton, N. (1974): A review of the shear strength of filled discontinuities in rock. In *Norwegian
Geotech. Inst. Publ.* (105).

Bell, F. G. (2007): Engineering geology. 2nd ed. Oxford, Burlington, MA: Butterworth-
Heinemann. Available online at
<http://search.ebscohost.com/login.aspx?direct=true&scope=site&db=nlebk&db=nlabk&AN=186102>.

Boulch, A. (2017): normals_Hough. Read Me. Available online at
https://github.com/aboulch/normals_Hough/blob/master/README.md, checked on
9/16/2018.

Boulch, A.; Marlet, R. (2016): Deep Learning for Robust Normal Estimation in Unstructured
Point Clouds. In *Computer Graphics Forum* 35 (5), pp. 281–290. DOI: 10.1111/cgf.12983.
Slides available online at [http://imagine.enpc.fr/~marletr/publi/SGP-2016-Boulch-
Marlet_slides.pdf](http://imagine.enpc.fr/~marletr/publi/SGP-2016-Boulch-Marlet_slides.pdf), checked on 4/28/2019.

Bueno Hernández, F.; Saldana Arce, D. (year unknown): Evolucion de la ingenieria de
presas en Espana. El caso de los "saltos del Duero". Edited by Area de Ingeniería
Hidráulica. Escuela Politécnica Superior. Universidad de Burgos. Burgos.

Buyer, A.; Schubert, W. (2016): Extraction of discontinuity orientations in point clouds. In
*2016 ISRM International Symposium: Rock Mechanics & Rock Engineering: From the Past
to the Future*.

Chen, Jianqin; Zhu, H.; Li, X. (2016): Automatic extraction of discontinuity orientation from rock mass surface 3D point cloud. In *Computers & Geosciences* 95, pp. 18–31. DOI: 10.1016/j.cageo.2016.06.015.

CloudCompareWiki (2018a): Normals\Compute. Available online at <https://www.cloudcompare.org/doc/wiki/index.php?title=Normals%5CComput>, checked on 9/19/2018.

CloudCompareWiki (2018b): Normals\Invert. Available online at <http://www.cloudcompare.org/doc/wiki/index.php?title=Normals%5CInvert>, checked on 9/16/2018.

CloudCompareWiki (2019a): Fit Plane. Available online at https://www.cloudcompare.org/doc/wiki/index.php?title=Fit_Plane, checked on 4/3/2019.

CloudCompareWiki (2019b): SOR. Available online at https://www.cloudcompare.org/doc/wiki/index.php?title=SOR_filter, checked on 4/27/2019.

Coelho Rocha, L. F. M. (2012): Response of Ricobayo Dam spillway walls to extensive rock scour. Master Thesis. Graz University of Technology, Graz. Institute of Applied Geosciences. Available online at <https://diglib.tugraz.at/download.php?id=576a7960f4210&location=search>.

Dewez, T. B.J.; Girardeau-Montaut, D.; Allanic, C.; Rohmer, J. (2016): Facets. A Cloudcompare Plugin to extract geological planes from unstructured 3D point clouds. In *Int. Arch. Photogramm. Remote Sens. Spatial Inf. Sci.* XLI-B5, pp. 799–804. DOI: 10.5194/isprsarchives-XLI-B5-799-2016.

Diederichs, M. S. (1990): Dips. An interactive and graphical approach to the analysis of orientation based data. University of Toronto, Toronto. Department of Civil Engineering.

Farahmand, K.; Vazaios, I.; Diederichs, M. S.; Vlachopoulos, N. (2018): Investigating the scale-dependency of the geometrical and mechanical properties of a moderately jointed rock using a synthetic rock mass (SRM) approach. In *Computers and Geotechnics* 95, pp. 162–179. DOI: 10.1016/j.compgeo.2017.10.002.

Feng, Q.; Röshoff, K. (2015): A Survey of 3D Laser Scanning Techniques for Application to Rock Mechanics and Rock Engineering. In R. Ulusay (Ed.): *The ISRM Suggested Methods for Rock Characterization, Testing and Monitoring. 2007-2014*. Cham: Springer International Publishing, pp. 265–292.

- Fernandez-Turiel, J. L.; Hernández Chiva, E.; Duran, M. E.; Querol, X. (1990): Lithogeochemical exploration in a Hercynian Tin-Bearing Batholith in the Northwest of the Iberian Peninsula. In *Acta Geologica Hispanica* (25), pp. 177–183.
- Fernandez-Turiel, J. L.; Saavedra Alonso, J.; Vaquer, R.; Duran, M. E.; Querol, X. (1991): Late and postmagmatic alterations in the tin-bearing batholith of Ricobayo (Iberian Massif, NW Spain). In *Acta Geologica Hispanica* 26 (1), pp. 17–22. Available online at <http://hdl.handle.net/10261/6819>.
- Genske, D. D. (2014): *Ingenieurgeologie. Grundlagen und Anwendung. 2., neu bearb. und aktualisierte Aufl.* 2014. Berlin: Springer Spektrum. Available online at <http://dx.doi.org/10.1007/978-3-642-55387-5>.
- Giordani, P.; Ferraro, M. B.; Serafini, A. (2018): Package 'fclust'.
- Golder Associates Inc. (2018): FracMan. Version 7.70. Build 2018.07.13.
- González Clavijo, E.; Martínez Catalán, J. R. (2002): Stratigraphic record of preorogenic to synorogenic sedimentation, and tectonic evolution of imbricate units in the Alcañices synform (northwestern Iberian Massif). In J. R. Martínez Catalán, Hatcher, R.D., Jr., R. Arenas, F. Díaz García (Eds.): *Variscan-Appalachian dynamics: The building of the late Paleozoic basement*. Special Paper 364, vol. 364. Boulder, Colorado: Geological Society of America, pp. 17–35.
- Guo, J.; Liu, S.; Zhang, P.; Wu, L.; Zhou, W.; Yu, Y. (2017): Towards semi-automatic rock mass discontinuity orientation and set analysis from 3D point clouds. In *Computers & Geosciences* 103, pp. 164–172. DOI: 10.1016/j.cageo.2017.03.017.
- Gutierrez-Alonso, G.; Pastor-Galán, D.; Collins, A. S. (2013): Strike-slip accommodation during the development of the Cantabrian and Central-Iberian oroclines: $^{40}\text{Ar}^*/^{39}\text{Ar}$ geochronological ages of major shear zones. EGU General Assembly 2013 (Geophysical Research Abstracts, 15).
- Hencher, S. R.; Lee, S. G.; Carter, T. G.; Richards, L. R. (2011): Sheeting Joints. Characterisation, Shear Strength and Engineering. In *Rock Mech Rock Eng* 44 (1), pp. 1–22. DOI: 10.1007/s00603-010-0100-y.
- Hoek, E. (2007): *Practical Rock Engineering*. Available online at <https://www.rocscience.com/assets/resources/learning/hoek/Practical-Rock-Engineering-Full-Text.pdf>.
- Hornik, K.; Feinerer, I.; Kober, M. (2017): Package 'skmeans'.

Hornik, K.; Feinerer, I.; Kober, M.; Buchta, C. (2012): Spherical k -Means Clustering. In *J. Stat. Soft.* 50 (10). DOI: 10.18637/jss.v050.i10.

Iberdrola (2009): Presa de Ricobayo. Available online at <https://www.iberdrola.com/sala-comunicacion/noticias/detalle/ricobayo-una-de-las-obras-de-ingenieria-mas-impresionantes-de-toda-europa-7741226520090408>.

ISRM (1978): Suggested methods for the quantitative description of discontinuities in rock masses. In *International Journal of Rock Mechanics and Mining Sciences & Geomechanics Abstracts* (15), pp. 319–368.

ISRM (1981): Suggested Methods, Rock Characterization: Testing and Monitoring.

Jaboyedoff, M.; Metzger, R.; Oppikofer, T.; Couture, R.; Derron, M.; Locat, J.; Turmel, D. (2007): New insight techniques to analyze rock-slope relief using DEM and 3D-imaging cloud points. In E. Eberhardt, D. Stead, T. Morrison (Eds.): *Rock Mechanics: Meeting Society's Challenges and Demands*: Taylor & Francis, pp. 61–68.

Jaboyedoff, M.; Oppikofer, T.; Abellán, A.; Derron, M.; Loye, A.; Metzger, R.; Pedrazzini, A. (2012): Use of LIDAR in landslide investigations. A review. In *Nat Hazards* 61 (1), pp. 5–28. DOI: 10.1007/s11069-010-9634-2.

Kaspar, M. (2012): Geological Conditions Favoring Extreme Scour of an Unlined Spillway at Ricobayo Dam, Zamora, Spain. Master Thesis. Graz University of Technology, Graz. Institute of Applied Geosciences. Available online at <https://diglib.tugraz.at/download.php?id=576a7622ba609&location=browse>.

Liu, Q. (2013): Remote sensing technologies in rock mass characterization. In X.-T. Feng (Ed.): *Rock characterisation, modelling and engineering design methods*. Proceedings of the 3rd ISRM SINOROCK Symposium Tongji University, Shanghai, PR China, 18 - 20 June 2013. London u.a.: CRC Press.

Martel, S. J. (2017): Progress in understanding sheeting joints over the past two centuries. In *Journal of Structural Geology* 94, pp. 68–86. DOI: 10.1016/j.jsg.2016.11.003.

Martínez Catalán, J. R. (2011): The Central Iberian arc: implications for the Iberian Massif. In *Geogaceta* (50-1), pp. 7–10.

Matteucci, M. (2019): A Tutorial on Clustering Algorithms. Available online at https://home.deib.polimi.it/matteucc/Clustering/tutorial_html/index.html, checked on 4/4/2019.

Ni, P.; Wang, S.; Wang, C.; Zhang, S. (2017): Estimation of REV Size for Fractured Rock Mass Based on Damage Coefficient. In *Rock Mech Rock Eng* 50 (3), pp. 555–570. DOI: 10.1007/s00603-016-1122-x.

Oppikofer, T.; Bunkholt, H. S. S.; Fischer, L.; Saintot, A.; Hermanns, R. L.; Carrea, D. et al.: Investigation and monitoring of rock slope instabilities in Norway by terrestrial laser scanning. In E. Eberhardt (Ed.): *Landslides and engineered slopes: protecting society through improved understanding*. Proceedings of the 11th International and 2nd North American Symposium on Landslides and Engineered Slopes, Banff, Canada, 3 - 8 June 2012. Boca Raton Fla. u.a.: CRC Press, pp. 1235–1240.

Pfiffner, O. A. (2010): *Geologie der Alpen*. 2. Aufl. Stuttgart: UTB GmbH (L). Available online at <http://www.utb-studi-e-book.de/9783838584164>.

Price, D. G.; Freitas, M. H. de (Eds.) (2009): *Engineering geology. Principles and practice ; with 54 tables*. Berlin: Springer. Available online at http://deposit.dnb.de/cgi-bin/dokserv?id=2681111&prov=M&dok_var=1&dok_ext=htm.

R Core Team (2018): *R: A language and environment for statistical computing*. Version 3.5.1 Feather Spray. Vienna: R Foundation for Statistical Computing. Available online at <https://www.R-project.org/>.

R documentation (2019): *Silhouette*. Available online at <https://www.rdocumentation.org/packages/cluster/versions/2.0.7-1/topics/silhouette>, checked on 1/27/2019.

Riquelme, A.; Abellán, A.; Tomás, R. (2015): Discontinuity spacing analysis in rock masses using 3D point clouds. In *Engineering Geology* 195, pp. 185–195. DOI: 10.1016/j.enggeo.2015.06.009.

Riquelme, A.; Abellán, A.; Tomás, R.; Jaboyedoff, M. (2014): A new approach for semi-automatic rock mass joints recognition from 3D point clouds. In *Computers & Geosciences* 68, pp. 38–52. DOI: 10.1016/j.cageo.2014.03.014.

Riquelme, A.; Cano, M.; Tomás, R.; Abellán, A. (2017): Identification of Rock Slope Discontinuity Sets from Laser Scanner and Photogrammetric Point Clouds. A Comparative Analysis. In *Procedia Engineering* 191, pp. 838–845. DOI: 10.1016/j.proeng.2017.05.251.

Rocscience Inc. (2018): *Dips*. 1989-2019. Version 7.013. Toronto. Available online at www.rocscience.com.

Rocscience Inc. (2019): Dips7 documentation. Available online at https://www.rocscience.com/help/dips/FAQs/Dips_FAQs__Input_Data_Format.htm, checked on 1/27/2019.

Rousseuw, P. J. (1987): Silhouettes: a graphical aid to the interpretation and validation of cluster analysis. In *Journal of Computational and Applied Mathematics* (20), pp. 53–65.

Rubio, R. (1940): El túnel aliviadero del salto del Esla. In *Revista de Obras Públicas* (2705).

Scheidegger, A. E. (1965): On the statistics of the orientation of bedding planes, grain axes, and similar sedimentological data. In *Geological Survey Research, U.S. Geol. Survey Prof. Paper* (525-C), C164-C167.

Sociedad Espanola di Presas y Embalses (SEPREM) (2018): Inventario de Presas: Presas Espanolas. Presa: Ricobayo. Available online at <http://www.seprem.es/ficha.php?idpresa=912#>, checked on 10/11/2018.

Stackexchange.com (2018): Difference between standarad and spherical k-means algorithms. Available online at <https://stats.stackexchange.com/questions/63558/difference-between-standard-and-spherical-k-means-algorithms>, checked on 12/15/2018.

Tung, W. Y.; Nagendran, S. K.; Mohamad Ismail, M. A. (2018): 3D rock slope data acquisition by photogrammetry approach and extraction of geological planes using FACET plugin in CloudCompare. In *IOP Conf. Ser.: Earth Environ. Sci.* 169, p. 12051. DOI: 10.1088/1755-1315/169/1/012051.

Vinx, R. (2015): Gesteinsbestimmung im Gelände. 4., neu bearb. u. aktual. Aufl. Berlin: Springer Spektrum. Available online at <http://dx.doi.org/10.1007/978-3-642-55418-6>.

Wallbrecher, E. (1986): Tektonische und gefügearalytische Arbeitsweisen. Graph., rechner. u. statist. Verfahren. Stuttgart: Enke.

Woodcock, N. H.; Naylor, M. A. (1983): Randomness testing in three-dimensional orientation data. In *Journal of Structural Geology* 5 (5), pp. 539–548.

Wu, Q.; Kulatilake, P.H.S.W. (2012): REV and its properties on fracture system and mechanical properties, and an orthotropic constitutive model for a jointed rock mass in a dam site in China. In *Computers and Geotechnics* 43, pp. 124–142. DOI: 10.1016/j.compgeo.2012.02.010.

Xie, X. L.; Beni, G. (1991): A validity measure for fuzzy clustering. In *IEEE Trans. Pattern Anal. Machine Intell.* 13 (8), pp. 841–847. DOI: 10.1109/34.85677.

Zhang, W.; Chen, Jian-ping; Liu, C.; Huang, R.; Li, M.; Zhang, Y. (2012): Determination of Geometrical and Structural Representative Volume Elements at the Baihetan Dam Site. In *Rock Mech Rock Eng* 45 (3), pp. 409–419. DOI: 10.1007/s00603-011-0191-0.

Appendix

R Code – Clustering and Silhouette Plot

```
# source("clustering_new.R")

# setwd("C:/Users/Lisa/Documents/STUDIUM/Master/Masterarbeit/method")

rm(list=ls()) # load required packages

if (require("skmeans")) {
  library(skmeans)}
require("cluster")

## prepare data - enter varying information HERE, don't forget to SAVE afterwards

noc = 7 # set number of clusters

datafile = "rico-segment1-noheader.txt" # set source datafile containing normals information
filename = paste("rico-segment1",noc,"clusters.txt") # create variable filename

## read points & normals out of ASCII:

p = read.table(datafile, row.names = NULL, header = F)

## clustering

n = data.matrix(p[6:8]) # generate matrix of normals

sets = skmeans(n, noc) # conduct a hard partition using skmeans

#p_sets = data.frame(p,c=strtoi(sets$cluster)) # add cluster class id to data.frame

#write.table(p_sets,file = filename,quote = FALSE, row.names = FALSE) # save as ascii

## silhouette plot

# = how well lies each object line within its cluster: high value = object well matched with
cluster

# Many low or negative values of points -> change number of clusters

plottitle=paste("Silhouette Plot for", noc, "clusters/sets")

sil = silhouette(sets)

plot(sil, main=plottitle, do.n.k=TRUE, do.clus.stat=TRUE)

print(summary(sil))

p_sil=data.frame(p,class=sil[,1],neighbor=sil[,2],similar=sil[,3]) # add silhouette data to
data.frame

write.table(p_sil, file=paste(filename),quote=FALSE,row.names=FALSE) # save as ascii
```

Plane data – Termination

nm = not mapped

Segment 1 – set 1

number of terminations	absolute	relative to number of planes [%]	number of terminations with neighborhood	absolute	relative to number of planes [%]
in set 1	76	44.4444	in set 1	140	81.8713
in set 2	9	5.2632	in set 2	21	12.2807
in set 3	31	18.1287	in set 3	42	24.5614
in set 4	7	4.0936	in set 4	30	17.5439
in set 5	9	5.2632	in set 5	16	9.3567
			not known or no comment	15	8.7719
in 0 sets (isolated)	73	42.6901	in 0 sets (isolated)	0	0.0000
in 1 set	70	40.9357	in 1 set	88	51.4620
in 2 sets	24	14.0351	in 2 sets	52	30.4094
in 3 sets	3	1.7544	in 3 sets	11	6.4327
in 4 sets	0	0.0000	in 4 sets	3	1.7544
in 5 sets	1	0.5848	in 5 sets	2	1.1696
total plane number (should: 171)	171		total plane number (should: 171)	171	
terminations in SJ sets (1+2)	78	45.6140	terminations in SJ sets (1+2)	140	81.8713

Problems	absolute number of planes concerned	relative number of planes concerned [%]
roundness	137	80.1170
data hole	12	7.0175
few points	8	4.6784
noise/vegetation	13	7.6023
plane not mapped (nm)	12	7.0175
plane underestimated	4	2.3392
plane ending outside segment	22	12.8655
none	7	4.0936
not known	1	0.5848

Segment 1 – set 2

number of terminations	absolute	relative to number of planes [%]	number of terminations with neighborhood	absolute	relative to number of planes [%]
in set 1	7	70	in set 1	10	100
in set 2	0	0	in set 2	0	0
in set 3	0	0	in set 3	2	20

in set 4	0	0	in set 4	1	10
in set 5	1	10	in set 5	1	10
			not known or no comment	0	0
in 0 sets (isolated)	3	30	in 0 sets (isolated)	0	0
in 1 set	6	60	in 1 set	6	60
in 2 sets	1	10	in 2 sets	4	40
in 3 sets	0	0	in 3 sets	0	0
in 4 sets	0	0	in 4 sets	0	0
in 5 sets	0	0	in 5 sets	0	0
total plane number (should: 10)	10		total plane number (should: 10)	10	
terminations in SJ sets (1+2)	7	70	terminations in SJ sets (1+2)	10	100

Problems	absolute number of planes concerned	relative number of planes concerned [%]
roundness	4	40
data hole	2	20
few points	5	50
noise/vegetation	0	0
plane not mapped (nm)	1	10
plane underestimated	0	0
plane ending outside segment	0	0
none	1	10
not known	0	0

Segment 1 - set 3

number of terminations	absolute	relative to number of planes [%]	number of terminations with neighborhood	absolute	relative to number of planes [%]
in set 1	18	51.4286	in set 1	35	100
in set 2	0	0	in set 2	1	2.8571
in set 3	0	0	in set 3	4	11.4286
in set 4	6	17.1429	in set 4	15	42.8571
in set 5	7	20	in set 5	8	22.8571
		0	not known or no comment	0	0
in 0 sets (isolated)	11	31.4286	in 0 sets (isolated)	0	0
in 1 set	19	54.2857	in 1 set	14	40
in 2 sets	3	8.5714	in 2 sets	14	40
in 3 sets	2	5.7143	in 3 sets	7	20
in 4 sets	0	0	in 4 sets	0	0
in 5 sets	0	0	in 5 sets	0	0
total plane number (should: 35)	35		total plane number (should: 35)	35	

Problems	absolute number of planes concerned	relative number of planes concerned [%]
roundness	24	68.5714
data hole	7	20
few points	5	14.2857
noise/vegetation	7	20
plane not mapped (nm)	4	11.4286
plane underestimated	2	5.71429
plane ending outside segment	1	2.8571
none	4	11.4286
not known	0	0

Segment 1 – set 4

number of terminations	absolute	relative to number of planes [%]	number of terminations with neighborhood	absolute	relative to number of planes [%]
in set 1	7	41.1765	in set 1	17	100
in set 2	0	0	in set 2	0	0
in set 3	6	35.2941	in set 3	11	64.7059
in set 4	1	5.8824	in set 4	1	5.8824
in set 5	8	47.0588	in set 5	8	47.0588
			not known or no comment	0	0
in 0 sets (isolated)	5	29.4118	in 0 sets (isolated)	0	0
in 1 set	5	29.4118	in 1 set	4	23.5294
in 2 sets	4	23.5294	in 2 sets	7	41.1765
in 3 sets	3	17.6471	in 3 sets	5	29.4118
in 4 sets	0	0	in 4 sets	1	5.8824
in 5 sets	0	0	in 5 sets	0	0
total plane number (should: 17)	17		total plane number (should: 17)	17	

Problems	absolute number of planes concerned	relative number of planes concerned [%]
roundness	14	82.3529
data hole	0	0
few points	1	5.8824
noise/vegetation	0	0
plane not mapped (nm)	1	5.8824
plane underestimated	2	11.7647

plane ending outside segment	1	5.8824
none	3	17.6471
not known	0	0

Segment 1 – set 5

number of terminations	absolute	relative to number of planes [%]	number of terminations with neighborhood	absolute	relative to number of planes [%]
in set 1	11	45.8333	in set 1	20	83.3333
in set 2	2	8.3333	in set 2	2	8.3333
in set 3	8	33.3333	in set 3	9	37.5000
in set 4	7	29.1667	in set 4	9	37.5000
in set 5	0	0	in set 5	0	0
		0	not known or no comment	0	0
in 0 sets (isolated)	5	20.8333	in 0 sets (isolated)	0	0
in 1 set	12	50	in 1 set	11	45.8333
in 2 sets	5	20.8333	in 2 sets	10	41.6667
in 3 sets	2	8.3333	in 3 sets	3	12.5000
in 4 sets	0	0	in 4 sets	0	0
in 5 sets	0	0	in 5 sets	0	0
total plane number (should: 24)	24		total plane number (should: 24)	24	

Problems	absolute number of planes concerned	relative number of planes concerned [%]
roundness	20	83.3333
data hole	2	8.3333
few points	5	20.8333
noise/vegetation	4	16.6666
plane not mapped (nm)	3	12.5000
plane underestimated	2	8.3333
plane ending outside segment	0	0
none	0	0
not known	1	4.1666

Segment 2 – set a

number of terminations	absolute number of planes	relative to number of planes [%]	number of terminations with neighborhood	absolute number of planes	relative to number of planes [%]
in set a	37	41.5730	in set a	60	67.4157
in set b	15	16.8539	in set b	16	17.9775
in set c+f	35	39.3258	in set c+f	60	67.4157
in set d	19	21.3483	in set d	26	29.2135

in set e (nm)	nm		in set e (nm)	nm	
			not known or no comment	8	8.9888
in 0 sets (isolated)	23	25.8427	in 0 sets (isolated)	0	0
in 1 set	35	39.3258	in 1 set	24	26.9663
in 2 sets	20	22.4719	in 2 sets	32	35.9551
in 3 sets	9	10.1124	in 3 sets	20	22.4719
in 4 sets	2	2.2472	in 4 sets	5	5.6180
in 5 sets	0	0	in 5 sets	0	0
total plane number (should: 89)	89		total plane number (should: 89)	89	
terminations in SJ sets (a+b)	46	51.6854	terminations in SJ sets (a+b)	66	74.1573

Problems	absolute number of planes concerned	relative number of planes concerned [%]
roundness	80	89.8876
data hole	28	31.4607
few points	9	10.1124
noise/vegetation	20	22.4719
plane not mapped (nm)	4	4.4944
plane underestimated	7	7.8652
plane ending outside segment	3	3.3708
none	1	1.1236
not known	0	0

Segment 2 – set b

number of terminations	absolute number of planes	relative to number of planes [%]	number of terminations with neighborhood	absolute number of planes	relative to number of planes [%]
in set a	9	81.8182	in set a	10	90.9091
in set b	0	0	in set b	0	0
in set c+f	5	45.4545	in set c+f	7	63.6364
in set d	2	18.1818	in set d	3	27.2727
in set e (nm)	nm		in set e (nm)	nm	
			not known or no comment	0	0
in 0 sets (isolated)	1	9.0909	in 0 sets (isolated)	0	0
in 1 set	4	36.3636	in 1 set	4	36.3636
in 2 sets	6	54.5455	in 2 sets	4	36.3636
in 3 sets	0	0	in 3 sets	3	27.2727
in 4 sets	0	0	in 4 sets	0	0
in 5 sets	0	0	in 5 sets	0	0

total plane number (should: 11)	11		total plane number (should: 89)	11	
terminations in SJ sets (a+b)	9	81.8182	terminations in SJ sets (a+b)	10.0000	90.9091

Problems	absolute number of planes concerned	relative number of planes concerned [%]
roundness	4	36.3636
data hole	3	27.2727
few points	2	18.1818
noise/vegetation	2	18.1818
plane not mapped (nm)	1	9.0909
plane underestimated	0	0
plane ending outside segment	2	18.1818
none	2	18.1818
not known	0	0

Segment 2 – set c+f

number of terminations	absolute number of planes	relative to number of planes [%]	number of terminations with neighborhood	absolute number of planes	relative to number of planes [%]
in set a	25	56.8182	in set a	39	88.6364
in set b	5	11.3636	in set b	8	18.1818
in set c+f	6	13.6364	in set c+f	18	40.9091
in set d	14	31.8182	in set d	19	43.1818
in set e (nm)	nm		in set e (nm)	nm	
			not known or no comment	4	9.0909
in 0 sets (isolated)	8	18.1818	in 0 sets (isolated)	0	0
in 1 set	24	54.5455	in 1 set	8	18.1818
in 2 sets	10	22.7273	in 2 sets	20	45.4545
in 3 sets	1	2.2727	in 3 sets	11	25
in 4 sets	1	2.2727	in 4 sets	1	2.2727
in 5 sets	0	0	in 5 sets	0	0
total plane number (should: 44)	44		total plane number (should: 44)	44	

Problems	absolute number of planes concerned	relative number of planes concerned [%]
roundness	38	86.3636
data hole	18	40.9091
few points	7	15.9091
noise/vegetation	12	27.2727
plane not mapped (nm)	1	2.2727

plane underestimated	1	2.2727
plane ending outside segment	5	11.3636
none	0	0
not known	0	0

Segment 2 – set d

number of terminatios	absolute number of planes	Relative to number of planes [%]	number of terminations with neighborhood	absolute number of planes	relative to number of planes [%]
in set a	8	66.6667	in set a	11	91.6667
in set b	2	16.6667	in set b	2	16.6667
in set c+f	9	75	in set c+f	10	83.3333
in set d	0	0	in set d	0	0
in set e (nm)	nm		in set e (nm)	nm	
			not known or no comment	0	0
in 0 sets (isolated)	2	16.6667	in 0 sets (isolated)	0	0
in 1 set	2	16.6667	in 1 set	3	25
in 2 sets	5	41.6667	in 2 sets	5	41.6667
in 3 sets	3	25	in 3 sets	4	33.3333
in 4 sets	0	0	in 4 sets	0	0
in 5 sets	0	0	in 5 sets	0	0
total plane number (should: 12)	12		total plane number (should: 12)	12	

Problems	absolute number of planes concerned	relative number of planes concerned [%]
roundness	8	66.6667
data hole	5	41.6667
few points	1	8.3333
noise/vegetation	8	66.6667
plane not mapped (nm)	0	0
plane underestimated	0	0
plane just estimated	4	33.3333
plane ending outside segment	3	25
none	0	0
not known	0	0

Segment 3 – set A

number of terminations	absolute number of planes	relative to number of planes [%]	number of terminations with neighborhood	absolute number of planes	relative to number of planes [%]
in set A	2	2.6667	in set A	22	29.3333
in set B	11	14.6667	in set B	14	18.6667
in set C+D	21	28	in set C+D	37	49
in set E	36	48	in set E	50	66.6667
			not known or no comment	10	13.3333
in 0 sets (isolated)	26	34.6667	in 0 sets (isolated)	0	0
in 1 set	33	44	in 1 set	21	28
in 2 sets	11	14.6667	in 2 sets	32	42.6667
in 3 sets	5	6.6667	in 3 sets	10	13.3333
in 4 sets	0	0.0000	in 4 sets	2	2.6667
total plane number (should: 75)	75		total plane number (should: 75)	75	
Problems	absolute number of planes concerned	relative number of planes concerned [%]			
roundness	62	82.6667			
data hole	45	60			
few points	12	16			
noise/vegetation	8	10.6667			
plane not mapped (nm)	5	6.6667			
plane underestimated	5	6.6667			
plane ending outside segment	3	4			
none	3	4			
not known	0	0			

Segment 3 – set B

number of terminations	absolute number of planes	relative to number of planes [%]	number of terminations with neighborhood	absolute number of planes	relative to number of planes [%]
in set A	11	25.5814	in set A	19	44.1860
in set B	2	4.6512	in set B	6	13.9535
in set C+D	14	32.5581	in set C+D	25	58.1395
in set E	22	51.1628	in set E	32	74.4186
			not known or no comment	2	4.6512
in 0 sets (isolated)	10	23.2558	in 0 sets (isolated)	0	0
in 1 set	18	41.8605	in 1 set	15	34.8837
in 2 sets	14	32.5581	in 2 sets	13	30.2326
in 3 sets	1	2.3256	in 3 sets	11	25.5814
in 4 sets	0	0	in 4 sets	2	4.6512

total plane number (should: 43)	43		total plane number (should: 43)	43	
terminations in SJ sets (B+E)	23	53.4884	terminations in SJ sets (B+E)	32	74.4186
Problems	absolute number of planes concerned	relative number of planes concerned [%]			
roundness	39	90.6977			
data hole	17	39.5349			
few points	16	37.2093			
noise/vegetation	3	6.9767			
plane not mapped (nm)	3	6.9767			
plane underestimated	7	16.2791			
plane ending outside segment	0	0			
none	1	2.3256			
not known	0	0			

Segment 3 – set C+D

number of terminations	absolute number of planes	relative to number of planes [%]	number of terminations with neighborhood	absolute number of planes	relative to number of planes [%]
in set A	21	15.2174	in set A	40	28.9855
in set B	13	9.4203	in set B	20	14.4928
in set C+D	14	10.1449	in set C+D	54	39.1304
in set E	64	46.3768	in set E	106	76.8116
			not known or no comment	11	7.9710
in 0 sets (isolated)	50	36.2319	in 0 sets (isolated)	0	0.0000
in 1 set	67	48.5507	in 1 set	53	38.4058
in 2 sets	18	13.0435	in 2 sets	58	42.0290
in 3 sets	3	2.1739	in 3 sets	13	9.4203
in 4 sets	0	0	in 4 sets	3	2.1739
total plane number (should: 138)	138		total plane number (should: 138)	138	
Problems	absolute number of planes concerned	relative number of planes concerned [%]			
roundness	120	86.9565			
data hole	53	38.4058			
few points	23	16.6667			
noise/vegetation	28	20.2899			
plane not mapped (nm)	18	13.0435			
plane underestimated	2	1.4493			

plane ending outside segment	2	1.4493
none	3	2.1739
not known	0	0

Segment 3 – set E

number of terminations	absolute number of planes	relative to number of planes [%]	number of terminations with neighborhood	absolute number of planes	relative to number of planes [%]
in set A	36	23.3766	in set A	51	33.1169
in set B	23	14.9351	in set B	31	20.1299
in set C+D	50	32.4675	in set C+D	73	47.4026
in set E	22	14.2857	in set E	66	42.8571
			not known or no comment	25	16.2338
in 0 sets (isolated)	61	39.6104	in 0 sets (isolated)	0	0
in 1 set	67	43.5065	in 1 set	64	41.5584
in 2 sets	16	10.3896	in 2 sets	43	27.9221
in 3 sets	8	5.1948	in 3 sets	17	11.0390
in 4 sets	2	1.2987	in 4 sets	5	3.2468
total plane number (should: 154)	154		total plane number (should: 154)	154	
terminations in SJ sets (B+E)	39	25.3247	terminations in SJ sets (B+E)	81	52.5974

Problems	absolute number of planes concerned	relative number of planes concerned [%]
roundness	140	90.9091
data hole	70	45.4545
few points	47	30.5195
noise/vegetation	30	19.4805
plane not mapped (nm)		0
plane underestimated	14	9.0909
plane ending outside segment	1	0.6494
none	0	0
not known	0	0

Segment 4 – set I

number of terminations	absolute number of planes	relative to number of planes [%]	number of terminations with neighborhood	absolute number of planes	relative to number of planes [%]
in set I	0	0	in set I	2	8.6957
in set II	3	13.0435	in set II	7	30.4348
in set III	6	26.0870	in set III	6	26.0870

in set IV	4	17.3913	in set IV	4	17.3913
in set V	5	21.7391	in set V	9	39.1304
in set VI	2	8.6957	in set VI	2	8.6957
in set VII	0	0	in set VII	2	8.6957
in set VIII	0	0	in set VIII	2	8.6957
			not known or no comment	0	0
in 0 sets (isolated)	7	30.4348	in 0 sets (isolated)	0	0
in 1 set (no SJ)	6	26.0870	in 1 set (no SJ)	7	30.4348
in 2 sets (no SJ)	0	0	in 2 sets (no SJ)	1	4.3478
in 3 sets (no SJ)	0	0	in 3 sets (no SJ)	0	0
only in SJ	7	30.4348	only in SJ	9	39.1304
in SJ + 1 set	3	13.0435	in SJ + 1 set	6	26.0870
in SJ + 2 sets	0	0	in SJ + 2 sets	0	0
in SJ + 3 sets	0	0	in SJ + 3 sets	0	0
total plane number (should: 23)	23		total plane number (should: 23)	23	

Problems	absolute number of planes concerned	relative number of planes concerned [%]
roundness	20	86.9565
data hole	3	13.0435
few points	0	0
noise/vegetation	5	21.7391
plane not mapped (nm)	0	0
plane underestimated	3	13.0435
plane ending outside segment	0	0
none	1	4.3478
not known	0	0

Segment 4 – set II

number of terminations	absolute number of planes	relative to number of planes [%]	number of terminations with neighborhood	absolute number of planes	relative to number of planes [%]
in set I	3	10	in set I	6	20
in set II	0	0	in set II	2	6.6667
in set III	0	0	in set III	2	6.6667
in set IV	4	13.3333	in set IV	6	20
in set V	15	50	in set V	21	70
in set VI	5	16.6667	in set VI	9	30
in set VII	2	6.6667	in set VII	4	13.3333
in set VIII	5	16.6667	in set VIII	8	26.6667
			not known or no comment	0	0
in 0 sets (isolated)	8	26.6667	in 0 sets (isolated)	0	0
in 1 set (no SJ)	0	0	in 1 set (no SJ)	1	3.3333

in 2 sets (no SJ)	0	0	in 2 sets (no SJ)	1	3.3333
in 3 sets (no SJ)	0	0	in 3 sets (no SJ)	0	0
only in SJ	19	63.3333	only in SJ	21	70
in SJ + 1 set	3	10	in SJ + 1 set	7	23.3333
in SJ + 2 sets	0	0	in SJ + 2 sets	0	0
in SJ + 3 sets	0	0	in SJ + 3 sets	0	0
total plane number (should: 30)	30		total plane number (should: 30)	30	

Problems	absolute number of planes concerned	relative number of planes concerned [%]
roundness	30	100
data hole	4	13.3333
few points	0	0
noise/vegetation	12	40
plane not mapped (nm)	0	0
plane underestimated	3	10
plane ending outside segment	0	0
none	0	0
not known	0	0

Segment 4 – set III

number of terminations	absolute number of planes	relative to number of planes [%]	number of terminations with neighborhood	absolute number of planes	relative to number of planes [%]
in set I	5	31.2500	in set I	6	37.5000
in set II	0	0	in set II	2	12.5000
in set III	0	0	in set III	2	12.5000
in set IV	0	0	in set IV	1	6.2500
in set V	3	18.7500	in set V	4	25
in set VI	2	12.5000	in set VI	4	25
in set VII	7	43.7500	in set VII	2	12.5000
in set VIII	0	0	in set VIII	0	0
			not known or no comment	3	18.7500
in 0 sets (isolated)	7	43.7500	in 0 sets (isolated)	0	0
in 1 set (no SJ)	4	25	in 1 set (no SJ)	4	25
in 2 sets (no SJ)	0	0	in 2 sets (no SJ)	1	6.2500
in 3 sets (no SJ)	0	0	in 3 sets (no SJ)	0	0
only in SJ	4	25	only in SJ	4	25
in SJ + 1 set	1	6.2500	in SJ + 1 set	4	25
in SJ + 2 sets	0	0	in SJ + 2 sets	0	0
in SJ + 3 sets	0	0	in SJ + 3 sets	0	0

total plane number (should: 16)	16		total plane number (should: 16)	16	
---------------------------------	----	--	---------------------------------	----	--

Problems	absolute number of planes concerned	relative number of planes concerned [%]
roundness	13	81.2500
data hole	3	18.7500
few points	0	0
noise/vegetation	5	31.2500
plane not mapped (nm)	0	0
plane underestimated	0	0
plane ending outside segment	0	0
none	0	0
not known	1	6.2500

Segment 4 – set IV

number of terminations	absolute number of planes	relative to number of planes [%]	number of terminations with neighborhood	absolute number of planes	relative to number of planes [%]
in set I	4	8.6957	in set I	4	8.6957
in set II	3	6.5217	in set II	5	10.8696
in set III	0	0	in set III	1	2.1739
in set IV	2	4.3478	in set IV	22	47.8261
in set V	21	45.6522	in set V	28	60.8696
in set VI	4	8.6957	in set VI	8	17.3913
in set VII	4	8.6957	in set VII	8	17.3913
in set VIII	6	13.0435	in set VIII	7	15.2174
			not known or no comment	6	13.0435
in 0 sets (isolated)	19	41.3043	in 0 sets (isolated)	0	0
in 1 set (no SJ)	2	4.3478	in 1 set (no SJ)	0	0
in 2 sets (no SJ)	0	0	in 2 sets (no SJ)	0	0
in 3 sets (no SJ)	0	0	in 3 sets (no SJ)	0	0
only in SJ	20	43.4783	only in SJ	31	67.3913
in SJ + 1 set	5	10.8696	in SJ + 1 set	8	17.3913
in SJ + 2 sets	0	0	in SJ + 2 sets	1	2.1739
in SJ + 3 sets	0	0	in SJ + 3 sets	0	0
total plane number (should: 46)	46		total plane number (should: 46)	46	

Problems	absolute number of planes concerned	relative number of planes concerned [%]
roundness	45	97.8261
data hole	1	2.1739
few points	3	6.5217

noise/vegetation	22	47.8261
plane not mapped (nm)	0	0
plane underestimated	1	2.1739
plane ending outside segment	4	8.6957
none	0	0
not known	1	2.1739

Segment 4 – set V

number of terminations	absolute number of planes	relative to number of planes [%]	number of terminations with neighborhood	absolute number of planes	relative to number of planes [%]
in set I	6	5.2632	in set I	13	11.4035
in set II	12	10.5263	in set II	17	14.9123
in set III	5	4.3860	in set III	7	6.1404
in set IV	28	24.5614	in set IV	32	28.0702
in set V	8	7.0175	in set V	47	41.2281
in set VI	32	28.0702	in set VI	37	32.4561
in set VII	29	25.4386	in set VII	41	35.9649
in set VIII	13	11.4035	in set VIII	16	14.0351
			not known or no comment	9	7.8947
in 0 sets (isolated)	36	31.5789	in 0 sets (isolated)	0	0
in 1 set (no SJ)	7	6.1404	in 1 set (no SJ)	4	3.5088
in 2 sets (no SJ)	0	0	in 2 sets (no SJ)	2	1.7544
in 3 sets (no SJ)	0	0	in 3 sets (no SJ)	0	0
only in SJ	56	49.1228	only in SJ	72	63.1579
in SJ + 1 set	14	12.2807	in SJ + 1 set	25	21.9298
in SJ + 2 sets	1	0.8772	in SJ + 2 sets	2	1.7544
in SJ + 3 sets	0	0	in SJ + 3 sets	0	0
total plane number (should: 114)	114		total plane number (should: 114)	114	

Problems	absolute number of planes concerned	relative number of planes concerned [%]
roundness	112	98.2456
data hole	3	2.6316
few points	7	6.1404
noise/vegetation	59	51.7544
plane not mapped (nm)	0	0
plane underestimated	0	0
plane ending outside segment	13	11.4035
none	0	0
not known	0	0

Segment 4 – set VI

number of terminations	absolute number of planes	relative to number of planes [%]	number of terminations with neighborhood	absolute number of planes	
in set I	2	3.5088	in set I	2	3.5088
in set II	8	14.0351	in set II	11	19.2982
in set III	1	1.7544	in set III	5	8.7719
in set IV	4	7.0175	in set IV	11	19.2982
in set V	33	57.8947	in set V	37	64.9123
in set VI	1	1.7544	in set VI	15	26.3158
in set VII	23	40.3509	in set VII	25	43.8596
in set VIII	3	5.2632	in set VIII	7	12.2807
			not known or no comment	3	5.2632
in 0 sets (isolated)	9	15.7895	in 0 sets (isolated)	0	0
in 1 set (no SJ)	4	7.0175	in 1 set (no SJ)	3	5.2632
in 2 sets (no SJ)	0	0	in 2 sets (no SJ)	0	0
in 3 sets (no SJ)	0	0	in 3 sets (no SJ)	0	0
only in SJ	37	64.9123	only in SJ	38	66.6667
in SJ + 1 set	7	12.2807	in SJ + 1 set	11	19.2982
in SJ + 2 sets	0	0	in SJ + 2 sets	2	3.5088
in SJ + 3 sets	0	0	in SJ + 3 sets	0	0
total plane number (should: 57)	57		total plane number (should: 57)	57	

Problems	absolute number of planes concerned	relative number of planes concerned [%]
roundness	57	100
data hole	6	10.5263
few points	5	8.7719
noise/vegetation	16	28.0702
plane not mapped (nm)	0	0
plane underestimated	0	0
plane ending outside segment	1	1.7544
none	0	0
not known	0	0

Segment 4 – set VII

number of terminations	absolute number of planes	relative to number of planes [%]	number of terminations with neighborhood	absolute number of planes	relative to number of planes [%]
in set I	0	0	in set I	2	2.9851
in set II	2	2.9851	in set II	5	7.4627
in set III	0	0	in set III	3	4.4776
in set IV	6	8.9552	in set IV	14	20.8955

in set V	30	44.7761	in set V	38	56.7164
in set VI	21	31.3433	in set VI	23	34.3284
in set VII	0	0	in set VII	13	19.4030
in set VIII	0	0	in set VIII	5	7.4627
			not known or no comment	9	13.4328
in 0 sets (isolated)	23	34.3284	in 0 sets (isolated)	0	0
in 1 set (no SJ)	0	0	in 1 set (no SJ)	0	0
in 2 sets (no SJ)	0	0	in 2 sets (no SJ)	0	0
in 3 sets (no SJ)	0	0	in 3 sets (no SJ)	0	0
only in SJ	42	62.6866	only in SJ	48	71.6418
in SJ + 1 set	2	2.9851	in SJ + 1 set	10	14.9254
in SJ + 2 sets	0	0	in SJ + 2 sets	0	0
in SJ + 3 sets	0	0	in SJ + 3 sets	0	0
total plane number (should: 67)	67		total plane number (should: 67)	67	

Problems	absolute number of planes concerned	relative number of planes concerned [%]
roundness	66	98.5075
data hole	2	2.9851
few points	0	0
noise/vegetation	28	41.7910
plane not mapped (nm)	0	0
plane underestimated	0	0
plane ending outside segment	0	0
none	0	0
not known	1	1.4925

Segment 4- set VIII

number of terminations	absolute number of planes	relative to number of planes [%]	number of terminations with neighborhood	absolute number of planes	relative to number of planes [%]
in set I	0	0	in set I	2	6.0606
in set II	4	12.1212	in set II	5	15.1515
in set III	0	0	in set III	0	0
in set IV	6	18.1818	in set IV	10	30.3030
in set V	16	48.4848	in set V	17	51.5152
in set VI	3	9.0909	in set VI	6	18.1818
in set VII	0	0	in set VII	5	15.1515
in set VIII	2	6.0606	in set VIII	8	24.2424
			not known or no comment	4	12.1212
in 0 sets (isolated)	11	33.3333	in 0 sets (isolated)	0	0
in 1 set (no SJ)	3	9.0909	in 1 set (no SJ)	3	9.0909
in 2 sets (no SJ)	0	0	in 2 sets (no SJ)	0	0

in 3 sets (no SJ)	0	0	in 3 sets (no SJ)	0	0
only in SJ	18	54.5455	only in SJ	22	66.6667
in SJ + 1 set	1	3.0303	in SJ + 1 set	4	12.1212
in SJ + 2 sets	0	0	in SJ + 2 sets	0	0
in SJ + 3 sets	0	0	in SJ + 3 sets	0	0
total plane number (should: 33)	33		total plane number (should: 33)	33	

Problems	absolute number of planes concerned	relative number of planes concerned [%]
roundness	31	93.9394
data hole	2	6.0606
few points	1	3.0303
noise/vegetation	17	51.5152
plane not mapped (nm)	0	0
plane underestimated	5	15.1515
plane ending outside segment	0	0
none	1	3.0303
not known	1	3.0303